

Evaluation of the Long-Term Degradation and Strength Characteristics of In-situ Wisconsin Virgin Base Aggregates under HMA Pavements

Hani H. Titi, Ph.D., P.E., M.ASCE
Habib Tabatabai, Ph.D., P.E., S.E.
University of Wisconsin-Milwaukee

Ahmed Faheem, Ph.D.
Temple University

WisDOT ID no. 0092-15-06

November 2018



RESEARCH & LIBRARY UNIT



WISCONSIN HIGHWAY RESEARCH PROGRAM

WISCONSIN DOT
PUTTING RESEARCH TO WORK

Technical Report Documentation Page

1. Report No. WHRP 0092-15-06	2. Government Accession No.	3. Recipient's Catalog No.	
4. Title and Subtitle Evaluation of the Long-Term Degradation and Strength Characteristics of In-situ Wisconsin Virgin Base Aggregates under HMA Pavements		5. Report Date November 2018	
7. Authors Hani H. Titi, Habib Tabatabai, and Ahmed Faheem		6. Performing Organization Code	
9. Performing Organization Name and Address Department of Civil Engineering and Mechanics University of Wisconsin-Milwaukee 3200 N. Cramer St. Milwaukee, WI 53211		8. Performing Organization Report No.	
12. Sponsoring Agency Name and Address Wisconsin Department of Transportation Hill Farms Building Research & Library Unit 4822 Madison Yards Way Madison, WI 53707		10. Work Unit No. (TRAIS)	
		11. Contract or Grant No. WHRP 0092-15-06	
		13. Type of Report and Period Covered Final Report November 2015 – November 2018	
15. Supplementary Notes		14. Sponsoring Agency Code	
16. Abstract This research investigated the performance of base layer aggregates in HMA pavements using laboratory tests on base layer materials and field tests on pavement sections. The purpose of this research was to investigate potential degradation of aggregate bases as well as to investigate strength reductions over time, and to evaluate the likely causes for both. Such information will be utilized for pavement design and performance evaluation using the AASHTOWare ME Pavement Design. Comprehensive field and laboratory testing programs were conducted to investigate base layer aggregates in which identified test sections at the selected pavement sites were subjected to testing using the FWD, GPR and DCP. Visual distress surveys were also conducted at the selected pavement sections. Base layer aggregate samples were collected from these pavement sites and subjected to a comprehensive laboratory testing program including: standard compaction, particle size analysis, Atterberg Limits, sodium sulfate soundness test, Micro Deval abrasion test, absorption, specific gravity, repeated load triaxial test – resilient modulus, and the CBR test. The base aggregates collected were crushed stone composed of mainly carbonates and gravel/crushed gravel materials. Comprehensive evaluation of test results was conducted with respect to base layer aggregate materials performance is well as performance within the pavement structure.			
17. Key Words Aggregate base layer, base construction specifications, FWD, HMA pavement, QC/QA, LWD, density-based specifications, modulus-based specifications, DARWin-ME		18. Distribution Statement No restriction. This document is available to the public through the National Technical Information Service 5285 Port Royal Road Springfield VA 22161	
19. Security Classif.(of this report) Unclassified	20. Security Classif. (of this page) Unclassified	21. No. of Pages 222	22. Price

DISCLAIMER

This research was funded through the Wisconsin Highway Research Program by the Wisconsin Department of Transportation and the Federal Highway Administration under Project 0092-15-06. The contents of this report reflect the views of the authors, who are responsible for the facts and accuracy of the data presented herein. The contents do not necessarily reflect the official views of the Wisconsin Department of Transportation or the Federal Highway Administration at the time of publication.

This document is disseminated under the sponsorship of the Department of Transportation in the interest of information exchange. The United States Government assumes no liability for its contents or use thereof. This report does not constitute a standard, specification or regulation.

The United States Government does not endorse products or manufacturers. Trade and manufacturers' names appear in this report only because they are considered essential to the object of the document.

Executive Summary

This research investigated the performance of base layer aggregates in HMA pavements using laboratory tests on base layer materials and field tests on pavement sections. The purpose of this research was to investigate potential degradation of aggregate bases as well as to investigate strength reductions over time, and to evaluate the likely causes for both. Such information will be utilized for pavement design and performance evaluation using the AASHTOWare ME Pavement Design.

Comprehensive field and laboratory testing programs were conducted to investigate base layer aggregates in which identified test sections at the selected pavement sites were subjected to testing using the FWD, GPR and DCP. Visual distress surveys were also conducted at the selected pavement sections. Base layer aggregate samples were collected from these pavement sites and subjected to a comprehensive laboratory testing program including: standard compaction, particle size analysis, Atterberg Limits, sodium sulfate soundness test, Micro Deval abrasion test, absorption, specific gravity, repeated load triaxial test – resilient modulus, and the CBR test. The base aggregates collected were crushed stone composed of mainly carbonates and gravel/crushed gravel materials.

The results of the laboratory tests indicated that the particle size distribution for majority of the investigated base aggregates fell outside – in part – the current WisDOT base aggregate gradation specifications, with a number of samples possessed amounts of fines greater than the permitted 12%. This could be due to degradation and disintegration of aggregate particles due to the impact of the freeze-thaw cycles coupled with the traffic repeated loads. However, it should be mentioned that the current gradation specifications were not part of the requirements when a number of these pavements were constructed and therefore these materials could have been selected with different gradations. The amounts of fines found in majority of the aggregate samples were non-plastic from consistency limits point of view. Visual inspection and comparisons with subgrade soils did not show – in general – a wide spread pumping and contamination of the base layers from subgrade soils. It should also be noted that in several of the investigated pavement sections, large stone – breaker run or select materials – subbase layers were used, which could provide a barrier for minimizing/eliminating contamination effect.

The absorption values of the aggregates as well as the durability and abrasion test results indicated reasonable numbers exhibited by the investigated aggregates and these numbers were within a reasonable range compared with the average values obtained from studies conducted on Wisconsin virgin aggregates.

Strength and modulus evaluations of the investigated base aggregates and pavement test sections were also conducted. The soaked CBR test results showed, in general, low CBR numbers especially for aggregate samples with larger fines amounts and for gravel/crushed gravel aggregate samples. The repeated load triaxial test results showed an acceptable level of resilient modulus values compared with a database of test results conducted on virgin Wisconsin aggregates from both pits and quarries (gravel/crushed gravel and crushed stone). However, when the aggregates are of gravel/crushed gravel origin, the resilient modulus are noticed to be lower compared with aggregates from crushed stone sources.

The back-calculated base layer modulus showed significant variability within the pavement test sections, especially pavement test sections possessed lower pavement condition index and higher IRI values. The averages back-calculated layer moduli for the investigated base layers of more than 20 years of age were lower compared with base layers of younger age (about 6 to 9 years) and higher pavement condition index and lower IRI values.

The research team proposed two methods to account for change in base layer materials performance over time as a results of degradation/disintegration and contamination: (1) using gradation of existing base layers by sampling then using the calibrated resilient modulus models to estimate the resilient modulus of these materials (sampling and basic aggregate testing – particle size distribution and compaction), and (2) by performing the FWD and GPR tests – due to the combined change in base layer materials as well as surface layer and subgrade soils – then using the Back-calculation Module of the AASHTOWare ME Pavement Design software. To evaluate pavement design and performance over periods of time.

Acknowledgements

This research project is financially supported by Wisconsin Highway Research Program (WHRP) and Wisconsin Department of Transportation (WisDOT).

The research team would like to acknowledge and thank Mr. Daniel Reid and Ms. Tracy Petersen of WisDOT for their help, support, and effort during field testing.

The input and guidance of WHRP Geotechnical Oversight Committee members and WisDOT engineers Mr. Andrew Zimmer, Mr. Robert Arndorfer, and Mr. Jeffrey Horsfall, is greatly appreciated.

The research team would like to thank Ms. Penny Rollins, Mr. Steven Hunter, and Mr. Joel Ruda of WisDOT drilling unit for their extensive effort to get the aggregate samples from various pavement sites.

The research team would like to thank Mr. Joseph Allaby and Mr. Michael Wolf of WisDOT Pavement Data Unit.

The research team would like to thank Dr. Dante Fratta, Mr. Brett Swenson, Mr. Chad Shihata and Mr. Josh Skarsten for their help.

The research team also acknowledges the help and support of UW-Milwaukee students for their help and support in various capacities for this project: Mr. Nicholas Coley, Dr. Roonak Ghaderi, Mr. Omar Saleh, Mr. Mohammad Sooman, Ms. Alise Fitzsimmons, Ms. Kelli Swenson, Mr. Mohammad Matar, Mr. Jessie Ramirez, Mr. Jason Steffke, and Mr. Ahmed Shatnawi.

Table of Contents

Chapter 1:	Introduction	1
	1.1 Problem Statement.....	1
	1.2 Research Objectives.....	1
	1.3 Background.....	1
	1.4 Organization of the Report.....	3
Chapter 2:	Background	4
	2.1 Characterization of Aggregate Particle Properties.....	4
	2.2 Durability and Abrasion Tests and Evaluation of Aggregates.....	8
	2.3 Resilient Modulus of Aggregates.....	16
	2.4 California Bearing Ratio Test.....	31
	2.5 Field Test Methods.....	31
	2.6 Base Layer Performance Survey.....	35
Chapter 3:	Research Methodology	43
	3.1 Selection of Pavement Test Sites.....	43
	3.2 Non-Destructive Field Testing at Selected Pavement Sites.....	51
	3.2.1 Falling Weight Deflectometer Tests.....	51
	3.2.2 Ground Penetrating Radar.....	52
	3.2.3 Visual and Automated Pavement Surface Distress Surveys	53
	3.3 Sampling of Base Layer Aggregates and Field Testing.....	54
	3.3.1 Sampling of Base Aggregates.	54
	3.3.2 Dynamic Cone Penetration Test.....	56
	3.4 Laboratory Testing of Base Aggregate.....	59
	3.4.1 Particle Size Analysis.....	59
	3.4.2 Standard Compaction Test.....	62
	3.4.3 Specific Gravity and Absorption.....	63
	3.4.4 Sodium Sulfate Soundness Test.....	63
	3.4.5 Micro-Deval Abrasion Test.....	64
	3.4.6 California Bearing Ratio.....	66
	3.4.7 Repeated Load Triaxial Test.....	68
Chapter 4:	Analysis of Laboratory Test Results on Base Aggregate Materials	72
	4.1 Particle Size Distribution.....	72
	4.2 Durability Tests of the Investigated Aggregates.....	83
	4.2.1 Specific Gravity and Absorption.....	83
	4.2.2 Micro-Deval Abrasion.	84
	4.2.3 Sodium Sulfate Soundness.	88
	4.2.4 Analyses of Durability Test Results.....	93
	4.3 Strength and Modulus Tests of the Investigated Base Layer Aggregates.....	99
	4.3.1 Standard Compaction Test	99
	4.3.2 California Bearing Ratio.....	100
	4.3.3 Repeated Load Triaxial Test – Resilient Modulus.....	104
Chapter 5:	Analysis of Field Test Results on Aggregate Base Layers	108
	5.1 Dynamic Cone Penetration Test	108
	5.2 Ground Penetrating Radar.....	110

	5.3 Falling Weight Deflectometer.....	118
	5.4 Visual and Automated Distress Surveys.....	126
Chapter 6:	Evaluation of Investigated Base Layer Aggregates.....	132
	6.1 Base Aggregate Properties – Correlations	132
	6.2 Strength and Modulus Based on Dynamic Cone Penetration Test.....	135
	6.3 Resilient Modulus Based on Repeated Load Triaxial Test.....	138
Chapter 7:	Summary and Conclusions.....	164
References	169
Appendix A	Soil Data Base Acquired from the USDA Website	A-1
Appendix B	Dynamic Cone Penetration Test Results and Corresponding Predicted CBR.....	B-1
Appendix C	Ground Penetrating Radar Results.....	C-1
Appendix D	Falling Weight Deflectometer Test Results	D-1
Appendix E	Visual and Automated Distress Surveys.....	E-1

List of Figures

Figure 2.1	Histogram and best fit distribution of the results of various tests conducted on Wisconsin aggregates from pits and quarries.	10
Figure 2.2	Histograms and best-fit distributions for tests performed in WHRP Phase I study.	12
Figure 2.3	Results of the various tests conducted on the twelve Wisconsin marginal aggregates versus the corresponding average value (shown in red line) from the Wisconsin aggregate database.	14
Figure 2.4	Results of the logistic regression analysis predicting the outcomes of the Micro-Deval test for the twelve aggregate sources assuming a threshold of 18 and 14% for Micro-Deval loss.	15
Figure 2.5	Results of repeated load triaxial tests on Wisconsin and Kentucky aggregates from pits (gravel/crushed gravel) and quarries (crushed stone).	23
Figure 2.6	Performance of existing models (presented in Table 2.6) in predicting the resilient modulus of measured WI aggregates.	25
Figure 2.7	Performance of the developed models (presented in Table 2.8) in predicting the resilient modulus of measured WI and KY aggregates.	29
Figure 2.7 (Cont.)	Performance of the developed models (presented in Table 2.8) in predicting the resilient modulus of measured WI and KY aggregates.	30
Figure 3.1	Locations of the investigated pavements in Wisconsin.	44
Figure 3.2	Geological and particle characteristic descriptions of the investigated base course layer aggregates.	45
Figure 3.2 (Cont.)	Geological and particle characteristic descriptions of the investigated base course layer aggregates.	46
Figure 3.3	Nondestructive testing using the WisDOT FWD KUAB/GSSI GPR unit at various HMA pavement sites.	53
Figure 3.4	Visual pavement surface distress surveys conducted by the research team.	54
Figure 3.5	Pictures of various pavement surface distresses at a number of test sections.	55
Figure 3.6	Coring of pavement surface to retrieve base aggregate samples.	57
Figure 3.7	Sampling of base aggregates using handheld tools.	58
Figure 3.8	Dynamic cone penetration test of aggregate base course layers.	59
Figure 3.9	Compaction test equipment used for base aggregates.	62
Figure 3.10	Aggregate preparation and testing – sodium sulfate and Micro-Deval.	65
Figure 3.11	Specimen preparation and testing for standard compaction and CBR tests.	67
Figure 3.12	Repeated load triaxial test conducted using Instron 8802 dynamic material test system to determine resilient modulus of soils.	69
Figure 3.13	Preparation and testing of base aggregate specimens for repeated load triaxial test according to AASHTO T 307 standard procedure.	70
Figure 4.1	Particle size distribution of the investigated base aggregates and the corresponding WisDOT gradation specification limits for base course materials.	74
Figure 4.1 (Cont.)	Particle size distribution of the investigated base aggregates and the corresponding WisDOT gradation specification limits for base course materials.	75

Figure 4.2	Large stone sized particles found in a number of the investigated base course layers.	79
Figure 4.3	Particle size characteristics of the investigated aggregates.	80
Figure 4.4	Pictures of the investigated base aggregates showing each aggregate sample (right) as used in the base course layer and its fraction finer than 0.425 mm (left).	81
Figure 4.4 (Cont.)	Pictures of the investigated base aggregates showing each aggregate sample (right) as used in the base course layer and its fraction finer than 0.425 mm (left).	82
Figure 4.5	Comparison of amount of fines in subgrade soils with fines found in the corresponding base layer aggregates.	82
Figure 4.6	Specific gravity and absorption test results for investigated coarse aggregates.	84
Figure 4.7	Mass loss of coarse and fine aggregates due to the Micro-Deval test.	86
Figure 4.8	Pictures of the investigated aggregates and the corresponding coarse aggregate abrasion due to the Micro-Deval test.	87
Figure 4.8 (Cont.)	Pictures of the investigated aggregates and the corresponding coarse aggregate abrasion due to the Micro-Deval test.	88
Figure 4.9	Final mass loss of coarse and fine aggregates due to the sodium sulfate soundness test.	90
Figure 4.10	Cumulative mass loss per sodium sulfate soundness test cycle for the investigated aggregates.	91
Figure 4.11	Percent rate change in mass loss between sodium sulfate soundness test cycles for the investigated coarse aggregate fractions.	92
Figure 4.12	Comparison of mass loss of coarse aggregates from Micro-Deval abrasion versus absorption for various Wisconsin virgin aggregates	94
Figure 4.13	Comparison of mass loss of coarse aggregates from Micro-Deval abrasion versus absorption for various Wisconsin virgin and in-service aggregates	95
Figure 4.14	Comparison of mass loss of coarse aggregates from Micro-Deval abrasion versus absorption for various Wisconsin virgin aggregates	97
Figure 4.15	Comparison of mass loss of coarse aggregates from the Sodium Sulfate Soundness test versus absorption for Wisconsin virgin and base layer coarse aggregates.	98
Figure 4.16	Comparison of mass loss of coarse aggregates from the Sodium Sulfate Soundness test versus Micro-Deval abrasion for Wisconsin virgin and base layer coarse aggregates.	98
Figure 4.17	Standard compaction test results for base layer aggregates.	99
Figure 4.18	Maximum dry unit weight ($\gamma_{d,max}$) and optimum moisture content (w_{opt}) of the investigated base layer aggregates.	100
Figure 4.19	Piston pressure versus penetration during soaked CBR tests on base layer aggregates.	101
Figure 4.20	CBR test results for the investigated in-service base layer aggregates (soaked CBR).	101
Figure 4.21	Soaked CBR test results for the investigated base layer aggregates based on their particle shape and composition.	103

Figure 4.22	Soaked CBR values versus amount of fines present in the investigated base layer aggregates.	104
Figure 4.23	Results of the repeated load triaxial test on base layer and virgin aggregates.	105
Figure 4.24	Results of the repeated load triaxial test on base layer and virgin aggregates.	106
Figure 4.25	Comparison of the resilient modulus performance of the tested base layer and virgin aggregates with Wisconsin virgin aggregates.	107
Figure 5.1	DCP test results for the base layer aggregates of investigated pavements.	109
Figure 5.2	Profiles of CBR values estimated from DCP test with depth compared with soaked CBR values from laboratory test.	110
Figure 5.3	Location, track of GPR testing, and pavement surface cores at USH 45 pavement in Pelican Lake, WI.	112
Figure 5.4	Pavement layer profiles obtained from analysis of GPR data from USH 45 PL	113
Figure 5.5	Location, track of GPR testing, and excavated pavement layers at STH 142 E pavement in east of Burlington, WI.	114
Figure 5.6	Pavement layer profiles obtained from analysis of GPR data from STH 142E.	115
Figure 5.6 (Cont.)	Pavement layer profiles obtained from analysis of GPR data from STH 142E.	116
Figure 5.7	Adjusted deflection under loading plate (D_0) normalized to 9,000 lb load for investigated HMA pavements.	119
Figure 5.8	Variation of deflection (D_0) under the loading plate.	120
Figure 5.9	Back-calculated layer moduli for HMA surface layers, aggregate base layers constructed with gravel/crushed gravel, and subgrade soils (STH 142 E and Edgerton Ave – weak bases).	122
Figure 5.10	Box-whisker plot for E_{HMA} of the investigated pavements.	123
Figure 5.11	Box-whisker plot for E_{Base} of the investigated pavements.	123
Figure 5.12	Box-whisker plot for E_{Base} of the investigated pavements.	124
Figure 5.13	Distribution of back-calculated layer moduli for aggregate base layers constructed with gravel/crushed gravel (STH 142 E and Edgerton Ave – weak bases).	125
Figure 5.14	Results of visual and automated distress surveys at USH 45 – Pelican Lake.	127
Figure 5.15	Results of visual and automated distress surveys at STH 59 – Edgerton.	128
Figure 5.16	Results of visual and automated distress surveys at STH 142 E – Burlington	129
Figure 5.17	Results of the visual distress survey at CTH B – Woodville (Ramp).	130
Figure 5.18	Comparison of PCI calculated from the visual and automated distress surveys ($PCI < 55$ is poor, $55 \leq PCI < 70$ is fair, $PCI \geq 70$ is good).	131
Figure 6.1	Plots and histograms of the individual properties and parameters of the investigated base layer aggregates.	134
Figure 6.2	PCI Predicted using various proposed relationships compared with PCI from visual distress surveys at different pavement test sections.	135
Figure 6.3	Comparison of CBR predicted by field DCP test and measured from soaked Laboratory test.	136
Figure 6.4	Lognormal distributions depicting the high variability of base layer strength of investigated pavement test sections.	137

Figure 6.5	Variability with depth of base layer modulus of CTH B as predicted by the DCP test.	137
Figure 6.6	Statistical analysis of the resilient modulus data for Wisconsin virgin aggregates at different stress levels.	138
Figure 6.7	Statistical analysis of the resilient modulus data for Wisconsin virgin aggregates from both quarries and pits.	139
Figure 6.8	Comparison of resilient modulus test results for investigated base layer aggregates with Wisconsin virgin aggregates.	139
Figure 6.9	Comparison of measured and predicted resilient modulus of investigated base layer aggregates using UW-Milwaukee Model	141
Figure 6.10	Comparison of measured and predicted resilient modulus of investigated base layer aggregates using LTPP Models.	142
Figure 6.11	AASHTOWare Pavement ME Design evaluation of performance of STH 33 Saukville pavement for various base layer aggregate resilient moduli (input).	144
Figure 6.11 (Cont.)	AASHTOWare Pavement ME Design evaluation of performance of STH 33 Saukville pavement for various base layer aggregate resilient moduli (input).	145
Figure 6.12	AASHTOWare Pavement ME Design evaluation of performance of USH 45 PL pavement for various base layer aggregate resilient moduli (input).	146
Figure 6.12 (Cont.)	AASHTOWare Pavement ME Design evaluation of performance of USH 45 PL pavement for various base layer aggregate resilient moduli (input).	147
Figure 6.13	Comparison of pavements with good and poor performance due to base layer modulus.	148
Figure 6.13 (Cont.)	Comparison of pavements with good and poor performance due to variation in base layer modulus.	149
Figure 6.14	Distribution of back-calculated base layer modulus for pavements with good performance.	150
Figure 6.15	Comparison of back-calculated base layer modulus for all investigated pavements with the pavements with good performance.	151
Figure 6.16	Comparison of overlay performance based on thickness using AASHTOWare Pavement ME Design Back-calculation Module for USH 45 PL.	152
Figure 6.16 (Cont.)	Comparison of overlay performance based on thickness using AASHTOWare Pavement ME Design Back-calculation Module for USH 45 PL.	153
Figure 6.17	Comparison of overlay performance based on thickness using AASHTOWare Pavement ME Design Back-calculation Module for USH 45 PL.	154
Figure 6.17 (Cont.)	Comparison of overlay performance based on thickness using AASHTOWare Pavement ME Design Back-calculation Module for USH 45 PL.	155
Figure 6.18	Comparison of overlay performance based on thickness using AASHTOWare Pavement ME Design Back-calculation Module for USH 45 PL.	156

Figure 6.18 (Cont.)	Comparison of overlay performance based on thickness using AASHTOWare Pavement ME Design Back-calculation Module for USH 45 PL.	157
Figure 6.19	Comparison of predicted and measured base layer modulus base on aggregate base layer age.	159
Figure 6.20	Comparison of predicted and measured base layer modulus (E_{base}) and resilient modulus (M_r) based on aggregate base layer age and PCI.	159
Figure 6.21	Variation of resilient modulus (M_r) to base layer modulus (E_{base}) ratio for aggregate base layers with age.	160
Figure 6.22	Performance of the developed models in predicting the resilient modulus of 15 base aggregates in HMA pavements in Wisconsin (measured values: lognormal distribution: $\mu=200.1$ MPa, $\sigma=94.4$ MPa)	162

List of Tables

Table 2.1	Relationship between aggregate properties and HMA pavement-performance parameters (after Saeed et al. 2001).	5
Table 2.2	Selected aggregate characterization tests (After Saeed et al., 2001).	7
Table 2.3	Basic statistics of the Wisconsin database aggregate test results.	9
Table 2.4	Basic statistics for the WHRP Phase I test results (Weyers et al., 2005).	11
Table 2.5	Basic statistics for the aggregate test results reported by Fowler et al. (2006).	13
Table 2.6	The resilient modulus constitutive model parameters proposed by various studies.	20
Table 2.7	Performance of various existing material models in predicting the measured resilient modulus of Wisconsin aggregates from pits (crushed gravel and uncrushed gravel) and quarries (crushed stone).	26
Table 2.8	Material parameter models developed in this study.	28
Table 2.9	Performance of proposed material models in predicting the measured resilient modulus of Wisconsin and Kentucky aggregates from pits (crushed gravel and uncrushed gravel) and quarries (crushed stone).	30
Table 2.10	Summary of material and layer properties used for design and acceptance of flexible pavements and HMA overlays (after Von Quintus et al., 2009).	32
Table 2.11	NDT methods used to measure properties and features of flexible pavements in place (after Von Quintus et al., 2009).	33
Table 3.1	Thickness and age of the samples collected from each project site from WisDOT plans and field measurements.	50
Table 3.2	Field tests conducted at the investigated pavement sites.	52
Table 3.3	ASTM and AASHTO standard test methods employed.	60
Table 3.4	Laboratory tests conducted on base aggregate samples obtained from pavement sites.	61
Table 3.5	Testing sequences for base/subbase materials (AASHTO T 307 – 99 (2017)).	71
Table 4.1	Particle size and plasticity characteristics of the investigated base aggregates.	78
Table 4.2	Particle size characteristics of the investigated base aggregates.	79
Table 4.3	Results of specific gravity and absorption tests on the investigated base aggregates (coarse fraction).	83
Table 4.4	Mass loss of coarse and fine aggregates from the Micro-Deval abrasion test.	85
Table 4.5	Mass loss of coarse and fine aggregates from the sodium sulfate soundness test.	89
Table 4.6	Soaked CBR values, amount of fines, and description of base layer aggregates.	102
Table 5.1	Statistical summary of adjusted deflection under loading plate (D ₀) normalized to 9,000 lb load for investigated HMA pavements	119
Table 5.2	Statistical summary of back-calculated layer moduli for investigated HMA pavements.	121
Table 6.1	Correlation matrix for various test results of 14 investigated aggregates: marked correlations (red) are significant at $p < 0.05000$.	134
Table 6.2	Summary of CBR from soaked laboratory test and CBR predicted by field DCP test for investigated aggregate base layers.	136

Chapter 1

Introduction

1.1 Problem Statement

The Wisconsin Department of Transportation (WisDOT) is deploying the AASHTOWare Pavement ME Design software for pavement structural design. As part of this pavement design procedure, assumptions about the long-term strength of the virgin base aggregate will influence the final pavement thickness design. The department performs over 1,500 borings per year as part of the soil/pavement design process. These borings are used to evaluate the existing soil and pavement materials for incorporation into the pavement design process. However, it has often been observed during construction that the virgin base aggregates have degraded since original placement. WisDOT has hypothesized three potential causes:

1. Individual aggregate chemical and physical breakdown/deterioration
2. Freeze/thaw action
3. Infiltration of subgrade materials

1.2 Research Objectives

The purpose of this research is to investigate potential degradation of virgin aggregate bases, investigate and document strength reductions over time, and evaluate the likely causes of both. This information will be used for current and future local calibration of the ME Design software. Aggregate degradation is defined as the breakdown of an aggregate into smaller particles (Barksdale, 1991).

1.3 Background

Unbound base layers function by supporting traffic loads from the asphalt concrete surface layer and dissipating and transferring such loads to the underlying pavement layer or subgrade. Therefore, the unbound aggregate layers comprise a significant intermediate component in pavement stability and performance. Performance of unbound aggregate materials (crushed stone and gravel/crushed gravel bases) in base course layers depends on the characteristics/properties of the individual aggregate particles and the interaction behavior of groups of particles associated/aggregated in a matrix (e.g., in the base course layer). The importance of the individual particle properties comes from its influence on the group behavior within the matrix. Particle properties include: size, shape, texture, angularity, durability, specific gravity, absorption, toughness, and mineralogical composition. Properties of aggregate particles within a matrix (such as aggregate base layers) include: shear strength, stiffness, density, resistance to permanent deformation, permeability, and frost susceptibility (Saeed et al., 2001).

The individual characteristics of aggregate particles (e.g., shape, angularity, texture) define their ability for interlocking behavior in a packed matrix, such as in base course layers, to provide the desirable structural stability to support traffic loads. Proper construction of aggregate base layers will produce densely packed materials with good interlocking among the particles, leading to increased shear strength and stability and decreased permanent deformation as the void space between particles is minimized. A lack of stability in the base course layers results in the lateral movement of aggregates, thereby causing pavement distress (Barksdale, 2001).

The particle and matrix properties of aggregate particles in unbound base layers influence the performance of flexible pavements. Within the context of aggregate particle durability and strength, the pavements are expected to perform very well; however, poor performance of base layers due to weak/deteriorated aggregate particles can lead to poor pavement performance and early distress and deterioration. Flexible pavement distresses such as fatigue cracking, rutting/corrugations, depressions, and frost heave can be attributed to the poor performance of unbound aggregate base course layers (Saeed et al., 2001).

Saeed et al. (2001) discussed the distresses that are attributed to the poor performance of unbound base course layers. These distresses include:

(a) Fatigue cracking occurs in areas subjected to repeated traffic loading. Cracking starts as fine, longitudinal hairline cracks running parallel to one another in the wheel path. High flexibility in the aggregate base allows excessive bending strains in the asphalt concrete surface. The same result can also be caused by inadequate thickness of the aggregate base. Changes in the base properties with time can render the base inadequate to support loads. The contributing factors to fatigue cracking related to the base layer are:

- (1) low elastic modulus of the base layer
- (2) improper gradation
- (3) high fines content
- (4) high moisture levels
- (5) lack of adequate particle angularity and surface texture (poor interlocking)
- (6) degradation under repeated loads and freeze-thaw cycling

(b) Rutting results from permanent deformation in one or more layers or at the subgrade, usually caused by consolidation and/or lateral movement of the material due to load. Rutting appears as a longitudinal surface depression in the wheel path and may not be noticeable, except during and following rainfall. Inadequate shear strength in the base allows lateral displacement of particles with applications of wheel loads, causing a decrease in the base layer thickness in the wheel path. Inadequate density causes settlement of the base. The contributing factors to rutting are:

- (1) low shear strength of aggregate base
- (2) inadequate compaction, as illustrated by low density

- (3) improper gradation
- (4) high fines content
- (5) high moisture levels
- (6) lack of adequate particle angularity and surface texture
- (7) degradation under repeated loads and freeze-thaw cycling

(c) Frost heave appears as an upward bulge in the pavement surface and may be accompanied by surface cracking, including alligator cracking with resulting potholes. Ice lenses are created within the base/subbase during freezing temperatures as moisture is pulled from below by capillary action. During spring thaw, large quantities of water are released from the frozen zone, which can include all unbound materials. The contributing factors to this distress are:

- (1) freezing temperatures
- (2) source of water
- (3) permeability of material high enough to allow free moisture movement to the freezing zone

1.4 Organization of the Report

This report is organized in seven chapters. Chapter One introduces the problem statement and objective of the research. The literature review and synthesis is presented in Chapter Two, and the research methodology is discussed in Chapter Three. Chapters Four and Five present a detailed analysis of laboratory and field testing programs, respectively, with critical analysis of the outcome. Evaluation of the research results and analysis utilizing the AASHTOWare Pavement ME Design is presented in Chapter Six. The conclusions and recommendations are provided in Chapter Seven.

Chapter 2

Background

This chapter presents background information on the influence of base layer aggregate properties on long term HMA pavement performance. Laboratory and field tests commonly used to characterize and evaluate aggregate durability, strength, and modulus are discussed. Base layer aggregate durability characterization tests as well as repeated load triaxial tests were focused on due to the importance of the test results on the HMA pavement performance and the use of the resilient modulus as input parameter for the AASHTOWare Pavement ME Design. The results of a survey on base layer aggregate performance and other related issues are also presented.

2.1 Characterization of Aggregate Particle Properties

Aggregates particle properties/characteristics are important for the performance of aggregate layers. The aggregate handbook (Barksdale, 2001) provides a detailed description of aggregate properties as well as quantification tests. NCHRP Project 4-23, “Performance-Related Tests of Aggregates for Use in Unbound Pavement Layers (NCHRP Report 453),” summarized the most important particle properties that relate to the performance of aggregates in pavement base layers as:

Gradation (Particle Size Distribution) is the distribution of different aggregate particles by size. Well-graded aggregates indicate good strength of the mixture despite the application. The particle size distribution that allows for the maximum amount of aggregate to be included in a unit volume of mixture can be considered the optimum gradation for most construction applications.

Particle Shape is the shape of the individual aggregate particles. Desired aggregates for an unbound aggregate base are angular, cubical particles for developing aggregate interlock, which increases the shear strength of the base layer.

Particle Texture is the degree of roughness or irregularity of the surface of an aggregate particle. The use of rough aggregates will increase the strength of an unbound aggregate base.

Toughness is the resistance to fracture from impact, and it is closely related to the absence of brittleness.

Particle Strength is the magnitude of the tensile and/or compressive stress that an individual aggregate particle can withstand before failure occurs. Determining the strength of individual aggregate particle is difficult because the particles have varying sizes and shapes.

Particle Stiffness is the resistance of an aggregate particle to deformation, as usually indicated by the modulus of elasticity of the particle. A high degree of stiffness is preferred for most construction applications.

Permeability is defined as the capacity of an aggregate particle, or group of particles, to transmit a fluid. The grading and density of the mixture of aggregate particles determines the overall permeability of a group of particles.

Frost Susceptibility is associated with aggregate resistance to freeze-thaw, and this is defined as the ability of an aggregate to resist deterioration due to cyclic freezing and thawing. When some types of aggregates are wet and subjected to freeze-thaw cycles, general flaking and cracking can occur. The resistance to freeze-thaw is influenced by the volume and size of accessible pores in the aggregate.

Various test methods are available to evaluate the properties of unbound granular materials and how these properties influence pavement performance in terms of distress, structural stability, and ride quality. Table 2.1 describes the relationship between aggregate properties/test parameters and pavement-performance.

Table 2.1: Relationship between aggregate properties and HMA pavement performance parameters (after Saeed et al., 2001).

Performance Parameter	Related Aggregate Property	Test Parameters that May Relate to Performance
Fatigue Cracking	Stiffness	Resilient modulus, Poisson's ratio, gradation, fines content, particle angularity and surface texture, frost susceptibility, degradation of particles, density
Rutting, Corrugations	Shear Strength	Failure stress, angle of internal friction, cohesion, gradation, fines content, particle geometrics (texture, shape, angularity), density, moisture effects
Fatigue Cracking, Rutting, Corrugations	Toughness	Particle strength, particle degradation, particle size, gradation, high fines
	Durability	Particle deterioration, strength loss
	Frost Susceptibility	Permeability, gradation, percent minus 0.02 mm size, density, type of fines
	Permeability	Gradation, fines content, density

The following laboratory tests are conducted on aggregates to assess their performance in base course layers (as summarized in Table 2.2):

Aggregate Screening Tests:

- i. ***Sieve Analysis:*** Gradation is used to indicate permeability, frost susceptibility, and shear strength. Test methods: AASHTO T 2: Standard Method of Test for Sampling of Aggregates, AASHTO T 11: Standard Method of Test for Materials Finer than 75- μm (No. 200) Sieve in Mineral Aggregates by Washing, and AASHTO T 27: Standard Method of Test for Sieve Analysis of Fine and Coarse Aggregates.
- ii. ***Atterberg Limits:*** Ensures that fine materials will have the correct amount of shear strength and not too much change in volume as it expands and shrinks with different moisture contents. Liquid Limit (LL) of aggregate fraction passing the No. 40 sieve (0.425-mm) is determined using AASHTO T 89: Standard Method of Test for Determining the Liquid Limit of Soils and Plastic Limit (PL) is determined using AASHTO T 90: Standard Method of Test for Determining the Plastic Limit and Plasticity Index of Soils.
- iii. ***Moisture-Density Relationship:*** Compaction of aggregate materials generally increases density, shear strength, and stiffness and decreases permeability with increasing moisture content prior to a point of maximum density beyond which these trends reverse. Test methods: AASHTO T 99: Standard Method of Test for Moisture-Density Relations of Soils Using a 2.5-kg (5.5-lb) Rammer and a 305-mm (12-in.) Drop and AASHTO T 180: Standard Method of Test for Moisture-Density Relations of Soils Using a 4.54-kg (10-lb) Rammer and a 457-mm (18-in.) Drop.
- iv. ***Specific Gravity:*** Known as the ratio of the mass of a given volume of aggregate solids to the mass of an equal volume of water. A high specific gravity provides stability to the system without requiring increased layer thickness or increased track cross-section. Test methods: AASHTO T 84: Specific Gravity and Absorption of Fine Aggregate and AASHTO T 85: Specific Gravity and Absorption of Coarse Aggregate.
- v. ***Absorption:*** Indicates the ability of aggregates to retain moisture due to porosity. Particles with high absorption are less durable and may experience freeze-thaw and soundness problems. Absorption test methods AASHTO T 84 and AASHTO T 85 are described earlier.
- vi. ***Flat and Elongated Particles:*** Can break under compaction and change gradation. An excess of these particles may interfere with compaction and consolidation. Test method ASTM D4791: Standard Test Method for Flat Particles, Elongated Particles, or Flat and Elongated Particles in Coarse Aggregate.
- vii. ***Uncompacted Void Content:*** Provides a good overall indicator of the potential for resisting permanent deformation and is a function of particle shape, angularity, and surface texture. Test methods: AASHTO TP 33: Standard Test Method for Uncompacted Void Content of Fine Aggregate (as Influenced by Particle Shape, Surface Texture and

Grading) and ASTM C1252: Standard Test Method for Uncompacted Void Content of Fine Aggregate (as Influenced by Particle Shape, Surface Texture, and Grading).

Table 2.2: Selected aggregate characterization tests (after Saeed et al., 2001).

Aggregate Property	Test Method	Test Reference	Test Parameter
Screening Tests	Sieve Analysis	T 27, T 11 ^a	Particle size distribution
	Atterberg Limits	T 89, T 90 ^a	PL, LL, PI
	Specific Gravity and Absorption	T 84, T 85 ^a	Specific gravity
	Moisture/Density Relationship	T 99, T 180 ^a	Maximum dry density
	Flat and Elongated Particles	D 4971 ^b	F or E, F, and E
	Uncompacted Void Content	TP 33 ^a	Percent uncompacted void
Shear Strength	Shape and Texture	D 3398 ^b	Particle shape and texture index
	Static Triaxial Shear	T 296 ^a	C, ϕ , shear strength
	Repeated Load Triaxial		Deviator stress
Stiffness	California Bearing Ratio	T 193 ^a	CBR
	Repeated Load Triaxial	**	Resilient modulus
Frost Susceptibility	Tube Suction Test	*	Dielectric constant
	Index Method	*	F categories
Toughness and Abrasion	Los Angeles Abrasion	C 131 ^b	% loss, passing #12 sieve
	Aggregate Impact Value	BS 812 ^c	% loss, passing BS 2.40 mm sieve
	Aggregate Crushing Value	BS 812 ^c	% loss, passing BS 2.40 mm sieve
	Micro-Deval Test	TP 58-99 ^a	% loss, passing #16 sieve
	Gyratory Degradation		Before and after gradation
Durability	Sulfate Soundness	T 104 ^a	Weighted average loss
	Aggregate Durability Index	T 210, T 176 ^a	Durability index

- i. a: AASHTO reference test method
- ii. b: ASTM reference test method
- iii. c: British reference test method
- iv. *: No test method is currently available
- v. **: Test method is developed in Saeed et al. (2001)

Aggregate Durability Tests:

- i. **Magnesium or Sodium Sulfate Soundness:** Estimates aggregates' resistance to weathering. Test method: AASHTO T 104: Soundness of Aggregate by Use of Sodium or Magnesium Sulfate.
- ii. **Unconfined Freeze-Thaw Test:** Indicates aggregate's resistance to freeze-thaw action. Test method: AASHTO T 103 Standard Method of Test for Soundness of Aggregates by Freezing and Thawing.

Aggregate Shear Strength Tests:

- i. ***Shear Strength:*** Considered to be the most important aggregate property that affects the performance of unbound base layers. The static triaxial test is the most common test to measure shear strength. Test method: AASHTO T 296: Standard Method of Test for Unconsolidated, Undrained Compressive Strength of Cohesive Soils in Triaxial Compression.
- ii. ***California Bearing Ratio (CBR):*** Is a comparative measure of the shearing resistance of aggregate and it is a widely used method, as a strength parameter, of pavement materials. Test method: AASHTO T 193: Standard Method of Test for The California Bearing Ratio.

Aggregate Stiffness Tests:

- i. ***Repeated Load Triaxial Test:*** Determines the resilient modulus (elastic modulus) based on the recoverable strain under repeated loads. Test method: AASHTO T 307: Standard Method of Test for Determining the Resilient Modulus of Soils and Aggregate Materials.

Aggregate Toughness and Abrasion Resistance Tests:

- i. ***Micro-Deval Abrasion:*** Indicates the potential of an aggregate to degrade. Test method: AASHTO T 327: Standard Method of Test for Resistance of Coarse Aggregate to Degradation by Abrasion in the Micro-Deval Apparatus.
- ii. ***Los Angeles Abrasion:*** Indicate aggregate toughness and abrasion resistance. Test method: AASHTO T 96: Standard Method of Test for Resistance to Degradation of Small-Size Coarse Aggregate by Abrasion and Impact in the Los Angeles Machine.

Aggregate Frost Susceptibility Tests:

- i. ***Tube Suction Test:*** Measures the amount of free water that exists within an aggregate sample.

2.2 Durability and Abrasion Tests and Evaluation of Aggregates

Several quality control aggregate tests have long been conducted on Wisconsin aggregates during construction projects. WisDOT has collected the test results in a database. The tests involved measured absorption (ABS) (ASTM C128), specific gravity (SG) (ASTM C127), Los Angeles abrasion (LAA) (ASTM C131), sodium sulfate soundness (SSS) (ASTM C88), and unconfined freeze-thaw (UFT) (ASTM T103). The newer Micro-Deval test (MD) (AASHTO TP58) has not been routinely performed. The WisDOT database, which included 2,052 sets of test results recorded prior to 2010, was obtained and analyzed in detail by Tabatabai et al. (2013).

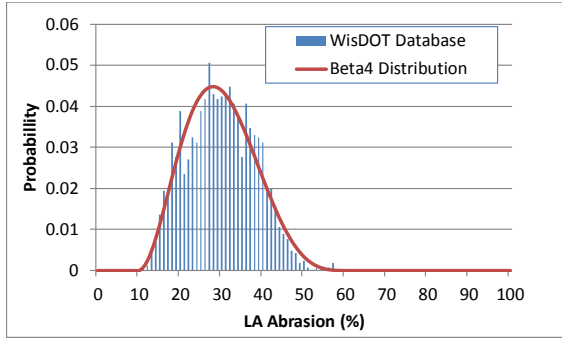
Table 2.3 summarizes basic statistics on the Wisconsin database test records for all aggregates (from pits and quarries together), aggregates from pits, and aggregates from quarries. Figure 2.1 depicts histograms of all test results in the database. The histogram data were fit to a number of standard statistical distributions to find the best-fit distributions for each parameter. The software programs Crystal Ball[®] and ModelRisk[®] were used to find the best-fit distributions. The types of distributions and relevant equation parameters are provided by Tabatabai et al. (2013). The percentiles for the actual data and the statistical distribution curve are also calculated. It should be noted that not all records had results from all tests; some test results were left blank and others had zeros in them. In such cases, the analyses were performed in two ways one excluding the zeroes (assuming that the tests were not performed) and the other including zeroes as valid results. The data analyzed without the zero records are used herein.

The distributions presented in Figure 2.1 can be used to perform statistical simulations; however, these distributions are determined without considering the interdependence between various parameters. These distributions are not independent of each other and cannot be used as independent parameters in simulations.

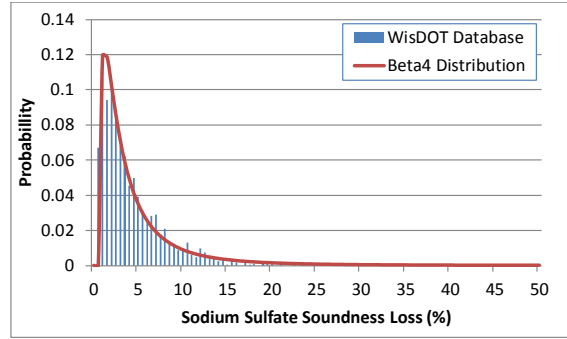
Table 2.3: Basic statistics of the Wisconsin database aggregate test results.

Aggregate Source	Statistical Parameter	L.A. Abrasion	Sodium Sulfate Soundness	Freezing and Thawing	Absorption (fine)	Specific Gravity (fine)	Absorption (coarse)	Specific Gravity (coarse)
Pits and Quarries	μ	29.34	3.36	1.57	0.76	2.66	1.71	2.66
	Median	29.14	2.00	0.00	0.75	2.66	1.50	2.66
	σ	8.257	4.399	4.553	0.017	0.033	0.024	0.002
	Min.	10.90	0.00	0.00	0.15	2.58	0.29	1.28
	Max.	56.70	46.82	57.71	1.95	2.79	9.14	3.19
	n	1700	2051	2036	314	314	1348	1348
Pits	μ	25.17	2.48	0.53	0.77	2.66	1.35	2.69
	Median	25.02	1.47	0.00	0.76	2.66	1.25	2.69
	σ	6.720	3.881	3.472	0.018	0.033	0.022	0.003
	Min.	11.46	0.00	0.00	0.15	2.58	0.40	2.19
	Max.	56.70	46.82	53.37	1.93	2.79	4.21	2.85
	n	722	1021	1021	277	277	590	590
Quarries	μ	32.42	4.22	2.62	0.73	2.65	1.99	2.64
	Median	32.99	2.70	0.47	0.64	2.65	2.03	2.62
	σ	7.928	4.700	5.225	0.055	0.028	0.035	0.004
	Min.	10.90	0.00	0.00	0.28	2.60	0.29	1.28
	Max.	56.50	33.05	57.71	1.95	2.72	9.14	3.19
	n	978	1030	1015	37	37	758	758

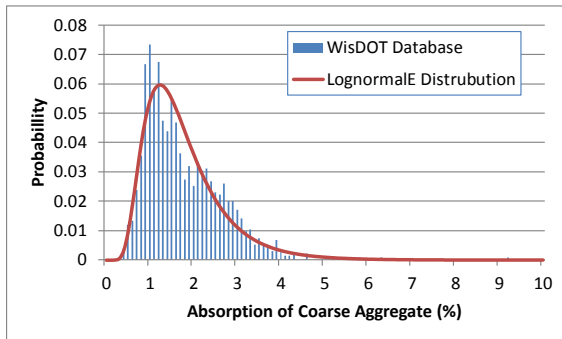
μ : mean, σ : standard deviation, n: number of tests



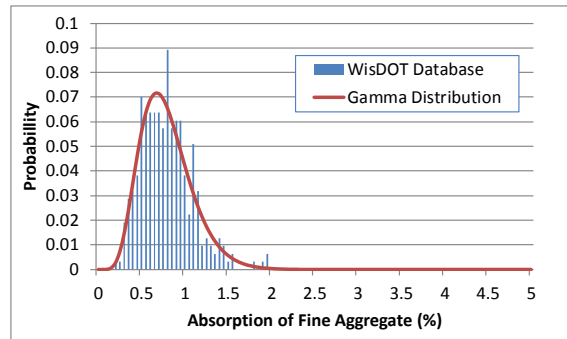
(a) LA abrasion loss



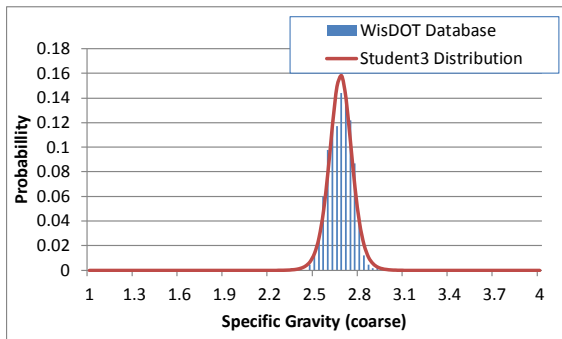
(b) Sodium sulfate soundness loss



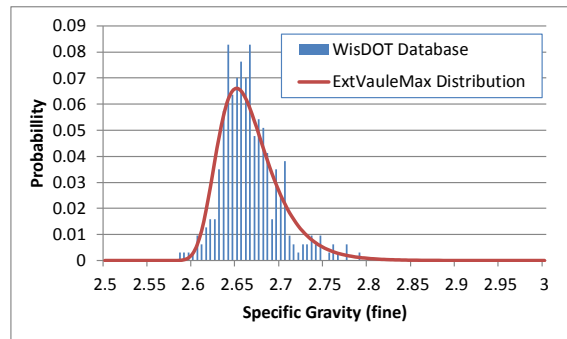
(c) Absorption of coarse aggregates



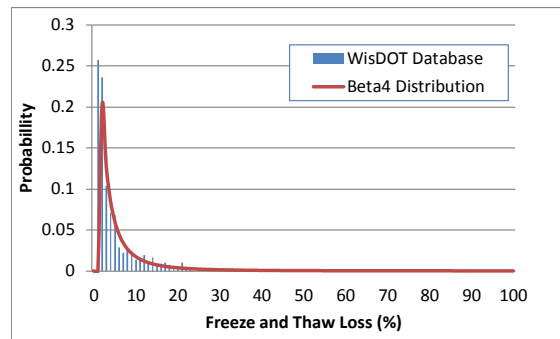
(d) Absorption of fine aggregates



(e) Specific gravity of coarse aggregates



(f) Specific gravity of fine aggregates



(g) Freeze and thaw loss

Figure 2.1: Histogram and best fit distribution of the results of various tests conducted on Wisconsin aggregates from pits and quarries.

In addition, test results reported by Weyers et al. (2005) on 69 Wisconsin aggregate sources were analyzed by Tabatabai et al. (2013). These tests included standard tests that WisDOT routinely performs, as well as newer tests including Aggregate Crushing Value (ACV) test (BS 812-110), Micro-Deval test, percent lightweight test, and freeze/thaw testing of concrete. Table 2.4 presents basic statistics for the results reported by Weyers et al. (2005) and Figure 2.2 shows histograms and distributions that were fit to the WHRP Phase I study results for various tests. The distribution types and parameters are provided by Tabatabai et al. (2013).

Table 2.4: Basic statistics for the WHRP Phase I test results (Weyers et al., 2005).

Statistical Parameter	Micro-Deval Abrasion Loss (%)	Absorption (coarse) (%)	LA Abrasion Loss (%)	Aggregate Crushing Value (%)	Sodium Sulfate Soundness Loss (%)	Unconfined Freezing and Thawing Loss (%)	% Lightweight
μ	16.70	2.58	27.68	20.47	5.16	6.28	2.80
Median	16.22	2.59	27.70	19.38	3.45	5.90	1.60
σ	1.077	0.173	1.279	0.583	0.764	0.431	0.444
COV (%)	6.5	6.7	4.6	2.85	14.8	6.9	15.9
Min.	3.42	0.38	9.89	11.39	0.03	0.90	0.00
Max.	39.98	5.91	56.88	29.46	31.42	13.90	16.20
n	58	60	59	57	60	60	60

μ : mean; σ : standard deviation; n: number of tests.

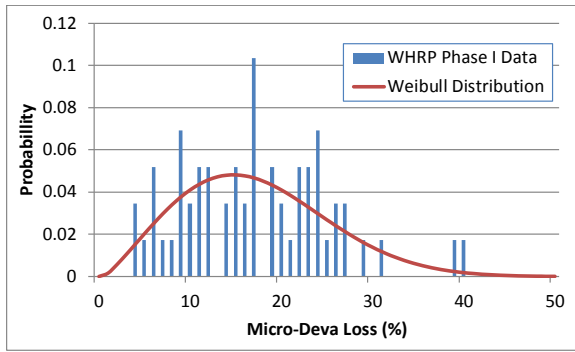
Fowler et al. (2006) conducted a major study on aggregate testing in which well over one hundred aggregate sources from most U.S. states and several Canadian provinces were obtained for testing. The aggregate tests were generally the same as those in the Weyers et al. (2005) study, except for magnesium sulfate soundness (MSS) which was used in lieu of SSS. Consequently, the two databases could not be analyzed as a combined set of data. Basic statistical information related to the Fowler et al. (2006) study are presented in Table 2.5.

Field performance evaluation criteria for coarse aggregates used in granular base (also in HMA and PCC pavements) was developed by Senior and Rogers (1991) as follows:

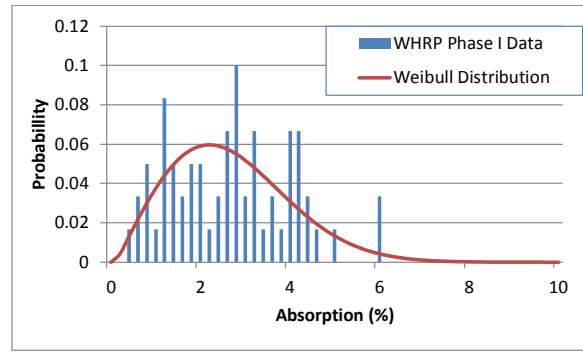
Good – used for many years with no reported failures, popouts, or other signs of poor durability.

Fair – used at least once where popouts or some reduced service life had resulted, but pavement or structure life extended for over 10 years.

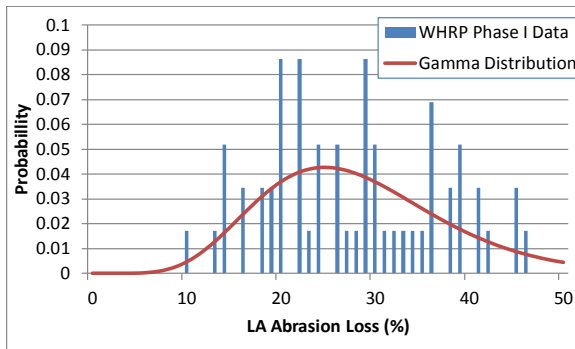
Poor – used once with noticeable disintegration of pavement after one winter, severely restricting pavement life.



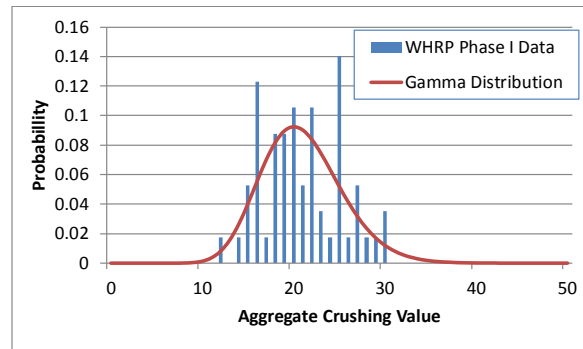
(a) Micro-Deval abrasion test results



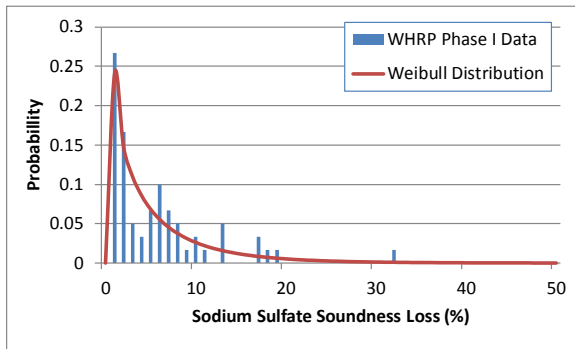
(b) Absorption test results



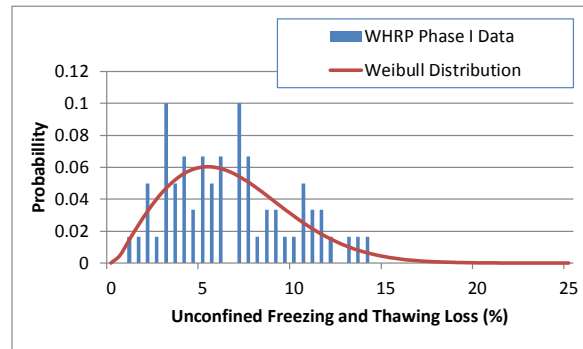
(c) LA abrasion test results



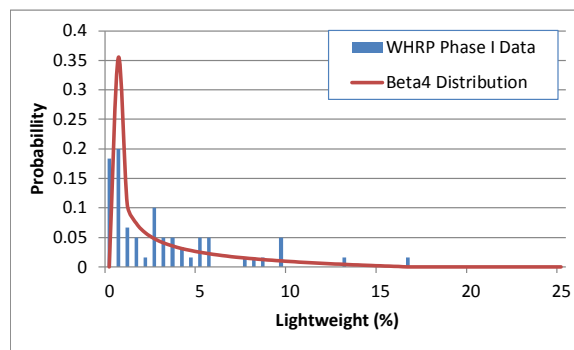
(d) Aggregate crushing value test results



(e) Sodium sulfate soundness test results



(f) Unconfined freeze/thaw test results



(g) Lightweight aggregate test results

Figure 2.2: Histograms and best-fit distributions for tests performed in WHRP Phase I study.

Table 2.5: Basic statistics for the aggregate test results reported by Fowler et al. (2006).

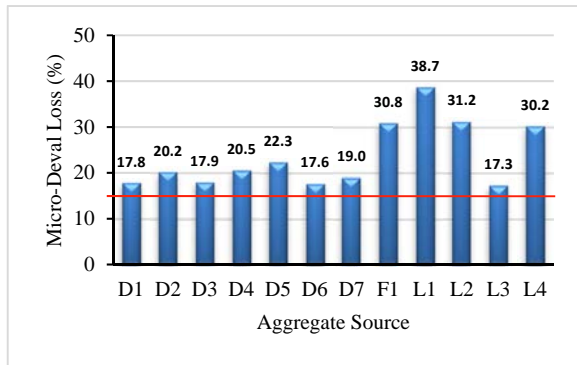
Statistical Parameter	Micro-Deval Abrasion Loss (%)	Absorption (coarse) (%)	Magnesium Sulfate Soundness Loss (%)	L.A. Abrasion Loss (%)	Unconfined Freezing and Thawing Loss (%)	Aggregate Crushing Value (%)
μ	15.05	1.46	27.23	21.39	10.53	4.56
Median	13.70	1.00	25.00	21.00	6.05	3.50
σ	0.787	0.116	1.084	0.602	1.265	0.332
COV (%)	5.2	7.9	4	2.8	12	7.3
Min.	1.40	0.10	11.00	11.00	0.30	0.60
Max.	48.80	5.70	66.00	48.00	70.30	22.40
n	111	110	111	111	110	111

μ : mean, σ : standard deviation, n: number of tests

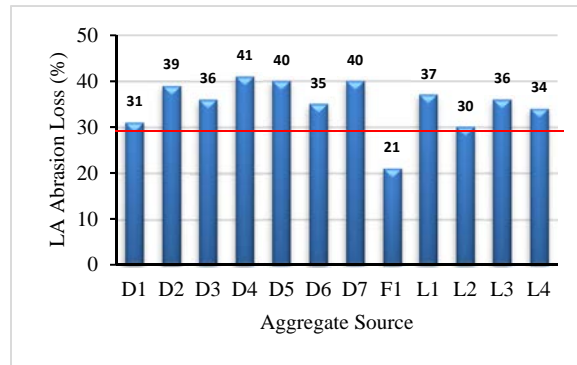
Tabatabai et al. (2013) performed laboratory tests on 12 Wisconsin virgin aggregate samples representing marginal or poor aggregates as characterized by WisDOT. These aggregates were selected because acceptable or good-quality aggregates were well represented in the tests performed under the WHRP Phase I study. Seven aggregates were described as “dolomite” (identified as D1 through D7), four as “limestone” (identified as L1 through L4), and one as “felsic meta-volcanic (schist and gneiss)” (identified as F1). All coarse aggregate samples were subjected to LAA, ABS, SG, SSS, UFT, and MD tests. These tests were done to determine whether the observations made based on prior studies or database information would also apply to aggregates with known marginal or poor performance. Figure 2.3 shows the results of tests on these twelve aggregate samples, with the horizontal red line in each graph representing the mean of the corresponding historical results from the Wisconsin database. The specific gravity results for all twelve aggregate samples were less than the corresponding Wisconsin mean while the absorption results for all twelve tests were higher than the Wisconsin mean.

The logistic regression equations developed by Tabatabai et al. (2013) were used to forecast the outcomes of the MD test for these twelve aggregate sources. The predicted pass/fail outcomes of the MD test were correct for eleven out of the 12 aggregates when a 14% threshold was used. Ten out of 12 correct predictions were made with a 16% threshold, and nine out of 12 correct predictions were made with an 18% threshold. It should be noted that the actual MD results for two of the incorrectly predicted outcomes were very close to the threshold value of 18%. The only sample for which the actual and predicted MD pass/fail results were clearly different was the F1 sample (described as felsic meta-volcanic quartz-sericite schist and quartzofeldspathic gneiss). For this sample, the measured UFT losses were high (11.9% – equivalent to the 89th percentile in the Wisconsin database); therefore, it is recommended that the UFT test be a part of any aggregate qualification test protocol. Figure 2.4 depicts the actual and

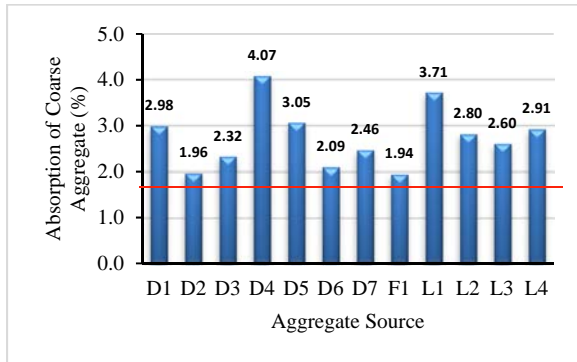
predicted MD test outcomes when assuming a threshold of 18% and 14%, respectively. The predictions are written above each bar (predicted pass or predicted fail).



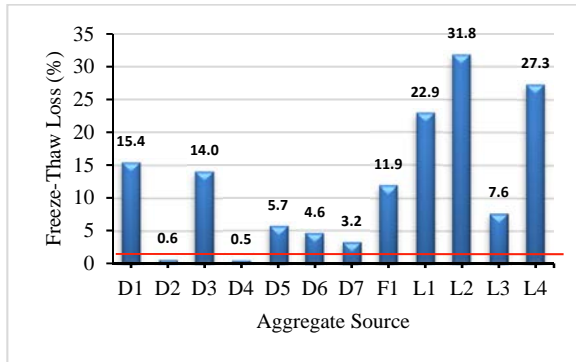
(a) Micro-Deval test results ($\mu=15.05\%$)



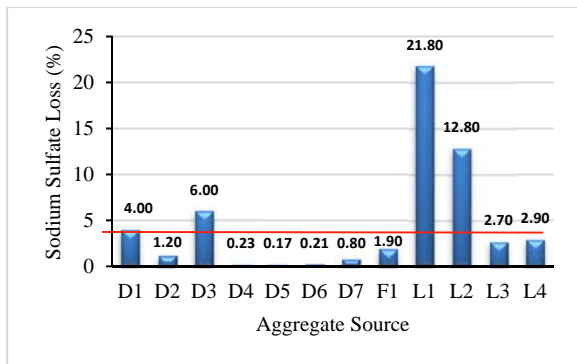
(b) LA abrasion test results ($\mu=29.3\%$)



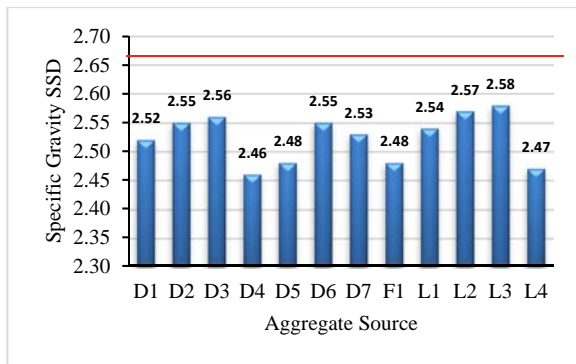
(c) Absorption test results ($\mu=1.71\%$)



(d) Unconfined freeze-thaw test results ($\mu=1.57\%$)

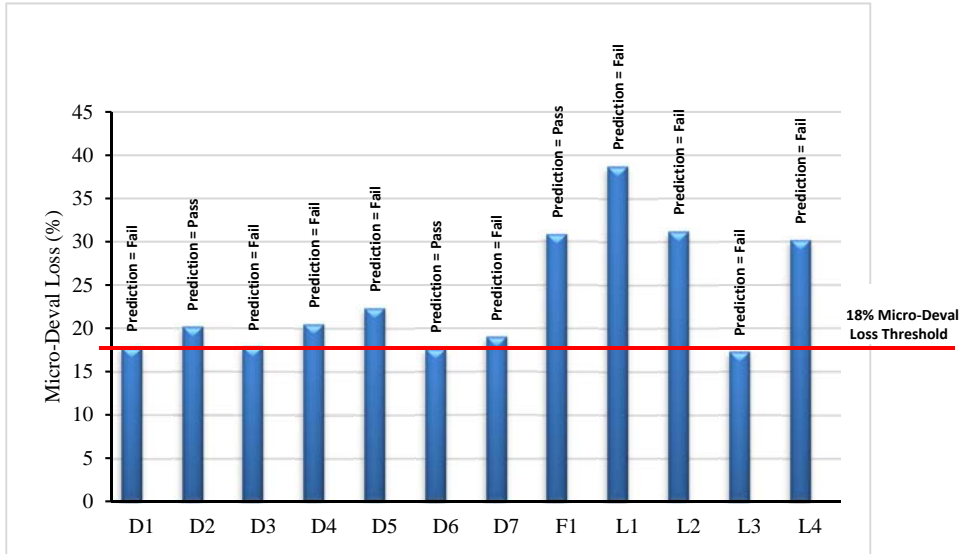


(e) Sodium sulfate test results ($\mu=3.36\%$)

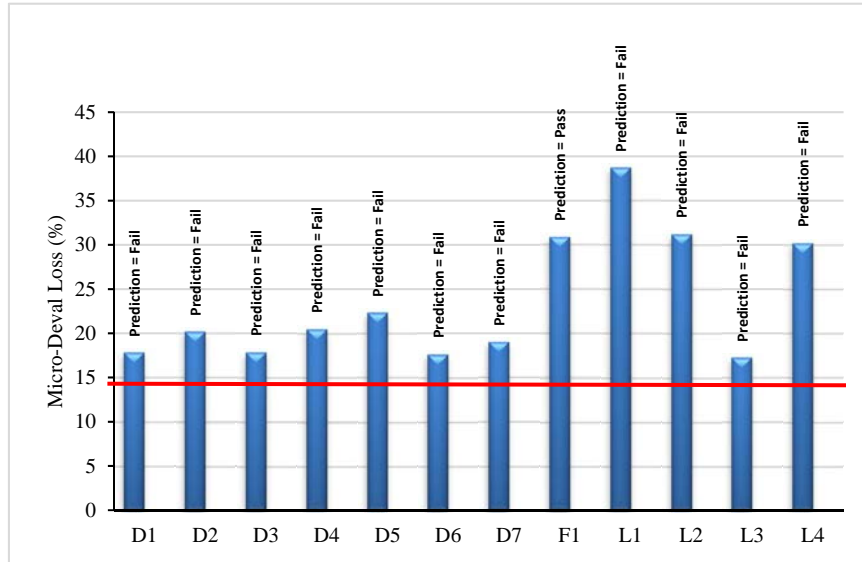


(f) Specific gravity test results ($\mu=2.66$)

Figure 2.3: Results of the various tests conducted on the twelve Wisconsin marginal aggregates versus the corresponding average value (shown in red line) from the Wisconsin aggregate database.



(a) Micro-Deval loss threshold of 18%



(b) Micro-Deval loss threshold of 14%

Figure 2.4: Results of the logistic regression analysis predicting the outcomes of the Micro-Deval test for the twelve aggregate sources assuming thresholds of 18 and 14%.

2.3 Resilient Modulus of Aggregates

The resilient modulus (M_R or M_r) of unbound pavement materials is an important input property in Mechanistic-Empirical (ME) pavement design and performance evaluation. The resilient modulus can be broadly defined as the elastic modulus (stress divided by recoverable strain) after the material has already accumulated some degree of permanent deformation (Puppala, 2008). It is the most important material property for the characterization of repeated loading behaviors of subgrade, subbase, and base course materials in pavement structures. Because the modulus (or stiffness) represents a basic mechanical property of the ability to resist deformation under stress, it can be effectively used in various pavement methodologies to predict pavement distress such as rutting and roughness. The current version of the American Association of State Highway and Transportation Officials (AASHTO) software, AASHTOWare Pavement ME Design (2018), requires the use of the resilient modulus as a primary material property for subgrade soils, subbase course, and base course.

Pavement stresses are composed of two principal parts: initial in-situ stresses and stresses due to moving wheel loads. The initial in-situ stresses are static stresses generated due to the overburden stresses. The initial stresses are typically lower at shallow depths than at greater depths and the major principal stress due to overburden is always aligned in the vertical direction regardless of the location of a moving wheel. Compaction-induced residual stresses that are compressive in nature can often exist in the unbound aggregate layers and contribute to the static stress states (Uzan, 1985). On the other hand, traffic loading due to moving wheel loads induces much higher dynamic stresses compared with static stresses. For example, the dynamic vertical stresses become the highest underneath the wheel where shear loading is nonexistent on a representative pavement element. At some radial distance away from the wheel, applied vertical stresses decrease and the shear stresses reach their maximum values. The incremental stresses imposed by a wheel load are not co-axial with this system, and as a result, the total principal stresses rotate as the wheel load passes. Because of these phenomena, a pavement element under vehicle loading experiences a combination of varying magnitudes of static and dynamic vertical (compressive), and shear stresses depending on the depth in the pavement layer and the radial offset from the wheel load.

Tutumluer et al. (2013) notes that an ideal pavement structure would only be subject to elastic deformation, assuming it is not loaded to failure. However, materials do exhibit permanent deformation with repeated loading via a variety of mechanical processes. This is why the resilient modulus of pavement structure layers is used in pavement engineering, as it measures the elastic modulus after a material has undergone a specified amount of permanent deformation. The standard laboratory test for resilient modulus values is the repeated-load triaxial test, which dynamically simulates repeated loading cycles while measuring deformation of a carefully prepared sample. Testing procedures are based on AASHTO T 307: Standard Method of Test for Determining the Resilient Modulus of Soils and Aggregate Materials

(AASHTO, 2017). However, the advanced equipment required for triaxial testing (hydraulic or pneumatic dynamic loading systems, confinement apparatuses, sensitive load and strain sensors, and complicated control systems) can be quite costly and require detailed knowledge in order to ensure reliable results. For these reasons, it is desirable to develop methodologies to estimate the resilient modulus of pavement materials using data obtained from other, less advanced, testing methodologies such as sieve analyses, Atterberg limits, and measurements of density and water content properties.

Resilient Modulus Models

Previous research has been conducted regarding the development of predictive models for resilient modulus of aggregate base courses using laboratory data. Hopkins et al. (2007) provides a review of regression models, which have been developed to estimate a material’s resilient modulus using data obtained from simple material parameters. These include the model proposed by Seed et al. (1967):

$$M_r = k_1 \left(\frac{\sigma_b}{p_a} \right)^{k_2} \dots\dots\dots (2.1)$$

where k_1 and k_2 are linear regression coefficients (material dependent), σ_b is bulk stress, and p_a is a reference pressure (atmospheric).

The model by May and Witczak (1981) and Uzan (1985):

$$M_r = k_1 \left(\frac{\sigma_{sum}}{p_a} \right)^{k_2} \left(\frac{\sigma_d}{p_a} \right)^{k_3} \dots\dots\dots (2.2)$$

where k_1 , k_2 , and k_3 are linear regression coefficients (material dependent), σ_{sum} is the sum of the principal stresses, and σ_d is deviator stress.

The model by Ni et al. (2002):

$$M_r = k_1 \left(\frac{\sigma_3}{p_a} + 1 \right)^{k_2} \left(\frac{\sigma_d}{p_a} + 1 \right)^{k_3} \dots\dots\dots (2.3)$$

where k_1 , k_2 , and k_3 are linear regression coefficients (material dependent) and σ_3 is confining stress.

The model used by NCHRP Project 1-28A to develop laboratory testing procedures for resilient modulus (Witczak, 2004) which has been incorporated into AASHTOWare Pavement ME Design:

$$M_r = k_1 P_a \left(\frac{\sigma_b}{P_a} \right)^{k_2} \left(\frac{\tau_{oct}}{P_a} + 1 \right)^{k_3} \dots\dots\dots (2.4)$$

where k_1 , k_2 and k_3 are linear regression coefficients (material dependent – the objects of interest for correlational modeling), P_a is atmospheric pressure (101.325 kPa), σ_b is bulk stress ($\sigma_1 + \sigma_2 + \sigma_3$), σ_1 is major principal stress, σ_2 is intermediate principal stress, and σ_3 is minor principal stress. In axisymmetric conditions (triaxial stress space) σ_3 is equal to σ_2 , which is the case for the repeated load triaxial test. The octahedral shear stress, τ_{oct} , is defined generally as

$$\tau_{oct} = \frac{1}{3} \sqrt{(\sigma_1 - \sigma_2)^2 + (\sigma_1 - \sigma_3)^2 + (\sigma_2 - \sigma_3)^2} \quad \text{where } \tau_{oct} = \frac{\sqrt{2}}{3} (\sigma_d) \text{ in axisymmetric stress}$$

conditions.

Multiple studies have used the Federal Highway Administration’s (FHWA) Long Term Pavement Performance (LTPP) program material testing database as a data source (FHWA, 2018). Yau and Von Quintus (2002) examined resilient modulus values (determined by using the LTPP test protocol P46) from 2,014 LTPP tests on a variety of soil and aggregate material types. The aggregate material categories included in the database and study were crushed stone (LTPP material code 303), crushed gravel (LTPP material code 304), and uncrushed gravel (LTPP material code 302). Significant efforts were required in order to control for data irregularities in the LTPP database as the LTPP tests were carried out by numerous agencies on various types of equipment over a relatively long timeframe. Nonetheless, the LTPP database contains large amounts of laboratory material testing parameters in addition to the resilient modulus data for tested samples, such as gradation, Atterberg limits, density, optimum density, moisture contents, and other properties.

Relationships between resilient modulus and physical properties were established for each material type using nonlinear regression optimization techniques. Models were developed for each material category (shown in Table 2.6) by determining optimal equations for the three regression constants k_1 , k_2 , and k_3 as functions of material properties for use in the resilient modulus constitutive equation adopted for use in AASHTOWare Pavement ME Design (Equation 2.4). Moisture content and material density were found to be important variables in predicting the resilient modulus of higher strength base/subbase materials. The authors note that the statistical fitness of the regressed models was generally better for base materials than soils, with the conclusion that the “resilient modulus from constitutive Equation 2.4 (see Table 2.6) can be reasonably predicted from the physical properties that are included in the LTPP database” (Yau and Von Quintus, 2002).

Puppala (2008) performed a comprehensive review of prior studies relating to testing and modeling of the resilient modulus of subgrade soils and unbound materials, including a survey of state DOTs, to determine the state of practice regarding the measurement and applications of resilient modulus properties. The exhaustive literature review noted that the amount of research regarding the resilient modulus of aggregate bases was somewhat limited compared with the

number of general studies or studies focused on subgrade soil properties. Puppala (2008) notes, “although a large number of correlations currently exist (for Level 2 M_r properties), their accuracy is still unknown to pavement designers.” The study found that most prior studies that included regression modeling of M_r based on soil properties yielded accurate correlations for the initial study data, but provided “poor predictions when used on other soils.” Therefore, Puppala (2008) notes the need for additional data and research to reduce the variability associated with resilient modulus testing of unbound materials as well as to better define the relationship between design moduli and moduli determined from other methods such as correlation models.

Li et al. (2010) conducted tests to determine the physical properties of granular base materials taken from three different regions in Alaska. Repeated load triaxial tests were performed on the samples to determine the resilient modulus. For the tests at subfreezing temperatures, a frost heave cell was used to simulate the frost heave effect in winter. Resilient modulus values were determined following the freeze-thaw cycles. Resilient modulus increased when the temperature decreased. At temperatures below -5°C , resilient modulus seemed to be stable and further reductions in the temperature did not affect M_r value. After one cycle of freeze-thaw, it was found that M_r decreased significantly at room temperature. Regression analysis was used to establish relationships to estimate M_r . For materials tested at room temperature, M_r was a function of deviator stress, moisture content, and fine content. For materials tested at subfreezing temperatures, M_r was a function of deviator stress, temperature, and aggregate type. Equations were developed to estimate M_r for Alaskan D-1 materials for pavement design, as presented in Table 2.6.

Rao et al. (2012) reviewed various models for estimating M_r . Using LTPP data, they also developed a constitutive model for M_r of unbound materials using gradation, Atterberg limits, optimum moisture content, and soil classification, which yielded a correlation between measured and predicted M_r of $R^2 = 0.566$ across all tested materials. However, they did not develop separate regression constant equations for different material types (the model included data from a variety of unbound soil types and was not limited to base materials).

Hossain et al. (2012) analyzed 105 samples of two different types of aggregates (limestone and sandstone) in Oklahoma; these aggregates were classified as A-2-4 according to AASHTO T 145 specifications. These researchers developed four stress-based models, one of which was based on the octahedral ($k \sim \tau_{\text{oct}}$) model. They established correlation equations for k_1 , k_2 , and k_3 using laboratory testing data such as specific gravity, Los Angeles abrasion test, optimum moisture content, sieve analysis, Atterberg limits, and unconfined compressive strength (which can be found in Table 2.6). The octahedral ($k \sim \tau_{\text{oct}}$) model was found to perform better than the other models and was recommended for use in level 1 analysis and design in AASHTOWare Pavement ME Design applications.

Table 2.6: The resilient modulus constitutive model parameters proposed by various studies.

Model	Equations for Model Parameters
LTPP Material Code 303* Crushed Stone	$k_1 = 0.7632 + 0.0084 P_{3/8} (\%) + 0.0088 LL - 0.0371 w_{opt} (\%) - 0.0001 \gamma_{d,max} \left(\frac{kg}{m^3}\right)$
	$k_2 = 2.2159 - 0.0016 P_{\frac{3}{8}} (\%) + 0.0008 LL - 0.038w_{opt}(\%) - 0.0006 \gamma_{d,max} \left(\frac{kg}{m^3}\right) + 2.4 \times 10^{-7} \left(\frac{\gamma_{d,max}^2 \left(\frac{kg}{m^3}\right)}{P_{40}(\%)}\right)$
	$k_3 = -1.172 - 0.0082 LL - 0.0014 w_{opt}(\%) + 0.0005 \gamma_{d,max} \left(\frac{kg}{m^3}\right)$
LTPP Material Code 304* Crushed Gravel	$k_1 = -0.8282 - 0.0065 P_{3/8} (\%) + 0.0114 LL + 0.0004 PI - 0.0187w_{opt}(\%) + 0.0036 w_s (\%) + 0.0013\gamma_s \left(\frac{kg}{m^3}\right) - 2.6 \times 10^{-6} \left(\frac{\gamma_{d,max}^2 \left(\frac{kg}{m^3}\right)}{P_{40}(\%)}\right)$
	$k_2 = 4.9555 - 0.0057 LL - 0.0075 PI - 0.047 w_s(\%) - 0.0022 \gamma_{d,max} \left(\frac{kg}{m^3}\right) + 2.8 \times 10^{-6} \left(\frac{\gamma_{d,max}^2 \left(\frac{kg}{m^3}\right)}{P_{40}(\%)}\right)$
	$k_3 = -3.514 + 0.0016 \gamma_s \left(\frac{kg}{m^3}\right)$
LTPP Material Code 302* Uncrushed Gravel	$k_1 = -1.8961 + 0.0014 \gamma_s \left(\frac{kg}{m^3}\right) - 0.1184 \left(\frac{w_s(\%)}{w_{opt}(\%)}\right)$
	$k_2 = 0.496 - 0.0074P_{200}(\%) - 0.0007\gamma_s \left(\frac{kg}{m^3}\right) + 1.6972 \left(\frac{\gamma_s \left(\frac{kg}{m^3}\right)}{\gamma_{d,max} \left(\frac{kg}{m^3}\right)}\right) + 0.1199 \left(\frac{w_s(\%)}{w_{opt}(\%)}\right)$
	$k_3 = -0.5979 + 0.0349w_{opt}(\%) + 0.0004 \gamma_{d,max} \left(\frac{kg}{m^3}\right) - 0.5166 \left(\frac{w_s(\%)}{w_{opt}(\%)}\right)$
Alaska Study Model (Li et al., 2010)	$k_1 = 2.54 + 5.37P_{200}(decimal) - 32.56 w_s(decimal) - 72.76 w_s(decimal)P_{200}(decimal)$
	$k_2 = 1.04 + 3.54 P_{200}(decimal) - 10.70 w_s(decimal) - 71.19 w_s(decimal)P_{200}(decimal)$
	$k_3 = -2.19 + 1.54 P_{200}(decimal) + 44.36 w_s(decimal) - 49.18 w_s(\%)P_{200}(decimal)$
Oklahoma Study Model (Hossain et al., 2012)	$k_1 = -425.926 + 1563.519 G_s + 41.445 (LAA) (\%) - 1.894 UCS(psi)$
	$k_2 = 3.196 - 0.040P_4 (\%) - 0.006 (LAA) (\%) - 0.002 UCS(psi) - 0.151 w_{opt} (\%)$
	$k_3 = -2.373 + 0.051P_4 (\%) - 0.039 (LAA) (\%) - 0.003 UCS(psi) + 0.230 w_{opt} (\%)$

* (Yau and Von Quintus, 2002)

w_s is moisture content; w_{opt} is optimum moisture content; γ_s is dry unit weight; $\gamma_{d,max}$ is maximum dry unit weight; LL is liquid limit; PI is plasticity index; $P_{3/8}$ is percent passing the 3/8" sieve; P_4 is percent passing the No. 4 sieve; P_{200} is percent passing the No. 200 sieve; G_s is specific gravity of aggregate solids; k_1 , k_2 , and k_3 are regression coefficients; LAA is Los Angeles abrasion loss; UCS is unconfined compressive strength.

Evaluation of Aggregate Resilient Modulus Data

Eggen and Brittnacher (2004) investigated the influences on the support strength of crushed aggregate base course (CABC) due to gradational, regional, and source variations. A key objective was to evaluate how variables such as physical characteristics, material type, source lithology, and regional factors influence the resilient modulus of CABC. Testing was conducted to evaluate M_r for 37 aggregate sources, with about 400 pounds of specimen collected from a total of 24 quarries and 13 sand and gravel pits located throughout Wisconsin. Gradation number 2 CABC was chosen for use in this study, due to its widespread use during the time of sampling. The samples were subject to a multitude of laboratory procedures, including tests for gradation (AASHTO T 11 & T 27), flat and elongated particles (ASTM D4791), specific gravity and absorption (ASTM C127 & C128), fine aggregate angularity, and sand equivalency; the Standard Proctor (AASHTO T99) was performed as well. These tests were conducted in order to ascertain the physical characteristics of the CABC in an inexpensive manner and to provide data that could plausibly be used to develop correlations between the resilient modulus and these physical characteristics. Los Angeles rattler (LAR) and sodium sulfate soundness data for the samples were already available via the Wisconsin Department of Transportation database of approved aggregate sources.

Representative portions of the samples were tested for M_r with the aggregate reduced to testing size per AASHTO T 248. Micro-Deval abrasion tests (AASHTO TP58-02) were performed at the WisDOT central laboratory in Madison, WI, while M_r tests (SHRP P46) were performed at the Braun Inertec of Edina, MN. The M_r tests involved applying a deviator stress to a sample that is simultaneously subjected to confining pressure; this is executed with 15 different loading combinations. Both water content and relative density were held as close to a specified value as possible for each sample during preparation. The optimum water content and 95% of Standard Proctor unit weight were selected as standard values for testing purposes. In order to determine the influence of gradation on M_r test results, 11 of the 37 samples were separated by sieve (12.5 mm, 9.5 mm, and 7.5 mm) to form gradations that spanned the WisDOT gradation No.2 specified grading band, ranging from fine to coarse. The remaining 26 specimens were tested with gradations kept as sampled.

The researchers adopted an ad-hoc lithological classification scheme, with characteristics assigned visually. One exception was in the case of determining the carbonate fraction in fines; this was calculated as the difference in weight after treatment with hydrochloric acid. For a typical base course layer bulk stress of 165.5 kPa (24 psi), the resilient modulus values were found to vary between 75.84 and 151.68 MPa (11 and 22 ksi) with an average value of 113.76 MPa (16.5 ksi). The researchers concluded that that resilient modulus did not differ appreciably between sand/gravel pit and quarry groups and that carbonate quarries generally gave significantly higher M_r values than Precambrian, felsic-plutonic quarries. They also noted that a change in the gradation of the base course from any given source affected M_r test results, but not

in any consistent or predictable way. The researchers also observed that certain physical parameters were found to influence M_r in some of the geologic subsets; however, none of the correlations were strong enough to predict M_r to within a sufficient degree of confidence.

Hopkins et al. (2007) conducted resilient modulus tests on multiple types of crushed stone aggregate bases used or of interest for future use in Kentucky, including dense graded aggregate (DGA), crushed stone base (CBS), river gravel, recycled concrete, Number 57 crushed stone, and asphalt drainage blankets. Data (from repeated load triaxial tests conducted on these samples) were correlated with stress variables using four separate constitutive equations for estimating the resilient modulus (from Seed et al. (1967), Uzan (1985), Ni et al. (2002), and the equation from NCHRP 1-28A and the 2002 AASHTO MEPDG methodology (current AASHTOWare Pavement ME Design)). Values of k_1 , k_2 , and k_3 were calculated using regression techniques for each aggregate sample tested and for each of the four models evaluated, except for the Seed et al. (1967) model which only utilizes two k parameters. Very good correlations were achieved with coefficient of determination R^2 values greater than 0.96 for the latter three models. However, the study did not relate the k -parameters to material properties, potentially limiting its applicability for different material categories or materials from different locales.

Analysis of Resilient Modulus Data and Models

In this study, a resilient modulus test database was developed from test data obtained from Eggen and Brittnacher (2004) and Hopkins et al. (2007). This data was subjected to a comprehensive analysis to evaluate existing resilient modulus models and develop new models to help in evaluating the resilient modulus of base aggregates for pavement design and performance evaluation. Figure 2.5 presents the results of repeated load triaxial tests on Wisconsin and Kentucky aggregates from pits (gravel/crushed gravel) and quarries (crushed stone). The best fit statistical distribution is obtained for the resilient modulus of Wisconsin aggregate for all bulk stress ranges as well as for confining stresses ranging from 34.47 to 68.95 kPa (5 to 10 psi), which represents a typical stress range experienced by pavement base layers. Based on the test results, the lognormal distribution was selected with a mean of 164.02 MPa (23.79 ksi), standard deviation of 74.26 MPa (10.77 ksi), and COV of 45.3% for resilient modulus values at all bulk stress ranges. However, for confining stresses between 34.47 and 68.95 kPa (5 and 10 psi), the lognormal distribution had a mean of 140.17 MPa (20.33 ksi), standard deviation of 42.75 MPa (6.20 ksi), and COV of 30.5% indicating a lower mean and less variability. It should be noted that these aggregates represent crushed stone and gravel/crushed gravel materials from quarries and pits, respectively. In order to compare aggregates of the same particle origin, a statistical analysis was performed on Wisconsin aggregates with aggregates from quarries and pits separated. The results for aggregates from pits with lognormal distribution are: a mean of 163.47 MPa (23.71 ksi), standard deviation of 74.94 MPa (10.87 ksi), and COV of 30.5%. On the other hand, the aggregates from quarries with lognormal distribution had a mean

of 164.37 MPa (23.84 ksi), standard deviation of 73.98 MPa (10.73 ksi), and COV of 40.02%. These results are similar to the results when all aggregates are analyzed together.

Analysis of Kentucky aggregates showed that the lognormal distribution best fit of data had a mean of 282.27 MPa (40.94 ksi), standard deviation of 123.9 MPa (17.97 ksi), and COV of 43.9% for resilient modulus values at all bulk stress ranges. When Kentucky data was separated based on source origin as aggregate from quarries and gravel from river, the results are: river gravel with lognormal distribution had a mean of 242.42 MPa (35.16 ksi), standard deviation of 123.83 MPa (17.96 ksi), and COV of 51%; while the aggregates from quarries with lognormal distribution had a mean of 299.92 MPa (43.5 ksi), standard deviation of 123.55 MPa (17.92 ksi), and COV of 41.2%. Unlike Wisconsin aggregates, Kentucky crushed stone aggregates showed higher resilient modulus values when compared with Kentucky river gravel.

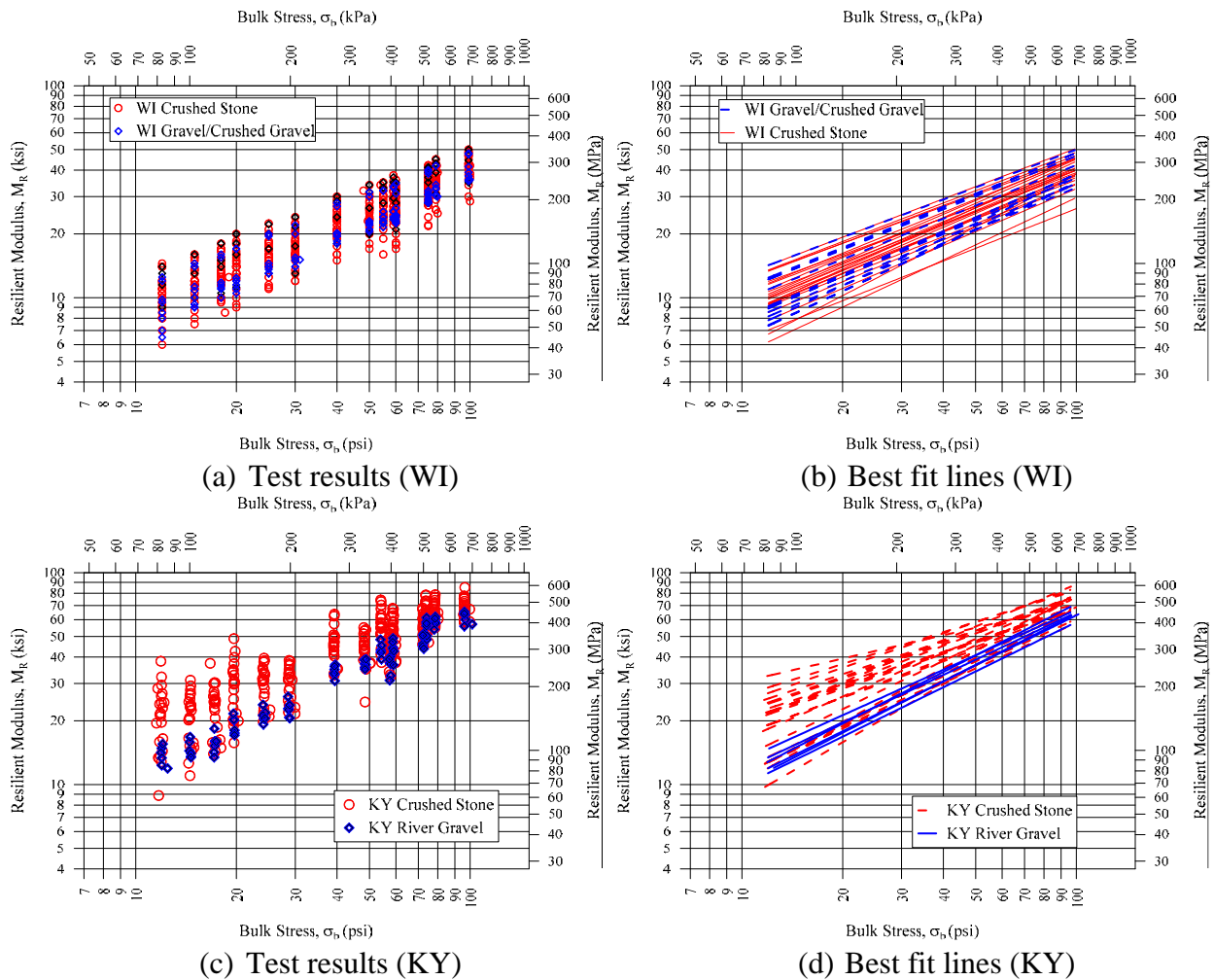


Figure 2.5: Results of repeated load triaxial tests on Wisconsin and Kentucky aggregates from pits (gravel/crushed gravel) and quarries (crushed stone).

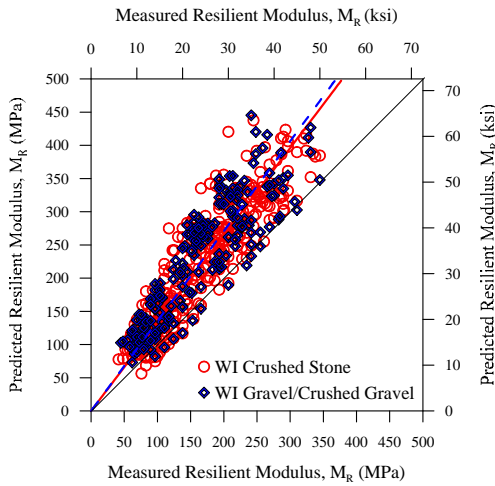
Figure 2.6 presents the performance of existing aggregate material models (presented in Table 2.6) in predicting the resilient modulus of measured Wisconsin aggregates. Inspection of Figure 2.6 indicates that there is a significant variability in the performance of the existing models to predict the resilient modulus of Wisconsin crushed stone as well as gravel/crushed gravel aggregates from pit and quarry sources. The performance data of these models are summarized in Table 2.7. Inspection of the relationships between predicted and measured resilient modulus values indicates that the LTPP uncrushed and crushed gravel models, the Alaska study model, and the Oklahoma study model did not predict the measured resilient modulus of Wisconsin aggregates reasonably. Such poor performance is consistent with the findings of Puppala (2008) presented earlier in this paper. The LTPP model for crushed stone (material code 303) showed the best performance while all other models did not perform very well in predicting the resilient modulus of Wisconsin aggregates. However, the LTPP crushed stone model requires the liquid limit as materials input for k_1 , k_2 , and k_3 . In the current study, we conducted laboratory testing on 18 aggregate samples retrieved from base course layers of in-service HMA Wisconsin pavements with age ranges between 6 and 85 years and found that fines in only three samples were plastic (plasticity indices of 1, 3, and 5%). The remaining 15 samples had fines that were non-plastic. Therefore, this research was initiated to develop models that can predict the resilient modulus from particle size distribution and compaction test results.

Development of Material Models for Wisconsin Aggregates

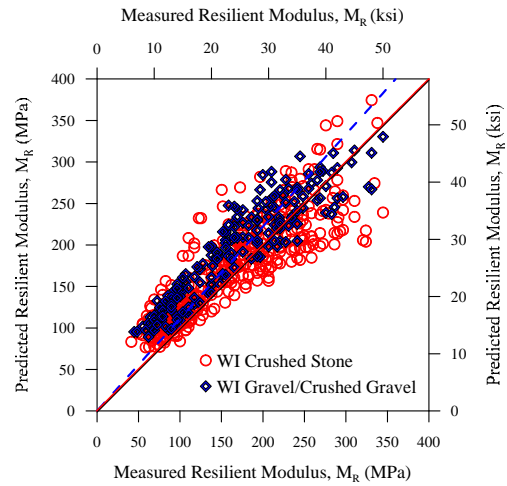
In order to provide an implementation tool that could be useful for WisDOT and the pavement engineering community in general, the research team conducted a comprehensive analysis on the resilient modulus of base aggregates using the data from Wisconsin and Kentucky and developed material models that are valid.

The general resilient modulus model described by Equation 2.4 was selected herein for evaluating the resilient modulus of aggregates since it was implemented into the AASHTOWare Pavement ME Design. The resilient modulus, bulk stress, and octahedral shear stress are normalized in Equation 2.4 by the atmospheric pressure which results in non-dimensional model parameters. Multiple linear regressions were utilized to determine the resilient modulus model parameters k_1 , k_2 , and k_3 using the statistical analysis software Statistica (2018). To determine k_1 , k_2 , and k_3 using the experimental test results, Equation 2.4 was transformed into:

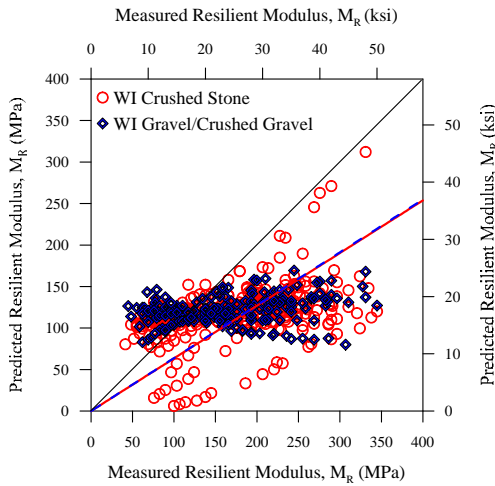
$$\log\left(\frac{M_r}{P_a}\right) = \log k_1 + k_2 \log\left(\frac{\sigma_b}{P_a}\right) + k_3 \log\left(\frac{\tau_{oct}}{P_a} + 1\right) \dots\dots\dots (2.5)$$



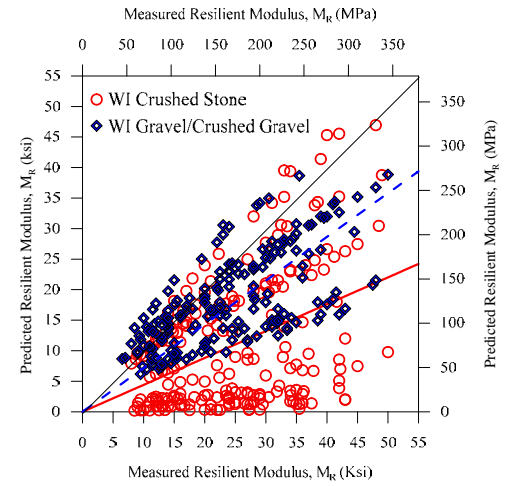
(a) LTPP Model - Uncrushed Gravel, Code 302



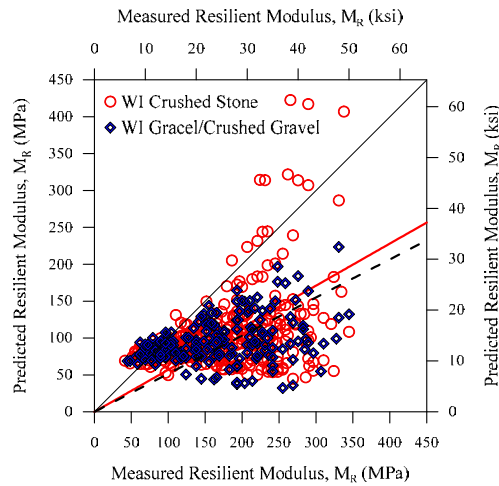
(b) LTPP Model - Crushed Stone, Code 303



(c) LTPP Model - Crushed Gravel, Code 304



(d) Alaska Study Model (Li et al., 2010)



(e) Oklahoma Study Model (Hossain et al., 2012)

Figure 2.6: Performance of existing models (presented in Table 2.6) in predicting the resilient modulus of measured WI aggregates.

Table 2.7: Performance of various existing material models in predicting the measured resilient modulus of Wisconsin aggregates from pits (crushed gravel and uncrushed gravel) and quarries (crushed stone).

Resilient Modulus Model		Aggregate Source	Predicted vs Measured Resilient Modulus	Average M_r (MPa)	
				Measured	Predicted
LTPP Models (Yau and Von Quintus, 2002)	Material code 302 Uncrushed Gravel	Pit (Gravel/Crushed Gravel)	$M_r (P) = 1.35 M_r (M)$	163.1	227.9
		Quarry (Crushed Stone)	$M_r (P) = 1.32 M_r (M)$	164.1	220.6
	Material code 303 Crushed Stone	Pit (Gravel/Crushed Gravel)	$M_r (P) = 1.11 M_r (M)$	163.1	191.0
		Quarry (Crushed Stone)	$M_r (P) = 0.99 M_r (M)$	164.1	172.5
	Material code 304 Crushed Gravel	Pit (Gravel/Crushed Gravel)	$M_r (P) = 0.64 M_r (M)$	163.1	121.6
		Quarry (Crushed Stone)	$M_r (P) = 0.63 M_r (M)$	164.1	117.7
Alaska Study Model (Li et al., 2010)	Pit (Gravel/Crushed Gravel)	$M_r (P) = 0.72 M_r (M)$	163.1	125.5	
	Quarry (Crushed Stone)	$M_r (P) = 0.44 M_r (M)$	164.1	75.0	
Oklahoma Study Model (Hossain et al., 2012)	Pit (Gravel/Crushed Gravel)	$M_r (P) = 0.52 M_r (M)$	163.1	95.5	
	Quarry (Crushed Stone)	$M_r (P) = 0.57 M_r (M)$	164.1	101.4	

The resilient modulus is the dependent variable, while bulk and octahedral shear stresses are the independent variables. The analysis was conducted to evaluate the material parameters k_1 , k_2 , and k_3 from the results of the 15 load sequences applied during repeated load triaxial tests. A total of 37 and 36 repeated load triaxial tests were used in the analysis from Wisconsin and Kentucky data, respectively. The resilient modulus model parameters k_1 , k_2 , and k_3 were determined, then correlated to aggregate properties using regression analysis. The values of the resilient modulus model parameters k_1 , k_2 , and k_3 were used as dependent variables while various aggregate properties were considered as independent variables. Various combinations of aggregate properties (independent variables) were used in the regression analysis. The distributions of the material model parameters k_1 , k_2 , and k_3 were evaluated to confirm that the distributions followed the requirement of linear regression (that they be normally distributed). A normal distribution was confirmed using “normal probability plots.” These plots include the value of the parameter on the x-axis and the accumulated percent probability of occurrence for a value on the y-axis. The resulting graph is a straight line in the case of a normal distribution. This is how the model parameters were examined and transformation was applied when needed to achieve a normal distribution of the data.

The regression analysis was conducted using the statistical analysis software Statistica. This software was used to find the best subset of soil properties that may correlate with the model parameters k_1 , k_2 , and k_3 .

The general multiple linear regression model is expressed as:

$$k_i = \beta_0 + \beta_1 x_1 + \beta_2 x_2 + \dots + \beta_k x_k + \epsilon \quad \dots \dots \dots (2.6)$$

where:

- k_i = the dependent variable for the regression (model parameters k_1 , k_2 , or k_3)
- β_0 = intercept of the regression plane
- β_i = regression coefficient
- x_i = the independent or regressor variable (in this study, soil property or a combination of soil properties)
- ϵ = random error

Factors that affect resilient modulus are stress state and the environmental conditions that influence the aggregate physical state (unit weight and moisture content). Stress state is expressed in the resilient modulus model by including bulk and octahedral stresses. Sets of independent variables are specified to reflect the aggregate properties include percent passing 3/8" sieve ($P_{3/8}$), percent passing the No. 40 sieve (P_{40}), percent passing the No. 200 sieve (P_{200}), water content (w_s), and dry unit weight (γ_d). The optimum water content (w_{opt}), maximum dry unit weight (γ_{dmax}), and combinations of other variables were also included. The goal of the regression analysis was to identify the best subset of independent variables that result in an accurate correlation between resilient modulus model parameters k_1 , k_2 , and k_3 and basic aggregate properties. Several combinations of regression equations were attempted and evaluated based on the criteria of the coefficient of multiple determination (R^2), the significance of the model, and the significance of the individual regression coefficients.

The coefficient of multiple determination was used as a primary measure to select the best correlation. However, a high R^2 does not necessarily imply that the regression model is good. Adding a variable to the model may increase R^2 (at least slightly) whether the variable is statistically significant or not. This may result in poor predictions of new observations. The significance of the model and individual regression coefficients was tested for each proposed model. In addition, the independent variables were checked for multicollinearity to insure the adequacy of the proposed models.

Based on the regression analysis, correlations for predicting the resilient modulus model parameters k_1 , k_2 , and k_3 were developed and are presented in Table 2.8. Models #1 and #2 are developed based on Wisconsin resilient modulus data with Model #1 including more input variables than Model #2. Wisconsin and Kentucky resilient modulus data were used to develop Model #3.

The performance of the models, developed herein and presented in Table 2.8, is depicted in Figure 2.7. The predicted resilient modulus values of Wisconsin and Kentucky aggregates from pits (crushed gravel and uncrushed gravel) and quarries (crushed stone) are compared with the measured values. In addition, the best fit line equation is obtained for each model for Wisconsin and Kentucky aggregates separately. Inspection of Figure 2.7 shows that the performance of the three models was very good in the case of both crushed stone and gravel/crushed gravel with a maximum variation of 5% in the average overprediction and underprediction. The best fit line equations and corresponding average values and coefficient of

determination are summarized in Table 2.9. The performance of models #1 and #2 in predicting the measured resilient modulus of Kentucky aggregates was not satisfactory. However, Model #3 did show acceptable results with a better performance in predicting the measured resilient modulus values of Kentucky river gravel compared with Kentucky crushed stone.

Table 2.8: Material parameter models developed in this study.

Model Name	Model Equations
UWM Model #1 (using WI data)	$k_1 = -179.23 - 48.18 w_{opt} (\%) - 21.195 P_{200}(\%) + 15655.34 D_{10} (\text{in}) + 966.45 D_{30} (\text{in}) - 1749.57 D_{60} (\text{in}) + 2.48 C_u + 22.98 C_c + 1.91 P_{3/8} (\%) + 6.91 P_{40} (\%) + 742.48 D_{85} (\text{in}) - 386.986 \left(\frac{w_s (\%)}{w_{opt} (\%)} \right) + 1285.52 \left(\frac{\gamma_s (\text{pcf})}{\gamma_{d,max} (\text{pcf})} \right)$
	$\text{Log} (k_2) = -0.85679 + 0.031876 w_{opt} (\%) + 0.0017715 \gamma_{d,max} (\text{pcf}) + 0.000271 \gamma_s (\text{pcf}) + 0.0051635 P_{200}(\%) - 1.12315 D_{10} (\text{in}) - 0.22246 D_{30} (\text{in}) + 0.37281 D_{60} (\text{in}) - 0.000739 C_u + 0.00008557 C_c + 0.00326 P_{3/8} (\%) - 0.0008311 P_{40} (\%) - 0.02326 w_s (\%) + 0.06093 D_{85} (\text{in})$
	$k_3 = 1.47932 - 0.01065 w_{opt} (\%) - 7.15894 D_{10} (\text{in}) + 0.2209 D_{30} (\text{in}) - 0.2369 D_{60} (\text{in}) + 0.0009104 C_u - 0.017941 C_c - 0.0149 P_{3/8} (\%) - 0.000271 P_{40} (\%) - 1.01648 D_{85} (\text{in}) + 0.0000162412 (\gamma_s \times \gamma_{d,max}) (\text{pcf})$
UWM Model #2 (using WI data)	$k_1 = -593 \gamma_{d,max} (\text{pcf}) + 602 \gamma_s (\text{pcf}) + 84816 \left(\frac{\gamma_{d,max} (\text{pcf}) - \gamma_s (\text{pcf})}{\gamma_{d,max} (\text{pcf})} \right) - 65.5 w_s (\%)$
	$k_2 = 0.0735 w_{opt} (\%) + 0.00273 \gamma_{d,max} (\text{pcf}) - 0.000231 C_u - 0.0048 (w_s (\%) \times w_{opt} (\%))$
	$k_3 = 2.66 + 0.212 \gamma_s (\text{pcf}) + 0.343 D_{60} (\text{in}) - 0.0118 C_c + 0.0325 w_s (\%) - 18.2 \left(\frac{\gamma_s (\text{pcf})}{\gamma_{d,max} (\text{pcf})} \right) - 0.000739 (\gamma_s \times \gamma_{d,max})$
UWM Model #3 (using WI and KY data)	$\text{Log} (k_1) = 3.64211 + .000265 \gamma_{d,max} (\text{pcf}) - 0.00367 \gamma_s (\text{pcf}) - .00082 C_u - .00536 C_c - .00275 P_{3/8} (\%)$
	$\text{Log} (k_2) = 0.206 - 0.000754 \gamma_{d,max} (\text{pcf}) - .002033 \gamma_s (\text{pcf}) - 0.00019 P_{3/8} (\%) + 0.177 D_{10} (\text{in}) - 0.593 D_{30} (\text{in}) + 0.235 D_{60} (\text{in})$
	$k_3 = -2.16299 + 0.00011 \gamma_{d,max} (\text{pcf}) + 0.013692 \gamma_s (\text{pcf}) + 0.001829 C_u + 0.007858 C_c + 0.000455 P_{3/8} (\%)$

D_{10} , D_{30} , D_{60} , and D_{85} are the aggregate particle sizes corresponding to 10, 30, 60, and 85 percent finer, respectively, G/F is gravel to fines ratio, C_c is coefficient of curvature, C_u is coefficient of uniformity, $P_{3/8}$ is percent passing the 3/8" sieve, P_{40} is percent passing the No. 40 sieve, P_{200} is percent passing the No. 200 sieve, w_s is moisture content, w_{opt} is optimum moisture content, γ_s is dry unit weight, $\gamma_{d,max}$ is maximum dry unit weight, and k_1 , k_2 , and k_3 are material parameters.

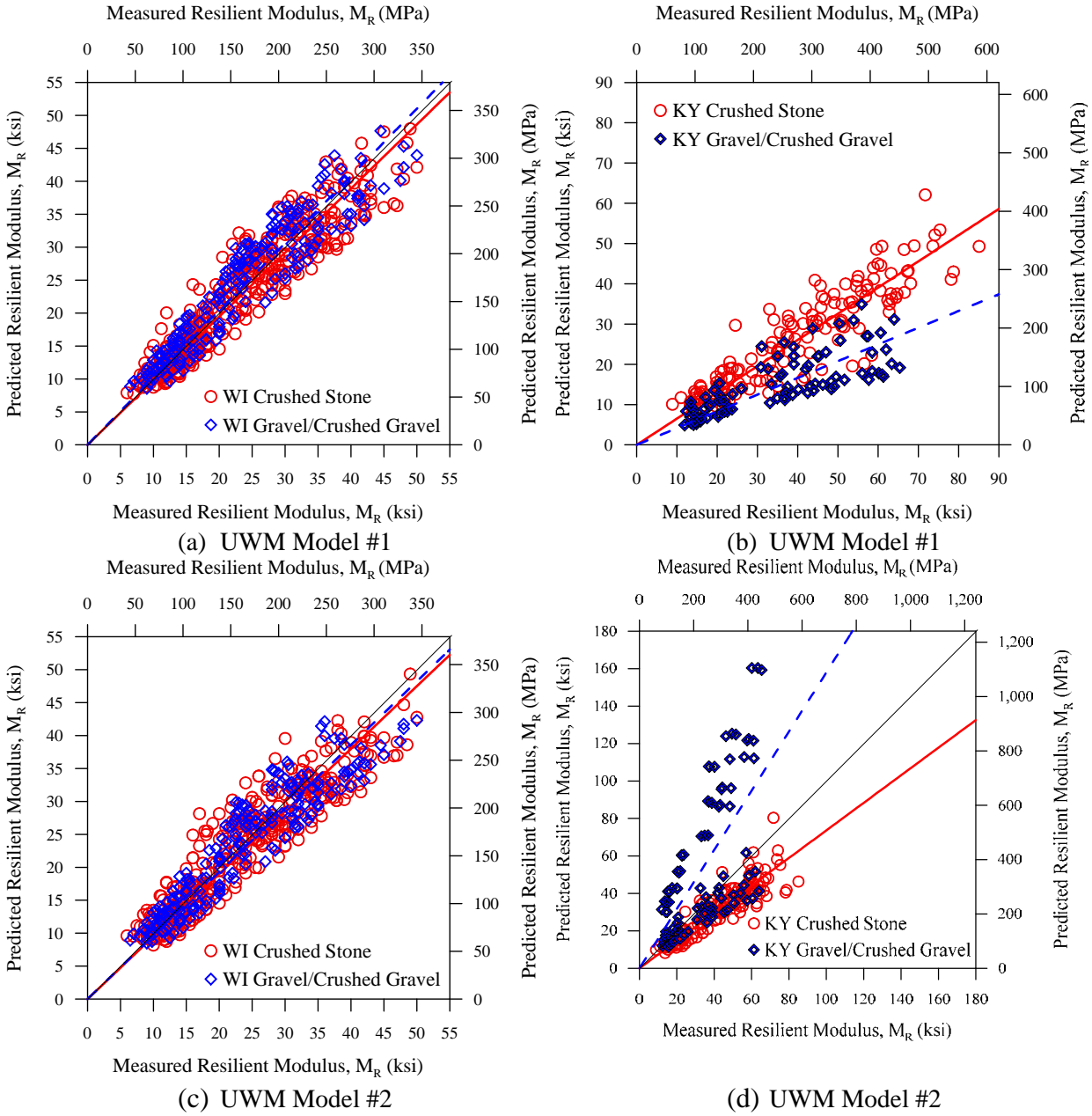


Figure 2.7: Performance of the developed models (presented in Table 2.8) in predicting the resilient modulus of measured WI and KY aggregates.

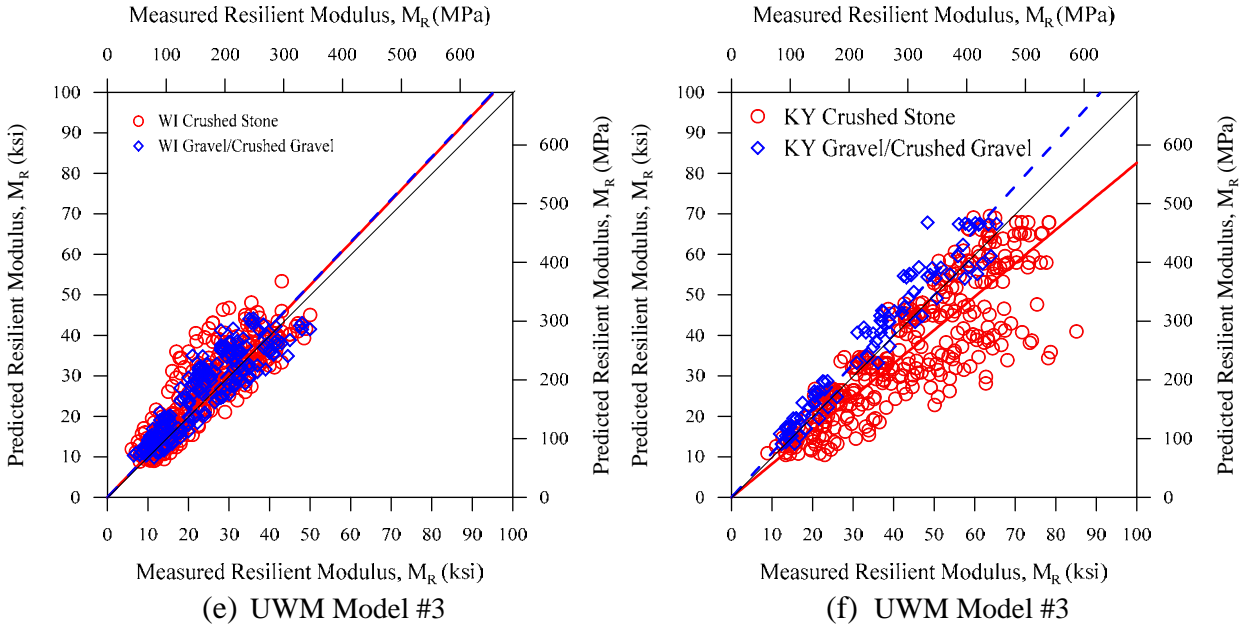


Figure 2.7 (cont.): Performance of the developed models (presented in Table 2.8) in predicting the resilient modulus of measured WI and KY aggregates.

Table 2.9: Performance of proposed material models in predicting the measured resilient modulus of Wisconsin and Kentucky aggregates from pits (crushed gravel and uncrushed gravel) and quarries (crushed stone).

Resilient Modulus Model		Aggregate Source	Predicted vs Measured Resilient Modulus	R ²	Average M_r (MPa)	
					Measured	Predicted
UWM Model #1	Wisconsin Aggregate	Pit (Gravel/Crushed Gravel)	$M_r (P) = 1.02 M_r (M)$	0.98	163.2	170.0
		Quarry (Crushed Stone)	$M_r (P) = 0.97 M_r (M)$	0.98	164.1	162.4
	Kentucky Aggregate	Pit (Gravel)	$M_r (P) = 0.42 M_r (M)$	0.92	241.3	104.1
		Quarry (Crushed Stone)	$M_r (P) = 0.65 M_r (M)$	0.97	273.7	180.5
UWM Model #2	Wisconsin Aggregate	Pit (Gravel/Crushed Gravel)	$M_r (P) = 0.96 M_r (M)$	0.98	163.2	161.3
		Quarry (Crushed Stone)	$M_r (P) = 0.95 M_r (M)$	0.98	164.1	159.2
	Kentucky Aggregate	Pit (Gravel)	$M_r (P) = 1.58 M_r (M)$	0.81	241.3	384.7
		Quarry (Crushed Stone)	$M_r (P) = 0.74 M_r (M)$	0.97	273.7	204.7
UWM Model #3	Wisconsin Aggregate	Pit (Gravel/Crushed Gravel)	$M_r (P) = 1.05 M_r (M)$	0.97	163.2	177.2
		Quarry (Crushed Stone)	$M_r (P) = 1.05 M_r (M)$	0.96	164.1	176.5
	Kentucky Aggregate	Pit (Gravel)	$M_r (P) = 1.09 M_r (M)$	0.99	241.3	267.9
		Quarry (Crushed Stone) *	$M_r (P) = 0.83 M_r (M)$	0.95	299.9	251.3

*reconstructed KY aggregates included

2.4 California Bearing Ratio Test

The California Bearing Ratio (CBR) test was conducted according to AASHTO T 193: Standard Method of Test for the California Bearing Ratio. The test is conducted by compacting aggregate in a 6 in diameter mold to form a specimen 4.6 in high with a maximum particle size of 0.75 in. The test can be conducted on soaked or dry specimens. Soaked specimens are conditioned for 96 hours in water to simulate wet pavement conditions. The specimen is subjected to penetration of 3 in² area plunger at 0.05 in/minute. The CBR value is determined from the penetration pressure at 0.1 or 0.2 in. Standard crushed aggregate material has a CBR of 100%, however, high-quality, dense-graded crushed stone can have CBR values as low as 80 percent (Tutumluer, 2012).

2.5 Field Test Methods

Field test methods for characterizing aggregate base layers can be divided into nondestructive test (NDT), minimally intrusive, and intrusive methods. There has been significant improvement in the NDT technologies for characterizing base course materials including ground-penetrating radar (GPR), falling weight deflectometer (FWD), light weight deflectometer (LWD), Soil Stiffness Gauge (GeoGauge), and penetration technology such as dynamic cone penetrometer (DCP). NCHRP synthesis 382 (Puppala 2008) and NCHRP report 626 (Von Quintus et al., 2009) provide detailed information and data on various technologies applicable for characterizing unbound aggregate base layers.

The importance of evaluating these technologies and their ability to characterize unbound aggregate base layers comes from the new ME pavement design in which pavement layer modulus is a key material property required for designing new and rehabilitated flexible pavements. Implementation of ME pavement design and availability of these NDT technologies for predicting pavement performance will help increase the use of such technologies (Von Quintus et al., 2009).

Von Quintus et al. (2009) identified NDT technologies that are available for immediate implementation and routine use in QC/QA of constructed unbound aggregate layers. These technologies were identified based on their ability to recognize construction anomalies and to predict material properties indicative of pavement performance. Based on this, Von Quintus et al. (2009) recommended the GeoGauge for estimating the modulus of unbound layers for its readiness and ease of use for routine practice.

The layer thickness and modulus are needed structural properties for predicting pavement performance and are termed as quality characteristics by the Transportation Research Board (TRB) circular E-C307 (Von Quintus et al., 2009). Methods and technologies used for characterizing the unbound aggregate base layers and materials for both structural design and mixture design (gradation) are summarized in Tables 2.10 and 2.11.

Table 2.10: Summary of material and layer properties used for design and acceptance of flexible pavements and HMA overlays (after Von Quintus et al., 2009).

Pavement Layer	Material-Layer Property	Property Needed For:		
		Structural Design	Mixture Design	Acceptance
HMA Layers: Dense-Graded Mixtures	Density – Air Voids at Construction	Yes	Yes	Yes
	Voids in Mineral Aggregate	Yes	Yes	Yes
	Effective Asphalt Binder Content	Yes	Yes	Yes
	Voids Filled with Asphalt		Yes	
	Gradation	Yes	Yes	Yes
	Asphalt Binder Properties	Yes	Yes	
	IDT Strength and Creep Compliance	Yes	Yes	
	Dynamic Modulus	Yes	Yes	
	Flow Time or Flow Number		Yes	
	Initial Smoothness	Yes		Yes
Unbound Layers: Dense Graded Granular Base, Embankment Soils	Density	Yes	Yes	Yes
	Water Content	Yes	Yes	
	Gradation	Yes	Yes	Yes
	Minus 200 Material	Yes	Yes	Yes
	Plasticity Index (Atterberg Limits)	Yes	Yes	
	Resilient Modulus	Yes	Yes	
	Strength		Yes	
	CBR or R-Value	Yes		
	DCP Penetration Rate	Yes		
IDT – Indirect Tensile Test CBR – California Bearing Ratio DCP – Dynamic Cone Penetrometer				

Falling Weight Deflectometer (FWD)

This testing device is used to measure pavement surface deflection due to an impact load. In the test, an impulse load is applied to the pavement surface by a weight mass dropped from a specified height and sensors (e.g. geophones) placed over the pavement surface are used to measure deflections. The deflections are used to calculate the moduli of the pavement layers. Different moduli for each layer are assumed through back calculation routines in which an algorithm is used to predict the deflections of the pavement surface. If the pattern and magnitude of the predicted deflections match with the measured deflections, then the assumed moduli are reported as the moduli of the pavement layers (NCHRP 382).

Table 2.11: NDT methods used to measure properties and features of flexible pavements in-place (after Von Quintus et al., 2009).

Type of Property or Feature		NDT Technologies and Methods	
		HMA Layers	Unbound Aggregate Base and Soil Layers
Volumetric	Density	<ul style="list-style-type: none"> • GPR • Non-Nuclear Gauges: PQI, PaveTracker 	<ul style="list-style-type: none"> • GPR • Non-Nuclear Gauges: EDG, Purdue TDR
	Air Voids or Percent Compaction	<ul style="list-style-type: none"> • GPR • Infrared Tomography • Acoustic Emissions • Roller-Mounted Density Devices 	<ul style="list-style-type: none"> • GPR • Roller-Mounted Density Devices
	Fluids Content	<ul style="list-style-type: none"> • GPR 	<ul style="list-style-type: none"> • GPR • Non-Nuclear Gauges: EDG, Purdue TDR
	Gradation: Segregation	<ul style="list-style-type: none"> • GPR • Infrared Tomography • ROSAN 	<ul style="list-style-type: none"> • N/A
	Voids in Mineral Aggregate	<ul style="list-style-type: none"> • GPR (Proprietary Method) 	<ul style="list-style-type: none"> • N/A
Structural	Thickness	<ul style="list-style-type: none"> • GPR • Ultrasonic: Impact Echo, SPA, SASW • Magnetic Tomography 	<ul style="list-style-type: none"> • GPR • Ultrasonic: SPA, SASW
	Modulus: Dynamic or Resilient	<ul style="list-style-type: none"> • Ultrasonic: SPA, SASW • Deflection-Based: FWD, LWD • Roller-Mounted Response System, Asphalt Manager 	<ul style="list-style-type: none"> • Impact/Penetration: DCP, Clegg Hammer • GPR • Ultrasonic: DSPA, SPA, SASW • Deflection-Based; FWD, LWD • Steady-State Vibratory: GeoGauge • Roller-Mounted Response Systems
	Bond/Adhesion Between Lifts	<ul style="list-style-type: none"> • GPR • Ultrasonic: SASW, Impulse Response • Infrared Tomography 	N/A
Functional	Profile: IRI	<ul style="list-style-type: none"> • Profilograph, Profilometer, Inertial Profilers 	N/A
	Noise	<ul style="list-style-type: none"> • Noise Trailers 	N/A
	Friction	<ul style="list-style-type: none"> • CT Meter, ROSAN 	N/A
SPA- Seismic Pavement Analyzer PSPA- Portable Seismic Pavement Analyzer SASW- Spectral Analysis of Surface Waves LWD- Light Weight Deflectometer ROSAN- Road Surface Analyzer EDG- Electrical Density Gauge TDR- Time Domain Reflectometry		DSPA- Dirt Seismic Pavement Analyzer PQI- Pavement Quality Indicator DCP- Dynamic Cone Penetrometer CT- Circular Texture FWD- Falling Weight Deflectometer	

Dynamic Cone Penetrometer (DCP)

The DCP is a testing device that measures penetration rate induced by a sliding hammer weight that drives a slender shaft into the compacted base and subgrade. It is widely used to estimate density, strength, or stiffness of in-situ soils by determining parameters such as dynamic cone resistance (q_d) or DCP index (DCPI) in millimeters per blow, or inches per blow, or blows per 300 mm penetration. One major limitation is the lack of standardization of the testing device. Different size cones, hammer weights, and drop heights have been used, resulting in different energies applied by each device (NCHRP 382). Compaction quality control and assurance is one of the applications of this device. The DCP measurements are reported in the literature to correlate with multiple mechanical properties (Baus, 2006).

Kleyn (1975) worked on developing a laboratory-based correlation between DCP and CBR on 2,000 specimens. He noticed that when the moisture content changed while maintaining the compaction level at standard Proctor effort, the DCP data varied similarly to that of the CBR. Based on these findings, he concluded that the DCP-CBR relationship is independent of moisture content. The correlation developed under his study was:

$$\log (CBR) = 2.62 - 1.27 \log (PR) \dots\dots\dots (2.7)$$

where PR is the DCP penetration rate (mm/blow).

Harison (1987) found that a good correlation exists between CBR and DCP for clay-like soils, well-graded sands, and gravels. In his study, Harison developed correlations for each individual type of material tested as well as a general correlation for all the materials tested. The developed correlations by Harison (1987) are based on DCP tests conducted in the laboratory on samples compacted in standard CBR molds. Equations 2.8 and 2.9 show the relationship between CBR and PR for gravel materials and the general correlation.

$$\log (CBR) = 2.55 - 0.96 \log (PR) \dots\dots\dots (2.8)$$

$$\log (CBR) = 2.81 - 1.32 \log (PR) \dots\dots\dots (2.9)$$

Harison (1987) stated that it is preferable to establish a single equation that has general applicability rather than a set of equations each for a different material. With a general correlation, all materials tested can be represented to an accuracy of $\pm 10\%$. He also found that moisture content, dry density, and soaking processes do not affect the relationship between CBR and DCP.

Penetration Rate and Moduli Correlation

Over the years, correlations have been developed to determine the resilient modulus from CBR or DCP results. Heukelom and Klomp (1962) tested fine-grained soils with a soaked CBR of 10 or less and proposed an equation that correlates resilient modulus to CBR. Equation 2.10 was adopted by the 1993 AASHTO Guide for Design of Pavement Structures for estimating resilient modulus.

$$M_R (psi) = 1500 \times CBR \text{ or } M_R (MPa) = 10.34 \times CBR \dots\dots\dots (2.10)$$

The proposed correlation was developed from moduli ranging from 750 to 3,000 times the CBR. Powell et al. (1984) also proposed a relationship between CBR and resilient modulus (Equation 2.11) which has been widely accepted.

$$E (psi) = 2550 \times CBR^{0.64} \text{ or } E(MPa) = 10.34 \times CBR^{0.64} \dots\dots\dots (2.11)$$

Chen et al. (2001) conducted more than 60 DCP tests on two pavements used for accelerated pavement testing to assess the validity of empirical equations proposed in previous literature to compute layer moduli from data with the DCP. One of his objectives was to recommend a method for estimating the modulus through DCP testing. Chen et al. (2001) used the U.S. Army Corps of Engineers equation to correlate DCP to CBR and then used the Powell et al. (1984) equation to estimate modulus from CBR values.

Ground Penetrating Radar

Ground penetrating radar (GPR) is a technique that sends high frequency (25 MHz to 3 GHz) pulses of electromagnetic waves and captures the reflection of the waves from material boundaries with contrasting electromagnetic properties (Annan 2005). It uses the coherent arrivals of the reflected signals to create images of the near subsurface. In most engineering applications, the contrasting electromagnetic properties are caused by changes in dielectric permittivity (for asphalt pavement and geological applications) or by the presence of metals (in reinforced concrete applications). For asphalt pavement applications, GPR uses air coupled horn antennas that are mounted in a vehicle to image the thickness and conditions of the pavement, base, and subbases layers (Hoegh et al., 2015; Dong et al., 2016). These antennas typically work in the higher range of the GPR spectrum (400 MHz to 3 GHz). A combination of two or more antenna frequencies are used to provide profiles of depths of penetration and resolution.

2.5 Base Layer Performance Survey

The research team designed a survey with various questions to obtain the current information on performance of base layers from a number of highway agencies in the U.S. and Canada. The research team conducted the survey by e-mail and found it challenging to get

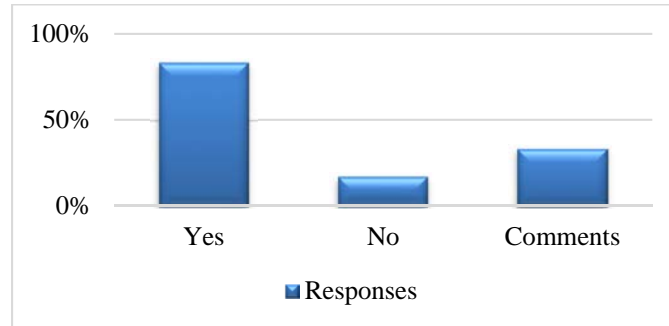
people to answer the survey questions. Out of the contacted state DOTs, only seven replies were obtained. The most important survey questions and answers are presented below.

Question: How common is the use of aggregate in base layers?

Answers:

- 1- In all new construction and reconstruction projects. In all rehabilitation projects for shoulder preparation. In some (~20%) of rehabilitation projects where existing asphalt surface to be fully milled or pulverized.
- 2- Every HMA reconstruct project will utilize aggregate base and sand subbase
- 3- Always used
- 4- Very common

Question: Do you have issues or problems associated with long term performance of base aggregates in HMA pavement?



Comments:

- 1- Generally, no known issues other than occasional spot failures.
- 2- Sometimes

Question: If your answer for the previous question is No, please describe how good the performance is and respond to questions related to aggregate base materials and construction methods.

Comments:

- 1- Not sure how to answer this very open-ended question. It is performing as anticipated other than as noted above. I cannot answer from the construction aspect.
- 2- As long the subgrade soundly supports the subbase and the subbase can be kept free of water, the material should perform well.

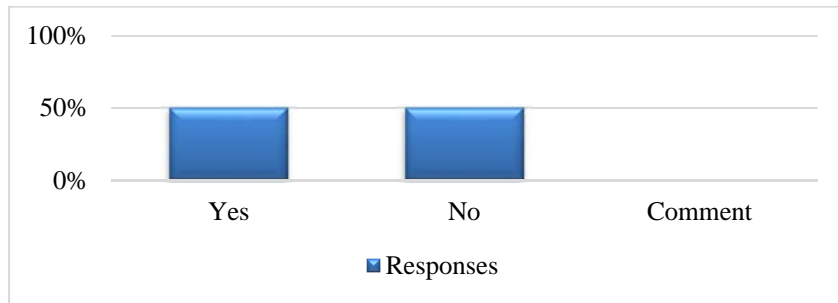
Question: If your answer for the previous question is Yes, please describe the problems and how serious they are?

Comments:

- 1- Contamination with subgrade, reduced stiffness and poor drainage performances.
- 2- infiltration of fines from the subgrade

- 3- Some of the problems we have encountered is Fatigue Cracking, Rutting, Base Failure, and Settlement. The seriousness of these problems varies but is often dependent upon the gradation of the base material used and the construction practices.
- 4- Aggregate bases that are primarily carbonate materials will sometimes degrade over time and be prone to frost heaving. Aggregate bases that are primarily gravel can be contaminated from the underlying non-granular soils.

Question: During HMA pavement rehabilitation (overlay, reconstruction) or surface preparation for overlay, do you inspect the quality of existing unbound base aggregates?

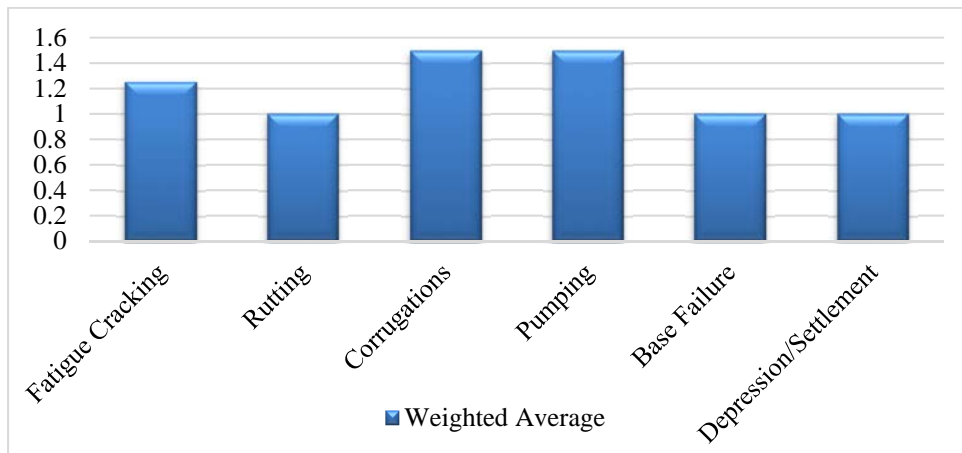


Question: If your answer for the previous question is Yes, describe methods of inspection.

Comments:

- 1- Not typically, but if the material is exposed it will be examined and compacted
- 2- Boreholes
- 3- Inspection can be visual, sometimes density testing is performed.
- 4- Gradations

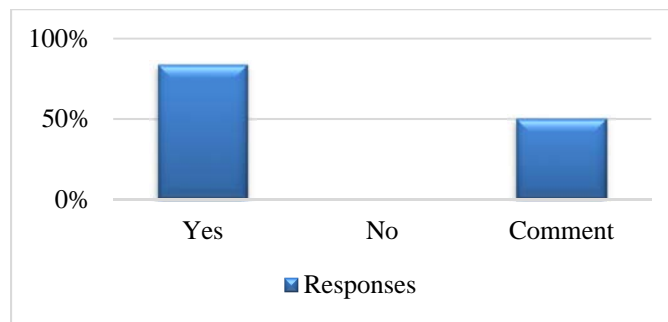
Question: What type of problems do you have with HMA pavement arising from unbound aggregate performance?



Comments:

- 1- We have not investigated the impacts yet.
- 2- We have some fatigue cracking and base failure, but not prevalent. Fatigue cracking assumed to be a support problem, but which layer is the problem is not investigated. Layers causing rutting generally not investigated either.
- 3- The above issues are not independently tied to the use of unbound aggregate - water presence and the quality of the subgrade are related
- 4- "base failure" can include all the types of problems listed above

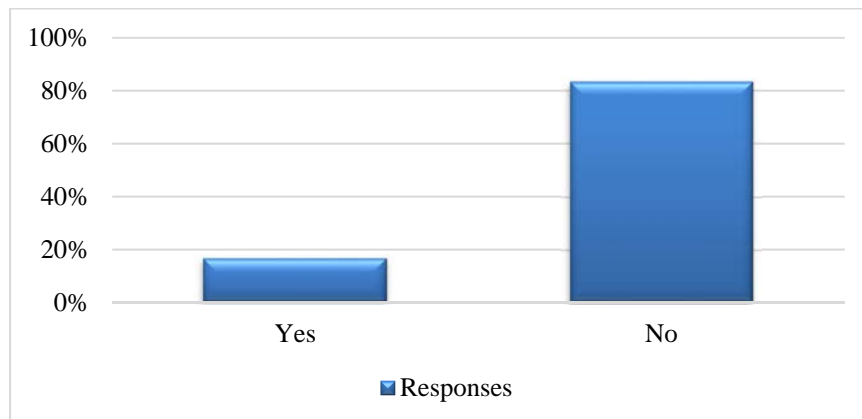
Question: Do you have freeze-thaw related problems associated with your unbound aggregate base layer?



Comments:(there are respondents who did not answer this question)

- 1- We are a wet-freeze state, but with 24" of unbound materials under our HMA pavements, we don't believe we have any freeze thaw. Unless water gets trapped somewhere in the pavement structure due to poor drainage.
- 2- It is possible where the aggregate does not drain properly.
- 3- Usually associated with a high - #200 material.

Question: Are you aware of any case histories in your area where unbound aggregate deterioration/degradation occurred?

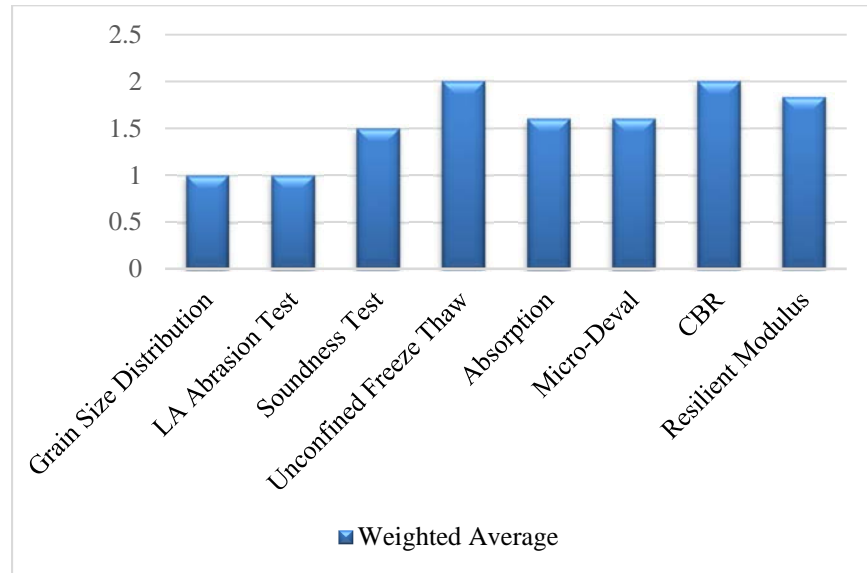


Question: If your answer for previous question is Yes, can you share information (papers, reports, etc.) on this case or describe the case?

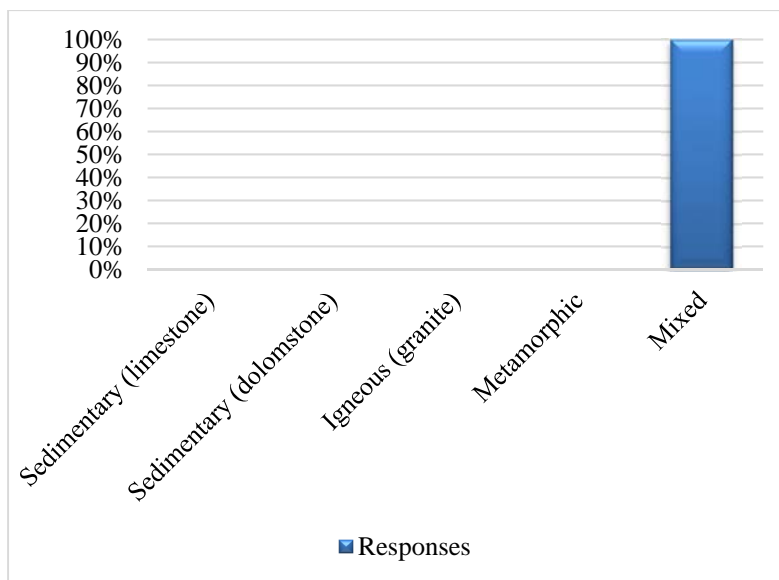
Comments:

1- No documented report other than visual observation during coring and soil survey.

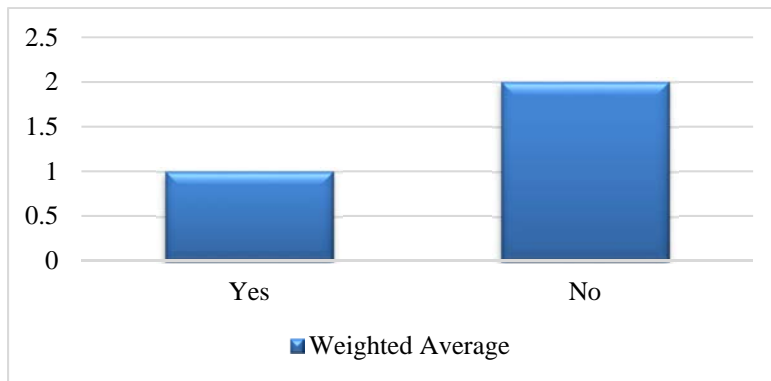
Question: For the unbound aggregate specifications and acceptance, do you require the following tests:



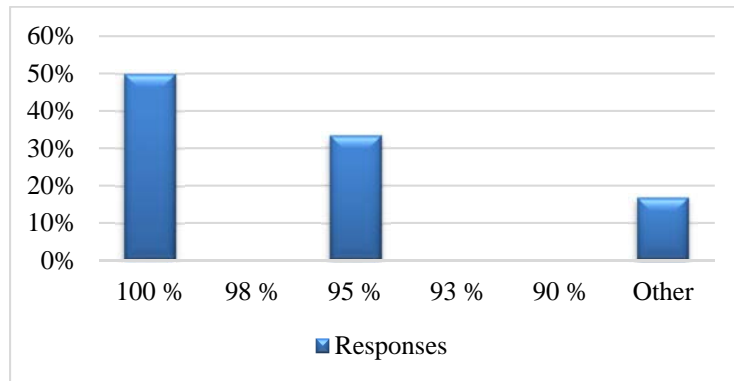
Question: What is the main rock type of the aggregate used as unbound base layer?



Question: Do you implement unit weight-based specifications (relative compaction) criteria for accepting construction aggregate bases?



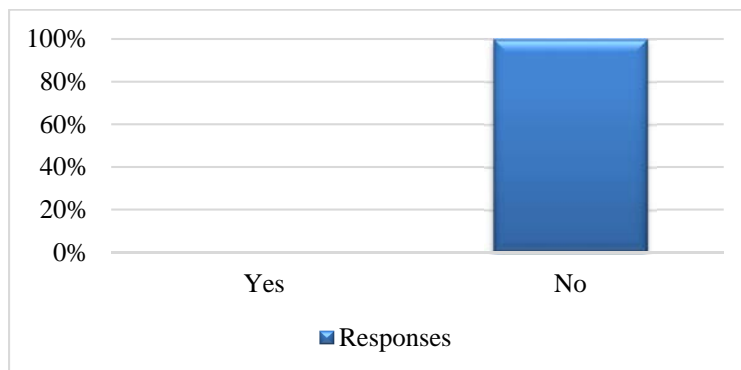
Question: If yes, what is the relative compaction minimum requirement?



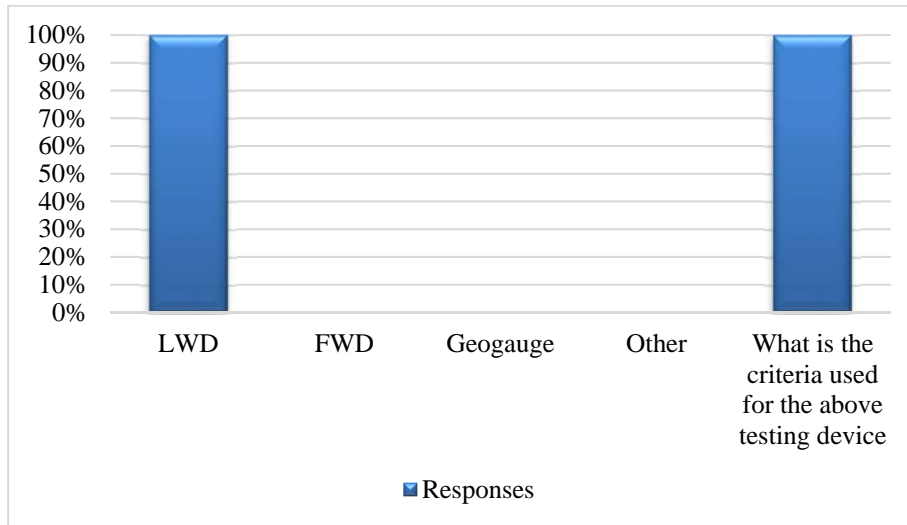
Comments:

- 1- For recycled materials we use modified proctor. For natural materials, we use standard proctor.

Question: Do you implement base modulus criteria for accepting construction aggregate bases?



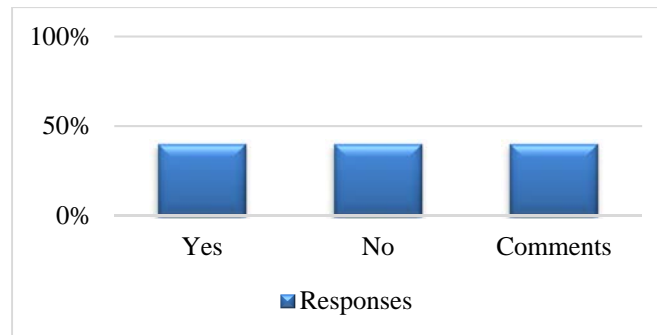
Question: If your answer for previous question is Yes, what is the testing tool used?



Comments:

- 1- In the process of implementing the use of modulus criteria.

Question: Do you use Geotextiles as a separation between unbound aggregate layer and subgrade?

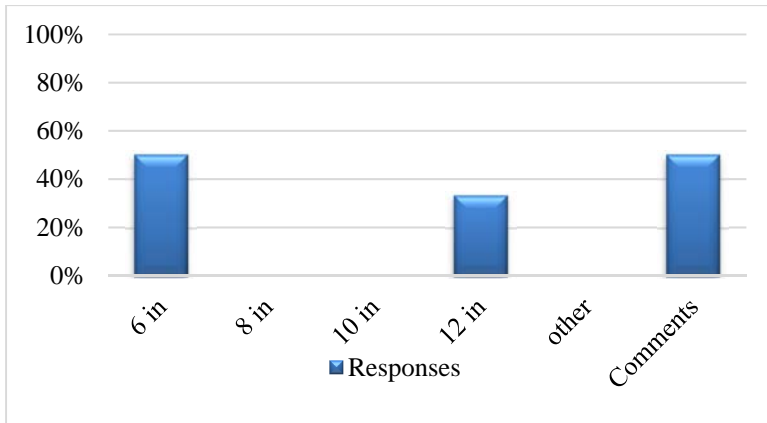


Note: One skipped this question

Comments:

- 1- Only between open graded aggregate base and sand subbase under concrete.
- 2- Occasionally, but not as a rule.

Question: What is the common unbound layer thickness used in your design (Please choose one and leave comments)



Comments:

- 1- 6 - 30 inches.
- 2- This goes over 18" of sand subbase.
- 3- Depending on the treatment, the thickness of the aggregate base can vary.

Chapter 3

Research Methodology

This chapter describes the field and laboratory testing program conducted to investigate aggregate base layers at primarily HMA pavement sites. Identified test sections at the selected pavement sites were subjected to nondestructive testing using the Falling Weight Deflectometer and Ground Penetrating Radar as well as visual pavement distress surveys and Dynamic Cone Penetrometer. Base layer aggregate samples were collected and subjected to a comprehensive laboratory testing program. Laboratory tests included standard compaction, particle size analysis, Atterberg limits (LL and PL), sodium sulfate soundness (SSS) (on fine and coarse aggregate), Micro-Deval (MD) (on fine and coarse aggregate), absorption, specific gravity (G_s), repeated load triaxial test (RLT) (resilient modulus, M_r), and California Bearing Ratio. Laboratory tests were conducted on base course aggregates at the pavement research laboratory at the University of Wisconsin-Milwaukee.

3.1 Selection of Pavement Test Sites

The research team, in coordination with the Project Oversight Committee (POC), identified and selected various existing HMA pavement sites for field testing and base aggregate sampling. The criteria used for the selection of sites considered three aspects: 1) geographical variations in Wisconsin, 2) base course layers that used virgin aggregates, and 3) HMA pavement type. The selected pavement sites are mostly pavements with aggregate base courses that were constructed in more than 10 years ago. Twenty-seven pavement locations/sites were selected for this study in such a way that twenty-one of the locations/sites contained aggregates from existing base-course layers and the other six contained more recently placed virgin aggregates. The pavement locations/sites that consisted of base course layers were STH 33 Middle Ridge, STH 162 Middle Ridge, STH 36 Waterford (Site #1, Site #2, and Site #3), STH 180 Marinette, USH 53 Minong, I 94 Zoo Interchange (Site #1 and Site #2), STH 59 Edgerton, STH 142 East Burlington, STH 142 West Burlington, STH 32 Forest County, Edgerton Avenue in Greenfield, and USH 45 Pelican Lake. The pavement sites that consisted of recently placed virgin aggregates were CTH B Woodville, STH 18 Jefferson, STH 33 Saukville, USH 45 Larsen, CTH JJ Appleton, and STH 33 Spencer. Selected pavement sites at STH 76 Appleton, STH 140 Clinton, STH 32 Oneida County, and USH 45 Yorkville did not yield base aggregate samples after coring/sampling attempts.

The pavement sites with younger age base aggregate are selected to be used as a reference of good performing pavements during their short service life; however, for the rest of the test sites, the pavements exhibited different types and levels of distress, which were

suspected to be the result of aggregate base course layer performance. Figure 3.1 depicts the locations of the investigated pavements in Wisconsin.

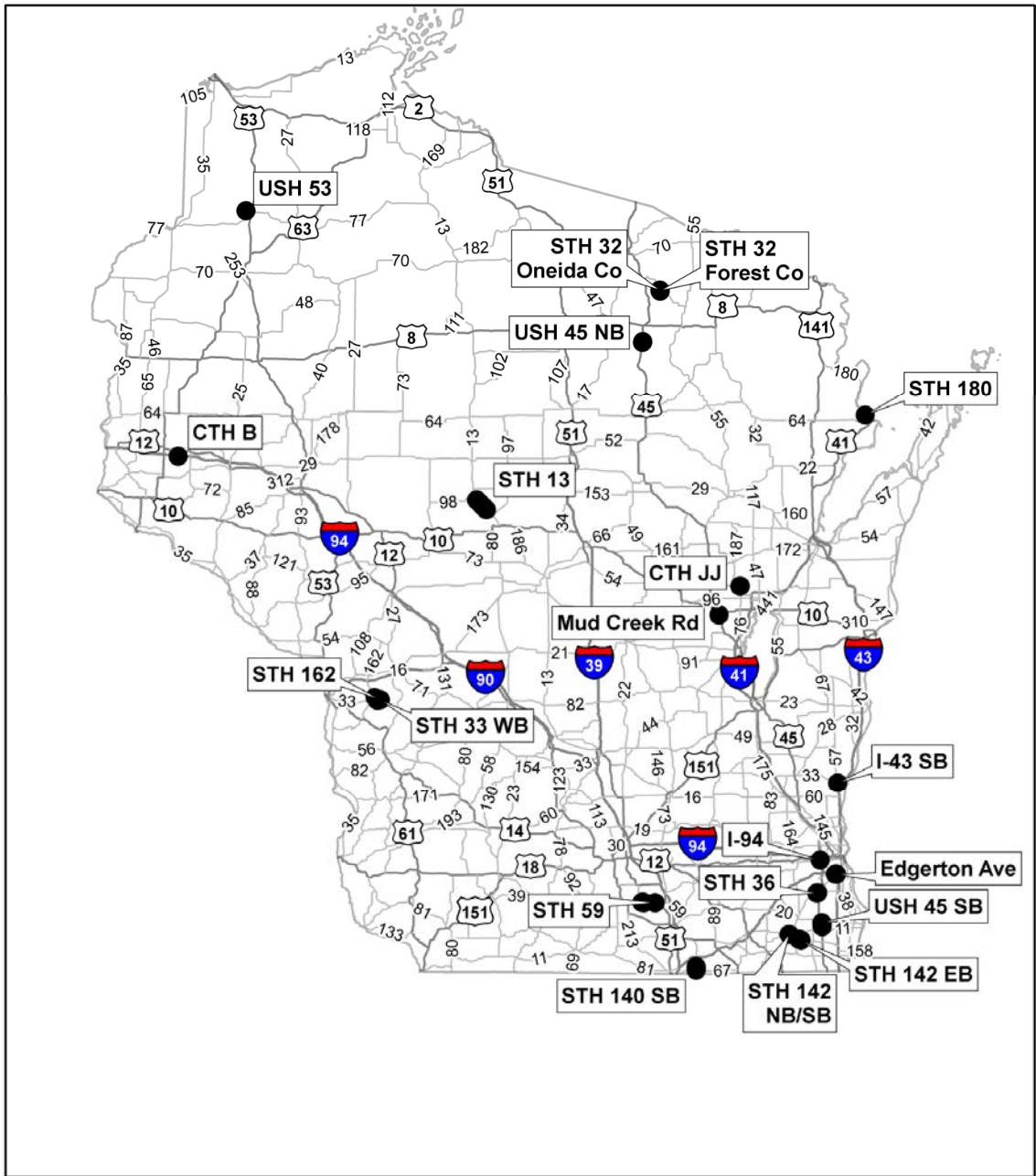


Figure 3.1: Locations of the investigated pavements in Wisconsin.

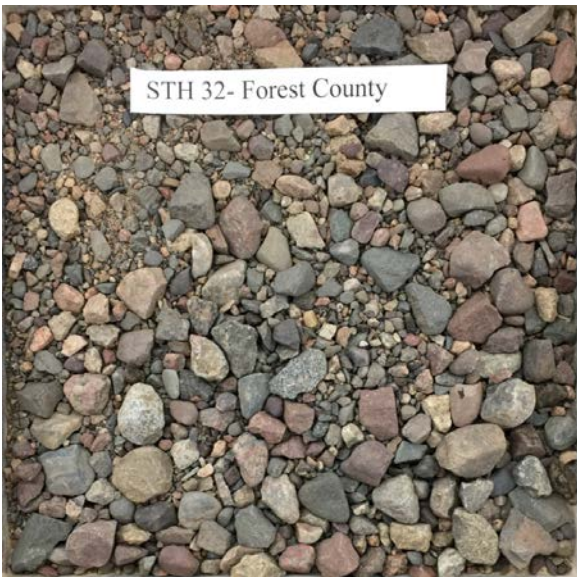
It is worth noting that all the sites selected consisted of asphalt pavement except for USH 53, which consisted of concrete pavement. The aggregate type of each sample collected is shown in Figure 3.2. The thicknesses and ages of the pavement and base-course aggregate layers are shown in Table 3.1.



STH 142 West – Burlington: Natural gravel of sedimentary origin (carbonates: limestone/ dolostone). Round and semi-round particles, a large percentage with smooth surface texture; some crushed particles with semi-angular shape. Presence of large sized particles.



USH 45 – Pelican Lake: Natural gravel of mixed origin: igneous, metamorphic and sedimentary (carbonates). Round and semi round particle shape and smooth surface texture; some crushed gravel particles with semi-angular/angular shape and rough surface texture.



STH 32 – Forest County: Natural gravel of igneous and metamorphic origin. Crushed particles of semi-round shape with smooth surface texture and some particles with semi-angular particles.



STH 180 – Marinette: Crushed aggregate of sedimentary origin (carbonates: dolostone/limestone). Angular and semi-angular particles with rough surface texture.

Figure 3.2: Geological and particle characteristic descriptions of the investigated base course layer aggregates.



I 94 – Zoo Interchange Site #2: Mixture of crushed aggregate of sedimentary origin (carbonates: limestone/dolostone) with smaller percentages of recycled crushed Portland cement concrete (RC) and recycled asphalt pavement (RAP). Angular/semi-angular particles with rough surface texture and noticeable porosity.



STH 36 Site #2 – Gray: Crushed aggregate of sedimentary origin (carbonates: dolostone/limestone). Angular and semi-angular particles with rough surface texture.

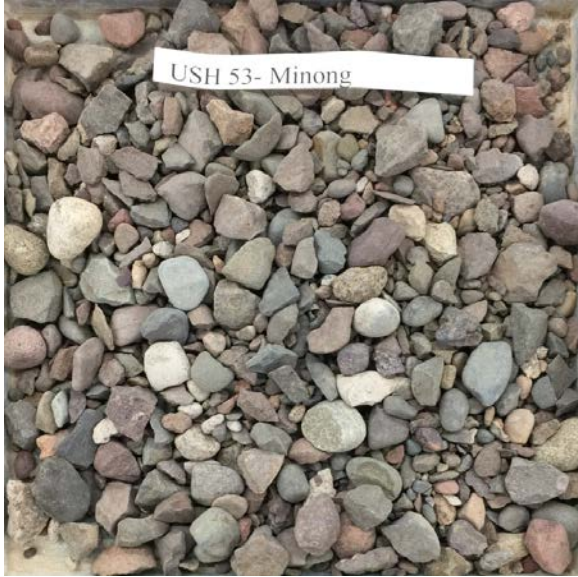


STH 36 Site #3 – Gray: Crushed aggregate of sedimentary origin (carbonates: dolostone/limestone). Angular and semi-angular particles with rough surface texture.

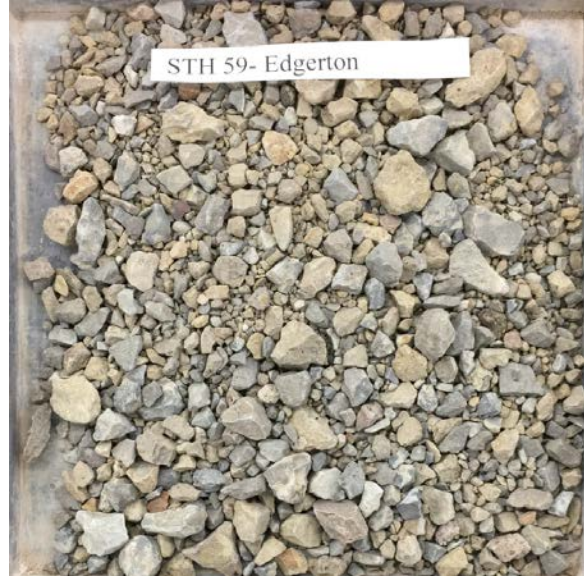


STH 36 Site #1 – Brown: Natural gravel of mixed origin but mainly sedimentary (carbonates: limestone/dolostone). Presence of crushed gravel composed of semi-round particles with smooth surface texture. Some semi-angular particles with rough surface texture present.

Figure 3.2 (Cont.): Geological and particle characteristic descriptions of the investigated base course layer aggregates.



USH 53 – Minong: Natural gravel of igneous and metamorphic origin. Semi-round particles with smooth surface texture. Crushed gravel composed of semi-round particles with rough surface texture.



STH 59 – Edgerton: Crushed aggregate of sedimentary origin (carbonates: dolostone/limestone). Angular and semi-angular particles with rough surface texture.

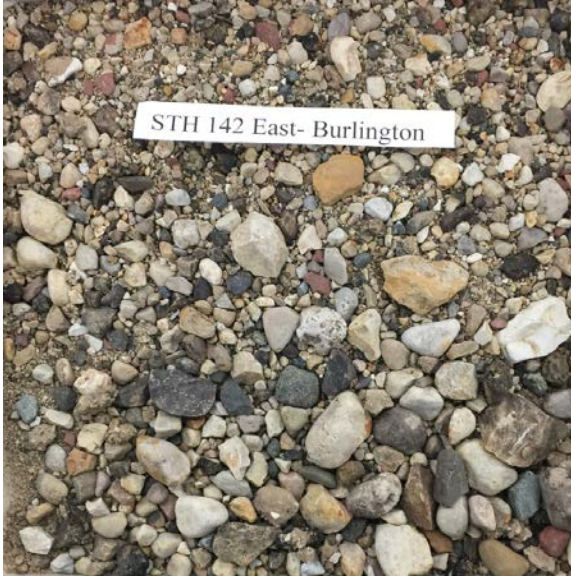


STH 162 – Middle Ridge: Crushed aggregate of sedimentary origin (carbonates: dolostone/limestone). Angular and semi-angular particles with rough surface texture.



STH 36 Site #2 – Brown: Natural gravel of mixed origin but mainly sedimentary (carbonates: limestone/dolostone). Presence of crushed gravel composed of semi-round particles with smooth surface texture. Some semi-angular particles with rough surface texture present.

Figure 3.2 (Cont.): Geological and particle characteristic descriptions of the investigated base course layer aggregates.



STH 142 East – Burlington: Natural gravel of sedimentary (carbonates: limestone/dolostone) with a smaller amount of igneous and metamorphic origin. Semi-round particles with smooth surface texture. Some crushed particles with semi-angular shape. Large sized particles.



STH 33 – Saukville: Crushed aggregate of sedimentary origin (carbonates: dolostone/limestone). Angular and semi-angular particles with rough surface texture.

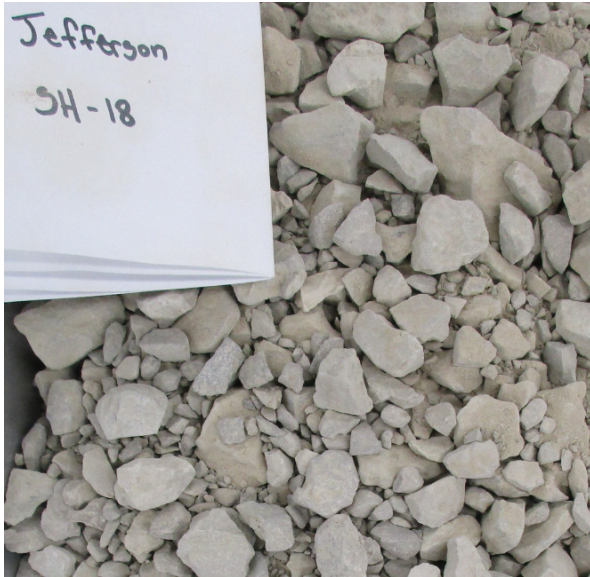


STH 33 – Middle Ridge: Crushed aggregate of sedimentary origin (carbonates: dolostone/limestone). Angular and semi-angular particles with rough surface texture.



Edgerton Ave. – Greenfield: Natural gravel of sedimentary origin (carbonates: limestone/dolostone) with a lesser amount of particles of igneous and metamorphic origin. Semi-round particles, a large percentage with smooth surface texture; some crushed particles with semi-angular shape.

Figure 3.2 (Cont.): Geological and particle characteristic descriptions of the investigated base course layer aggregates.



STH 18 – Jefferson: Crushed aggregate of sedimentary origin (carbonates: dolostone/limestone). Angular and semi-angular particles with rough surface texture.



USH 45 – Larsen: Crushed aggregate of sedimentary origin (carbonates: dolostone/ limestone). Angular and semi-angular particles with rough surface texture.



CTH JJ – Appleton: Crushed aggregate of sedimentary origin (carbonates: dolostone/limestone). Angular and semi-angular particles with rough surface texture.



STH 13 – Spencer: Crushed aggregate of igneous and metamorphic origin. Angular and semi-angular particles with rough surface texture.

Figure 3.2 (Cont.): Geological and particle characteristic descriptions of the investigated base course layer aggregates.

Table 3.1: Thickness and age of the samples collected from each project site from WisDOT plans and field measurements.

Project Site	Surface Layer (HMA)		Base-Course Layer		
	Thickness (in)		Age (years)	Thickness (in)	
	WisDOT	Field		WisDOT	Field
STH 33 – Middle Ridge	6	3-20	85	2-11	2-5
STH 162 – Middle Ridge	10-13	8	85	4-15	4-12
STH 36 – Waterford	4-11 (surface)	4	>18	6	8
		9		4	6
STH 180 – Marinette	8.5	N/A	79	4	4
USH 53 – Minong	9	N/A	18	6	6
Zoo-Site 1&2 – Milwaukee	7.5	8	20	13	11
STH 18 – Jefferson	N/A	N/A	8	N/A	N/A
STH 33 – Saukville	N/A	16.5	6	16.5	16.5
USH 45 – Larsen	4	N/A	6	6	6
STH 59 – Edgerton	4	3.75	>15	8	7.5
Edgerton Ave – Greenfield	11	10	>50	8.5	8
CTH B – Woodville	7	8	6	10	9
CTH JJ – Appleton	5	N/A	6	10	10
STH 13 – Spencer	6	N/A	6	6	6
STH 32 – Forest County	variable	10.5	>50	variable	3
STH 142 East – Burlington	14.5	14	>40	10-12	20
STH 142 West – Burlington	8-14.5	7-10	>40	10-12	5-12
USH 45 – Pelican Lake	6.25	5.75	>20	14	10

3.2 Non-Destructive Field Testing at Selected Pavement Sites

The research team in coordination with WisDOT planned the field testing program for the selected pavement sites. The testing program consisted of Falling Weight Deflectometer, Ground Penetrating Radar, visual distress surveys, and Dynamic Cone Penetration. Table 3.2 presents a summary of the field tests conducted at the investigated pavement sections.

3.2.1 Falling Weight Deflectometer Tests

The FWD testing was conducted by WisDOT and required extensive efforts by the WisDOT team and the researchers. This included travel to various pavement sites across Wisconsin, implementing full traffic control and lane closure, selecting test sections, and executing the testing program. Once at the pavement site, the research team conducted a windshield visual distress survey/evaluation of the whole length of the site to identify representative test section(s).

The FWD test was conducted according to ASTM D4694: Standard Test Method for Deflections with a Falling-Weight-Type Impulse Load Device. The WisDOT KUAB FWD was used with three different load drops of 5,000, 9,000, and 12,000 lb. Seven geophones were used to record pavement surface deflection located at the center of the loading plate and at 12, 24, 36, 48, 60, and 72 inches behind the loading plate. In another configuration, nine geophones were used to record pavement surface deflection with two additional geophones located at 12 inches in front of and to the left of the loading plate. Pavement surface and air temperatures and GPS coordinates were acquired at each test point. Figure 3.3 shows the FWD during testing at various pavement sites.

The total length of the FWD test section for each pavement site varied between 528 ft ($\frac{1}{10}$ of a mile) and more than 5,000 ft depending on field conditions and availability of equipment. The FWD test point spacing ranged from 10 to 100 ft. The majority of the FWD tests were conducted at the outside wheel path of the outside lane of the pavement section. For a limited number of pavement test sections, FWD testing was conducted on both the outside and inside wheel paths.

Table 3.2: Field tests conducted at the investigated pavement sites.

Project Site	Base Aggregate Sampling	Dynamic Cone Penetration	Falling Weight Deflectometer	Ground Penetrating Radar	Visual Distress Survey
STH 33 – Middle Ridge	✓	✓	✓	✓	✓
STH 162 – Middle Ridge	✓	✓			✓
STH 36-S1-B – Waterford	✓	✓	✓	✓	✓
STH 36-S2-B – Waterford	✓		✓	✓	✓
STH 36-S1-G – Waterford	✓	✓	✓	✓	✓
STH 36-S2-G – Waterford	✓	✓	✓	✓	✓
STH 36-S3-G – Waterford	✓	✓	✓	✓	✓
STH 180 – Marinette	✓	✓			✓
USH 53 – Minong	✓	✓			
I-94 – Zoo-S1 – Milwaukee	✓	✓			✓
I-94 – Zoo-S2 – Milwaukee	✓	✓			✓
STH 18 – Jefferson	✓				
STH 33 – Saukville	✓	✓	✓	✓	✓
USH 45 – Larsen	✓	✓	✓	✓	✓
STH 142 East – Burlington	✓		✓	✓	✓
STH 142 West – Burlington	✓		✓	✓	✓
Edgerton Ave – Greenfield	✓		✓	✓	✓
STH 59 – Edgerton	✓		✓	✓	✓
USH 45 – Pelican Lake	✓		✓	✓	✓
STH 32 – Forest County	✓		✓	✓	✓
STH 32 – Oneida County	(✓)		✓	✓	✓
CTH B – Woodville	✓	✓	✓	✓	✓
CTH JJ – Appleton	✓	✓	✓	✓	✓
STH 13 – Spencer	✓	✓	✓	✓	✓
STH 140 – Clinton	(✓)		✓	✓	✓
USH 45 – Yorkville	(✓)		✓	✓	✓
STH 76 – Appleton	(✓)		✓	✓	✓

(✓): Coring/sampling did not yield any aggregate samples.

3.2.2 Ground Penetrating Radar

WisDOT owns and operates a GSSI SIR 3000 ground penetrating radar system (depicted in Figure 3.3 e). The system consists of a high-resolution 2.0 GHz air-coupled horn antenna for primary analysis of pavement layer thicknesses. The system could also be used for assessing pavement condition/deterioration. The maximum depth of penetration is approximately 18-24 in below the pavement surface. The system also includes a 900 MHz ground-coupled antenna for primary analysis of base course and subbase layer thickness and subgrade assessment. The maximum depth of penetration is approximately 5 ft.

The GPR testing was used in conjunction with the FWD testing. Therefore, the pavement test sites and sections selected for the GPR testing are the same as for the FWD testing. The data files were compiled by WisDOT team and given to the research team for layer thickness analysis.



(a) FWD testing



(b) FWD testing



(c) FWD plate and sensors on pavement surface



(d) FWD plate and sensors on pavement surface



(e) The 2 GHz GPR antenna



(f) The 900 MHz GPR antenna

Figure 3.3: Nondestructive testing using the WisDOT FWD KUAB/GSSI GPR unit at various HMA pavement sites.

3.2.3 Visual and Automated Pavement Surface Distress Surveys

Visual surveys were conducted (as shown in Figure 3.4) to identify and quantify the various types of pavement surface distress exhibited at the investigated pavements and to obtain

data needed to evaluate pavement performance in terms of a Pavement Condition Index (PCI). Each distress survey was conducted for one 528 ft section at each pavement site. The section was selected to be representative of the overall pavement condition. It should be noted that the WisDOT Pavement Data Unit conducts automated pavement surface distress surveys as part of pavement management of the state/national highway network. The collected data is compiled in the Pavement Information File (PIF) database where the performance indicators such as the PCI and the International Roughness Index (IRI) are calculated for the length of the fourth $\frac{1}{10}$ of a mile for each highway segment. The research team was given time to work on the PIF workstations at WisDOT Truax Center to retrieve and analyze the data corresponding to pavement sections investigated in this study.



(a) Visual distress survey



(b) Measuring distresses

Figure 3.4: Visual pavement surface distress surveys conducted by the research team.

At the investigated pavement sites, surface distresses were visually identified, quantified, and recorded. Pavement distress types, extent, and levels of severity were identified and quantified according to the FHWA distress identification manual. Figure 3.5 shows examples of pavement surface conditions noted during a visual distress survey.

3.3 Sampling of Base Layer Aggregates and Field Testing

3.3.1 Sampling of Base Aggregates

The research team and POC coordinated efforts to obtain aggregate base samples from the selected pavement sites. Base aggregate samples with a volume of approximately three 5-gallon buckets were collected from these sites using three different methods:



(a) Rutting



(b) Delamination (slippage)



(c) Rutting



(d) Edge cracking



(e) Fatigue cracking and transverse cracking



(f) Fatigue and block cracking



(g) Fatigue cracking



(h) Fatigue cracking

Figure 3.5: Pictures of various pavement surface distresses at a number of test sections.

1. Coring pavement surface by WisDOT drilling unit and removal of base aggregate samples by the research team. This was carried out at the existing pavement sites where rehabilitation work was not being performed: STH 59, STH 32 OC, STH 32 FC, STH 140, STH 76, and USH 45 PL.
2. Saw cutting of pavement surface and removal of aggregate samples by the research team. This was carried out at pavement sites during reconstruction work.
3. Pavement surface removal by the contractor's heavy equipment and removal of aggregate samples by the research team. This was carried out at pavement sites during reconstruction work.

Figures 3.6 and 3.7 depict pictures of the various efforts involved in base aggregate sampling. The aggregate samples were collected with the aid of basic tools such as small size shovels and hand-held pickaxes to dig down to the bottom of base course aggregate layers. The collected samples were placed in 5-gallon buckets, covered, and transported to the Pavement and Geotechnical Research Laboratory at UW-Milwaukee for testing and evaluation. It should be noted that the research team visually inspected the base course layers during sampling and looked for evidence of contamination, infiltration, or pumping of fine materials from subgrade soils. The virgin aggregate samples were obtained from a previous study; one bucket of each sample was available.

3.3.2 Dynamic Cone Penetration Test

The field testing program included aggregate base course layer and subgrade testing using the DCP. A dynamic cone penetrometer with a single-mass hammer was used to perform tests on the project sites. The DCP was driven into the aggregate base layer by the impact of a single-mass 17.6 lb hammer dropped from a height of 22.6 in. The test was conducted according to the standard test procedure described by ASTM D6951: Standard Test Method for Use of the Dynamic Cone Penetrometer in Shallow Pavement Applications. For several pavement test sites, two or more tests were conducted at 100 ft spacing in which the cone was driven through the whole aggregate base course layer and into the subgrade. Figure 3.8 depicts the DCP test conducted on selected pavement sites.



(a) WisDOT coring rig at STH 59



(b) 8-inch coring barrel



(c) Exposed base aggregate at STH 59



(d) Sampling base aggregate



(e) Core from distressed area



(f) Bottom of base layer



(g) Coring at STH 76



(h) Coring at STH Forest County



(i) Base aggregate sampling

Figure 3.6: Coring of pavement surface to retrieve base aggregate samples.



(a) Saw-cutting of pavement surface at STH 33 MR



(b) Base aggregate sampling at STH 33 MR



(c) Pavement surface removal at STH 162



(d) Aggregate sample from STH 162



(e) Pavement surface removal at Edgerton Ave



(f) Exposed aggregate base layer at Edgerton Ave



(g) Exposed aggregate base at STH 142E Burlington



(h) Aggregate sampling at STH 36



(i) Pavement layer thickness at STH 36



(j) Aggregate sampling at USH 53 Minong



(k) Aggregate sampling at STH 36



(l) Base aggregate at I 94 Zoo

Figure 3.7: Sampling of base aggregates using handheld tools.



(a) I 94 Zoo Interchange



(b) USH 53 Minong



(c) STH 162 Middle Ridge



(d) STH 180 Marinette

Figure 3.8: Dynamic cone penetration test on aggregate base course layers.

3.4 Laboratory Testing of Base Aggregate

Representative aggregate samples were collected from the investigated pavement sites as described earlier. Table 3.3 presents the ASTM and AASHTO standard test procedures and Table 3.4 presents the types of tests conducted on the base aggregates from each investigated pavement site.

3.4.1 Particle Size Analysis

Sieve analysis was used to determine the particle size distribution of the base course aggregate specimens. First, the sample was oven-dried to constant mass at 230 °F. Then quartering was used to reduce the sample into a test sample that was at least 15 kg. The purpose was to prepare a test sample that was representative of the sampled project site location. Next, the sample was washed over a No. 200 sieve so that material finer than the No. 200 sieve would pass through the opening of the sieve. Then the sample was oven-dried to constant mass once again.

Afterwards, the following set of sieves were stacked: 1.25", 3/4", 3/8", No. 4, No. 10, No. 40, No. 200, and a pan. These sieve sizes are in compliance with the WisDOT specifications for the particle size distribution of 1 ¼ in dense graded base course aggregate layers described in Section 305.2.2.1 of WisDOT Standard Specifications for Highway and Structure Construction (2108). The stacked sieves were then placed onto an automatic sieve shaker and were agitated according to the standard procedures. The retained masses on each sieve were weighed and used to calculate the percentage of material passing each sieve and subsequently plot the particle size distribution curves.

Table 3.3: ASTM and AASHTO standard test methods employed.

Standard Test Procedure	Standard Designation	
	ASTM	AASHTO
Standard Test Method for Materials Finer than 75-µm (No. 200) Sieve in Mineral Aggregates by Washing	C117 -17	T 11-05 (13)
ASTM: Standard Test Method for Relative Density (Specific Gravity) and Absorption of Coarse Aggregate AASHTO: Standard Method of Test for Specific Gravity and Absorption of Coarse Aggregate	C127 - 15	T 85-14
ASTM: Standard Test Method for Relative Density (Specific Gravity) and Absorption of Fine Aggregate AASHTO: Standard Method of Test for Specific Gravity and Absorption of Fine Aggregate	C128 - 15	T 84 - 13
Standard Test Method for Sieve Analysis of Fine and Coarse Aggregates	C136 - 14	T 27 - 14
Standard Practice for Reducing Samples of Aggregate to Testing Size	C702 - 11	T 248 - 14
Standard Practice for Sampling Aggregates	D75 - 14	T 2 - 91 (15)
ASTM: Standard Test Methods for Laboratory Compaction Characteristics of Soil Using Standard Effort (12 400 ft-lbf/ft ³ (600 kN-m/m ³)): (Method C) AASHTO: Standard Method of Test for Moisture–Density Relations of Soils Using a 2.5-kg (5.5-lb) Rammer and a 305-mm (12-in) Drop	D698 - 12	T 99 (17)
ASTM: Standard Test Method for California Bearing Ratio (CBR) of Laboratory-Compacted Soils AASHTO: Standard Method of Test for The California Bearing Ratio	D1883 - 16	T 193 - 13
Standard Test Method for Resistance of Coarse Aggregate to Degradation by Abrasion in the Micro-Deval Apparatus	D6928 - 17	T 327 - 12
Standard Test Method for Resistance of Fine Aggregate to Degradation by Abrasion in the Micro-Deval Apparatus	D7428 - 15	
Standard Test Method for Soundness of Aggregates by Use of Sodium Sulfate or Magnesium Sulfate	C88 - 13	T 104 (99)
Standard Method of Test for Determining the Resilient Modulus of Soils and Aggregate Materials		T 307 - 99 (17)
ASTM: Standard Test Methods for Liquid Limit, Plastic Limit, and Plasticity Index of Soils AASHTO: Standard Method of Test for Determining the Liquid Limit of Soils AASHTO: Standard Method of Test for Determining the Plastic Limit and Plasticity Index of Soils	D4318 - 17	T 89 (13) T 90 (16)

Table 3.4: Laboratory tests conducted on base aggregate samples obtained from pavement sites.

Project Site	Grain-Size Distribution	Atterberg Limits	Standard Compaction	Specific Gravity & Absorption	Micro-Deval		Sodium Sulfate Soundness		California Bearing Ratio	Repeated Load Triaxial Test
					Coarse Aggregate	Fine Aggregate	Coarse Aggregate	Fine Aggregate		
STH 33 – Middle Ridge	✓		✓	✓	✓	✓	✓	✓	✓	
STH 162 – Middle Ridge	✓		✓	✓	✓	✓	✓	✓	✓	
STH 36-S1-B – Waterford	✓	✓	✓	✓	✓	✓	✓	✓	✓	
STH 36-S2-B – Waterford	✓		✓	✓	✓	✓	✓	✓	✓	
STH 36-S1-G – Waterford	✓		✓	✓	✓	✓	✓	✓	✓	
STH 36-S2-G – Waterford	✓	✓	✓	✓	✓	✓	✓	✓	✓	
STH 36-S3-G – Waterford	✓	✓	✓	✓	✓	✓	✓	✓	✓	
STH 180 – Marinette	✓	✓	✓	✓	✓	✓	✓	✓	✓	
USH 53 – Minong	✓	✓	✓	✓	✓	✓	✓	✓	✓	
I-94 – Zoo-S1 – Milwaukee	✓	✓	✓	✓	✓	✓	✓	✓	✓	
I-94 – Zoo-S2 – Milwaukee	✓	✓	✓	✓	✓	✓	✓	✓	✓	
STH 18 – Jefferson			✓	✓	✓	✓	✓	✓	✓	✓
STH 33 – Saukville	✓	✓	✓	✓	✓	✓	✓	✓	✓	✓
USH 45 – Larsen	✓	✓	✓	✓	✓	✓	✓	✓	✓	✓
STH 142 East – Burlington	✓	✓	✓	✓	✓	✓	✓	✓	✓	✓
STH 142 West – Burlington	✓	✓	✓	✓	✓	✓	✓	✓	✓	✓
Edgerton Ave – Greenfield	✓	✓	✓	✓	✓	✓	✓	✓	✓	✓
STH 59 – Edgerton	✓	✓	✓	✓	✓	✓	✓	✓	✓	✓
USH 45 – Pelican Lake	✓	✓	✓	✓	✓	✓	✓	✓	✓	✓
STH 32 – Forest County	✓	✓	✓	✓	✓	✓	✓	✓	✓	✓
STH 32 – Oneida County					✓					
CTH B – Woodville	✓		✓							✓
CTH JJ – Appleton	✓		✓							✓
STH 13 – Spencer	✓		✓							✓
STH 140 – Clinton										
USH 45 – Yorkville										
STH 76 – Appleton										

3.4.2 Standard Compaction Test

The standard compaction test was used to obtain a relationship between the moisture content and dry unit weight and from this relationship determine the optimum moisture content (w_{opt}) and the maximum dry unit weight ($\gamma_{d,max}$) of the aggregate. Such parameters are important and needed for the resilient modulus test as well as the CBR.

The standard compaction test was conducted using a 6 in diameter cylindrical mold with a height of 4.59 in, with detachable base-plate and collar, and using a 5.5 lb mechanical rammer. A representative sample of the aggregate was obtained and sieved over a $\frac{3}{4}$ in sieve where the material retained on the sieve was replaced with material passing the $\frac{3}{4}$ in sieve and retained on the No. 4 sieve. A specimen was obtained from the sample and a selected amount of water was added. The aggregate specimen was compacted into the mold in three layers. Each layer was compacted by dropping the rammer from a 12 in height 56 times using a mechanical compactor (as shown in Figure 3.9). The weight of the final compacted specimen was determined, and the bulk unit weight was calculated. The compacted moist specimen was then oven dried and used to determine the moisture content. Finally, the dry unit weight was calculated.

On average, approximately five specimens with different moisture contents were compacted for each aggregate source. The compaction curve (dry unit weight – moisture content relationship) was then constructed for each aggregate source and the maximum dry unit weight and the optimum moisture content were determined.



(a) Mechanical compactor



(b) Compacting aggregate samples

Figure 3.9: Compaction test equipment used for base aggregates.

3.4.3 Specific Gravity and Absorption

The absorption of aggregates is significant especially with respect to durability and resistance to harsh freeze-thaw deterioration. The specific gravity and absorption tests were used to measure the oven-dry specific gravity, saturated-surface-dry specific gravity, apparent specific gravity, and absorption of the aggregate specimens. Aggregate samples consisted of particles larger than the No. 8 sieve and were submerged in water for 24 hours so that they reached saturation. The aggregate samples were removed from the water and an absorbent towel was used to dry the surface of the aggregate particles so that they were in the saturated-surface-dry condition. The aggregate sample was then weighed to get the saturated-surface-dry weight. Next, the sample was placed into a wire basket and weighed while submerged in water to obtain the weight of the sample while in water. The sample was then dried to constant mass in the oven at 230 °F and the weight of the dry sample was recorded. The oven-dry specific gravity, G_s (OD), the saturated-surface-dry specific gravity, G_s (SSD), and the apparent specific gravity, G_s (Apparent), were then calculated. Absorption was also calculated from these measurements.

3.4.4 Sodium Sulfate Soundness Test

The sodium sulfate soundness test was used as a measure of the long-term durability of aggregates. For this test, each sample was divided into seven specimens. The test consisted of five cycles and each cycle was performed in two stages: first placing and soaking the specimen in a container of sodium sulfate solution and then oven-drying the specimen to constant mass.

The sodium sulfate solution was prepared by mixing 215 g of anhydrous salt (sodium sulfate) with one L of distilled water. The solution was mixed using a mixing attachment connected to a power drill and then left to settle for a minimum of 48 hours. The specific gravity of the solution was measured and checked to ensure that it fell between 1.151 and 1.174.

The aggregate samples were then sub-divided by using the following sieves: $\frac{3}{4}$ in, $\frac{1}{2}$ in, $\frac{3}{8}$ in, No. 4, No. 8, No. 16, No. 30, and No. 50. The coarse aggregate specimens were divided up into the following two fractions: passing the $\frac{3}{4}$ in sieve retained on the $\frac{3}{8}$ in sieve and passing the $\frac{3}{8}$ in sieve retained on the No. 4 sieve. The coarse aggregate specimens had masses of 1,000 and 330 g, respectively. As a note, the specimen passing the $\frac{3}{4}$ in sieve retained on the $\frac{3}{8}$ in sieve consisted of two fractions: 700 g retained on the $\frac{1}{2}$ in sieve (placed between the $\frac{3}{4}$ in and $\frac{3}{8}$ in sieves) and 300 g retained on the $\frac{3}{8}$ in sieve. The fine aggregate specimens were divided up into the following five fractions: passing the $\frac{3}{8}$ in sieve and retained on No. 4 sieve, passing No. 4 sieve and retained on No. 8 sieve, passing No. 8 sieve retained on No. 16 sieve, passing No. 16 sieve retained on No. 30 sieve, and passing No. 30 sieve retained on No. 50 sieve. Each had a mass of approximately 100 g.

Next, the specimens were placed into small plastic containers of sodium sulfate solution, which provided at least half an inch of cover, and lids were used to close the containers (shown

Figure 3.10 a and b). The specimens were kept in the solution for 16 to 18 hours. Afterwards, the specimens were taken out of the solution and drained for five to ten minutes over a sieve with smaller openings to preserve the specimen. Then, the specimens were placed into the oven at 230 °F and dried to constant mass. Oven-drying the specimens to constant mass took approximately four to six hours. Finally, each specimen was sieved over the designated sieve in order to determine the mass at the end of the cycle. This part is not part of the standard test procedure but was performed by the research team to investigate the amount of material loss per cycle, which could provide useful information about the in-service degradation and remaining quality of the aggregates. The process of immersing, draining, oven-drying, and sieving was repeated over a span of five cycles. After the fifth and final cycle was completed, the final masses of the specimens were recorded and used to calculate the final loss percentages.

3.4.5 Micro-Deval Abrasion Test

The Micro-Deval abrasion test measures the resistance of aggregates to abrasion. As a brief overview of the test, a specimen is placed into a container that also includes stainless steel balls and water. The container is placed into the Micro-Deval apparatus and revolved to produce an abrasive charge (shown in Figure 3.10 c, d, e, and f). Because of the impact of the abrasive charge, the sample degrades. Water is used in the test because many aggregates are more susceptible to abrasion when wet than dry. The Micro-Deval abrasion test was run on both coarse aggregates and fine aggregates. The steps for the Micro-Deval abrasion test are explained for the coarse aggregate specimens. The steps for the fine aggregate specimens are the same except that the sieve sizes and masses retained, volume of water, mass of the steel balls, and number of revolutions are different from those used for coarse aggregates.

The coarse aggregate specimens consisted of the following fractions: 375 g passing the $\frac{3}{4}$ in sieve retained on the $\frac{5}{8}$ in sieve, 375 g passing the $\frac{5}{8}$ in sieve retained on the $\frac{1}{2}$ in sieve, and 750 g passing the $\frac{1}{2}$ in sieve retained on the $\frac{5}{8}$ in sieve. For a few of the coarse aggregate specimens, the following gradation was used: 750 g passing the $\frac{1}{2}$ in sieve retained on the $\frac{3}{8}$ in sieve, 375 g passing the $\frac{3}{8}$ in sieve retained on the $\frac{1}{4}$ in sieve, and 750 g passing the $\frac{1}{4}$ in sieve retained on the No. 4 sieve. The initial weight of the coarse specimens was 1,500 g. For each test, the specimen was placed into the Micro-Deval container and 2 L of water was added to the container. The specimen was immersed in water for at least one hour. Then 5 kg of steel balls were added to the container. The container was then placed into the Micro-Deval apparatus. The apparatus had a revolution counter, so the number of revolutions was set to 12,000 revolutions (10,500 revolutions for the alternate gradation). The container revolved at a rate of 100 revolutions per minute for two hours and then the container was taken out of the apparatus once the revolutions were completed. The specimen was then poured out of the container over a No. 4 sieve superimposed onto a No. 16 sieve and the specimen was washed over the sieves. Then the steel balls were removed with a magnet. Next, the sample was oven dried at a temperature of 230

°F for 24 hours. The sample was weighed afterwards and the final mass was recorded. The percent loss was then calculated using the initial and final masses of the specimen.



(a) Sodium sulfate



(b) Aggregate specimens prepared for sodium sulfate test



(c) Soaking Micro-Deval test specimen



(d) Micro-Deval test container and charge



(e) Loading aggregate and charge



(f) Running Micro-Deval test

Figure 3.10: Aggregate preparation and testing - sodium sulfate and Micro-Deval.

For the fine aggregates, the specimens consisted of the following fractions: 50 g passing the No. 4 sieve retained on the No. 8 sieve, 125 g passing the No. 8 sieve retained on the No. 16

sieve, 125 g passing the No. 16 sieve retained No. 30 sieve, 100 g passing the No. 30 sieve retained on the No. 50 sieve, 75 g passing the No. 50 sieve retained on the No. 100 sieve, and 25 g passing the No. 100 sieve retained on the No. 200 sieve. The initial mass of the fine aggregate specimens was 500 g. For each test, the specimen was placed into the Micro-Deval container and 0.75 L of water was added to the container. The specimen was immersed in water for at least one hour. Then, 1.2 kg of steel balls were added to the container. The container was subsequently placed into the Micro-Deval apparatus. The number of revolutions was set to 1,500. The container revolved at a rate of 100 revolutions per minute (RPM) for 15 minutes and then the container was taken out of the apparatus once the revolutions were completed. The specimen was then poured out of the container over a No. 4 sieve superimposed onto a No. 200 sieve and the specimen was washed over the sieves. Then the steel balls were removed with a magnet. Next, the sample was oven dried at a temperature of 230 °F for 24 hours. The sample was weighed afterwards and the final mass was recorded. The percent loss was then calculated by using the same equation that was used to determine the percent loss of the coarse aggregate specimen.

3.4.6 California Bearing Ratio

The California Bearing Ratio test is one way of evaluating the strength of base course aggregates. The equipment used for the CBR test included a CBR mold, perforated base plate, spacer disk, filter paper, a large container of water, and a loading machine. Samples of base-course aggregate were prepared in a similar manner as they were for the standard compaction test. As was done for compaction, the samples were sieved over a $\frac{3}{4}$ in sieve and the material retained on the sieve was replaced with material passing the $\frac{3}{4}$ in sieve retained on the No. 4 sieve. The samples were prepared at optimum moisture content.

For each test, the CBR mold (with an inside diameter of 6 in and a height of 7 in) was weighed and the mass was recorded. The spacer disk was placed onto the base plate and the CBR mold was placed over it. A sheet of filter paper was placed on the spacer disk. Then, the sample was prepared in the same manner as it was for compaction except that 76 blows were applied to each layer. After compaction, the mold and the sample were weighed together. The mold with the sample inside was then flipped upside down and placed back onto the base plate. Two surcharge weights weighing 10 lbs in total were placed on top of the specimen. Then the sample was fully submerged in a container of water for 96 hours so that the sample would be tested while it was in its weakest condition (as shown in Figure 3.11). After 96 hours passed, the sample was removed from the water container. The free water on the top was removed and the sample was allowed to drain for at least 15 minutes. Afterwards, the sample was placed onto the loading machine and a piston was attached to the load frame. Bluehill software was used to run the test. The piston was lowered through the circular hole in the surcharge weights and seated onto the top of the specimen. The load was then applied at a rate of 0.05 in/min and the load values were recorded by the software, ensuring that the load values at the necessary penetration depths were obtained.

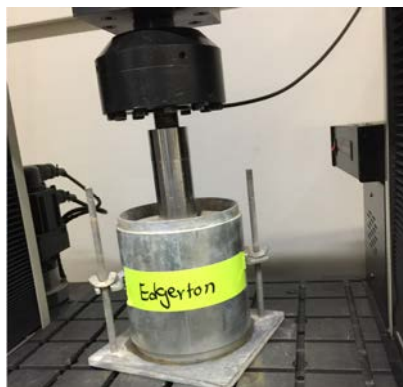
After the load and penetration data were collected, the load was divided by the cross-sectional area of the piston (3 in^2) to calculate the stress on the piston. The penetration depth was plotted against the stress to get the curve that was needed to determine the CBR value. The first step in determining the CBR value was to make a correction to the CBR curve if necessary. The correction was made by drawing a line over the linear portion of the CBR curve until it hit the x-axis (penetration). The x-intercept was used as a reference point. For the penetration located at 0.1 in from the reference point, the corresponding stress was determined. Once the stress was determined, the CBR value (expressed in terms of percent) was calculated by dividing the stress determined at 0.1 in from the reference point by the standard stress of 1,000 psi and multiplying that value by 100.



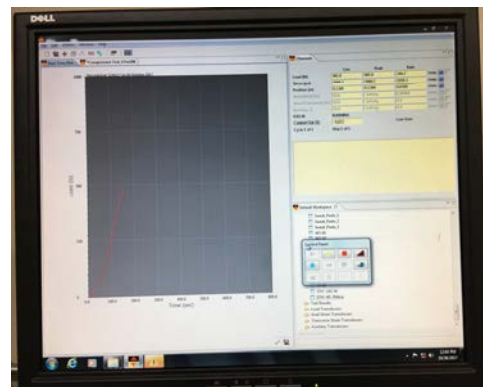
(a) Compacting samples



(b) Soaking CBR test specimen



(c) CBR test



(d) CBR plots

Figure 3.11: Specimen preparation and testing for standard compaction and CBR tests.

3.4.7 Repeated Load Triaxial Test

The repeated load triaxial test was conducted to determine the resilient modulus of the investigated aggregates according to AASHTO T 307: Standard Method of Test for Determining the Resilient Modulus of Soils and Aggregate Materials. The test was conducted on compacted

aggregate specimens that were prepared in accordance with the procedure described by AASHTO T 307.

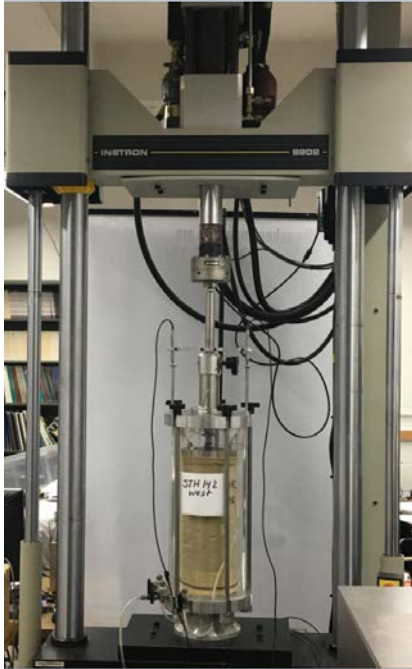
Dynamic Test System for Materials

The repeated load triaxial test was conducted using the Instron FastTrack 8802 closed loop servo-hydraulic dynamic material test system at UWM. The system utilizes an 8800 Controller with four control channels of 19-bit resolution and data acquisition. A computer with FastTrack Console is the main user interface. This is a fully digitally controlled system with adaptive control that allows continuous updating of PID terms at 1 kHz, which automatically compensates for the specimen stiffness during repeated load testing. The loading frame capacity of the system is 250 kN (56 kip) with a series 3690 actuator that has a stroke of 150 mm (6 in) and with a load capacity of 250 kN (56 kip). The system has two dynamic load cells with 1 and 5 kN (0.22 and 1.1 kip) load capacity for measurement of the repeated applied load. The load cells include an integral accelerometer to remove the effect of dynamic loading on the moving load cell. Figure 3.12 depicts pictures of the dynamic material test system used in this study.

Specimen Preparation

Compacted aggregate specimens were prepared in 6 in diameter mold to produce a 12 in high aggregate specimen under the maximum dry unit weight and optimum moisture content. The amounts of dry aggregate and mixing water corresponding to γ_{dmax} and w_{opt} for each source were measured. After mixing, the aggregates were compacted in the mold in five lifts using a standard compaction hammer. The amount of aggregate needed to fill a volume of one fifth of the mold was compacted in each lift. This compaction method provided uniformly compacted lifts while using the same weight of aggregate for each lift. Figure 3.13 depicts pictures of the molds used to prepare aggregate specimens and pictures of the specimen preparation procedure.

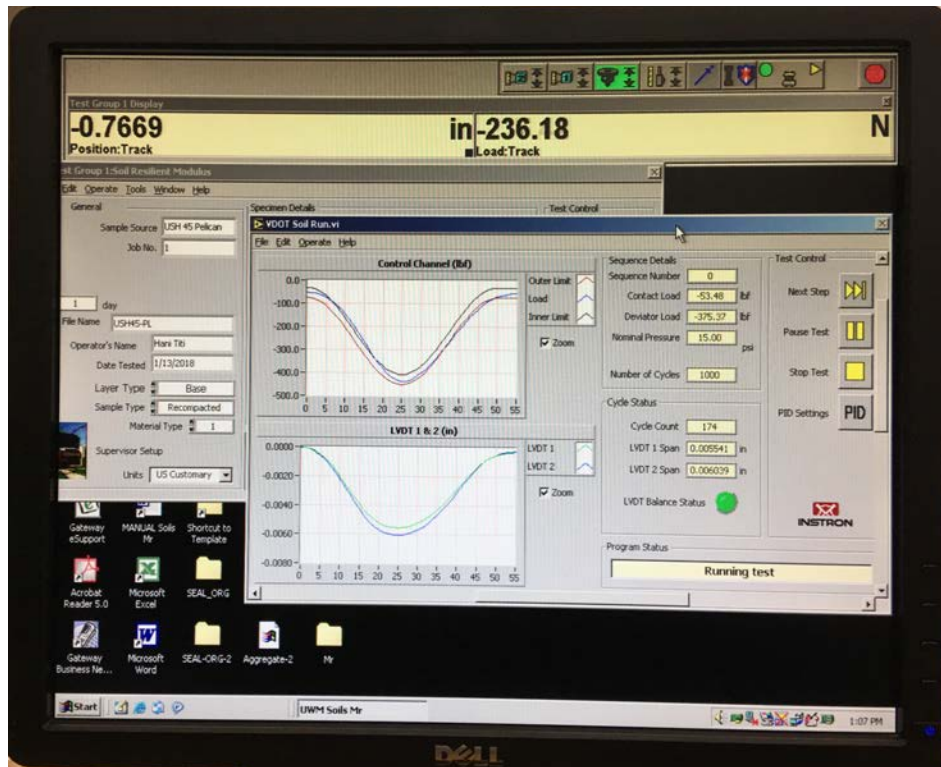
For each aggregate, after specimen was prepared under γ_{dmax} and w_{opt} , it was placed in a membrane and mounted on the base of the triaxial cell. Porous stones were placed at the top and bottom of the specimen with filter paper for separation between the specimen and the porous stones. The triaxial cell was sealed and mounted on the base of the dynamic material test system frame. All connections were tightened and checked. Cell pressure, LVTDs, load cell, and all other required setup components were connected and checked.



(a) Instron FastTrack 8802 closed loop servo-hydraulic dynamic material test system



(b) 6 in diameter triaxial cell



(c) Resilient modulus software

Figure 3.12: Repeated load triaxial test conducted using Instron 8802 dynamic material test system to determine resilient modulus of soils.



(a) Mechanical mixer



(b) Mixing Aggregate



(c) 6 in \times 12 in mold



(d) Compacting aggregate



(e) 6 in \times 12 in specimen



(f) 6 in \times 12 in specimen



(g) Specimen in triaxial cell



(h) Specimen on testing system



(i) Testing aggregate specimen

Figure 3.13: Preparation and testing of base aggregate specimens for repeated load triaxial test according to AASHTO T 307 standard procedure.

Specimen Testing

The software of the material dynamic test system was programmed to apply repeated loads according to the test sequences specified by AASHTO T 307 as depicted in Table 3.5. Once the triaxial cell was mounted on the system, the air pressure panel was connected to the cell and the required confining pressure (σ_c) was applied. Figure 3.12 c shows pictures of the software used to control and run the repeated load triaxial test.

For each test, the aggregate specimen was conditioned by applying 1,000 repetitions of a deviator stress σ_d of 13.5 psi at a confining pressure σ_c of 15 psi. Conditioning eliminates the effects of specimen disturbance from compaction and specimen preparation procedures and minimizes the imperfect contacts between end platens and the specimen. The specimen was then subjected to different deviator stress sequences. The stress sequence is selected to cover the expected in-service range that a pavement or subgrade material experiences because of traffic loading.

Table 3.5: Testing sequences for base/subbase materials (AASHTO T 307 – 99 (2017)).

Sequence No.	Confining Pressure, S_3		Max. Axial Stress, S_{max}		Cyclic Stress, S_{cyclic}		Constant Stress, $0.1S_{max}$		No. of Load Applications
	kPa	psi	kPa	psi	kPa	psi	kPa	psi	
0	103.4	15	103.4	15	93.1	13.5	10.3	1.5	500–1000
1	20.7	3	20.7	3	18.6	2.7	2.1	0.3	100
2	20.7	3	41.4	6	37.3	5.4	4.1	0.6	100
3	20.7	3	62.1	9	55.9	8.1	6.2	0.9	100
4	34.5	5	34.5	5	31.0	4.5	3.5	0.5	100
5	34.5	5	68.9	10	62.0	9.0	6.9	1.0	100
6	34.5	5	103.4	15	93.1	13.5	10.3	1.5	100
7	68.9	10	68.9	10	62.0	9.0	6.9	1.0	100
8	68.9	10	137.9	20	124.1	18.0	13.8	2.0	100
9	68.9	10	206.8	30	186.1	27.0	20.7	3.0	100
10	103.4	15	68.9	10	62.0	9.0	6.9	1.0	100
11	103.4	15	103.4	15	93.1	13.5	10.3	1.5	100
12	103.4	15	206.8	30	186.1	27.0	20.7	3.0	100
13	137.9	20	103.4	15	93.1	13.5	10.3	1.5	100
14	137.9	20	137.9	20	124.1	18.0	13.8	2.0	100
15	137.9	20	275.8	40	248.2	36.0	27.6	4.0	100

It is very difficult to apply the exact specified loading on aggregate specimens in a repeated load (dynamic load) configuration. This is in part due to the controls of the equipment and aggregate specimen stiffness. However, the closed-loop servo hydraulic system is one of the most accurate systems used to apply repeated loads. In this system, the applied loads and measured displacements are continuously monitored as depicted in Figure 3.12 c. This is to make sure that the applied loads are within acceptable tolerance. If there is out of range applied loads or measured displacements, then the system will display warning messages and can be programmed to terminate the test.

Chapter 4

Analysis of Laboratory Test Results on Base Aggregate Materials

This chapter presents the results of the laboratory testing program on the base layer aggregate materials collected from the investigated pavement sections. Laboratory test results are analyzed and critically evaluated.

4.1 Particle Size Distribution

Figure 4.1 depicts the particle size distribution of the investigated base aggregates as well as the historical WisDOT base course layer specifications, including the current lower and upper WisDOT specifications for the particle size distribution of 1¼ in dense graded base course aggregate layers (Section 305.2.2.1 of WisDOT Standard Specifications for Highway and Structure Construction, 2108).

Visual examination of Figure 4.1 shows that the particle size distributions of the aggregate samples are generally within WisDOT specification limits, but partly cross the lower limit boundary towards the fine aggregate fraction. The percentages of materials finer than 75 µm (No. 200 sieve), the observed maximum particle size, and the Atterberg limits (LL, PL, and PI) of the base aggregate fraction finer than 0.425 mm (No. 40 sieve) are summarized in Table 4.1. Inspection of the particle size distribution data shows that eight base aggregate samples possessed percent of fines (< 75 µm) greater than corresponding WisDOT specification limits at the time of base layer construction. Base aggregate samples from Edgerton Avenue and STH 142 E near Burlington possessed the highest percentages of fines with 34.1 and 28.0%, respectively. In total, 16 base aggregate specimens possessed particle size distributions that exceeded the corresponding WisDOT specification limits; however, the majority of these specimens only slightly exceeded the specification limits.

Base aggregate materials could experience durability issues such as particle size reduction (degradation) as a result of disintegration and degradation due to factors such as heavy loads and freeze/thaw cycles. Degradation and disintegration is more significant when the aggregate material quality is poor. The impact of freeze/thaw and traffic loads on the base aggregate degradation depends, to a significant extent, on the quality, composition, and properties of the base aggregate particles (such as particle shape, absorption, composition, etc.). In four base aggregate samples, the maximum particle size was larger than 1.25 in (as depicted in Figure 4.2). It may not be possible to draw conclusions regarding base aggregate degradation and disintegration based only on particle size analysis.

In order to further evaluate the aggregate gradation, the fineness modulus (FM) was calculated according to ASTM C125: Standard Terminology Relating to Concrete and Concrete

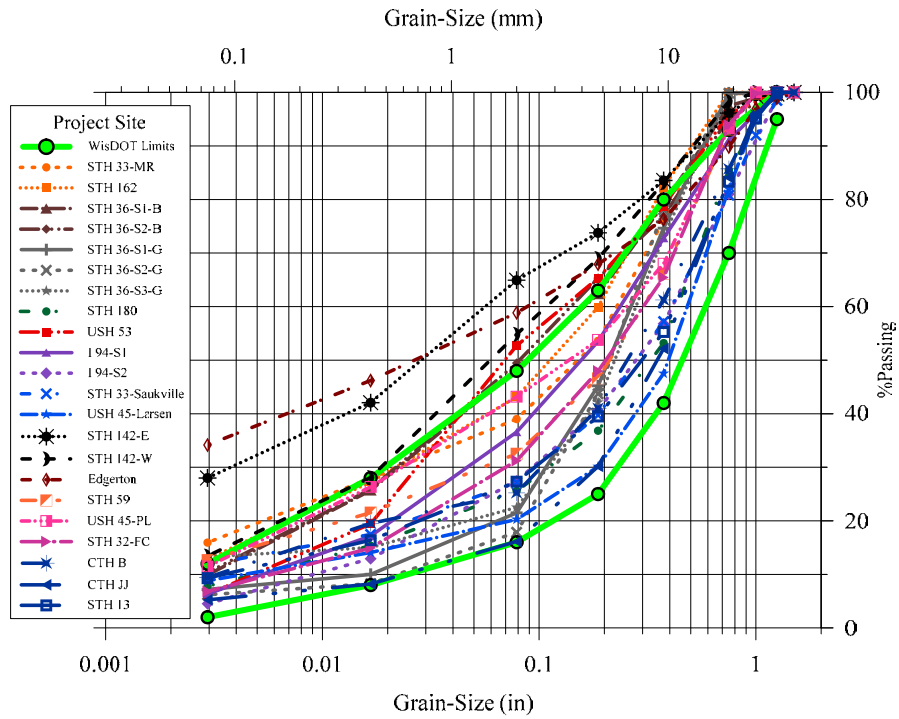
Aggregates. The FM is obtained by adding the percentages of material in the aggregate sample that is coarser than each of the following sieves (cumulative percentages retained) and dividing the sum by 100: No. 100, No. 50, No. 30, No. 16, No. 8, No. 4, $\frac{3}{8}$ in, $\frac{3}{4}$ in, $1\frac{1}{2}$ in, 3 in, and 6 in. The larger the FM, the coarser the aggregate is. Table 4.2 presents the fractions of gravel, sand, and fines and the FM of the investigated aggregates. The results are also depicted in Figure 4.3. Inspection of the data presented shows that aggregates from STH 162 MR, STH 36 S#1 and S#2 (the brown aggregate), STH 142E, STH 142W, and Edgerton Ave exhibited FM values that were less than or equal to 3.96, which corresponds to the current WisDOT gradation lower limit. In addition, all these aggregates possessed a sand fraction greater than the gravel fraction. Base aggregates from USH 53, USH 45 PL, and STH 33 MR can also be considered among the aggregates with high amounts of fine aggregates (sand and fines fractions) according the FM values, which brings the total number of aggregates samples to nine.

Another way to evaluate the base aggregate particle size distribution is by using the Grading Number (GN), which is an index introduced to represent the effect of gradation on DCP test results (Dai and Kremer, 2006). The GN concept is derived from the FM but it uses the percent passing rather than the percent retained. The GN is calculated by:

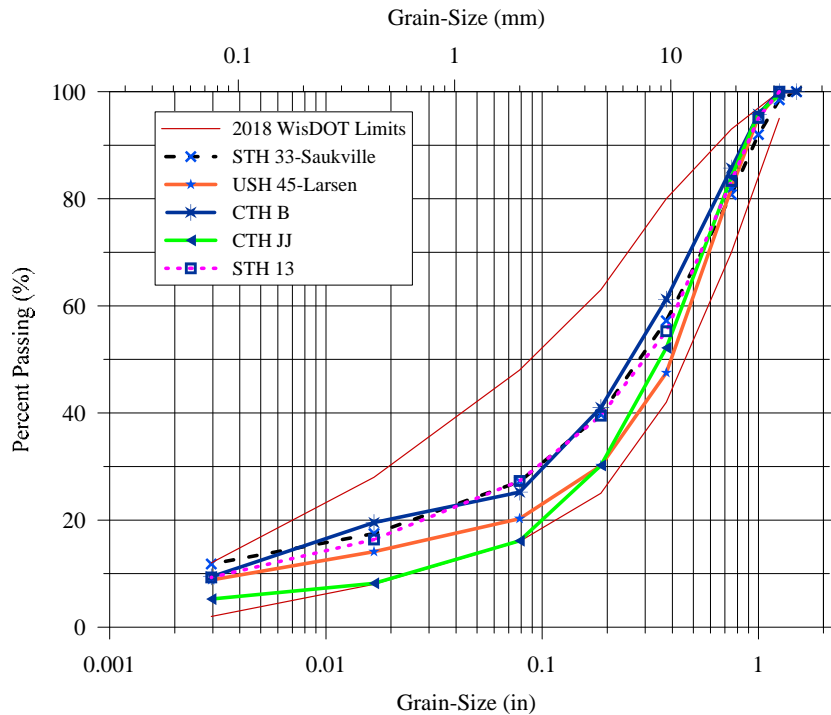
$$GN = \frac{\text{Percent Passing Sieve}(25\text{mm} + 19\text{mm} + 9.5\text{mm} + 4.75\text{mm} + 2.00\text{mm} + 425\mu\text{m} + 75\mu\text{m})}{100}$$

The maximum value of GN is 7 when 100% of the material passes the sieve No. 200. This represents an extremely fine material (all silt and clay particles). On the other hand, the minimum value of GN is 0 when 0% of the material passes the largest sieve. This indicates a very coarse material. The calculated GNs for the investigated aggregates are presented in Table 4.2 and Figure 4.3. The nine base aggregates described earlier with low FM values possess the highest GN values (approximately greater than or equal to 4.2) which consistently indicates finer materials.

Atterberg limits test results of the base aggregate fraction finer than the No. 40 sieve indicated that the majority of the investigated samples were non-plastic. These results are important with respect to pumping or infiltration of fines from subgrade soils to base course layers. Figure 4.4 shows pictures of the base aggregate samples as well as the fraction finer than the No. 40 sieve (listed in Table 4.1). Visual inspection, by the research team, of the fines from the base aggregates indicated that these fines have the same aggregate material origin for the majority of the inspected samples.

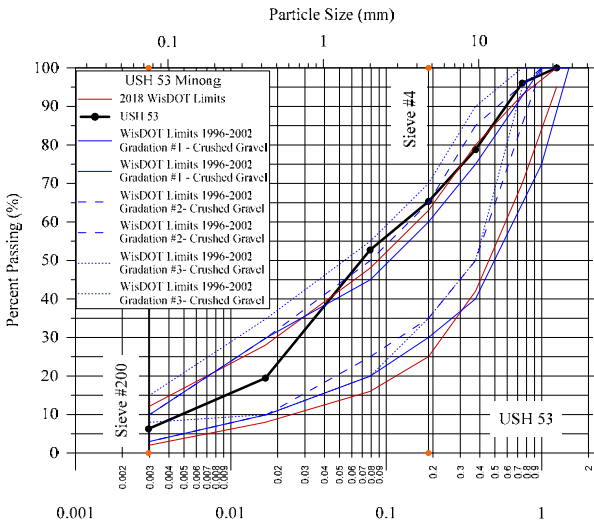


(a) All investigated samples versus 2018 WisDOT gradation specifications

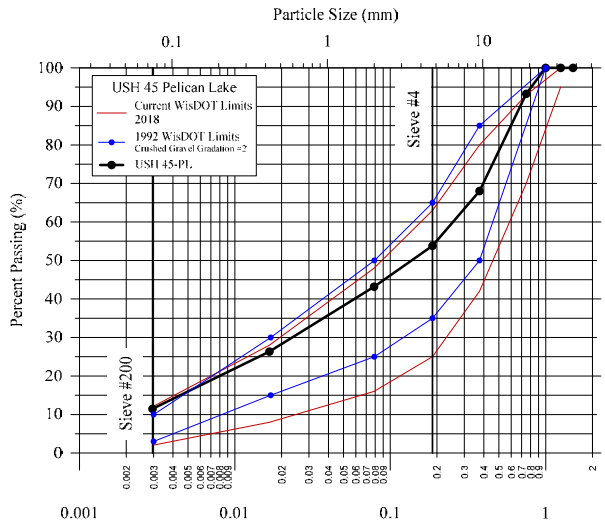


(b) Virgin aggregate samples versus 2018 WisDOT gradation specifications

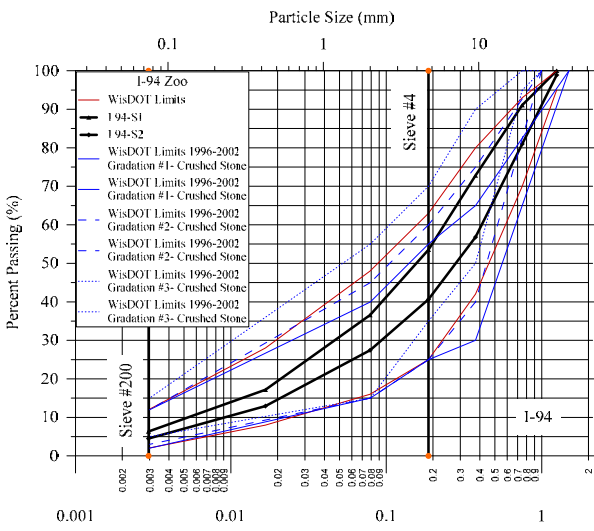
Figure 4.1: Particle size distribution of the investigated base aggregates and the corresponding WisDOT gradation specification limits for base course materials.



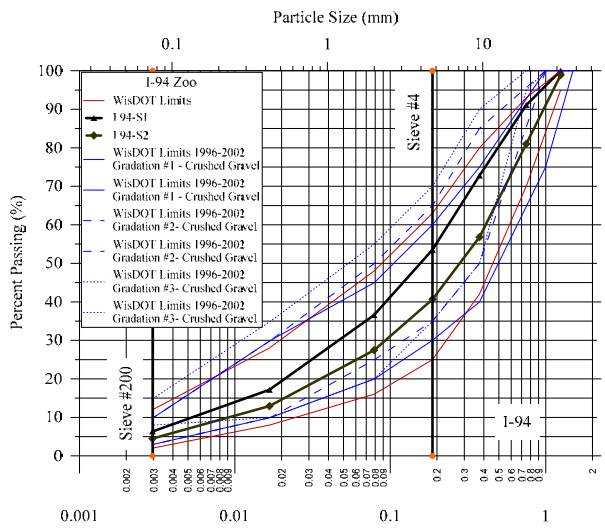
(c) USH 53 Minong and 2000 WisDOT gradation specifications



(d) USH 45 Pelican Lake and 1992 WisDOT gradation specifications

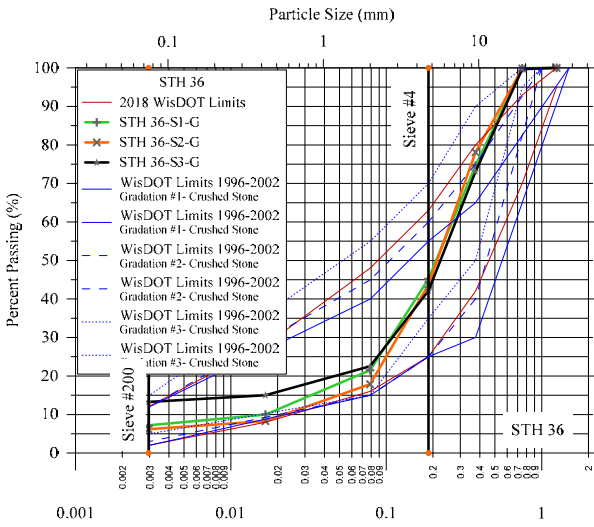


(e) I-94 Zoo and 1997 WisDOT crushed stone gradation specifications

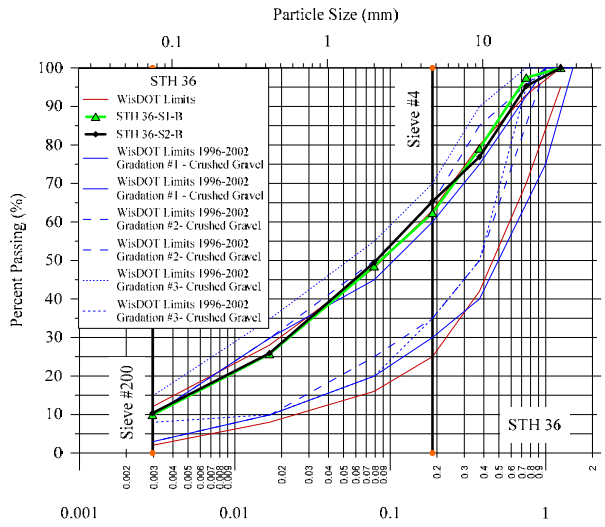


(f) I-94 Zoo and 1997 WisDOT crushed gravel gradation specifications

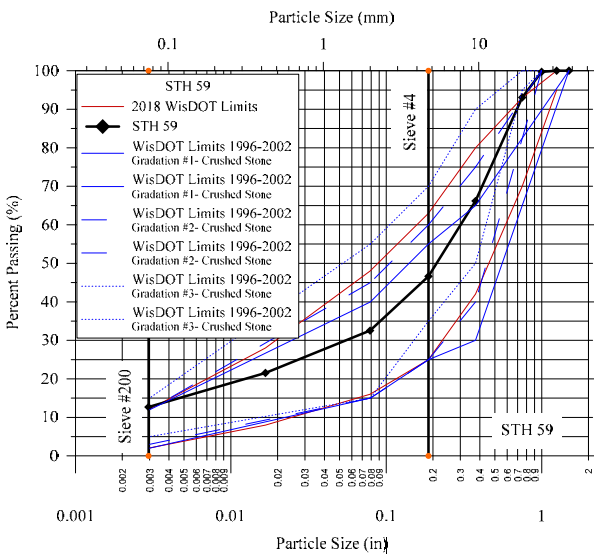
Figure 4.1 (Cont.): Particle size distribution of the investigated base aggregates and the corresponding WisDOT gradation specification limits for base course materials.



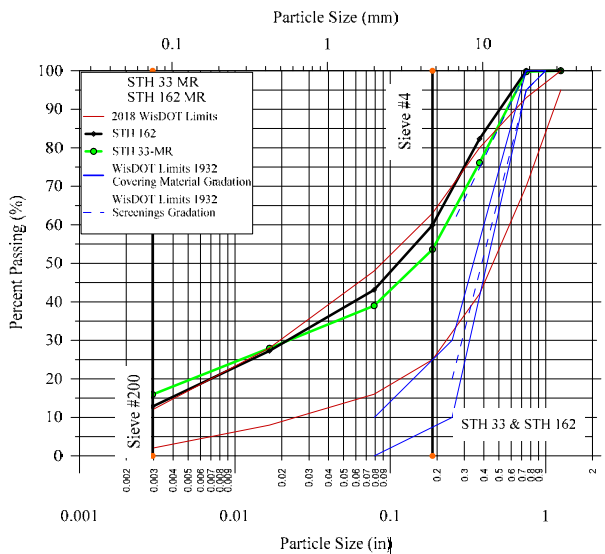
(g) STH 36 and 1999 WisDOT crushed stone gradation specifications



(h) STH 36 and 1999 WisDOT crushed gravel gradation specifications

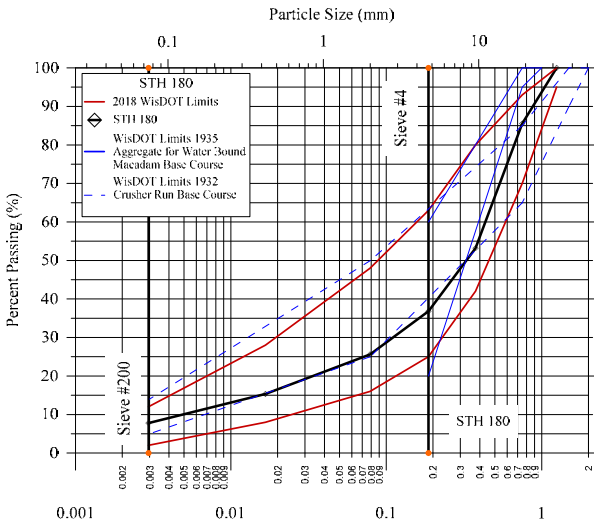


(i) STH 59 and 1999 WisDOT crushed stone gradation specifications

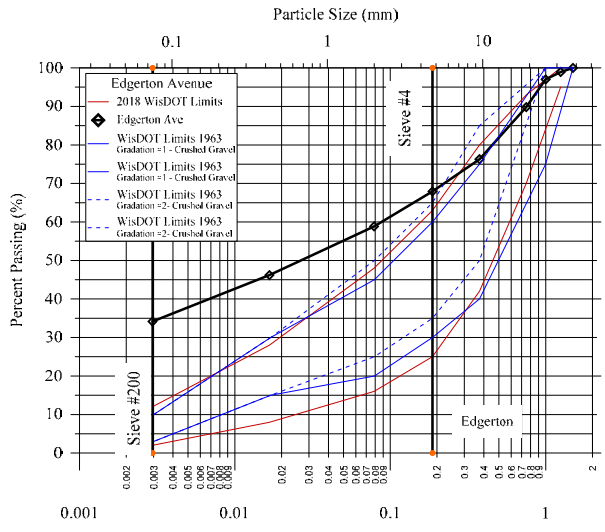


(j) STH 162, STH 33, and 1932 WisDOT gradation specifications

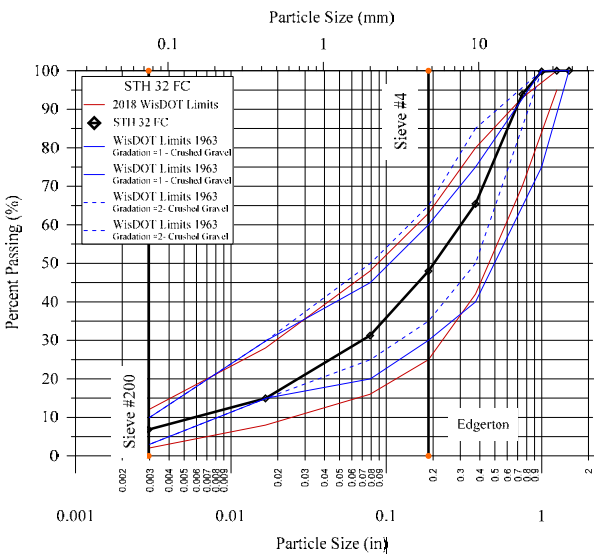
Figure 4.1 (Cont.): Particle size distribution of the investigated base aggregates and the corresponding WisDOT gradation specification limits for base course materials.



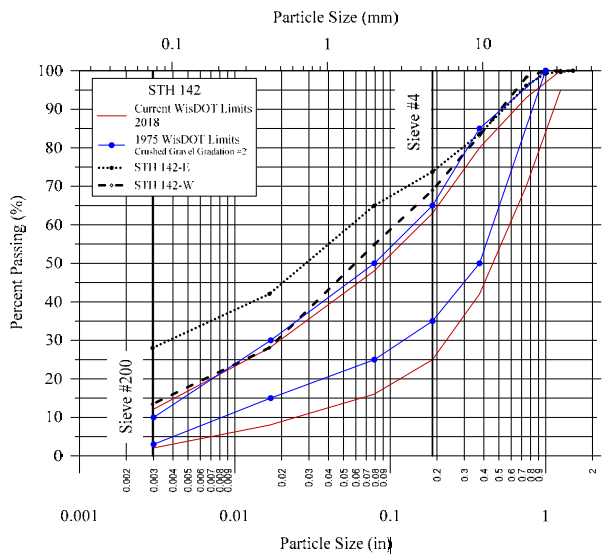
(k) STH 180 and 1935 WisDOT gradation specifications



(l) Edgerton and 1963 WisDOT crushed gravel gradation specifications



(m) STH 32 and 1963 WisDOT crushed gravel gradation specifications



(n) STH 142 and 1975 WisDOT crushed gravel gradation specifications

Figure 4.1 (Cont.): Particle size distribution of the investigated base aggregates and the corresponding WisDOT gradation specification limits for base course materials.

In order to further investigate potential pumping and contamination of the base aggregate from subgrade soils, the properties of subgrade soils were obtained from the USDA web soil survey (<https://websoilsurvey.sc.egov.usda.gov/App/HomePage.htm>), soil reports and pavement coring reports available from WisDOT and private consultants, and soil testing by the research team. Figure 4.5 presents a comparison of the percent fines of subgrade soils with percent fines from the investigated aggregates. Most of subgrade soils possessed more significant amounts of

finer compared with base layer aggregates. When pumping occurs, fines/subgrade soil from pavement subgrade would infiltrate into the base layer material and could also be ejected to the surface through pores and cracks. Aggregates from USH 53 and STH 32 FC possessed percent fines that are comparable with subgrade soils. The percent of fines in the base aggregates from Edgerton and STH 142 E are significant and with plasticity index of 3% and 5%, respectively, indicating potential pumping and contamination of base aggregate from subgrade soils. It should be noted that several pavement test sections have subbase layers of large stone (select materials and breaker run) that could represent a barrier/boundary and may reduce the amount of subgrade fines infiltrating into the base course layers. Examples are pavements at STH 13 Spencer, STH 59 Edgerton, and CTH JJ Appleton. A detailed description of subgrade soils including classification, as obtained from the USDA web soil surveys, are presented in Appendix A.

Table 4.1: Particle size and plasticity characteristics of the investigated base aggregates.

Aggregate Source	Percent Fines (Passing Sieve No. 200)	Maximum Particle Size Observed, D _{max} (in)	WisDOT Base Course Gradation (1932-2018)		Atterberg Limits		
			Exceeding Limits	Within Limits	Liquid Limit (LL) (%)	Plastic Limit (PL) (%)	Plastic Index (PI) (%)
STH 33 – Middle Ridge	15.9	1	✓		NP	NP	NP
STH 162 – Middle Ridge	12.8	0.75	✓		N/A	N/A	N/A
STH 36 (S#1-B) – Waterford	9.9	1	✓		NP	NP	NP
STH 36 (S#2-B) – Waterford	10.4	1	✓		NP	NP	NP
STH 36 (S#1-G) – Waterford	7.2	1	✓		NP	NP	NP
STH 36 (S#2-G) – Waterford	6.2	1	✓		NP	NP	NP
STH 36 (S#3-G) – Waterford	13.3	1	✓		NP	NP	NP
STH 180 – Marinette	7.8	1	✓		NP	NP	NP
USH 53 – Minong	6.3	1	✓ (No. 1 & 2)	✓ (No. 3)	NP	NP	NP
Zoo-Site #1 – Milwaukee	6.3	1	✓ (No. 2 & 3)	✓ (No. 1)	NP	NP	NP
Zoo-Site #2 – Milwaukee	4.5	1.25	✓ (No. 2 & 3)	✓ (No. 1)	NP	NP	NP
STH 18 – Jefferson	7.0	2		✓	N/A	N/A	N/A
STH 33 – Saukville	11.8	1.25		✓	NP	NP	NP
USH 45 – Larsen	8.8	1.25		✓	NP	NP	NP
STH 142 East – Burlington	28.0	3	✓		20	15	5
STH 142 West – Burlington	13.4	3	✓		NP	NP	NP
Edgerton Ave – Greenfield	34.1	1.5	✓		18	15	3
STH 59 – Edgerton	12.7	1	✓		NP	NP	NP
USH 45 – Pelican Lake	11.5	1	✓		NP	NP	NP
STH 32 – Forest County	6.8	1		✓	18	17	1
CTH B – Woodville	9.4	1.25		✓	N/A	N/A	N/A
CTH JJ – Appleton	5.3	1.25		✓	N/A	N/A	N/A
STH 13 – Spencer	9.3	1.25		✓	N/A	N/A	N/A

NP: non-plastic



(a) Edgerton Avenue



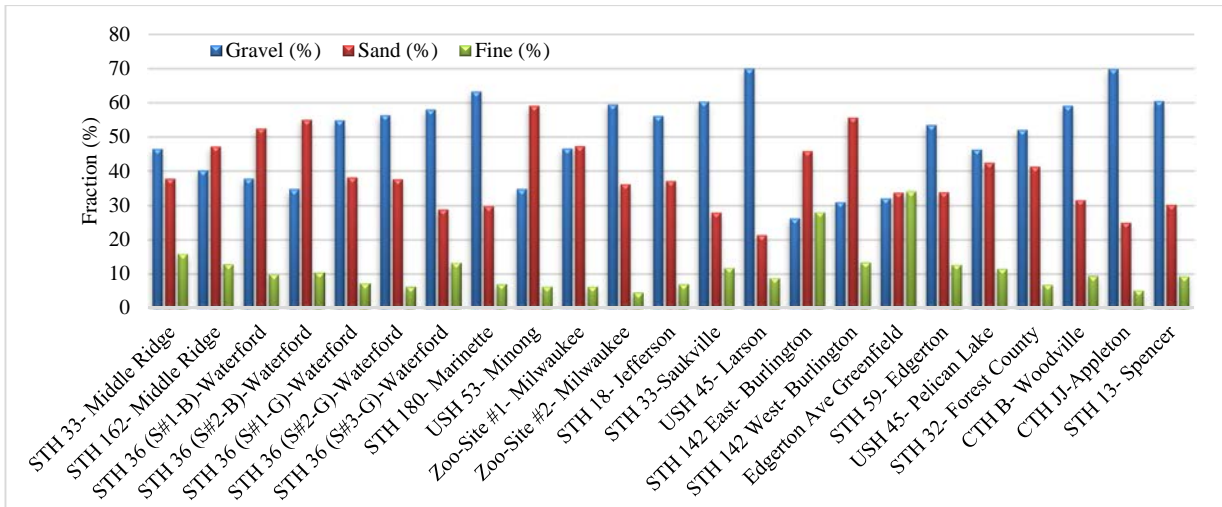
(b) STH 142E Burlington

Figure 4.2: Large stone sized particles found in a number of the investigated base course layers.

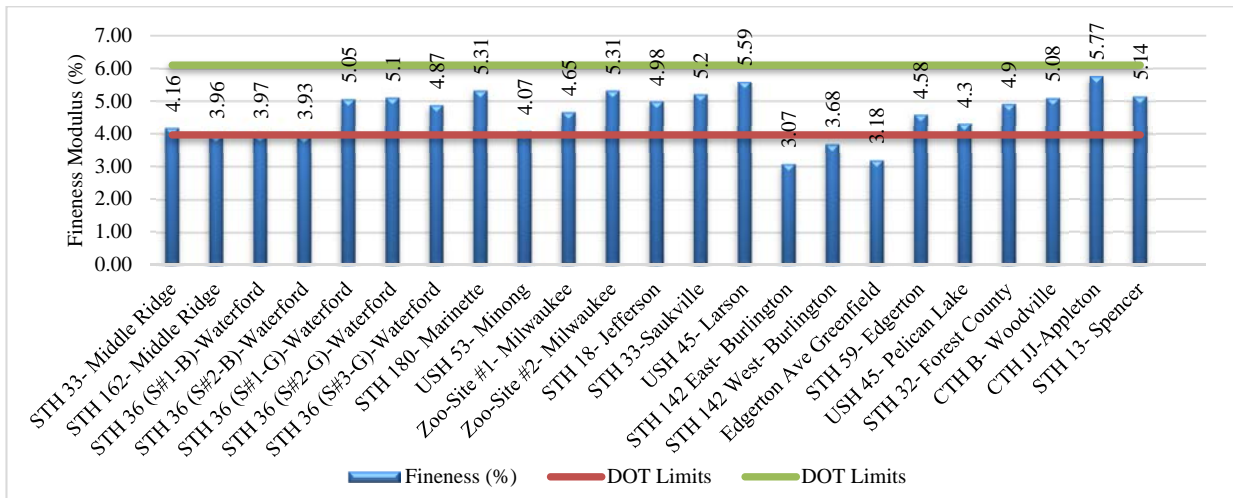
Table 4.2: Particle size characteristics of the investigated base aggregates.

Aggregate Source	Gravel (%)	Sand (%)	Fine (%)	Fineness Modulus	Grading Number
STH 33 – Middle Ridge	46.40	37.70	15.90*	4.16	4.1
STH 162 – Middle Ridge	40.1	47.1	12.8*	3.96	4.3
STH 36 (S#1-B) – Waterford	37.7	52.4	9.9	3.97	4.2
STH 36 (S#2-B) – Waterford	34.7	54.9	10.4	3.93	4.2
STH 36 (S#1-G) – Waterford	54.8	38	7.2	5.05	3.6
STH 36 (S#2-G) – Waterford	56.3	37.5	6.2	5.1	3.5
STH 36 (S#3-G) – Waterford	57.9	28.8	13.3*	4.87	3.7
STH 180 – Marinette	63.2	29.8	7	5.31	3.2
USH 53 – Minong	34.7	59	6.3	4.07	4.2
Zoo-Site #1 – Milwaukee	46.5	47.2	6.3	4.65	3.7
Zoo-Site #2 – Milwaukee	59.4	36.1	4.5	5.31	3.1
STH 18 – Jefferson	56	37	7	4.98	3.3
STH 33 – Saukville	60.3	27.9	11.8	5.2	3.3
USH 45 – Larsen	69.9	21.3	8.8	5.59	3.0
STH 142 East – Burlington	26.2	45.8	28*	3.07	4.9
STH 142 West – Burlington	31	55.6	13.4*	3.68	4.5
Edgerton Ave Greenfield	32.1	33.8	34.1*	3.18	4.7
STH 59 – Edgerton	53.4	33.9	12.7*	4.58	3.7
USH 45 – Pelican Lake	46.2	42.3	11.5*	4.3	4.0
STH 32 – Forest County	52	41.2	6.8	4.9	3.6
CTH B – Woodville	59	31.6	9.4	5.08	3.4
CTH JJ – Appleton	69.8	25	5.2	5.77	2.9
STH 13 – Spencer	60.5	30.2	9.3	5.14	3.3

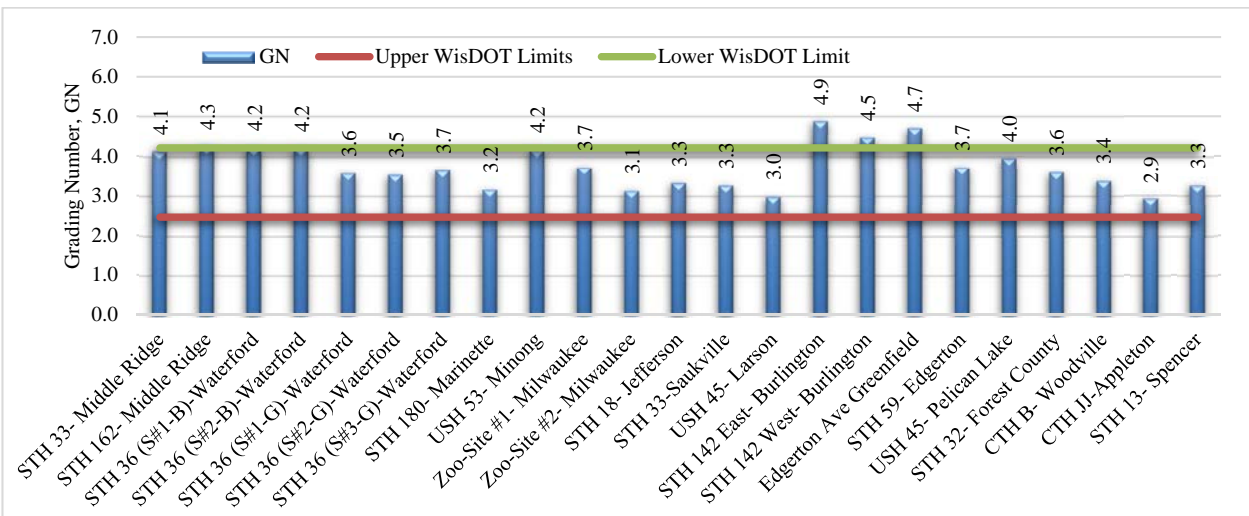
* Percent fines exceed the corresponding WisDOT specification limits (based on the time of base layer construction)



(a) Aggregate fraction composition



(b) Fineness Modulus (FM) of the investigated aggregates (WisDOT limits are 3.96 to 6.1)



(c) Grading Number (GN) of the investigated aggregates (WisDOT limits are 2.5 to 4.2)

Figure 4.3: Particle size characteristics of the investigated aggregates.

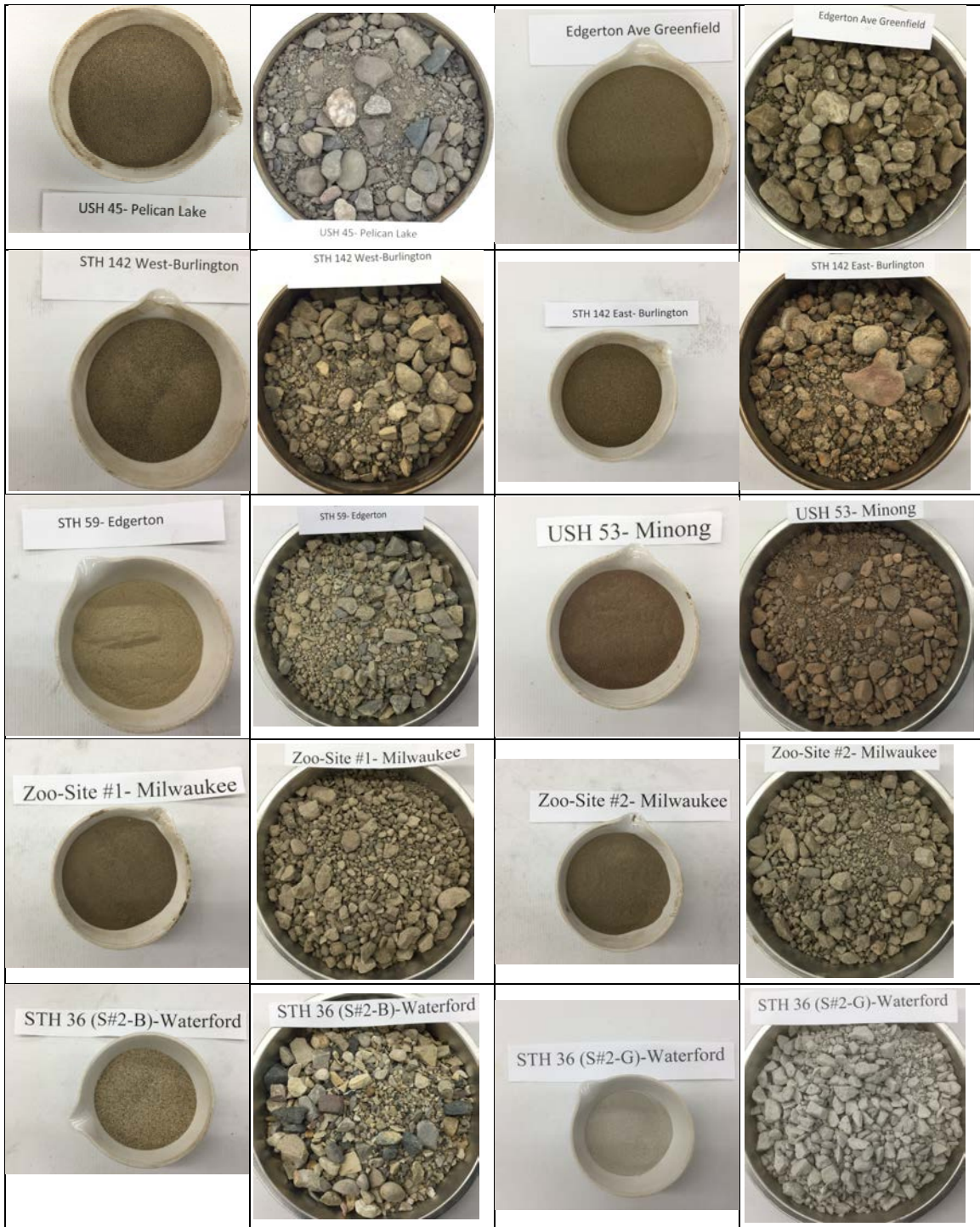


Figure 4.4: Pictures of the investigated base aggregates showing each aggregate sample (right) as used in the base course layer and its fraction finer than 0.425 mm (left).

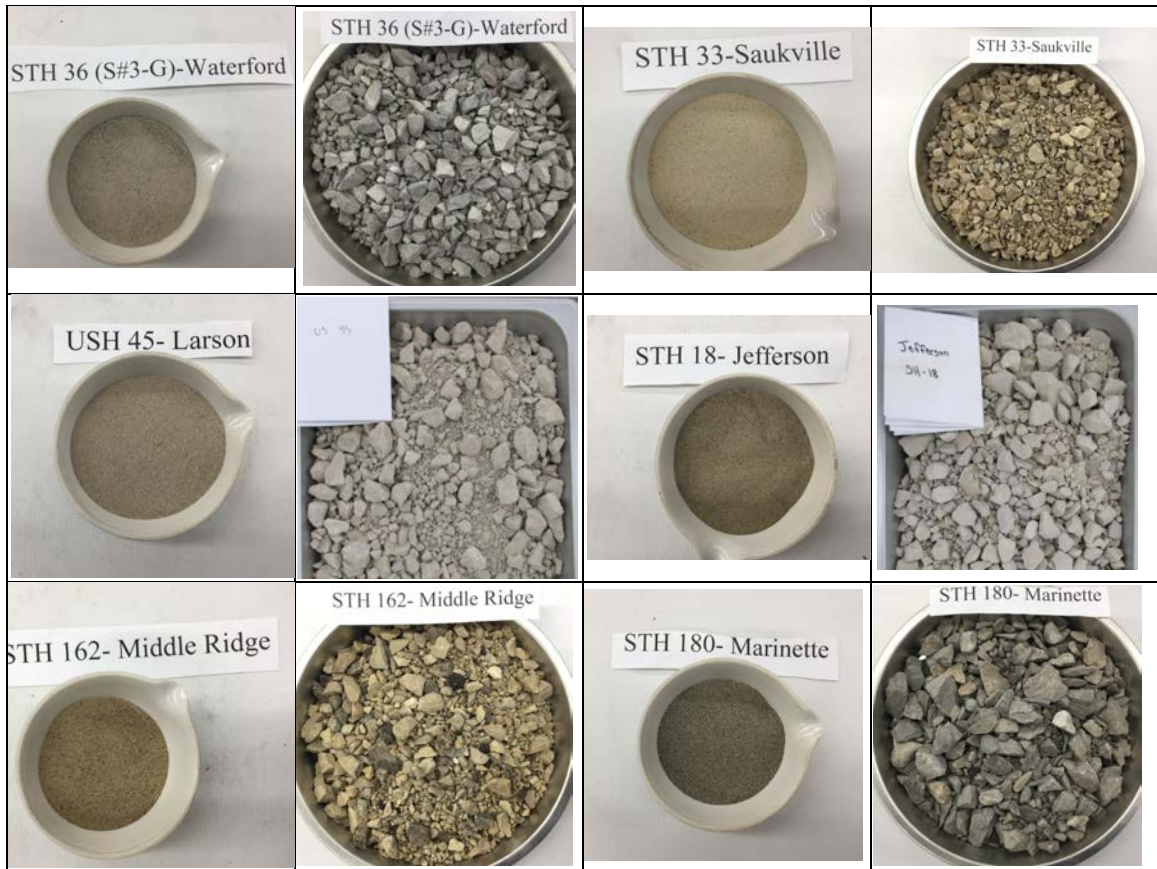


Figure 4.4 (Cont.): Pictures of the investigated base aggregates showing each aggregate sample (right) as used in the base course layer and its fraction finer than 0.425 mm (left).

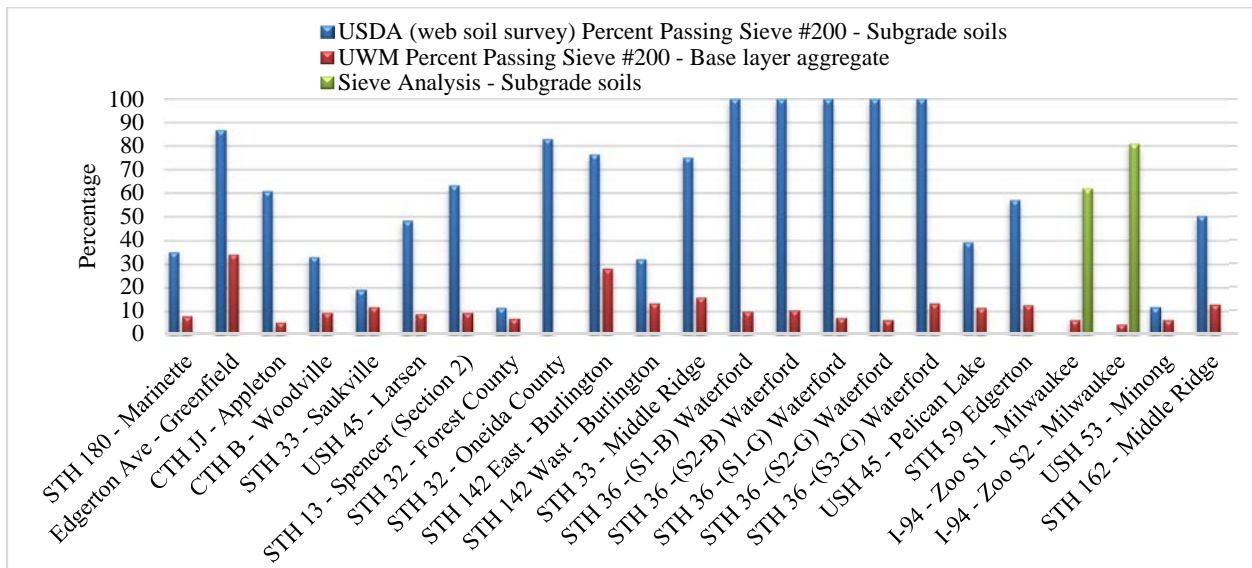


Figure 4.5: Comparison of the amount of fines in subgrade soils with fines found in the corresponding base layer aggregates.

4.2 Durability Tests of the Investigated Aggregates

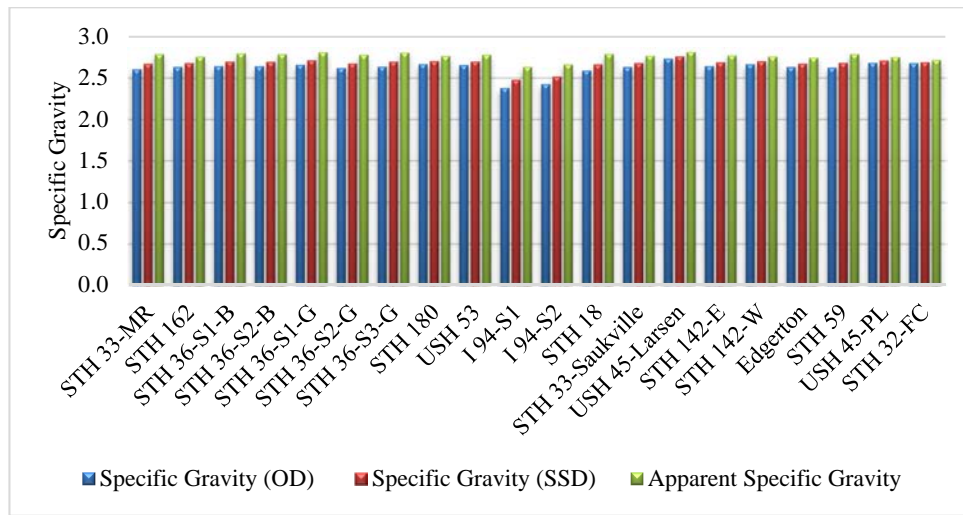
4.2.1 Specific Gravity and Absorption

The oven-dry (OD) specific gravity, saturated-surface dry (SSD) specific gravity, and apparent specific gravity of the coarse aggregate fraction for number of the investigated aggregates are summarized in Table 4.3 and depicted in Figure 4.6. The results of the oven dry specific gravity ranged from 2.38 (for the base aggregate at I 94-S1) to 2.73 (for the base aggregate at USH 45 Larsen). The same aggregate sources exhibited the typical trends. For saturated-surface-dry specific gravity, the values ranged from 2.47 to 2.76 and the apparent specific gravity ranged from 2.63 to 2.81. Tabatabai et al. (2013) conducted an analysis on various Wisconsin coarse aggregates and found the average SSD specific gravity to be 2.66. In general, all aggregates possessed specific gravity values within the range of typical values except the aggregates from the I 94 Zoo Interchange due to the presence of particles from recycled concrete and asphalt pavements.

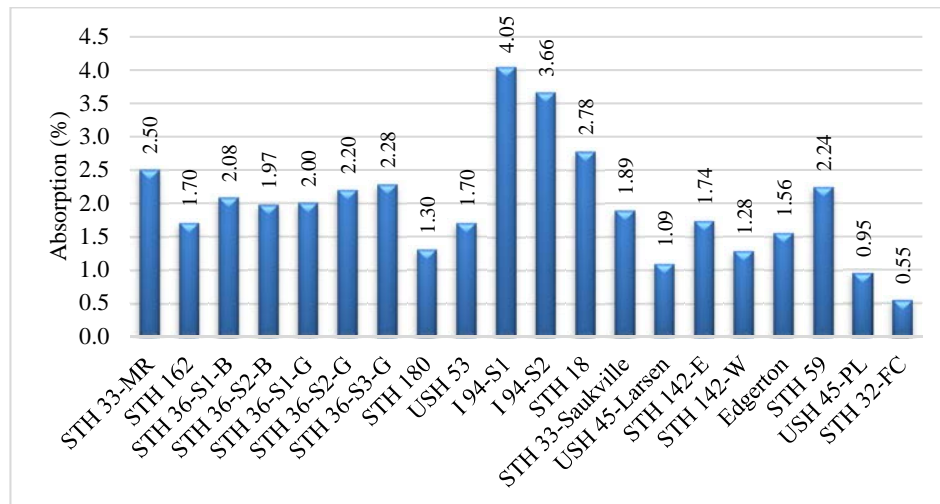
Table 4.3: Results of specific gravity and absorption tests on the investigated base aggregates (coarse fraction).

Aggregate Source	Specific Gravity			Absorption
	OD	SSD	Apparent	
STH 33 – Middle Ridge	2.60	2.67	2.79	2.50
STH 162 – Middle Ridge	2.63	2.68	2.75	1.70
STH 36 (S#1-B) – Waterford	2.64	2.70	2.80	2.08
STH 36 (S#2-B) – Waterford	2.64	2.69	2.79	1.97
STH 36 (S#1-G) – Waterford	2.66	2.71	2.81	2.00
STH 36 (S#2-G) – Waterford	2.62	2.68	2.78	2.20
STH 36 (S#3-G) – Waterford	2.64	2.70	2.81	2.28
STH 180 – Marinette	2.67	2.70	2.76	1.30
USH 53 – Minong	2.65	2.70	2.78	1.70
Zoo-Site #1 – Milwaukee	2.38	2.47	2.63	4.05
Zoo-Site #2 – Milwaukee	2.42	2.51	2.66	3.66
STH 18 – Jefferson	2.59	2.66	2.79	2.78
STH 33 – Saukville	2.63	2.68	2.77	1.89
USH 45 – Larsen	2.73	2.76	2.82	1.09
STH 142 East – Burlington	2.64	2.69	2.77	1.74
STH 142 West – Burlington	2.67	2.70	2.76	1.28
Edgerton Ave Greenfield	2.63	2.67	2.74	1.56
STH 59 – Edgerton	2.62	2.68	2.78	2.24
USH 45 – Pelican Lake	2.68	2.71	2.75	0.95
STH 32 – Forest County	2.68	2.69	2.72	0.55

The absorption test results showed the investigated aggregates exhibited a range from 0.55% (STH 32 FC aggregate) to 4.05% (I 94-S1 aggregate). The analysis by Tabatabai et al. (2013) of various Wisconsin coarse aggregates indicated that the mean absorption value is 1.71%. Twelve out of twenty aggregate samples included in this study possessed absorption values greater than this average value.



(a) Specific gravity



(b) Absorption

Figure 4.6: Specific gravity and absorption test results for investigated coarse aggregates.

4.2.2 Micro-Deval Abrasion

The mass loss (expressed as a percentage) by Micro-Deval abrasion of a number of the investigated aggregates (both coarse and fine fractions) are summarized in Table 4.4 and depicted in Figure 4.7. Inspection of test results shows that the fine aggregates exhibited more mass loss, in general, compared with the coarse aggregates from the same aggregate source. The mass loss exhibited by the fine aggregates fraction varies between 6.9% for USH 53 aggregate (fine natural sand from gravel of igneous and metamorphic origin) and 29.7% for STH 33 Saukville aggregate (fine particles of crushed limestone – carbonates). On the other hand, the mass loss for the coarse aggregates fraction ranged from 7% for Edgerton aggregate (natural

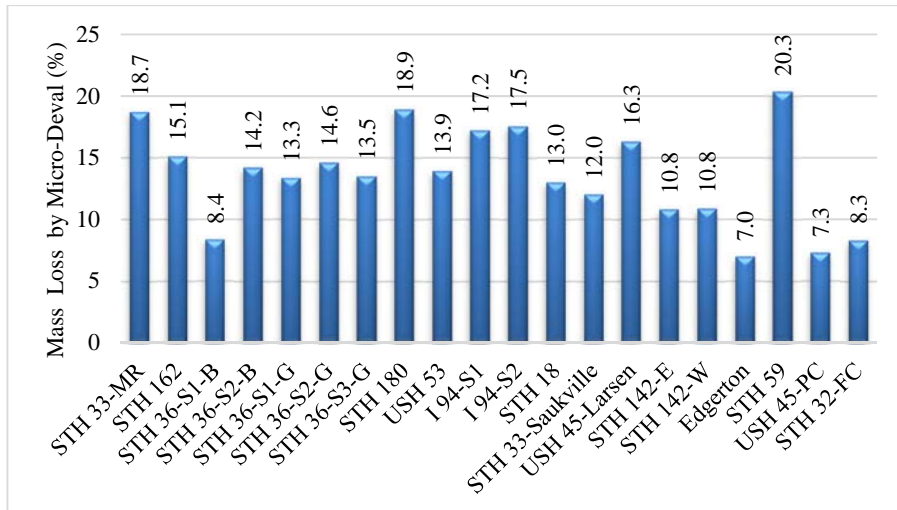
gravel of mixed origin, dominantly carbonates) to 20.3% for STH 59 aggregate (crushed limestone-carbonates).

Table 4.4: Mass loss of coarse and fine aggregates from the Micro-Deval abrasion test.

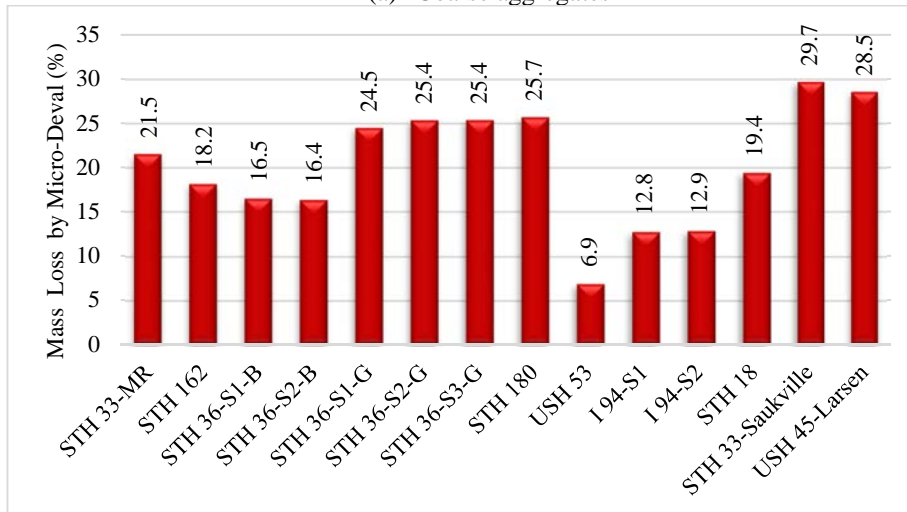
Base Layer Aggregate Source	Mass Loss (%)	
	Coarse Aggregate	Fine Aggregate
STH 33 – Middle Ridge	18.7	21.5
STH 162 – Middle Ridge	15.1	18.2
STH 36 (S#1-B) – Waterford	8.4	16.5
STH 36 (S#2-B) – Waterford	14.2	16.4
STH 36 (S#1-G) – Waterford	13.3	24.5
STH 36 (S#2-G) – Waterford	14.6	25.4
STH 36 (S#3-G) – Waterford	13.5	25.4
STH 180 – Marinette	18.9	25.7
USH 53 – Minong	13.9	6.9
Zoo-Site #1 – Milwaukee	17.2	12.8
Zoo-Site #2 – Milwaukee	17.5	12.9
STH 18 – Jefferson	13.0	19.4
STH 33 – Saukville	12.0	29.7
USH 45 – Larsen	16.3	28.5
STH 142 East – Burlington	10.7	N/A
STH 142 West – Burlington	10.8	N/A
Edgerton Ave Greenfield	7.0	N/A
STH 59 – Edgerton	20.3	N/A
USH 45 – Pelican Lake	7.3	N/A
STH 32 – Forest County	8.3	N/A

Tabatabai et al. (2013) conducted an analysis on Micro-Deval test results of various Wisconsin coarse aggregates. The mean Micro-Deval mass loss was found to be 15.05% for coarse aggregates. Seven out of the twenty investigated existing base layer aggregate exhibited mass loss that exceeded this average.

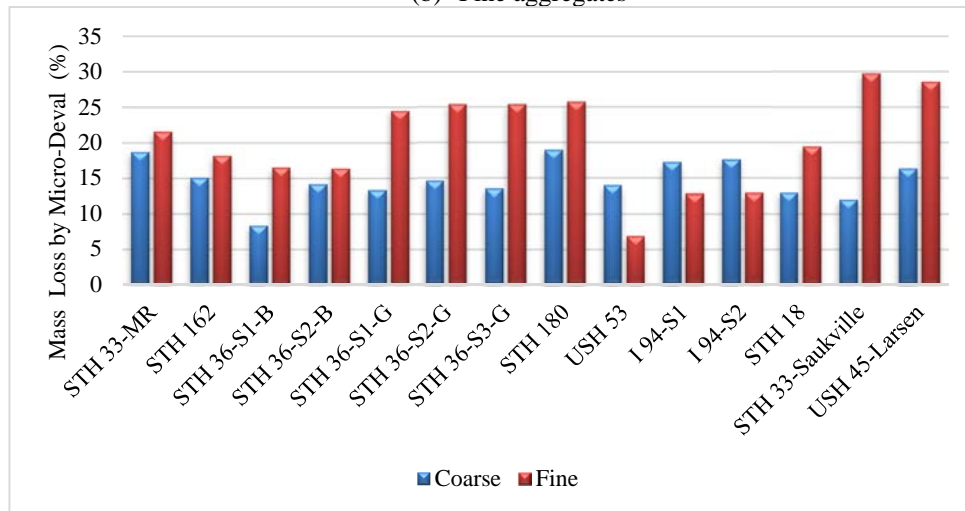
Pictures of the investigated aggregates and the corresponding coarse aggregate abrasion due to Micro-Deval testing are presented in Figure 4.8. The pictures depict the impact of the Micro-Deval test on the abrasion of the aggregate particles; angular and semi-angular particles are more susceptible to shape change than natural round gravel.



(a) Coarse aggregates



(b) Fine aggregates



(c) Coarse and fine aggregates

Figure 4.7: Mass loss of coarse and fine aggregates due to the Micro-Deval test.





















			
Aggregate sample	Abrasion after MD test	Aggregate sample	Abrasion after MD test
			
Aggregate sample	Abrasion after MD test	Aggregate sample	Abrasion after MD test
			
Aggregate sample	Abrasion after MD test	Aggregate sample	Abrasion after MD test
			
Aggregate sample	Abrasion after MD test	Aggregate sample	Abrasion after MD test
			
Aggregate sample	Abrasion after MD test	Aggregate sample	Abrasion after MD test

Figure 4.8: Pictures of the investigated aggregates and the corresponding coarse aggregate abrasion due to the Micro-Deval test.

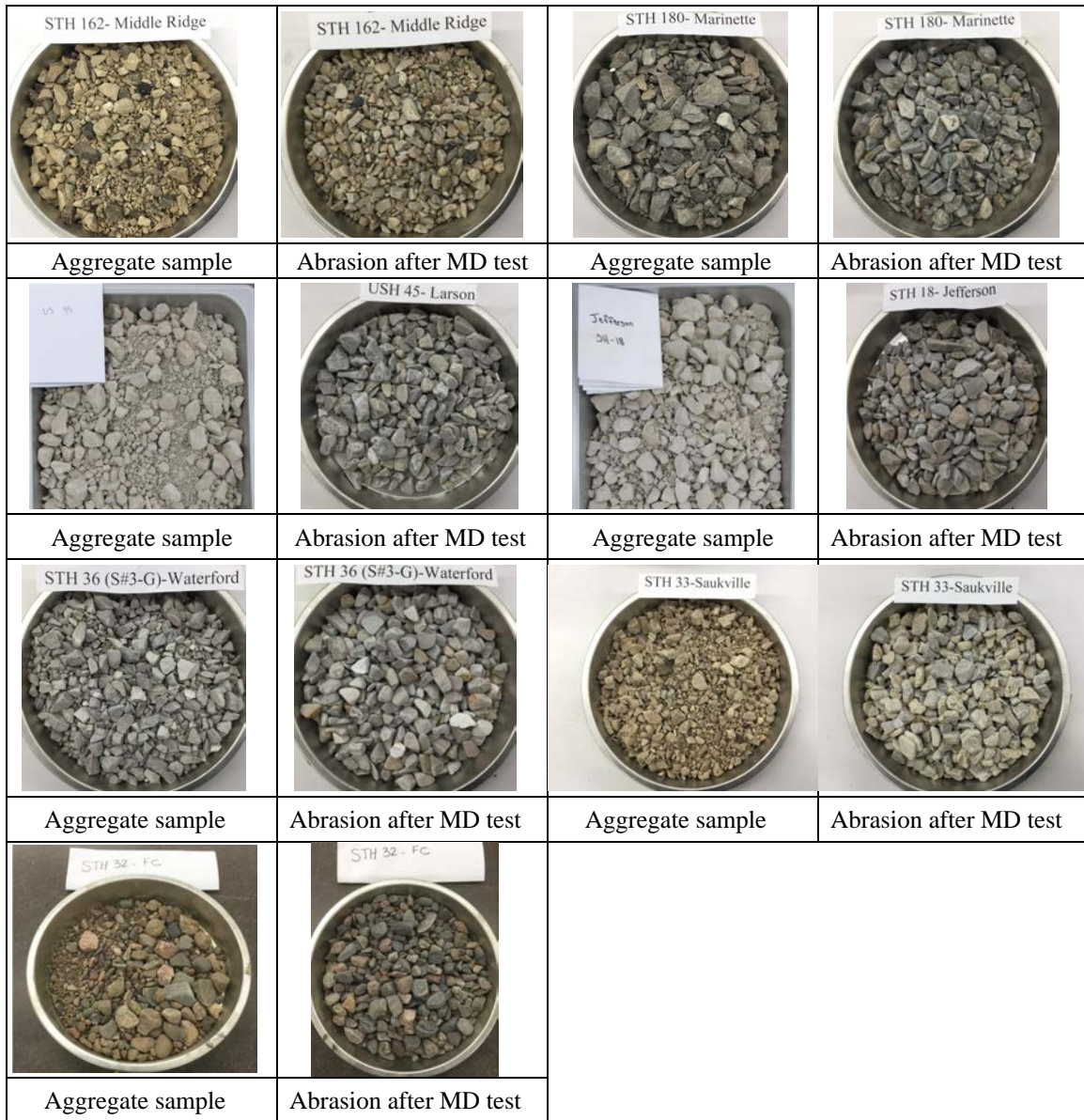


Figure 4.8 (Cont.): Pictures of the investigated aggregate and the corresponding coarse aggregate abrasion due to the Micro-Deval test.

4.2.3 Sodium Sulfate Soundness

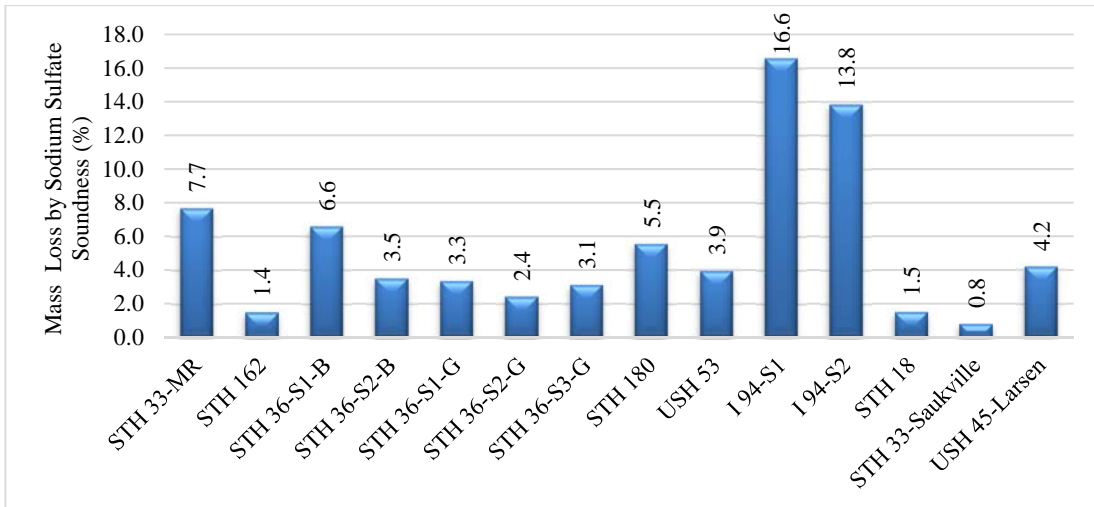
The sodium sulfate soundness test was conducted on the coarse and fine aggregate fractions on a number of the of the investigated aggregates. The percentage of mass loss by sodium sulfate soundness for 14 base aggregate samples are summarized in Table 4.5 and presented in Figure 4.9.

Table 4.5: Mass loss of coarse and fine aggregates from the sodium sulfate soundness test.

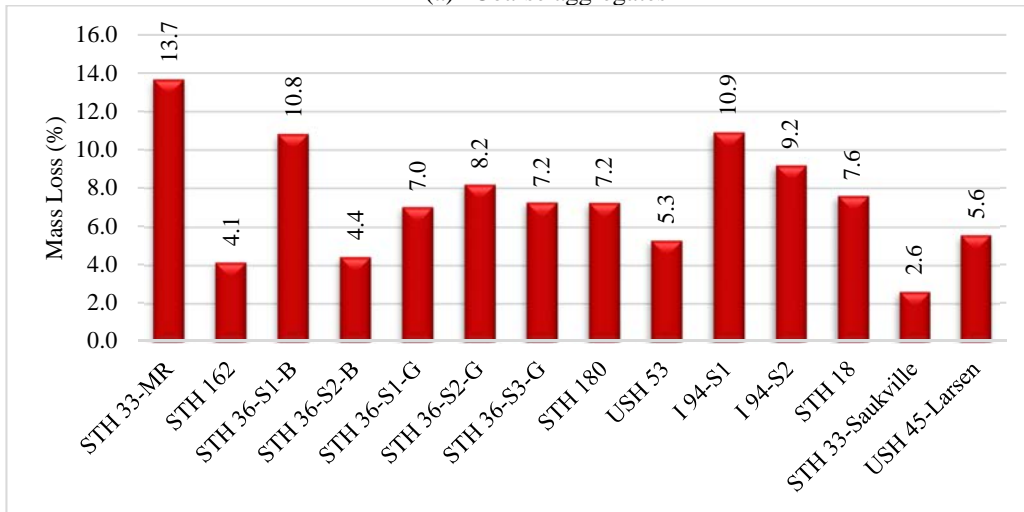
Base Layer Aggregate Source	Mass Loss (%)	
	Coarse Aggregate	Fine Aggregate
STH 33 – Middle Ridge	7.7	13.7
STH 162 – Middle Ridge	1.4	4.1
STH 36 (S#1-B) – Waterford	6.6	10.8
STH 36 (S#2-B) – Waterford	3.5	4.4
STH 36 (S#1-G) – Waterford	3.3	7.0
STH 36 (S#2-G) – Waterford	2.4	8.2
STH 36 (S#3-G) – Waterford	3.1	7.2
STH 180 – Marinette	5.5	7.2
USH 53 – Minong	3.9	5.3
Zoo-Site #1 – Milwaukee	16.6	10.9
Zoo-Site #2 – Milwaukee	13.8	9.2
STH 18 – Jefferson	1.5	7.6
STH 33 – Saukville	0.8	2.6
USH 45 – Larsen	4.2	5.6

Examination of the test results shows that the mass loss for coarse aggregates ranged from 0.8% for STH 33 Saukville aggregate (crushed limestone - carbonates) to 16.6% for I 94-S1 aggregate (mixture of crushed carbonates, gravel, and some recycled PCC/RAP). For the fine aggregate fraction, the mass loss varied between 2.6% for STH 33 Saukville aggregate (crushed limestone - carbonates) and 13.7% for STH 33 Middle Ridge (crushed limestone - carbonates). The sodium sulfate soundness test showed that the fine aggregate fraction exhibited higher percentages of mass loss compared with the coarse aggregate fraction from the same aggregate source for the majority of the investigated aggregates.

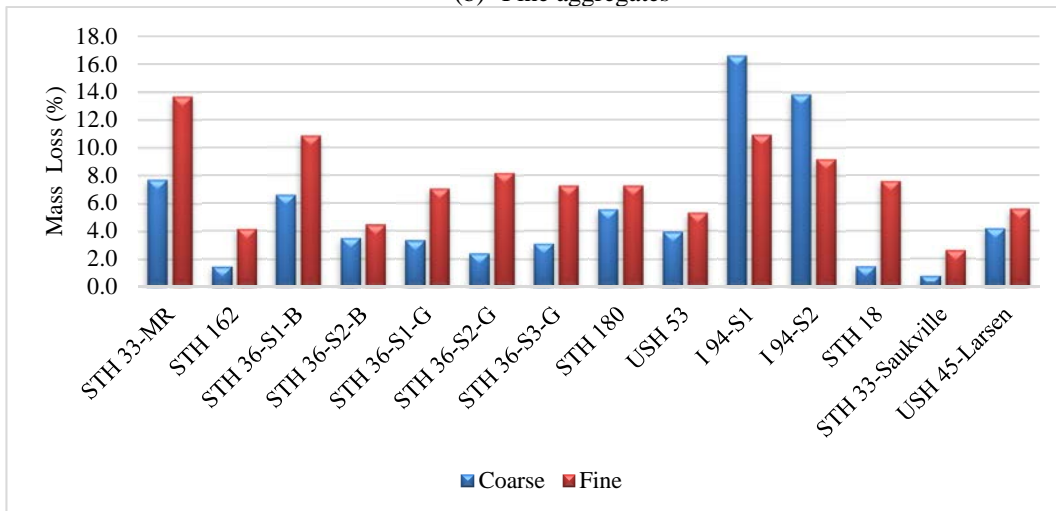
The cumulative mass loss was also determined after each sodium sulfate wetting/drying test cycle for the coarse aggregate fraction for the 14 base layer aggregates. For the fine aggregate fraction, the cumulative mass loss after each cycle was only determined for the following specimens: STH 33 MR, STH 162 MR, STH 36-S1-B, STH 180, USH 53, I 94-S1, and I 94-S2. The cumulative mass loss per cycle for the coarse aggregate fraction is depicted in Figure 4.10 a and the cumulative mass loss per cycle for the fine aggregate fraction is presented in Figure 4.10 b.



(a) Coarse aggregates



(b) Fine aggregates



(c) Coarse and fine aggregates

Figure 4.9: Final mass loss of coarse and fine aggregates due to the sodium sulfate soundness test.

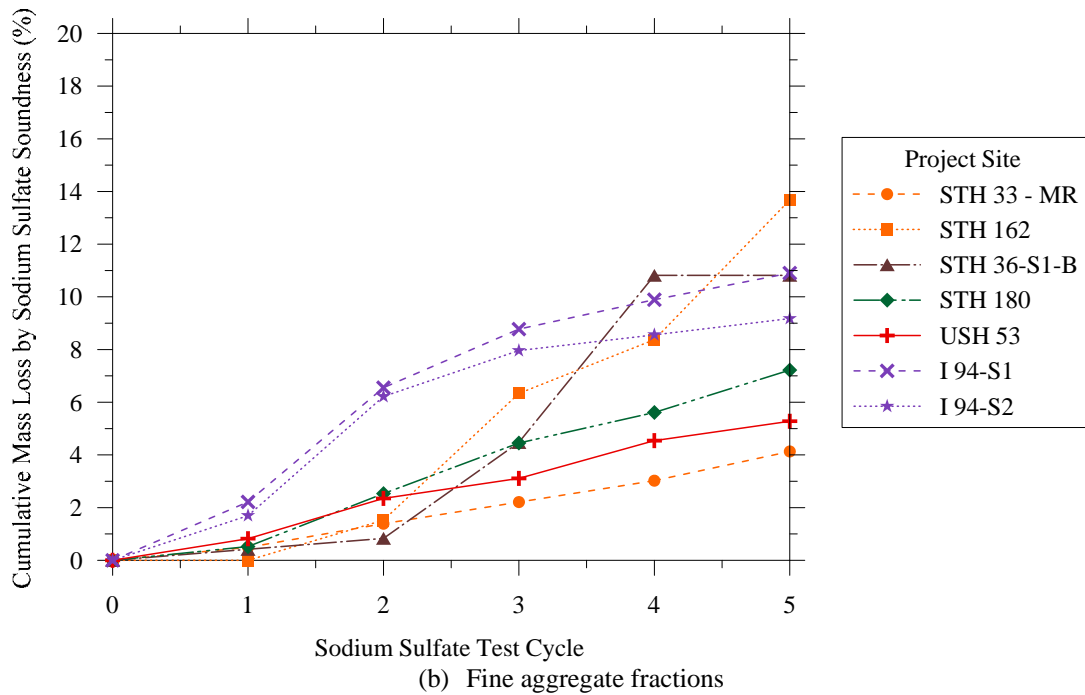
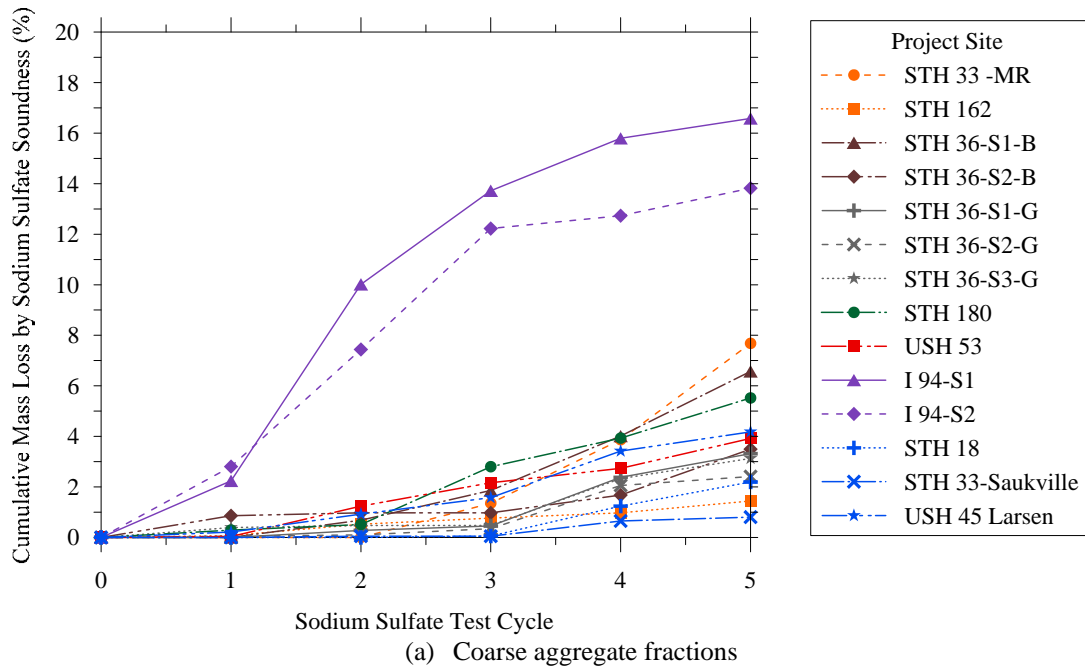


Figure 4.10: Cumulative mass loss per sodium sulfate soundness test cycle for the investigated aggregates.

The percent rate change in mass loss between sodium sulfate soundness test cycles for the investigated coarse aggregate fractions is presented in Figure 4.11. For the coarse aggregate, the highest rate of mass loss occurred between cycles 1 and 2 for the following two samples: STH 162 and USH 53. The highest rate of mass loss occurred between cycles 2 and 3 for the

following two samples: STH 180 and STH 36-S3-G. The highest rate of mass loss occurred between cycles 3 and 4 for the following two samples: STH 18 and STH 33 Saukville. It is also worth noting that there seemed to be a trend where the highest rate of mass loss occurred either between cycle 1 and 2 or cycles 3 and 4 for most samples.

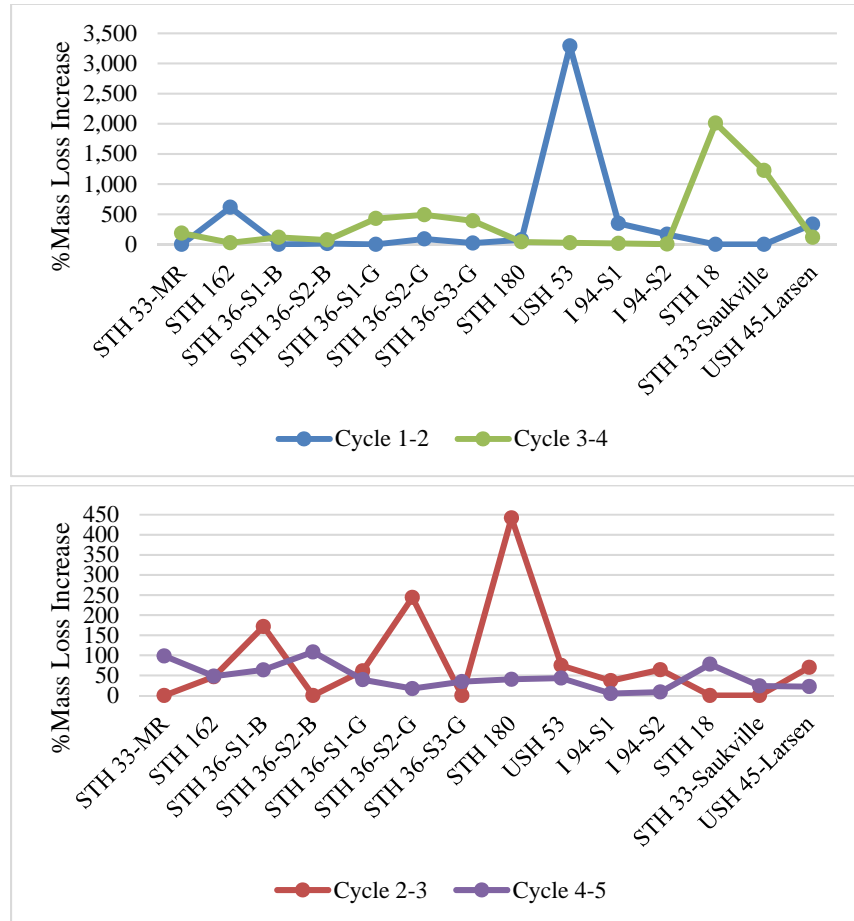


Figure 4.11: Percent rate change in mass loss between sodium sulfate soundness test cycles for the investigated coarse aggregate fractions.

For the fine aggregate fractions, the highest rate of mass loss occurred between cycle 1 and 2 for samples STH 180, USH 53, I 94-S1, and I 94-S2, between cycle 2 and 3 for STH 180, between cycle 3 and 4 for STH 36-S1-B, and between cycles 4 and 5 for STH 33 and STH 162.

Tabatabai et al. (2013) conducted an analysis on sodium sulfate soundness test results for various Wisconsin coarse aggregates. The mean sodium sulfate soundness mass loss was 3.36% for coarse aggregates. Eight out of the 14 investigated existing base layer aggregates exhibited mass loss that exceeded 3.36%. The mass loss values of the investigated aggregates are compared with a threshold limit of 18% specified by Section 301.2.4.5 of WisDOT Standard Specifications for Highway and Structure Construction (2108). All observed mass losses fell below the limit of 18%.

4.2.4 Analyses of Durability Test Results

For the durability evaluation, the analysis of the Micro-Deval abrasion, sodium sulfate soundness, and absorption data were conducted for the investigated coarse aggregates that have been subjected to these tests. Regression analyses were performed on the Micro-Deval abrasion, sodium sulfate soundness, and aggregate absorption data collected for this study in combination with data obtained from other studies, namely: WHRP-1 (Weyers et al., 2005), WHRP-2 (Tabatabai et al., 2013), WHRP-3, and WHRP-4 (data obtained from WisDOT materials testing files/database via personal communications with the research team).

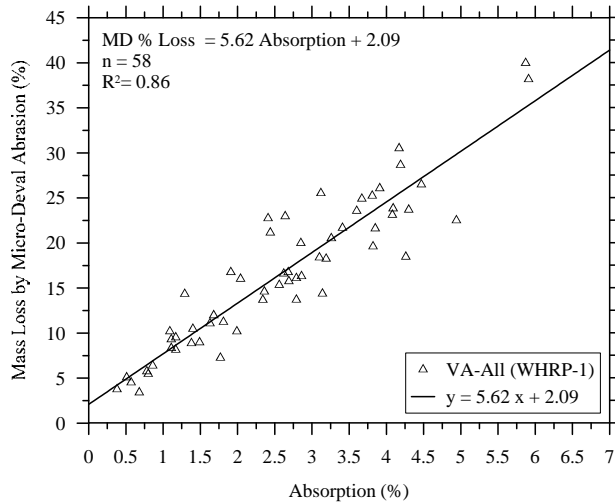
The mass losses of coarse aggregates quantified by the Micro-Deval abrasion test are plotted against absorption in Figure 4.12 for various Wisconsin aggregates obtained from the WHRP-1, WHRP-2, WHRP-3 and WHRP-4 studies. The best fit line for the test data points is also shown in each figure. For the WHRP-1 results presented in Figure 4.12 a, the aggregates were obtained from Wisconsin pits and quarries (i.e., crushed stone and natural gravel) and included virgin aggregates of good, intermediate, and poor performance quality as specified in Weyers et al. (2005). For these aggregates, mass loss during the Micro-Deval abrasion test ranged between 3.42% (for coarse aggregate with 0.68% absorption) and 39.98% (for coarse aggregate with 5.87 % absorption). A correlation between coarse aggregate mass loss from Micro-Deval abrasion and absorption showed a coefficient of determination of 0.86. This trend is consistent with the results reported by Rismantojo (2000) which suggested there was a significant relationship between Micro-Deval abrasion and aggregate absorption.

When separating the coarse aggregate test results from the WHRP-1 study into groups based on performance (shown in Figure 4.12 b), the virgin aggregates with good performance quality exhibited a mass loss ranging from 3.76% (for coarse aggregate with 0.38% absorption) and 23.57% (for coarse aggregate with 3.6% absorption). Figure 4.12 b shows a correlation between the mass loss from Micro-Deval abrasion and absorption with R^2 of 0.87 for virgin aggregates with good performance quality. For the virgin aggregates with intermediate performance quality, the mass loss varied between 3.42% (for the coarse aggregate with 0.68% absorption) to 26.5% (for the coarse aggregate with 4.47% absorption). Figure 4.12 b shows the correlation between mass loss and absorption with R^2 of 0.70 for virgin aggregates with intermediate performance quality. Finally, for the virgin aggregates with poor performance quality, the mass loss ranged between 5.09% (for the coarse aggregate with 0.51% absorption) and 39.98% (for the coarse aggregate with 5.87 % absorption). Figure 4.12 b shows a correlation between coarse aggregate mass loss and absorption with R^2 of 0.92 for virgin aggregates with poor performance quality.

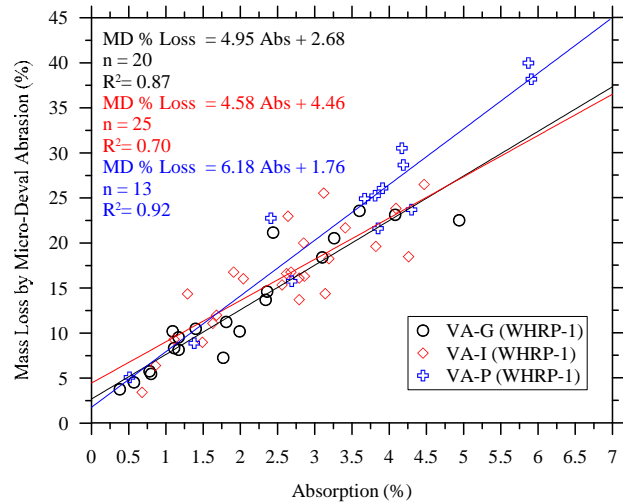
Figure 4.12 c shows the mass loss during the Micro-Deval abrasion test versus absorption for Wisconsin aggregates with poor performance from the WHRP-2 study (Tabatabai et al., 2013). The mass loss ranged between 17.26% (for coarse aggregate with 2.6% absorption) and 38.7% (for coarse aggregate with 3.71% absorption). The data plotted in the figure shows no

correlation between coarse aggregate absorption and mass loss from Micro-Deval abrasion (R^2 of 0.09).

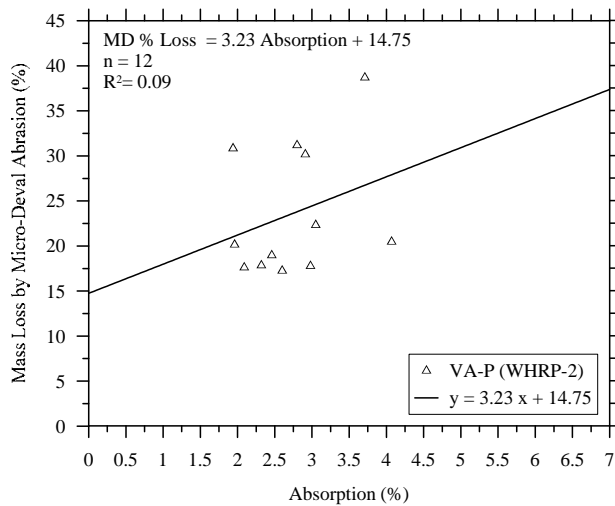
WHRP-3 data consisted of test results on virgin aggregates with mixed performance. The mass loss during the Micro-Deval abrasion test is plotted against absorption in Figure 4.12 d. The mass loss ranged between 6.3% (for coarse aggregate with 0.7% absorption) and 27.5% (for coarse aggregate with 4.09% absorption). The best fit line shown in the figure showed a correlation with R^2 of 0.52.



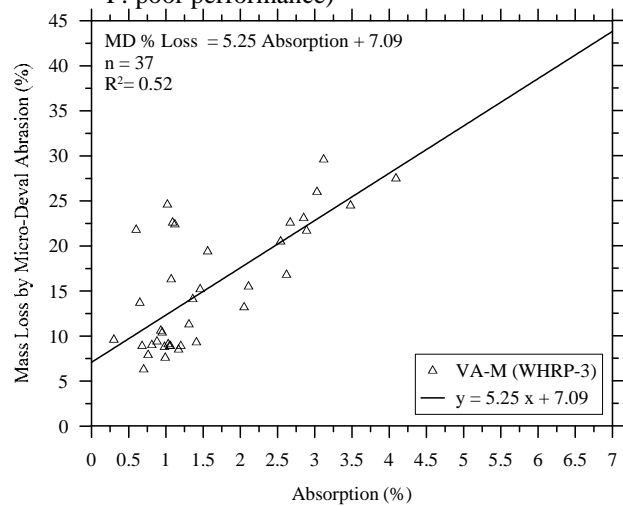
(a) WHRP-1 (VA: virgin aggregate)



(b) WHRP-1 (VA: virgin aggregate, G: good performance, I: intermediate performance, and P: poor performance)



(c) WHRP-2 (VA: virgin aggregate, P: poor performance)

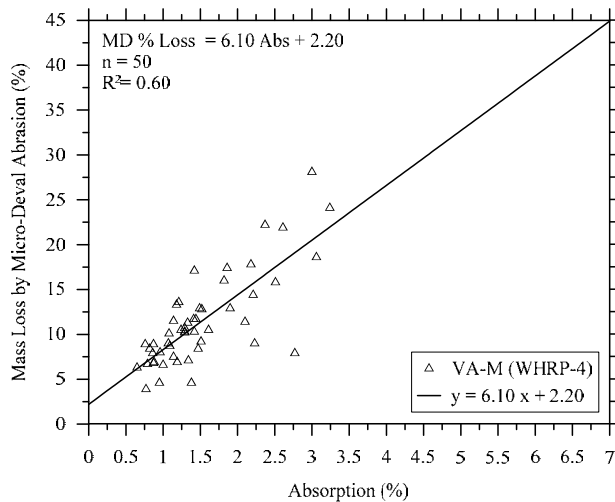


(d) WHRP-3 (VA: virgin aggregate, M: mixed performance)

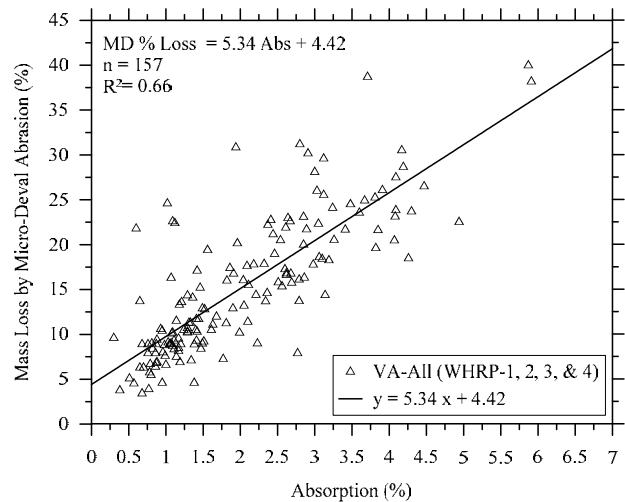
Figure 4.12: Comparison of mass loss of coarse aggregates from Micro-Deval abrasion versus absorption for various Wisconsin virgin aggregates.

For the WHRP-4 data with aggregates of mixed performance, the mass loss of coarse aggregate during the Micro-Deval abrasion test is plotted against absorption in Figure 4.13 a with the best fit line shown in the figure (R^2 of 0.6). The mass loss during the Micro-Deval abrasion test ranged between 3.9% (for coarse aggregate with 0.77% absorption) and 28.1% (for coarse aggregate with 3.9% absorption).

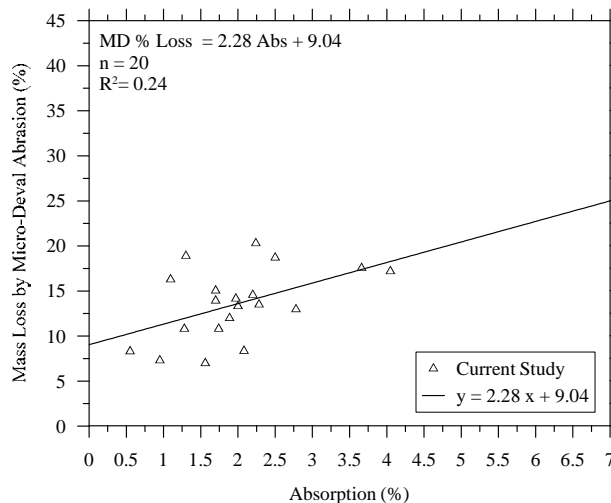
The test results for the Wisconsin virgin aggregates from both sources (quarries and pits) comprising all performance categories (good, intermediate, and poor) are presented in Figure 4.13 b. The best fit line for the relationship between mass loss percent and absorption resulted in a coefficient of determination R^2 of 0.66, indicating a reasonable, but not very strong, trend.



(a) WHRP-4 (VA: virgin aggregate, M: mixed performance)



(b) All WHRP studies (virgin aggregates with mixed performance from quarries and pits)



(c) Current study on base layer aggregates

Figure 4.13: Comparison of mass loss of coarse aggregates from Micro-Deval abrasion versus absorption for various Wisconsin virgin and in-service aggregates.

The preceding analysis considered only Wisconsin virgin aggregates. However, the current study is investigating base layer aggregates that have been in service for years. Twenty aggregate samples were subjected to Micro-Deval abrasion tests, three of which were virgin aggregates that had been serving in base layers for 6 to 8 years (STH 18, STH 33 Saukville, and USH 45 Larsen/CTH II Mudcreek). The remaining 17 aggregate samples have been serving in base layers for many years, ranging between 15 and 85 years. Figure 4.13 c presents the results of the Micro-Deval abrasion test results versus the absorption for the coarse aggregates investigated by this research. The best fit line shows a poor trend with R^2 of 0.24.

Figure 4.14 d depicts comparisons of mass loss percent versus absorption for the investigated base layer aggregates with the various WHRP studies on Wisconsin virgin aggregates. The mass loss percent versus absorption best fit line for the WHRP-1 study is also plotted since it had the highest coefficient of determination (R^2 of 0.86)

Inspection of Figure 4.14 does not lead to solid conclusions with respect to predicting the Micro-Deval abrasion test results from the absorption or identifying the performance of base aggregate layers based only on the results of the Micro-Deval test. However, both the Micro-Deval abrasion and absorption tests provided important information that will be used later with other test results to provide a more complete characterization of base layer aggregate performance.

The sodium sulfate soundness test is specified as a standard acceptance test for base layer aggregates (for both crushed stone and gravel) with a maximum acceptable loss by weight of 18% for dense graded bases and 12% for open graded bases (Section 301.2.4.5 of Standard Specifications for Highway and Structure Construction, 2018). In order to evaluate the durability of the investigated base layer aggregates and to assess methods of identifying base layer aggregate performance, an analysis was conducted on the sodium sulfate soundness test results of 14 of the base layer aggregates investigated and consequently correlations with both absorption and Micro-Deval mass loss were attempted.

The mass loss of the base layer coarse aggregates quantified by the sodium sulfate soundness test are plotted against absorption in Figure 4.15. Test results from WHRP-1, WHRP-2, WHRP-3, and the current study on both virgin and base layer aggregates are presented in the figure. The best fit line for the test data is also shown in the figure. Inspection of the figure shows that the percent mass loss ranged between 0.06% (for the coarse aggregate with 0.59% absorption) and 31.42% (for the coarse aggregate with 5.87% absorption). The best fit line shown in the figure did not produce an acceptable correlation (R^2 of 0.33). Thus, it was reasonable to conclude that the sodium sulfate soundness test results may not be predicted using solely the aggregate absorption. It should be noted that three out of the 123 coarse aggregates with sodium sulfate test results exceeded the mass loss threshold of 18% set by WisDOT, none of which are from the investigated base layer aggregates.

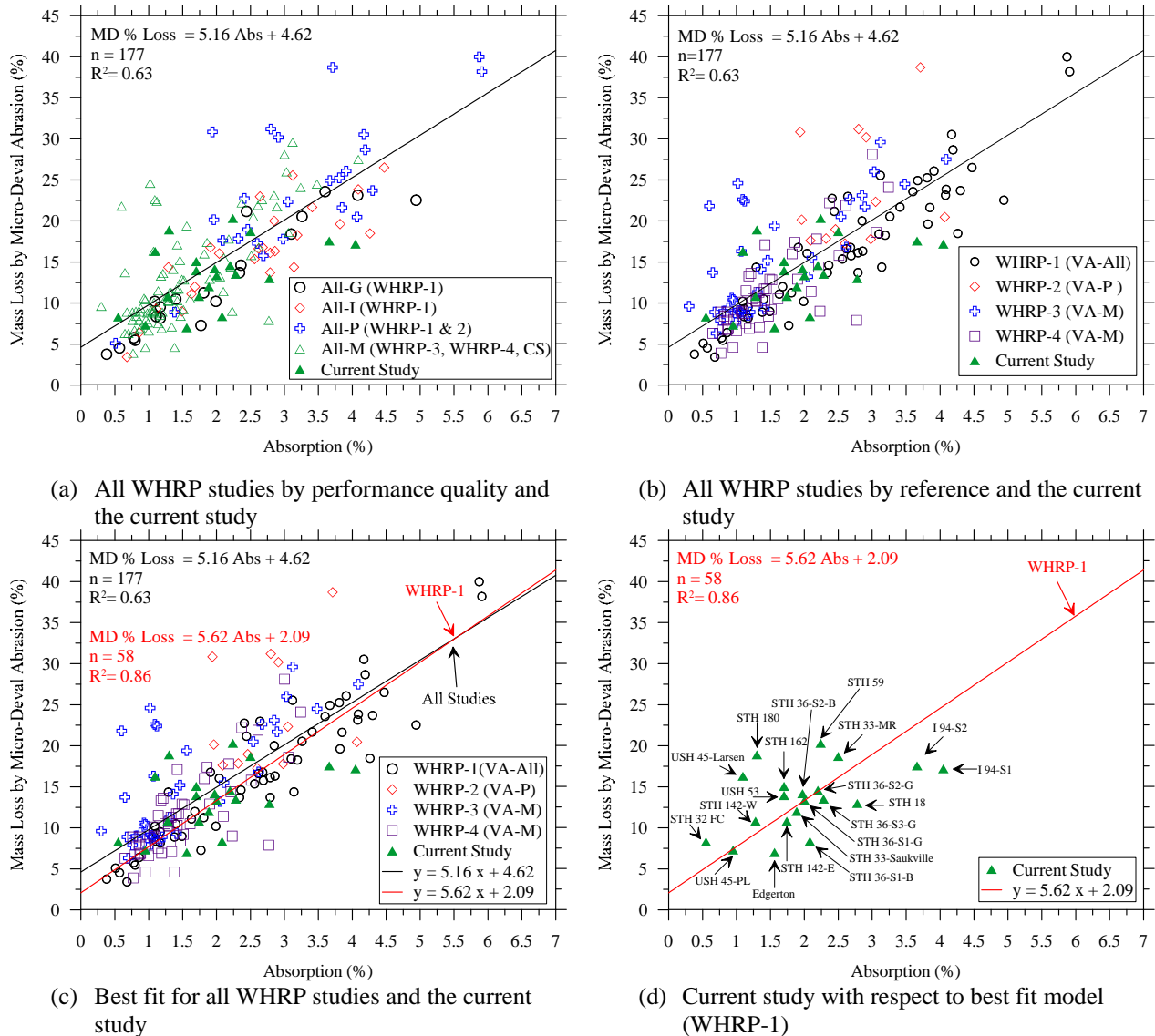


Figure 4.14: Comparison of mass loss of coarse aggregates from Micro-Deval abrasion versus absorption for various Wisconsin virgin aggregates.

The results of the sodium sulfate soundness test were also compared with the Micro-Deval abrasion for both the virgin and base layer coarse aggregates as depicted in Figure 4.16. The results presented in the figure indicate a poor correlation between the mass loss percent from the two tests, which is consistent with Cooley's (2000) findings that there was no correlation between Micro-Deval abrasion and sodium sulfate soundness.

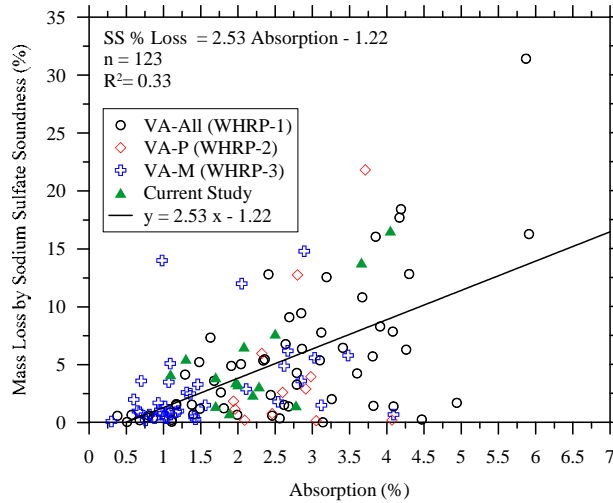


Figure 4.15: Comparison of mass loss of coarse aggregates from the Sodium Sulfate Soundness test versus absorption for Wisconsin virgin and base layer coarse aggregates.

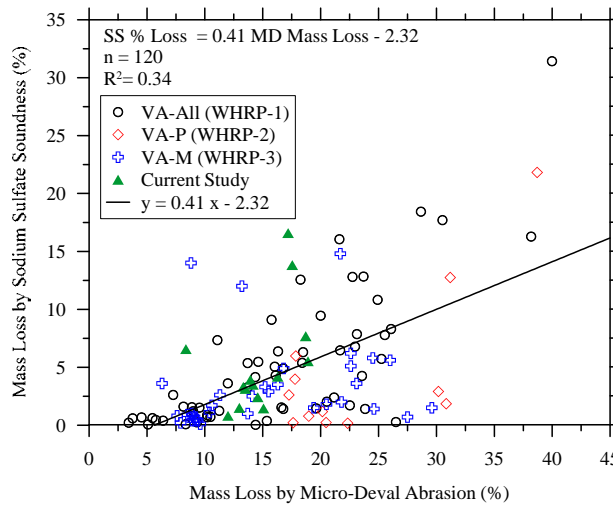


Figure 4.16: Comparison of mass loss of coarse aggregates from Sodium Sulfate Soundness test versus Micro-Deval abrasion for Wisconsin virgin and base layer coarse aggregates.

4.3 Strength and Modulus Tests of the Investigated Base Layer Aggregates

Determination of strength and resilient modulus of the investigated base layer aggregates is important for the performance evaluation and design/analysis of pavements. California Bearing Ratio provides a simple strength evaluation of the quality of the aggregate compared with the strength of well-graded crushed stone. The resilient modulus of base aggregates is also needed as an input parameter for the AASHTOWare Pavement ME Design. In order to determine the CBR and resilient modulus of base layer aggregate samples, they must be prepared at the maximum dry unit weight (γ_{dmax}) and optimum moisture content (w_{opt}); therefore, the standard compaction test is required to identify these two parameters.

4.3.1 Standard Compaction Test

The results of the laboratory compaction test on the base layer aggregates collected from twenty sources are presented in Figures 4.17 and 4.18. Inspection of the test results shows variations in the maximum dry unit weight and optimum moisture content among the investigated base layer aggregates. The range of γ_{dmax} was between 131.55 lb/ft³ (for I-94 Zoo Interchange Site 1 base layer aggregate) and 149.2 lb/ft³ (for CTH II/Mudcreek – USH 45 in Larsen base layer aggregate). The optimum moisture content varied between 3.64% and 8.75%.

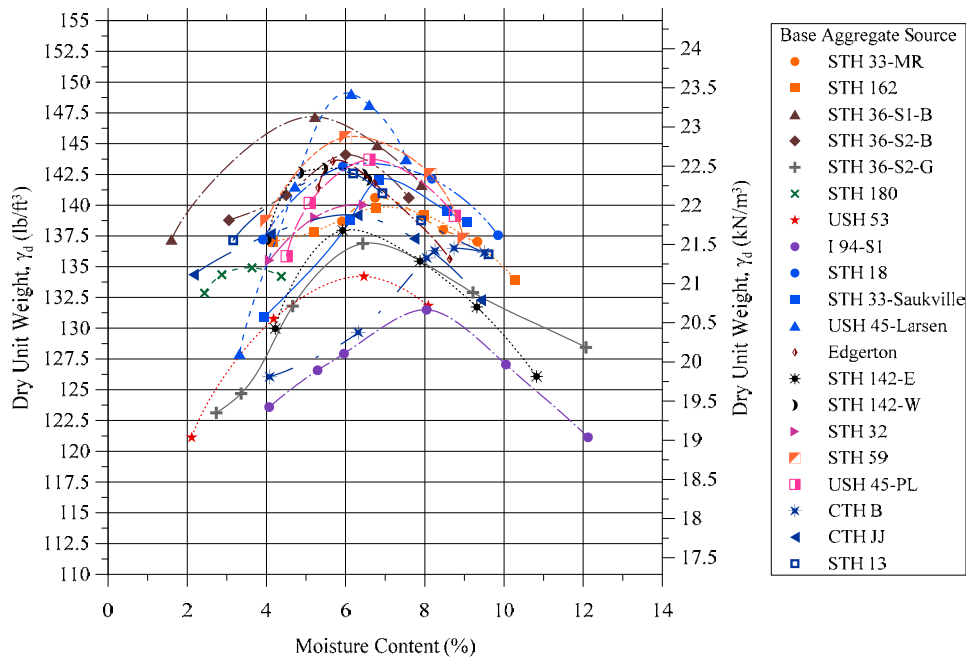
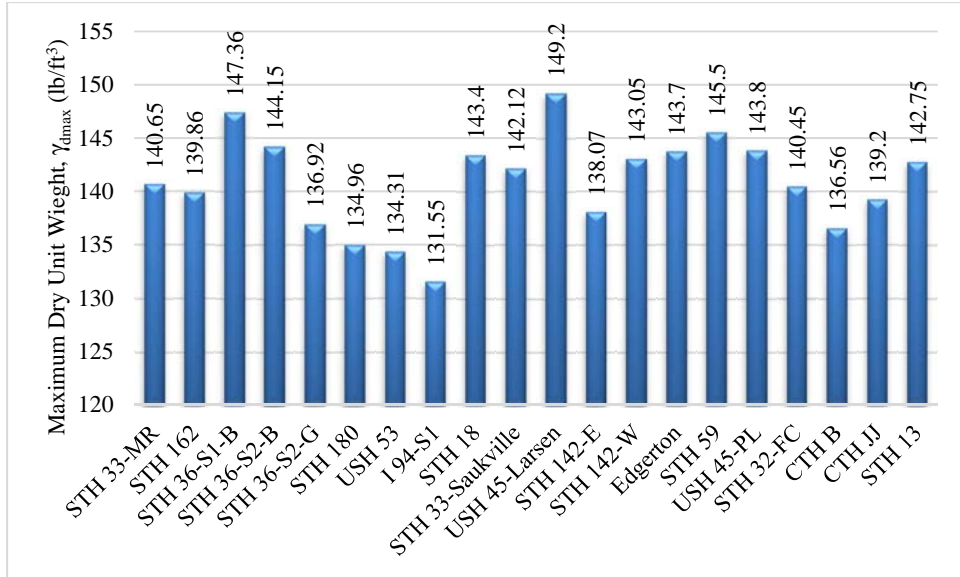
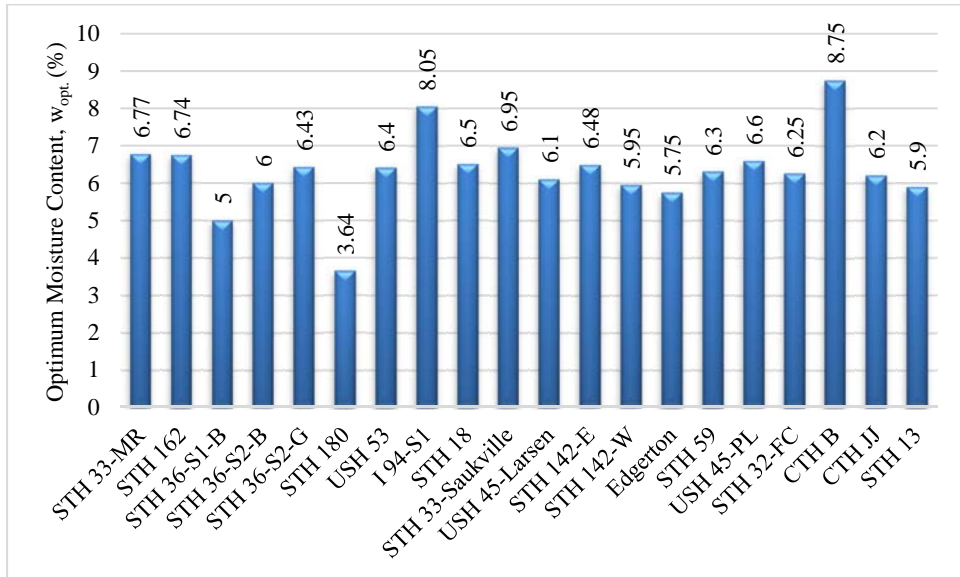


Figure 4.17: Standard compaction test results for base layer aggregates.



(a) Maximum dry unit weight



(b) Optimum moisture content

Figure 4.18: Maximum dry unit weight ($\gamma_{d,max}$) and optimum moisture content (w_{opt}) of the investigated base layer aggregates.

4.3.2 California Bearing Ratio

The results of the soaked CBR test are depicted in Figure 4.19 as stress on piston versus penetration curves. The soaked CBR values calculated from these curves are shown in Figure 4.20. The soaked base aggregate samples were prepared at maximum dry unit weight and optimum moisture content.

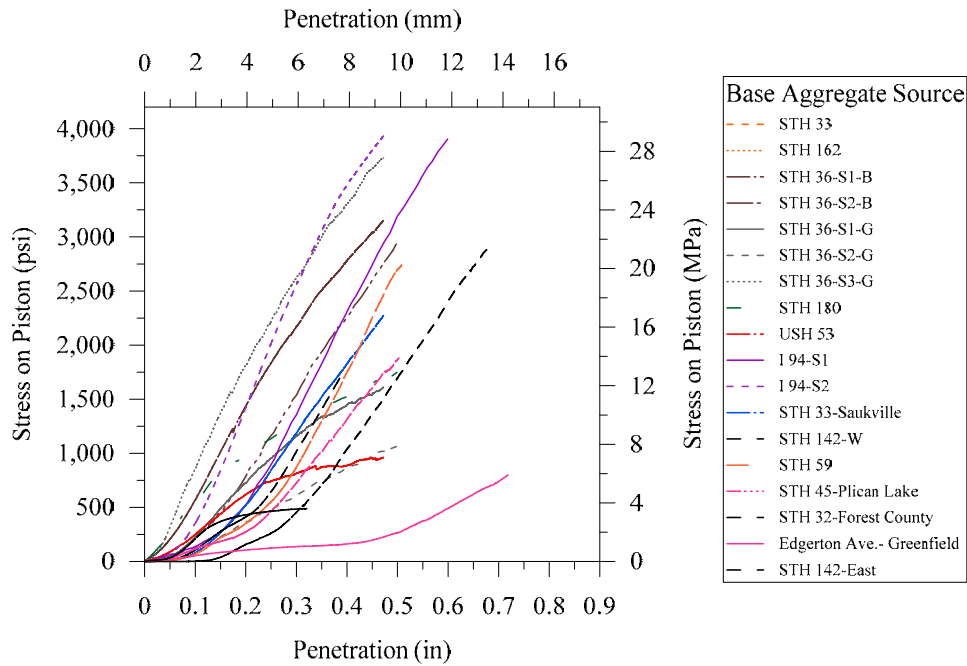


Figure 4.19: Piston pressure versus penetration during soaked CBR tests on base layer aggregates.

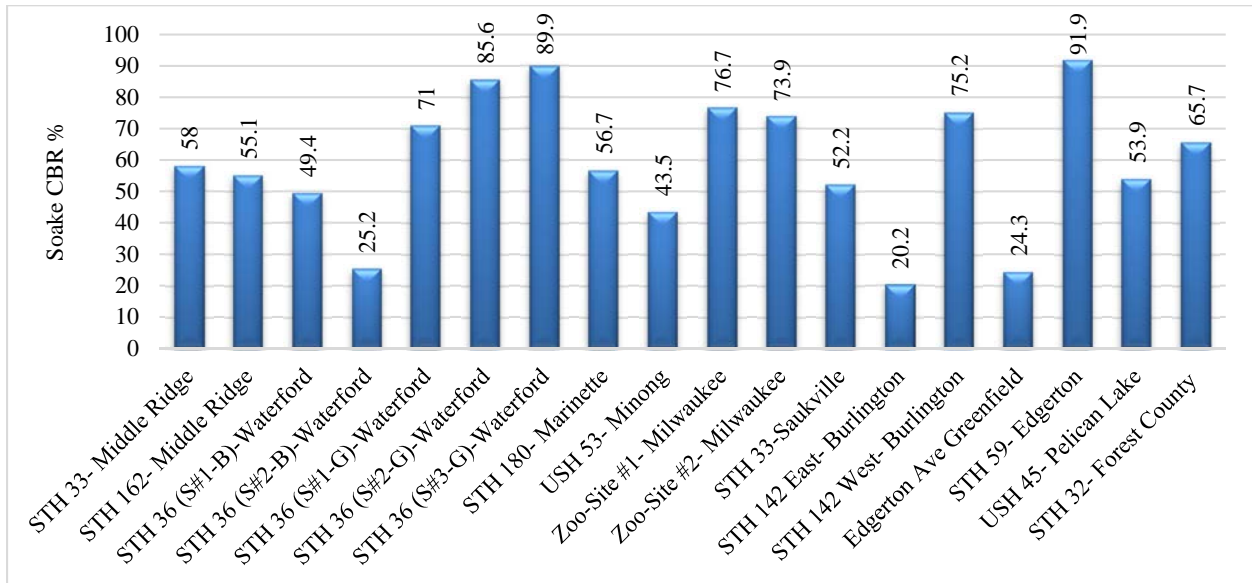
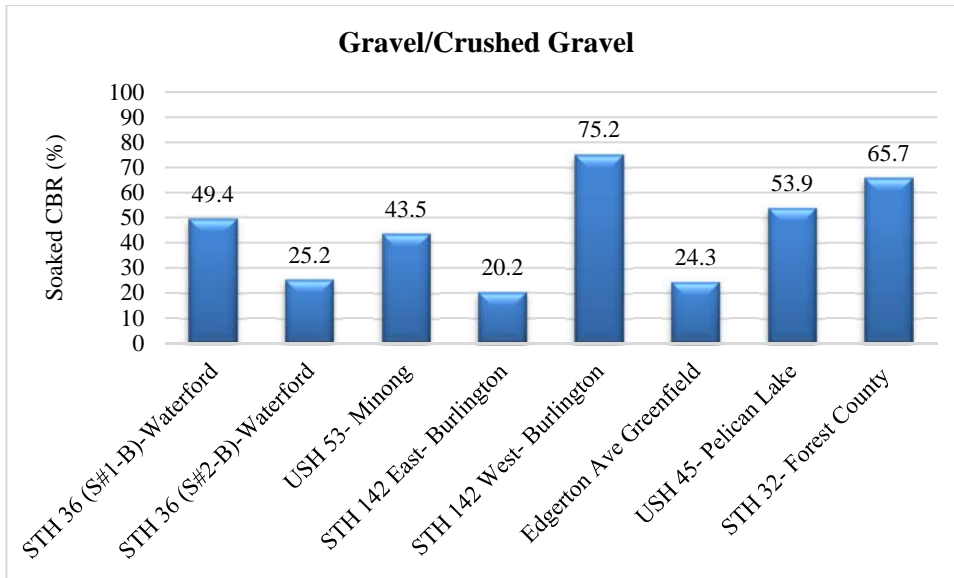


Figure 4.20: CBR test results for the investigated in-service base layer aggregates (soaked CBR).

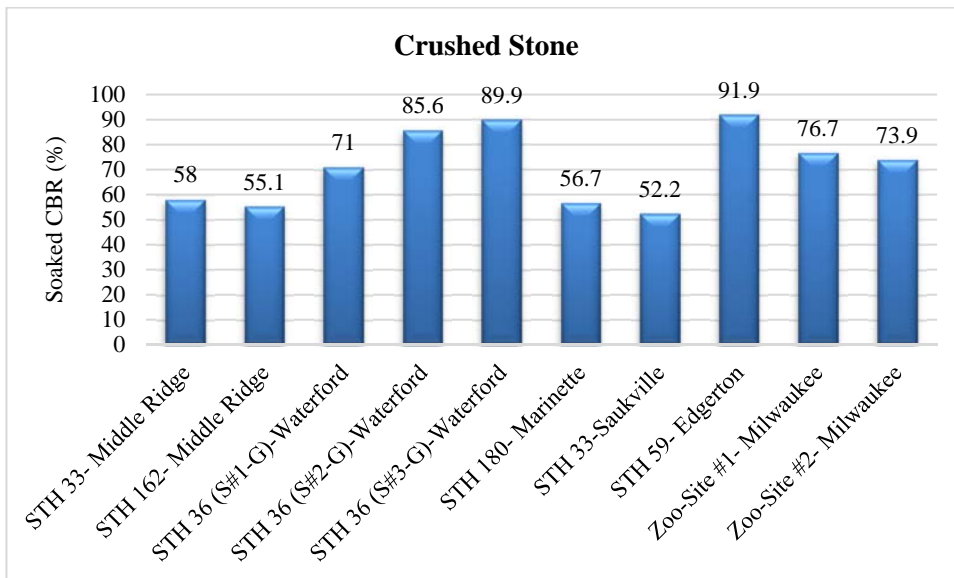
Inspection of Figure 4.20 shows that the soaked CBR values ranged from 20.2% for STH 142 E base aggregate to 91.9% for STH 59 base aggregate. The soaked CBR test results are affected by particle characteristics such as shape, size, size distribution, and amount of fines in the aggregate specimen. Table 4.6 presents the soaked CBR values, the amount of fines, and a description of the base layer aggregate tested. The soaked CBR values are grouped into either gravel/crushed gravel or crushed stone and presented in Figure 4.21. For base layer aggregates composed of gravel/crushed gravel, the soaked CBR values varied between 20.2% and 75.2%. For base layer aggregates composed of crushed stone, the soaked CBR values ranged from 52.2% to 91.9%. In general, the base layer aggregates composed of crushed stone exhibited higher soaked CBR values compared with gravel/crushed gravel base layer aggregates. One reason for this is because the crushed stone particles with angular shape and rough surface texture result in better interlocking and resistance to penetration than natural gravel particles with round/semi-round particles. The presence of a large amount of fines in the aggregate specimen retain moisture better after soaking, which weakens the resistance to piston penetration during testing. The base layer materials composed of gravel/crushed gravel with high amounts of fines showed the lowest soaked CBR values of: 20.2% and 24.3% for STH 142E (28% fines) and Edgerton (34.1% fines) aggregates, respectively. The soaked CBR values are plotted against the amount of fines in Figure 4.22 in order to assess the possibility of a correlation between these variables. The best fit line shows a weak correlation (R^2 of 0.43); however, the influence of the amount of fines on the CBR values and therefore the strength of base layer aggregate is still significant.

Table 4.6: Soaked CBR values, amount of fines, and description of base layer aggregates.

Base Layer Aggregate	Soaked CBR (%)	Percent Fines	Description of Base Aggregate
STH 33 – Middle Ridge	58.0	15.9	Crushed Carbonate
STH 162– Middle Ridge	55.1	12.8	Crushed Carbonate
STH 36 (S#1-B) – Waterford	49.4	9.9	Gravel and Crushed Gravel
STH 36 (S#2-B) – Waterford	25.2	10.4	Gravel and Crushed Gravel
STH 36 (S#1-G) – Waterford	71.0	7.2	Crushed Carbonate
STH 36 (S#2-G) – Waterford	85.6	6.2	Crushed Carbonate
STH 36 (S#3-G) – Waterford	89.9	13.3	Crushed Carbonate
STH 180 – Marinette	56.7	7.8	Crushed Carbonate
USH 53 – Minong	43.5	6.3	Gravel and Crushed Gravel
Zoo-Site #1 – Milwaukee	76.7	6.3	Gravel, Crushed Aggregate, RC, and RAP
Zoo-Site #2 – Milwaukee	73.9	4.5	Gravel, Crushed Aggregate, RC, and RAP
STH 33 – Saukville	52.2	11.8	Crushed Carbonate
STH 142 East – Burlington	20.2	28	Gravel and Crushed Gravel
STH 142 West – Burlington	75.2	13.4	Gravel and Crushed Gravel
Edgerton Ave – Greenfield	24.3	34.1	Gravel and Crushed Gravel
STH 59 – Edgerton	91.9	12.7	Crushed Carbonate
USH 45- Pelican Lake	53.9	11.5	Gravel and Crushed Gravel
STH 32- Forest County	65.7	6.8	Gravel and Crushed Gravel



(a) Base aggregate composed of natural gravel and crushed gravel



(b) Base aggregate composed of crushed stone

Figure 4.21: Soaked CBR test results for the investigated base layer aggregates based on their particle shape and composition.

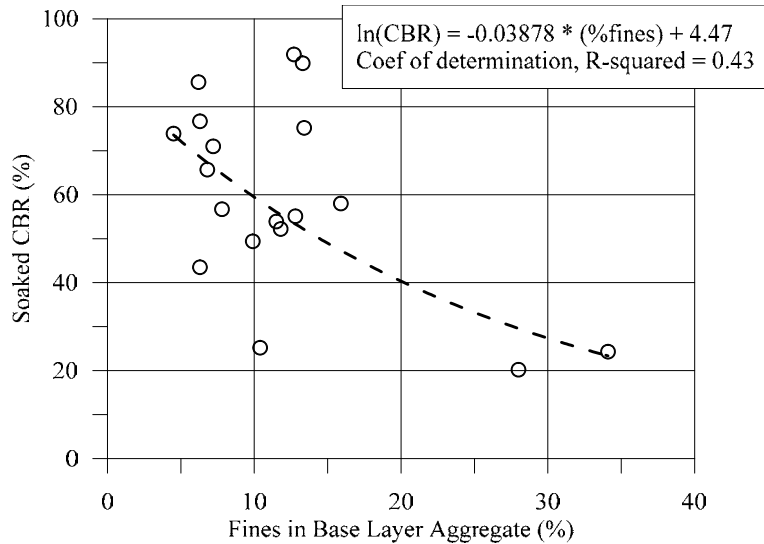


Figure 4.22: Soaked CBR values versus amount of fines present in the investigated base layer aggregates.

4.3.3 Repeated Load Triaxial Test – Resilient Modulus

The results of the repeated load triaxial test (AASHTO T 307) on the base layer aggregates are shown in Figure 4.23. In each test, the base layer aggregate specimen was subjected to repeated loading at the maximum dry unit weight and optimum moisture content. It should be noted that only six samples presented are specimens from existing base layers and the remaining four are crushed stone virgin aggregates for comparison (CTH BB, CTH JJ, STH 33 Ramp, and USH 45 – CTH II Larsen). The resilient modulus values of the investigated aggregates increase with increasing bulk stress under the same confining pressure, which is consistent with typical unbound material behavior. An exception to this is the base layer aggregate from STH 142E which has a very high amount of fines. Inspection of the figure indicates low to high range of resilient modulus values were obtained. For example, for a confining pressure of 20.7 kPa (3 psi) and bulk stress of 80.3 kPa (11.6 psi), the lowest resilient modulus value of 52 MPa (7,542 psi) was obtained for the base aggregate from STH 32 FC (gravel/crushed gravel). For a confining pressure of 137.9 kPa (20 psi) and bulk stress of 589 kPa (85.4 psi), the highest resilient modulus value of 409 MPa (59,320 psi) was obtained for the base aggregate from STH 59 (crushed carbonate).

Figure 4.24 a presents the variation of the resilient modulus with bulk stress for four virgin crushed stone aggregates that were used in base layer construction at four highways with variable locations (CTH B Woodville, CTH JJ Appleton, USH 45 Larsen, and STH 33 Saukville). The resilient modulus values varied between 81 MPa (11.75 ksi) and 383 MPa (55.5 ksi).

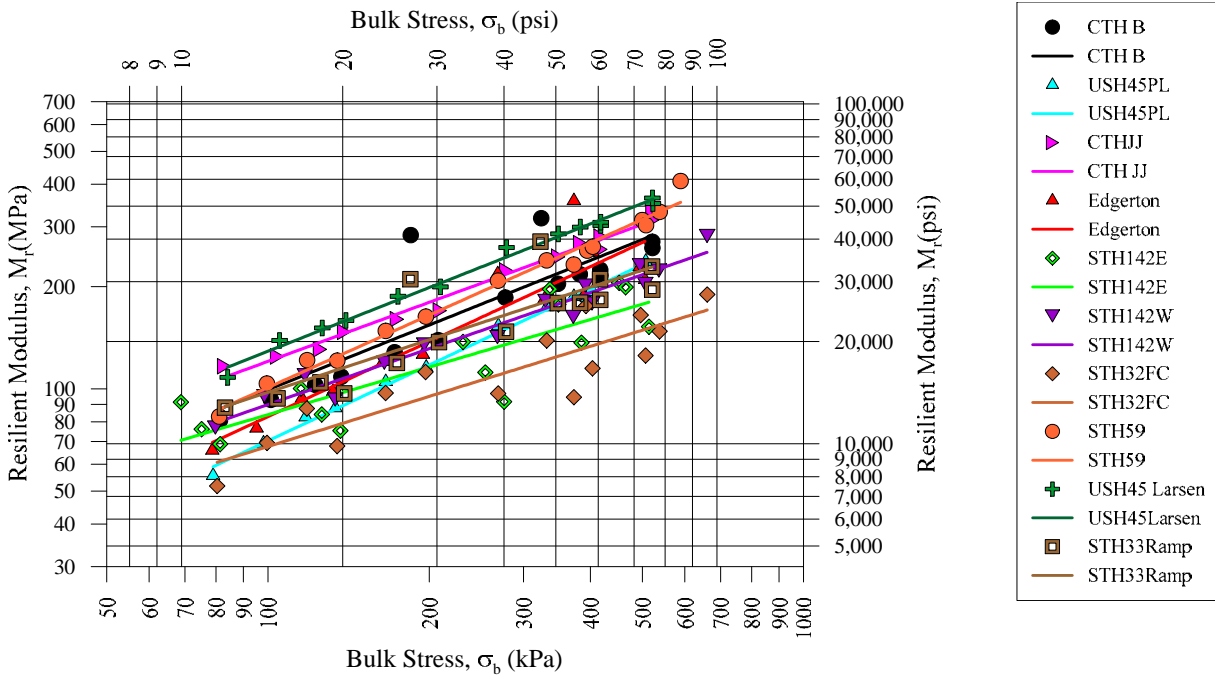
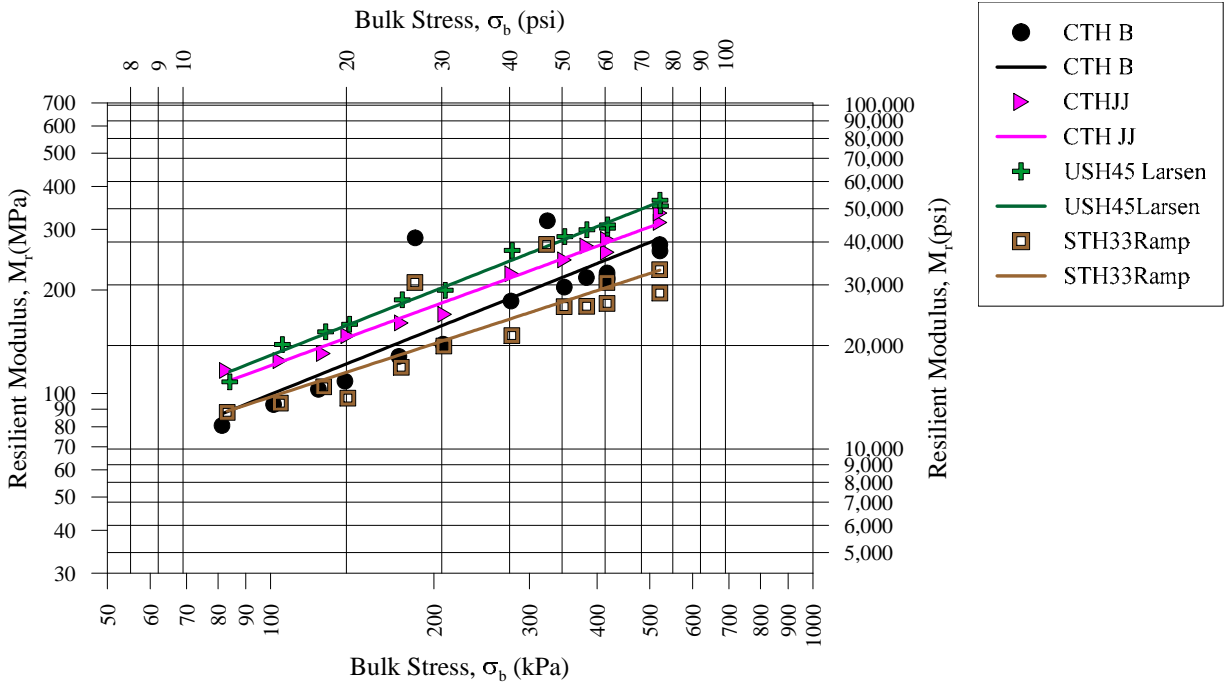


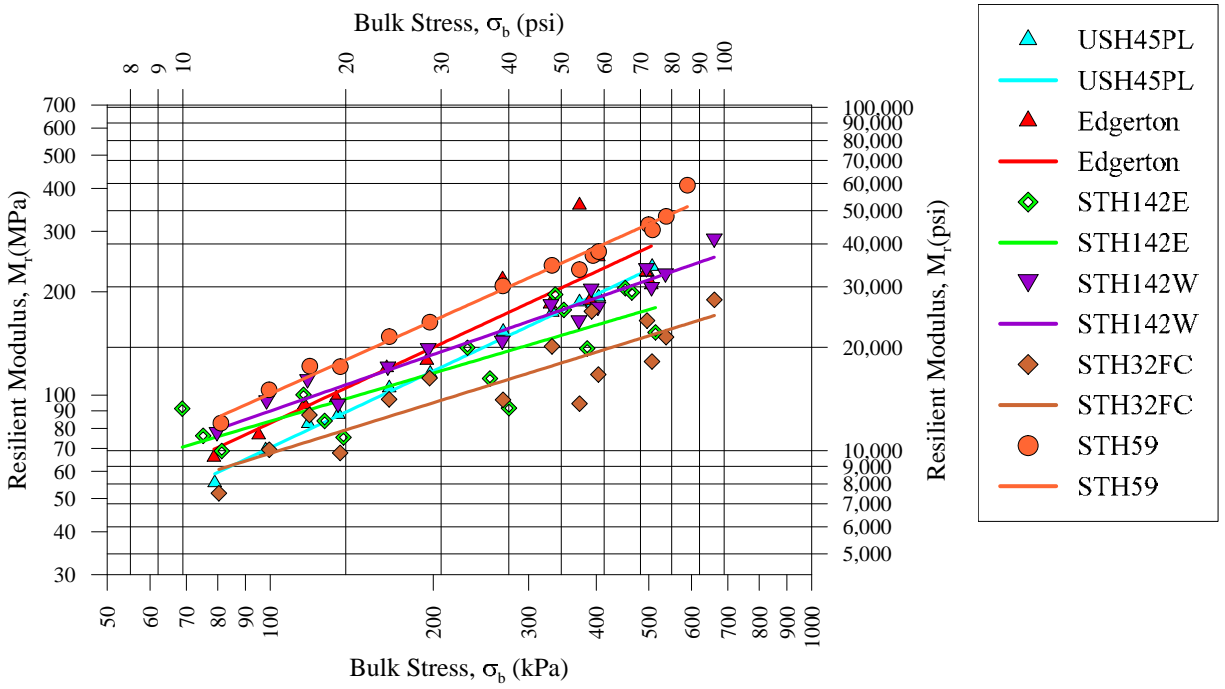
Figure 4.23: Results of the repeated load triaxial test on base layer and virgin aggregates.

The variation of the resilient modulus with bulk stress for six base layer aggregates (one crushed stone aggregate and five gravel/crushed gravel aggregates) are depicted in Figure 4.24 b. The resilient modulus values varied between 52 MPa (7.54 ksi) and 409 MPa (59.32 ksi).

The variation of the resilient modulus trend lines with bulk stress is depicted in Figure 4.25 a. Examination of this figure and the previous figures/data on resilient modulus demonstrates that crushed stone aggregates (both virgin and existing in base layers) exhibited higher resilient modulus values compared with gravel and crushed gravel base layer aggregates. The research team conducted a comprehensive analysis on resilient modulus data of Wisconsin aggregates that were acquired from both quarries (crushed stone) and pits (gravel/crushed gravel). The variation of the resilient modulus with bulk stress for all aggregates mentioned is presented in Figure 4.25 b. Inspection of the figure shows that Wisconsin virgin aggregates (crushed stone and gravel/crushed gravel) exhibited a wide variation in resilient modulus with bulk stress. However, the crushed stone aggregates tested in this study (both virgin and existing base layer) outperformed Wisconsin virgin aggregates as well as the tested base layer gravel/crushed gravel aggregates. The performance of the base layer gravel/crushed gravel aggregates was scattered within a general range with a few point falling below the lower limit as shown in Figure 4.25 b.

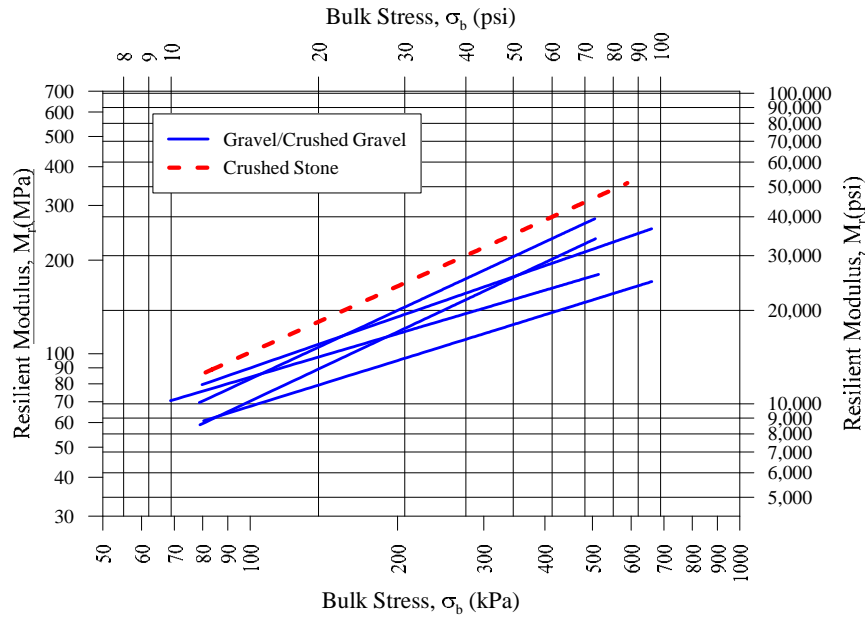


(a) Virgin aggregate used in base layer construction

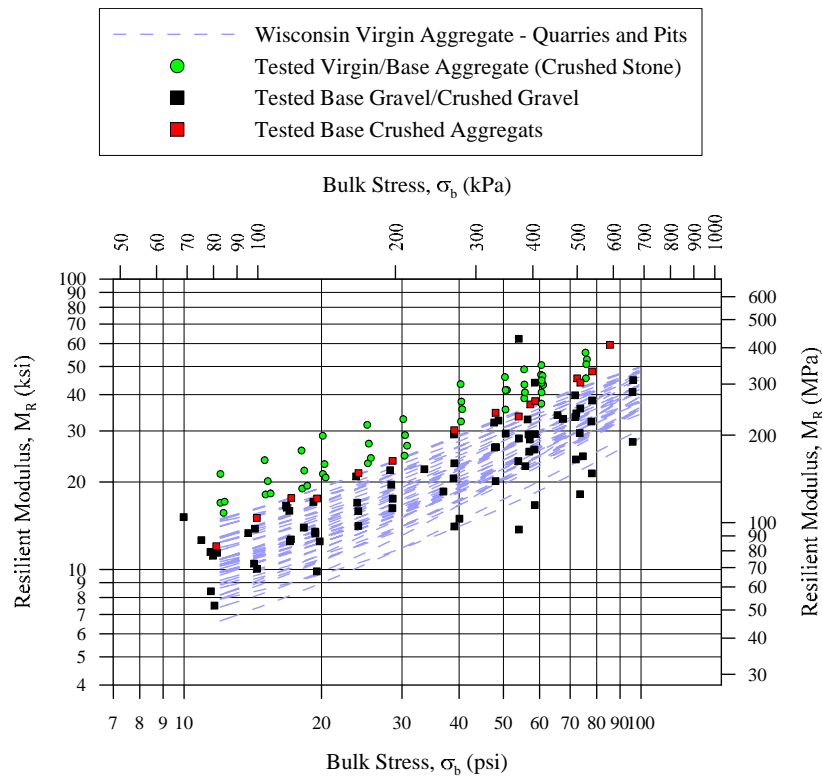


(b) Base layer aggregate (crushed stone and gravel)

Figure 4.24: Results of the repeated load triaxial test on base layer and virgin aggregates.



(a) Crushed stone versus gravel/crushed gravel



(b) Crushed stone and gravel/crushed gravel versus combined Wisconsin aggregate

Figure 4.25: Comparison of the resilient modulus performance of the tested base layer and virgin aggregates with Wisconsin virgin aggregates.

Chapter 5

Analysis of Field Test Results on Aggregate Base Layers

This chapter presents the results of the field testing program on the aggregate base layers of the investigated pavement sections. Field test results are analyzed and critically evaluated.

5.1 Dynamic Cone Penetration Test

The results of the DCP tests on four of the investigated aggregate base layers are shown in Figure 5.1. Multiple DCP tests were conducted at each site whenever possible. The penetration rate profile in in/blow is presented with depth. Figure 5.1 indicates the variability of the aggregate base layer resistance to penetration and therefore, variability in density and uniformity of the base materials at different test locations and depths.

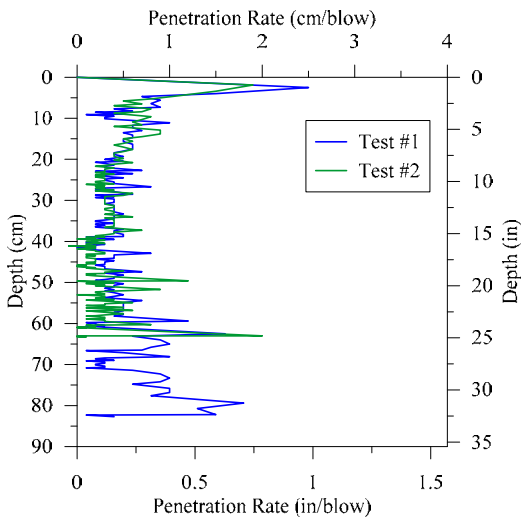
For example, an inspection of Figure 5.1 a shows the resistance to penetration is low in the upper part of the aggregate base layer, with a maximum penetration rate of about 1.0 in/blow for the upper 2.0 in of the I 94-S2 base layer. Then, the penetration resistance increases with depth with an average penetration rate of about 0.25 in/blow, indicating higher density in the lower portions of the base course layer.

The results of the DCP tests were used to estimate changes in the CBR with depth using Kleyn's (1975) equation. The estimated CBR values along with the estimated base course layer thicknesses are presented in Figure 5.2; the figure also compares the soaked CBR values with the DCP-based, estimated CBR values. In Figure 5.2 a, the soaked CBR values for the base aggregates from I 94-S1 and I 94-S2 sources are 76.7% and 73.9%, respectively. The DCP test was performed on the aggregate base layer at I 94-S2 only. The CBR values estimated from the DCP tests are 64.2% and 67.2% for tests 1 and 2, respectively, which are lower than both soaked CBR values. The field measured thicknesses of the aggregate base layer and the underlying subbase/select material layer at the I 94 -S2 site are 11 and 16 in, respectively. The DCP test profiles and the corresponding estimated CBR profile with depth shows agreement with measured field layer thicknesses.

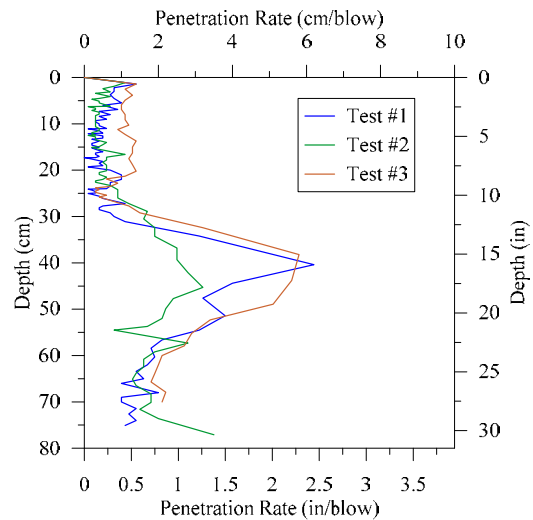
In Figure 5.2 b, the soaked CBR for the base aggregate measured at site STH 33 MR was 58.0% compared with estimated CBR values ranging from 32.7% to 73% using three DCP tests. The CBR values estimated from DCP tests 1 and 2 were higher than the soaked CBR value while the CBR value estimated from DCP test 3 was lower.

The results of the DCP tests and the corresponding estimated CBR profiles with depth demonstrate the spatial variability as well as variability in aggregate base performance (i.e.

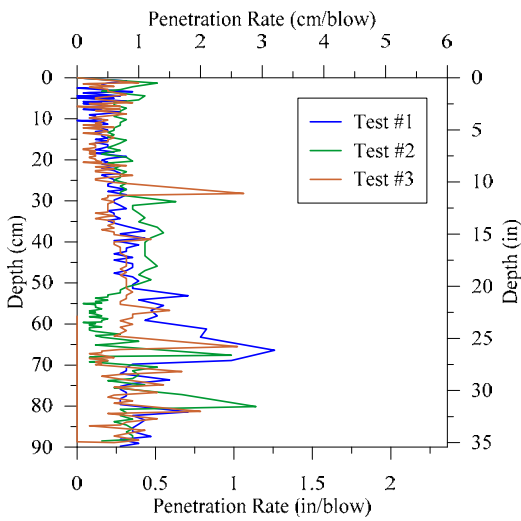
variability of the strength, density and modulus). The results of the DCP tests and corresponding estimated CBR values for the investigated aggregate base layers are presented in Appendix B.



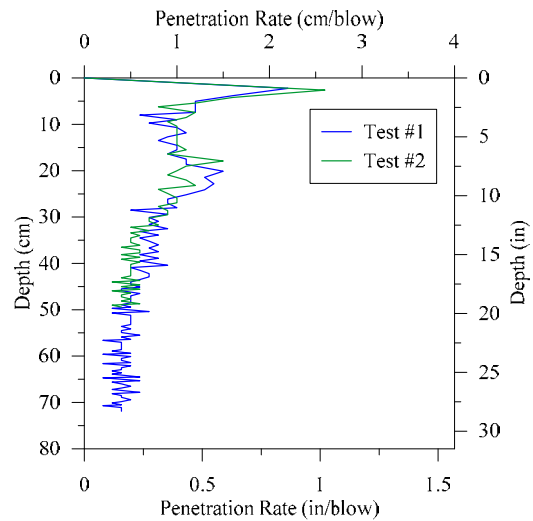
(a) I 94 Zoo Interchange S2



(b) STH 33 Middle Ridge



(c) STH 180 Marinette



(d) USH 53 Minong

Figure 5.1: DCP test results for the base layer aggregates of investigated pavements.

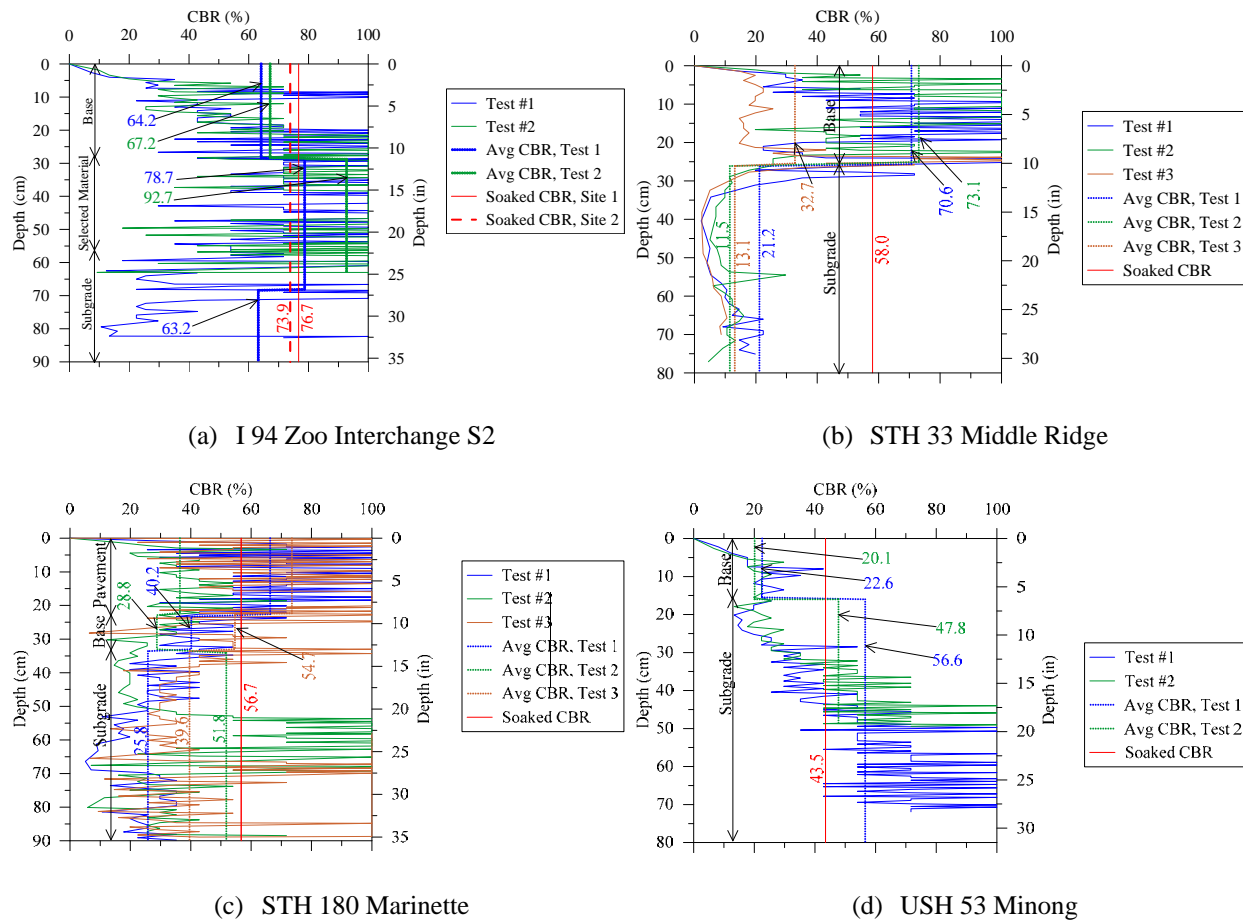


Figure 5.2: Profiles of CBR values estimated from DCP test with depth compared with soaked CBR values from laboratory test.

5.2 Ground Penetrating Radar

The GPR scan files were obtained from WisDOT and analyzed by the research team. The analysis was performed using the RADAN® Software (a GSSI GPR Post Processing Software) utilizing the RoadScan Module. The RoadScan Module uses a signal calibration technique that measures significant layer interface amplitudes from the pavement data and calculates the propagation velocity of the GPR signal through the pavement layer (GSSI, 2018).

For this study, 400 MHz and 1 GHz antennae were used to image the thickness profiles of HMA pavements, including surface, base, and subbase layers. Because GPR systems only capture signal amplitudes versus time, two different calibrations were implemented in the data analysis. The first calibration is needed to determine the reflection at the top of the pavement and to correct the GPR signatures as the antenna height changes as the vehicle moves along the road. The second calibration is required to convert the travel time obtained from the GPR records to the thickness of different layers. There are two alternatives for this calibration. The first alternative is to measure the electromagnetic wave velocity in the pavement structures while the

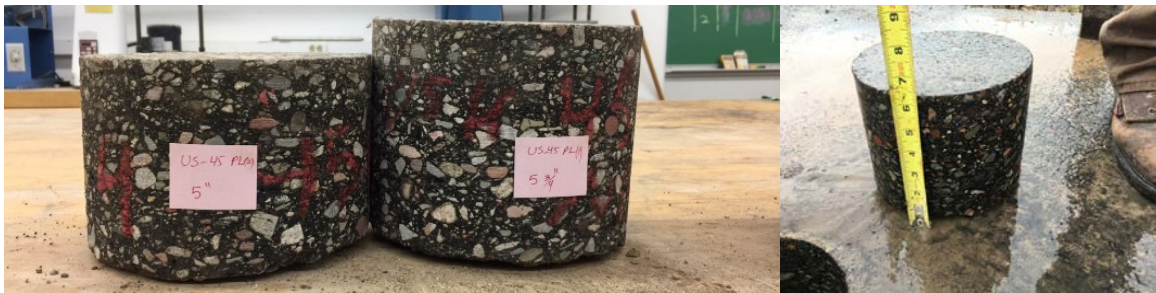
second alternative involves calibrating the data using pavement cores. The second alternative was used in this study. It should be noted that the quality of the profiles can be improved if several cores are collected along the length of the profile. If a limited number of cores were collected, the analysis assumed that the material properties were uniform. If no cores were extracted, velocities were assumed from published velocities for similar materials. Using cores and assuming constant profile properties along road sections, the thicknesses of the layers in pavement substructures were delineated for the investigated pavement test sections.

The location, track of GPR testing, and pavement surface cores for the USH 45 pavement in Pelican Lake are shown in Figure 5.3. The GPR testing was conducted in the N-S direction on the north bound lane. Analysis of the test data (using a relative dielectric permittivity k' of 5) indicated the existence of three layers with the first layer (yellow dots in Figure 5.4) corresponding to the bottom of the HMA layer. The next two layers appear to be base layers; however, the thicknesses of these layers appear to be thinner than the thicknesses presented in the typical cross-section and the thicknesses that were measured by the research team during pavement coring and aggregate sampling. Statistical analyses were conducted on the pavement layer profiles depicted in Figure 5.4. The results showed that the average HMA pavement layer (layer 1) was 5.98 in with a coefficient of variation of 16%, the average thickness of the upper base layer (layer 2) was 2.06 in with a coefficient of variation of 31%, and the average thickness of the lower base layer (layer 3) was 2.83 in with a coefficient of variation of 35%. The profiles of the pavement layer thicknesses, presented in Figure 5.4, show that the average thickness of the HMA layer thickness was 5.98 in compared with the 5 and 5.75 in thick cores extracted from the test site. The average total base layer thickness (layers 2 and 3 in Figure 5.4) was approximately 4.9 in compared with a thickness of 10 in measured by the research team. The GPR test results demonstrate the existence of variability in pavement layer thickness, which is an important factor affecting pavement performance.

Figure 5.5 depicts the location, track of GPR testing, and measured pavement surface thickness of STH 142 E. At this test location, coring was not done, however, there was local pavement reconstruction which allowed the research team to make field measurements as shown in Figure 5.5 b. Analysis of the test data indicates that reflections were not strong and depths varied throughout the survey. In spite of this, it appears that the depth of the HMA layer is at the bottom of the second layer (as shown in Figure 5.6). The survey also appears to show a reflection from the bottom of the base layer, with the depth varying along the length of the survey. The results of the GPR tests on a number of the investigated pavements are presented in Appendix C.

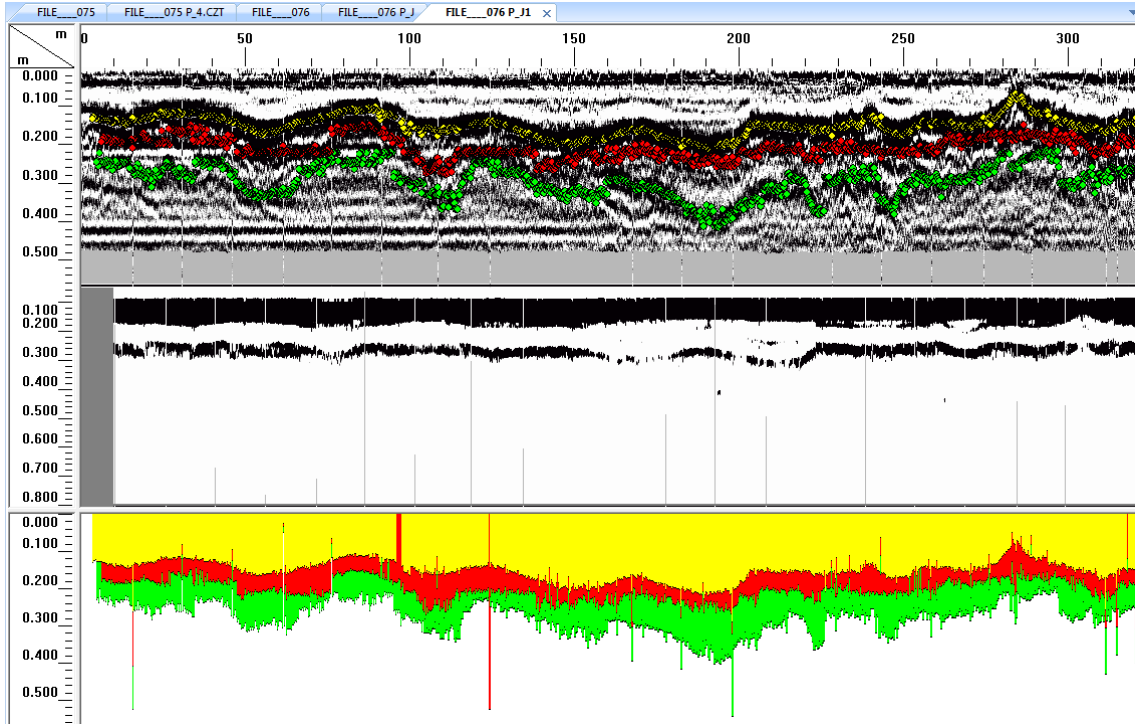


(a) Track of the GPR testing at USH 45 Pelican Lake: outside wheel path of the northbound lane (bottom to top in the picture)

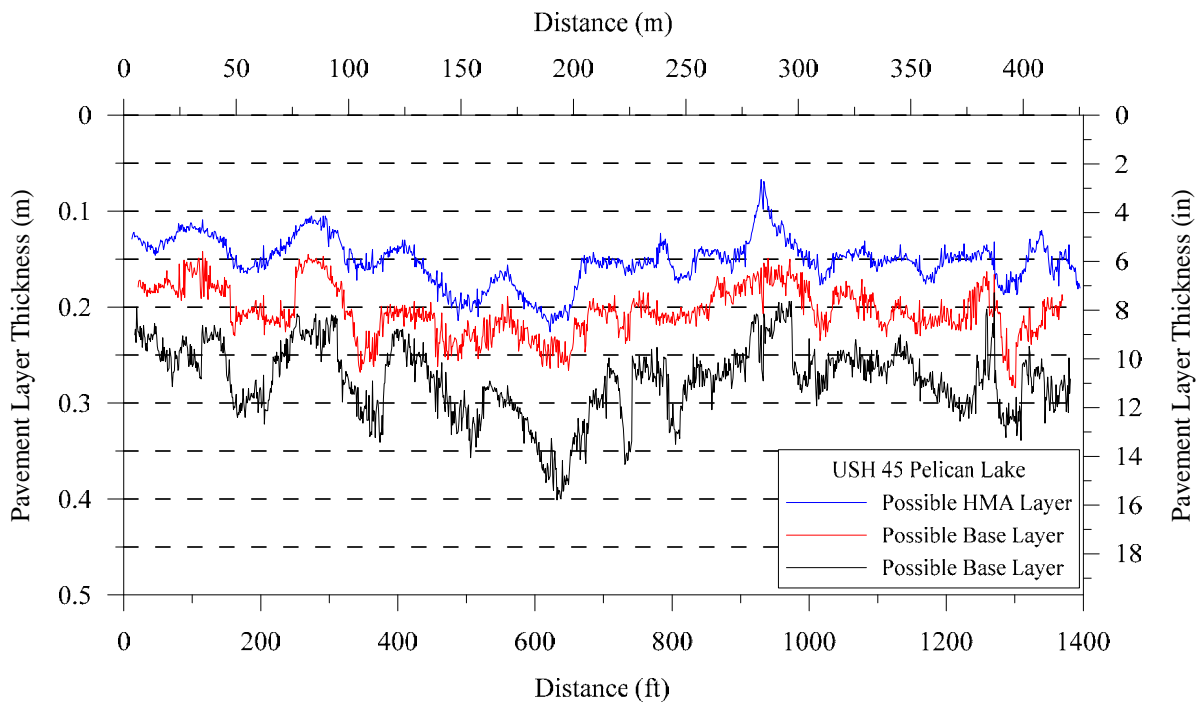


(b) Pavement HMA surface cores of variable thicknesses obtained from USH 45 Pelican Lake

Figure 5.3: Location, track of GPR testing, and pavement surface cores of USH 45 pavement in Pelican Lake, WI.



(a) Pavement layer profiles directly from RADAN



(b) Pavement layer profiles

Figure 5.4: Pavement layer profiles obtained from analysis of GPR data from USH 45 PL

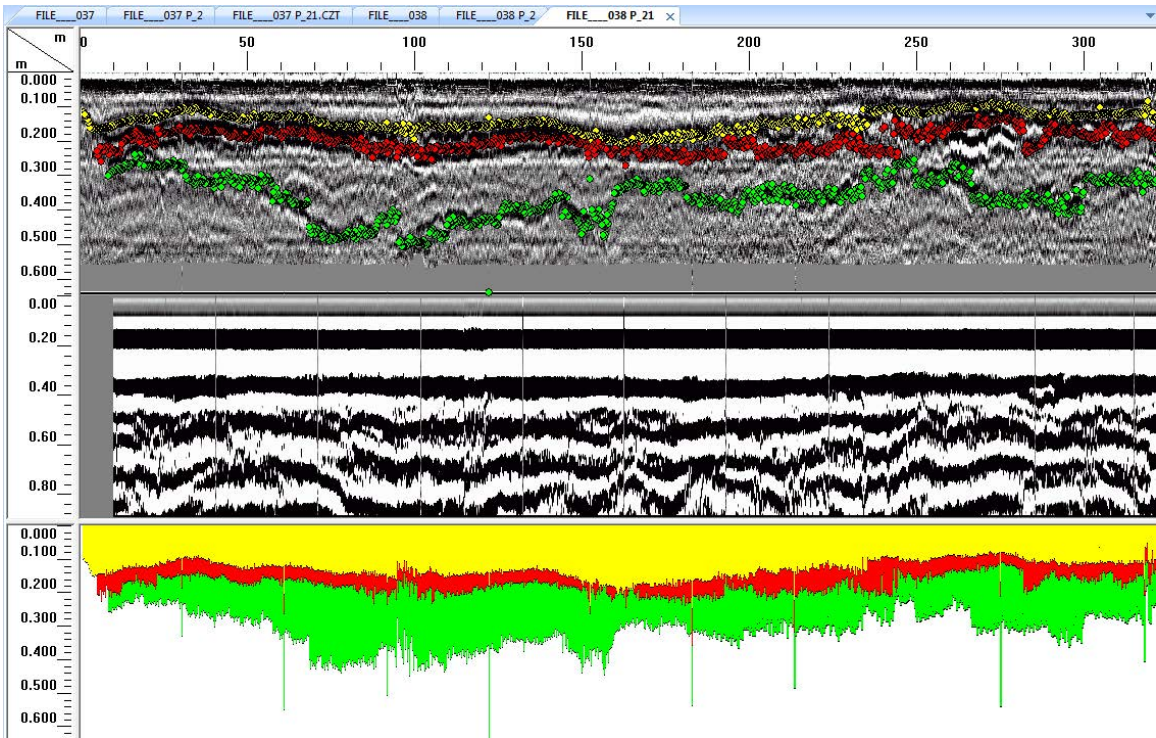


(a) Track of the GPR testing at STH 142 East of Burlington: outside wheel path of the eastbound (left to right in the picture)

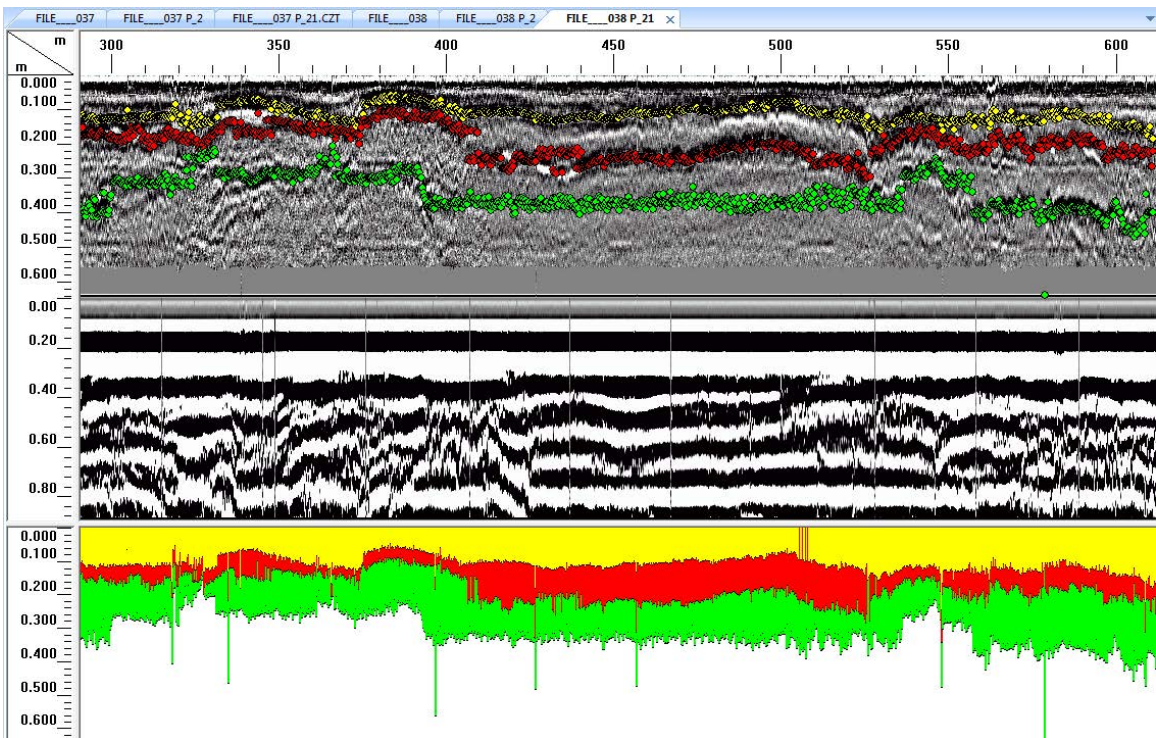


(b) Measured thickness of the excavated pavement layers

Figure 5.5: Location, track of GPR testing, and excavated pavement layers at STH 142 E pavement in east of Burlington, WI.

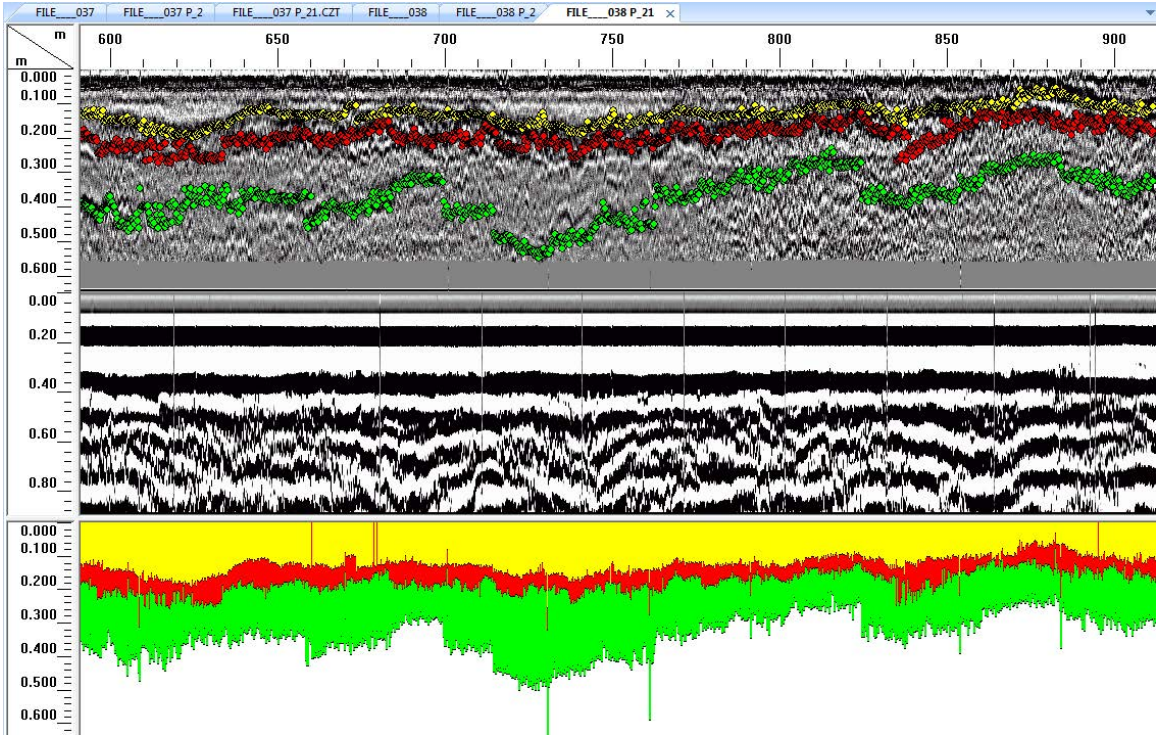


(a) Pavement layer profiles directly from RADAN (0 ~ 350 m)

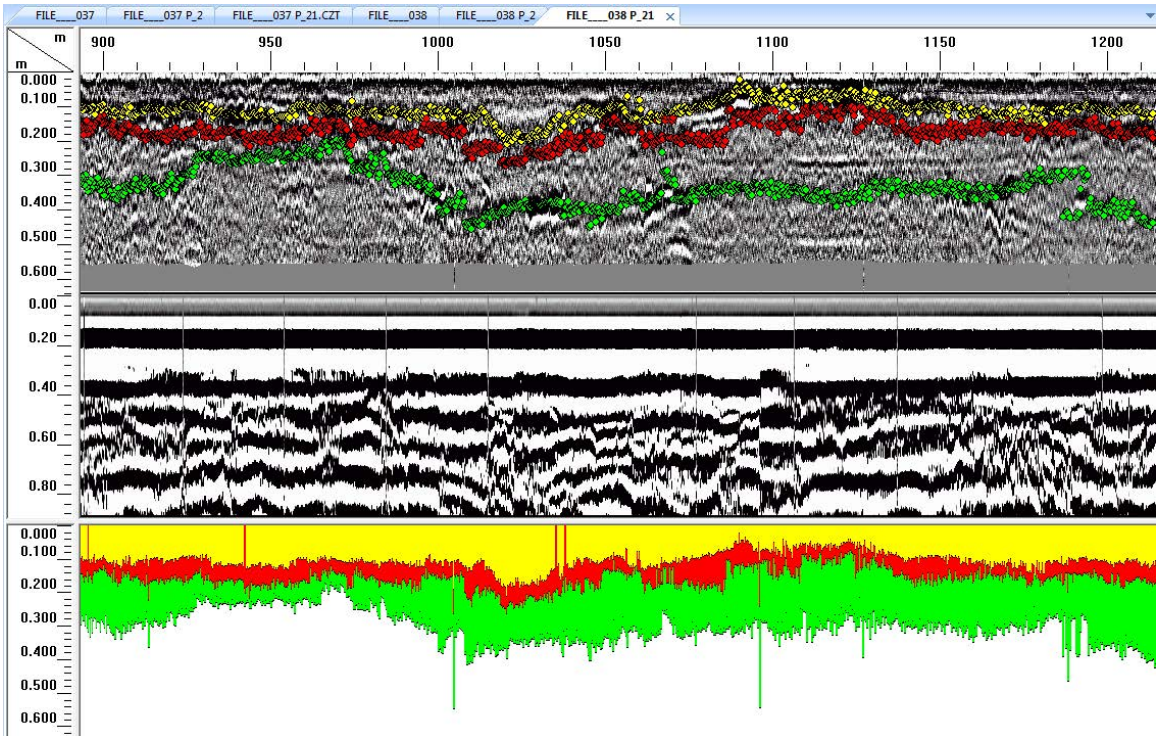


(b) Pavement layer profiles directly from RADAN (275 ~ 625 m)

Figure 5.6: Pavement layer profiles obtained from analysis of GPR data from STH 142E.



(c) Pavement layer profiles directly from RADAN (575 ~ 925 m)



(d) Pavement layer profiles directly from RADAN (875 ~ 1,225 m)

Figure 5.6 (Cont.): Pavement layer profiles obtained from analysis of GPR data from STH 142E.

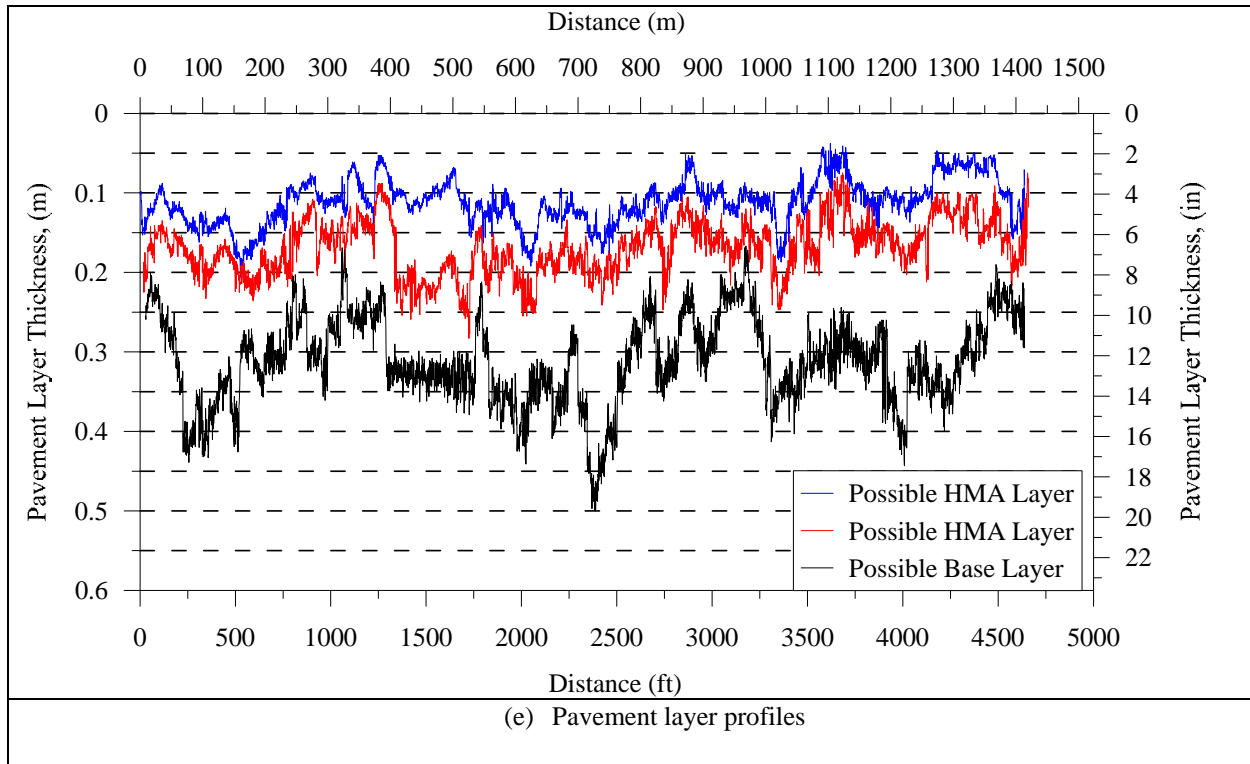


Figure 5.6 (Cont.): Pavement layer profiles obtained from analysis of GPR data from STH 142E.

5.3 Falling Weight Deflectometer

The FWD test data was analyzed using the pavement layer moduli back-calculation software from ERI, Inc. The back-calculation program is widely used to estimate pavement layer moduli from FWD test results. The analysis was conducted by the research team in which pavement layer thicknesses were obtained from WisDOT project plans, existing soils reports/pavement coring by WisDOT and consultants, and measurement by the research team during pavement coring/excavation/cutting. All analysis steps necessary to predict layer moduli values were executed. For example, pavement deflections were normalized to the 9,000 lb load and then adjusted for temperature variations.

The variation with distance of the deflection under the loading plate (D_0) for all investigated HMA investigated pavements is presented in Table 5.1 and depicted in Figure 5.7. In general, the adjusted normalized, D_0 variation range was between 3.3 and 36.6 mils. In order to consider a poor performing pavement, Figure 5.8 depicts the variation of the adjusted normalized D_0 with distance for Edgerton Ave and STH 142 E, respectively. Inspection of this figure indicates that D_0 values showed high variability with distance, with D_0 values ranging between 7.98 and 32.12 mils (COV of 33.34%) for FWD testing on Edgerton Ave pavement and with D_0 ranging from 4.5 to 16.5 mils (COV of 27.8%) for STH 142 E. The variation with

distance of the deflection under the loading plate for all investigated HMA pavements is shown in Appendix D.

The results of the back-calculation analysis conducted on the FWD results are summarized in Table 5.2. The back-calculated modulus for the HMA layer (E_{HMA}) for all investigated pavements varies significantly among the pavement test sections and within individual pavement sections with COVs ranging between 11% and 183%. As an example, for Edgerton Ave, E_{HMA} ranged from 69 to 375 ksi with an average of 177 ksi and COV of 44%. For STH 142 E, the E_{HMA} values varied between 65 and 409 ksi with an average of 150 ksi and COV of 49%. The distribution with distance of the back-calculated elastic moduli for the HMA surface layer, the aggregate base layers, and subgrade for Edgerton Ave and STH 142 E is presented in Figure 5.9. An inspection of this figure indicates significant variability of layer and subgrade moduli.

The maximum, minimum, and average E_{HMA} as well as COV values are summarized in Table 5.2. The variability in E_{HMA} is not necessarily exclusively dependent on the base course layer variability. There are other factors that may influence the mechanical stability of HMA (mix design, compaction temperature, compaction effort, density) and, most importantly, variability in layer thickness (as demonstrated by the GPR profiles).

Table 5.1: Statistical summary of adjusted deflection under loading plate (D_0) normalized to 9,000 lb load for investigated HMA pavements.

Pavement Test Section	Average (mils)	COV (%)	Max. (mils)	Min. (mils)
STH 142 E	9.1	27.8	16.5	4.5
USH 45 PL	7.9	47.1	22.6	4.1
STH 33 Ramp	11.6	12.5	14.1	8.9
CTH JJ	6.9	13.7	8.8	5.2
CTH B	10.4	13.9	12.1	7.1
Edgerton	16.7	33.4	32.1	8.0
CTH II	13.0	18.9	18.2	9.9
STH 59	13.8	22.9	21.1	9.5
STH 13 Spencer S1	7.5	14.5	9.9	6.3
STH 13 Spencer S2	4.1	15.4	5.3	3.3
STH 13 Spencer S3	7.5	14.3	9.8	5.7
STH 13 Spencer S4	7.1	24.2	10.4	5.2
STH 32 FC	13.3	23.5	20.8	5.0
STH 32 OC	12.6	27.7	24.6	9.0
STH142W-SB	16.7	33.2	22.6	4.1
SHT142-W-NB	20.1	22.7	27.9	12.7
STH 33 MR	24.3	19.0	36.6	11.4
STH36-SB-PL	8.9	29.6	12.6	5.2
STH36-SB-PL2	9.8	34.6	17.2	4.8
STH36-NB-PL	8.9	19.5	12.9	6.0

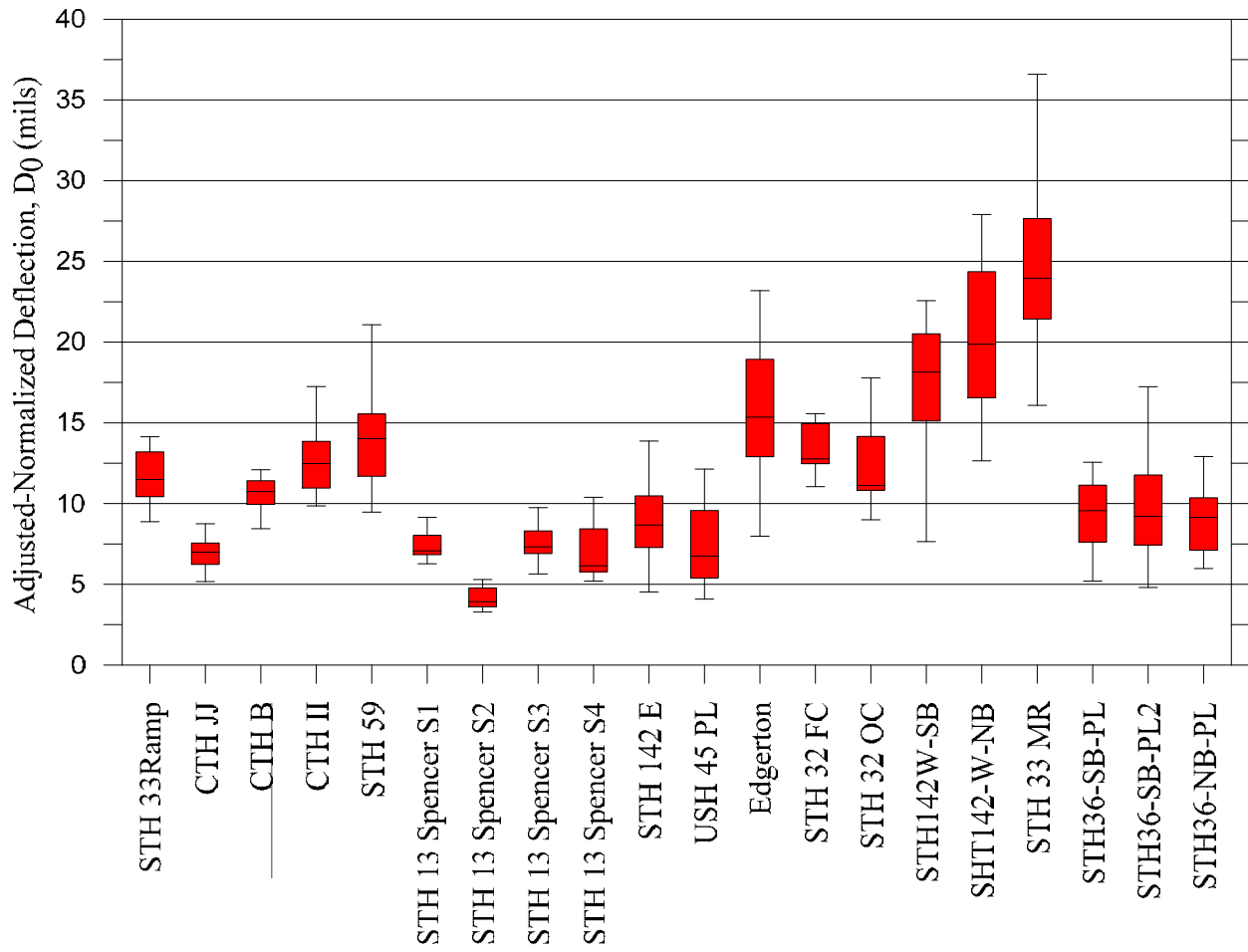


Figure 5.7: Adjusted deflection under loading plate (D_0) normalized to 9,000 lb load for investigated HMA pavements.

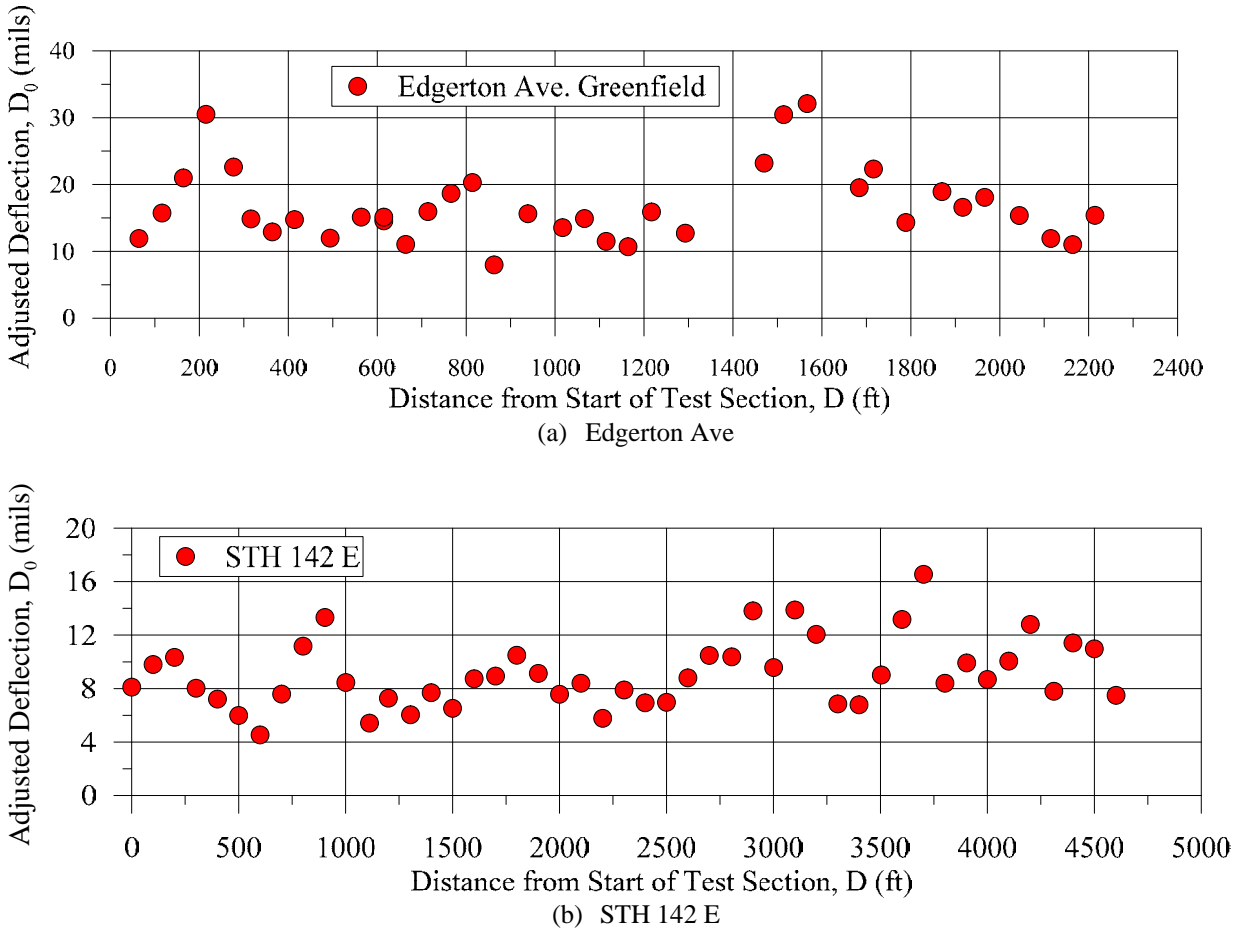


Figure 5.8: Variation of deflection (D_0) under the loading plate.

The back-calculated moduli for the aggregate base layers (E_{Base}) for all investigated pavement test sections are summarized in Table 5.2. These indicate significant variability of E_{Base} (ranging from 4 to 400 ksi) within individual pavement test sections and among pavements. The back-calculated E_{Base} for Edgerton ranges from 3.91 to 50.5 ksi with an average of 21 ksi and COV of 56%. A similar trend was observed for the layer moduli of STH 142 E where the lognormal distribution was used to represent the test results for the base layer moduli as shown in Figure 5.9. An inspection of this figure demonstrates the variability of the back-calculated E_{Base} distribution along test sections of Edgerton Ave and STH 142E. The variability of the back-calculated E_{Base} is evident from the statistical analysis of E_{Base} .

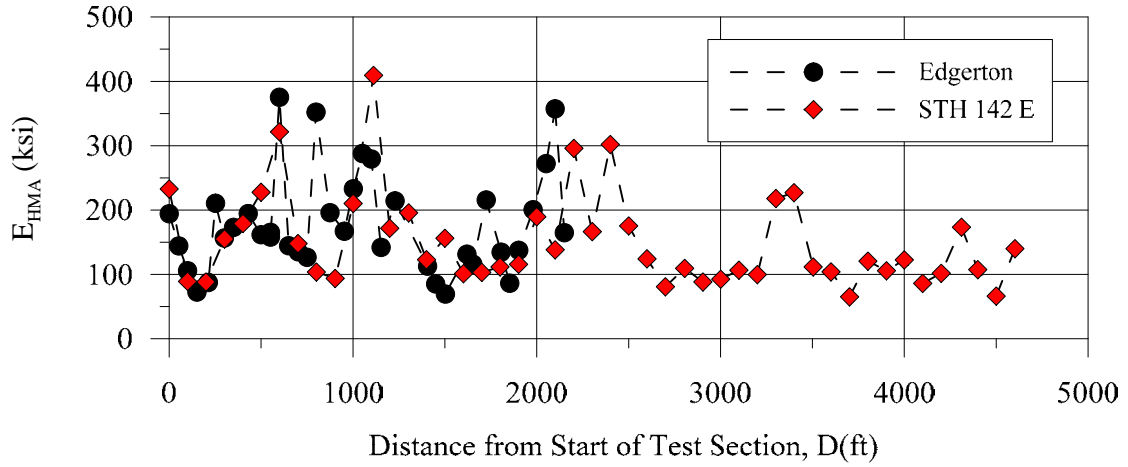
The results of the back-calculated subgrade modulus ($E_{Subgrade}$) are presented in Table 5.2. For Edgerton Ave, $E_{Subgrade}$ ranged from 8 to 26 ksi with an average of 14 ksi and COV of 26%. For STH 142 E, $E_{Subgrade}$ varied between 11 and 43 ksi with an average of 19 ksi and COV of 34%. The distribution with distance of $E_{Subgrade}$ for both pavement test sections is shown in Figure 5.9. The maximum and minimum predicted $E_{Subgrade}$ as well as average and COV values

are summarized in Table 5.2. The variability with distance of the subgrade modulus is evident in all investigated sections.

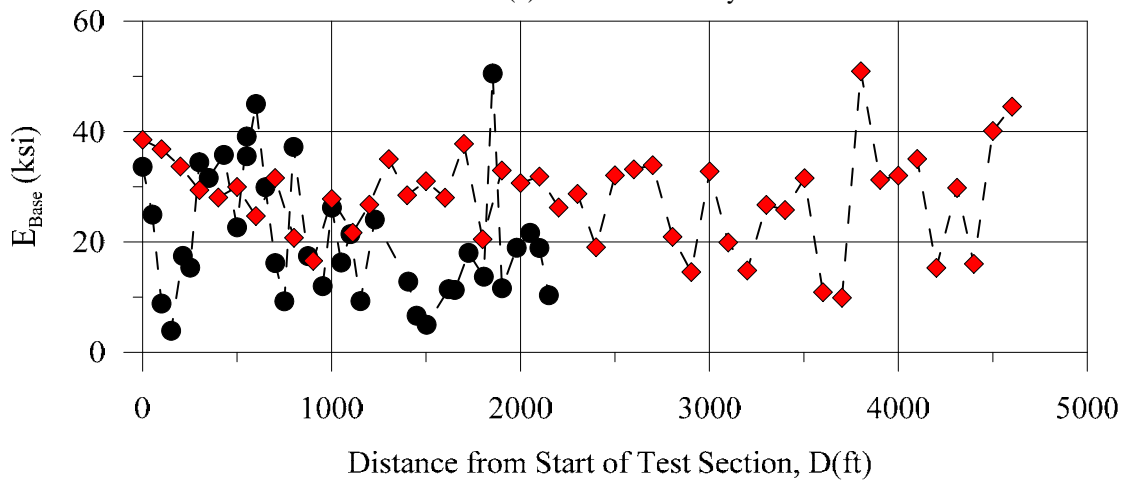
Figures 5.10 and 5.12 present the back-calculated layer moduli values for each pavement test section in a box-whisker plot. The plots show the range and median of the back-calculated layer moduli. Figure 5.13 depicts the lognormal distributions of back-calculated layer moduli for aggregate base layers constructed with gravel/crushed gravel for weak bases at the STH 142 E and Edgerton Ave sites.

Table 5.2: Statistical summary of back-calculated layer moduli for investigated HMA pavements.

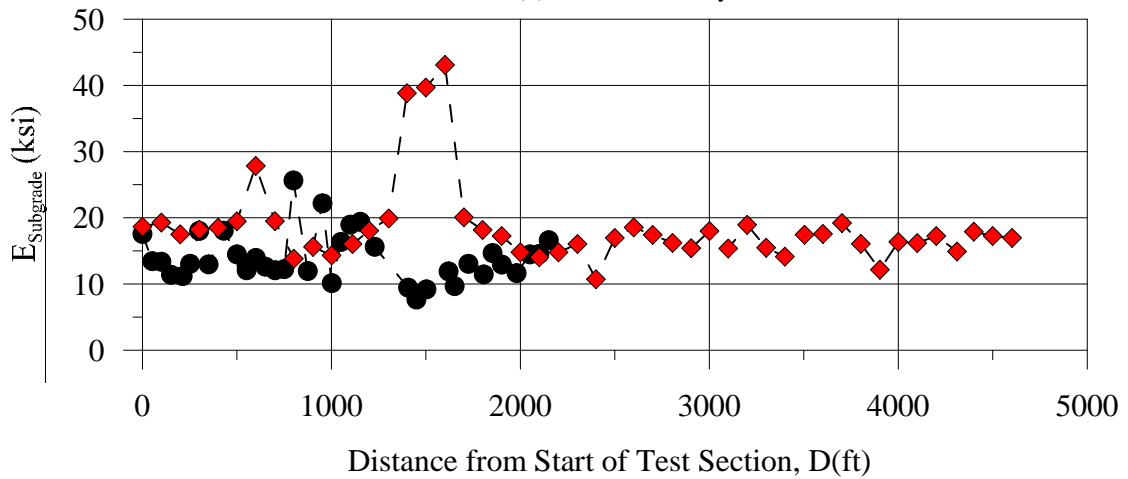
Pavement Test Section	E_{HMA} (ksi)				E_{Base} (ksi)				$E_{Subgrade}$ (ksi)			
	Mean (ksi)	COV (%)	Max. (ksi)	Min. (ksi)	Mean (ksi)	COV (%)	Max. (ksi)	Min. (ksi)	Mean (ksi)	COV (%)	Max. (ksi)	Min. (ksi)
STH142E	150	49	409	65	28	30	51	10	19	34	43	11
USH45PL	4,319	56	8,451	419	26	89	100	8	37	29	63	21
STH33 Ramp	792	33	1,553	358	18	28	30	9	19	12	23	15
CTH JJ	192	19	288	143	126	23	180	80	24	13	29	18
CTH B	875	41	1,687	390	34	16	46	30	19	18	25	14
Edgerton	177	44	375	69	21	56	51	4	14	26	26	8
CTH ii	488	57	1,233	297	45	21	58	24	23	20	33	16
STH 59	181	32	291	114	54	51	102	20	17	42	33	12
STH 13-S1	406	15	573	323	41	18	55	24	18	13	22	15
STH 13-S2	204	11	233	164	133	25	187	83	23	10	26	19
STH 13-S3	391	14	461	243	38	30	65	18	23	12	28	17
STH 13-S4	454	33	725	238	39	50	71	14	16	9	18	14
STH 32 FC	243	63	781	100	21	8	24	17	25	32	54	18
STH 32 OC	753	43	1,186	200	16	22	23	10	9	47	21	6
STH142W SB	160	70	440	50	26	15	34	19	12	17	19	10
STH142W NB	652	183	4,156	68	23	30	36	9	16	39	34	11
STH 33 MR	180	72	792	50	25	17	35	17	10	21	16	7
STH36-SB PL2	735	59	2,663	296	60	130	257	5	37	27	52	23
STH36-SB PL	720	38	1,140	353	139	123	400	9	32	19	43	22
STH36NB PL	1,058	132	9,000	465	64	98	261	12	30	33	54	17



(a) HMA surface layer



(b) Base course layer



(c) Subgrade

Figure 5.9: Back-calculated layer moduli for HMA surface layers, aggregate base layers constructed with gravel/crushed gravel, and subgrade soils (STH 142 E and Edgerton Ave – weak bases).

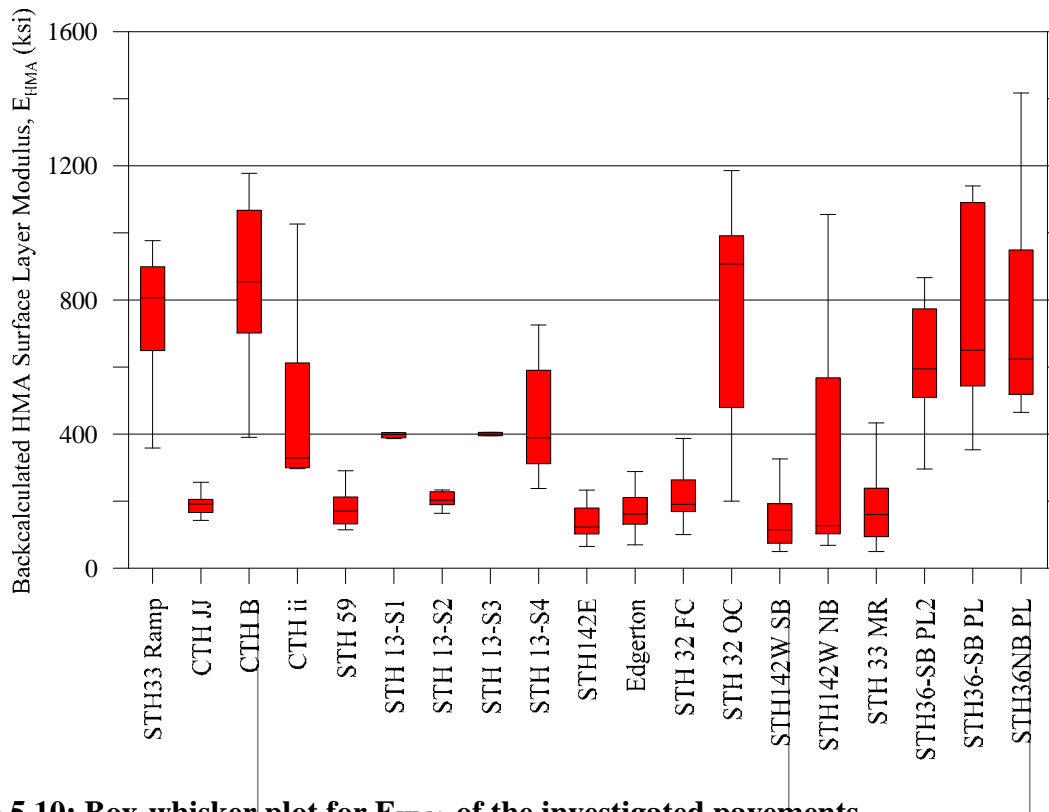


Figure 5.10: Box-whisker plot for E_{HMA} of the investigated pavements.

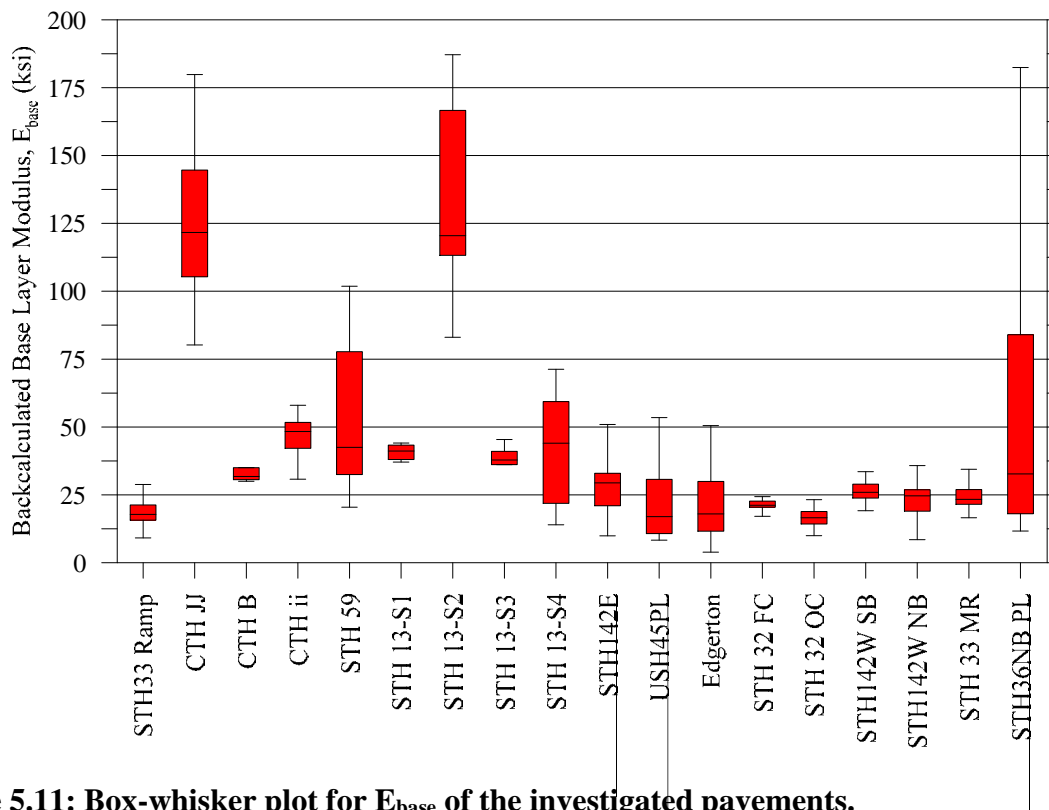


Figure 5.11: Box-whisker plot for E_{base} of the investigated pavements.

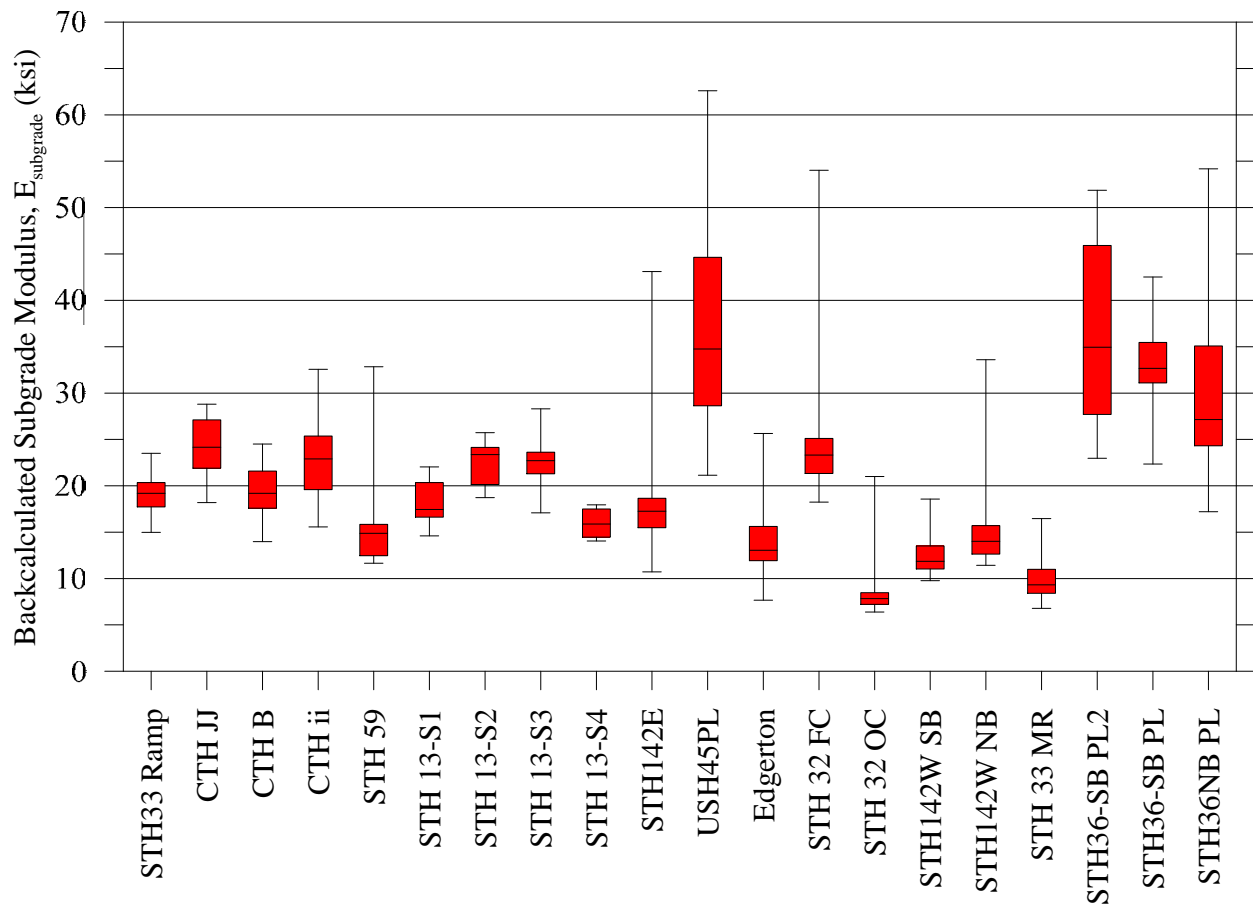
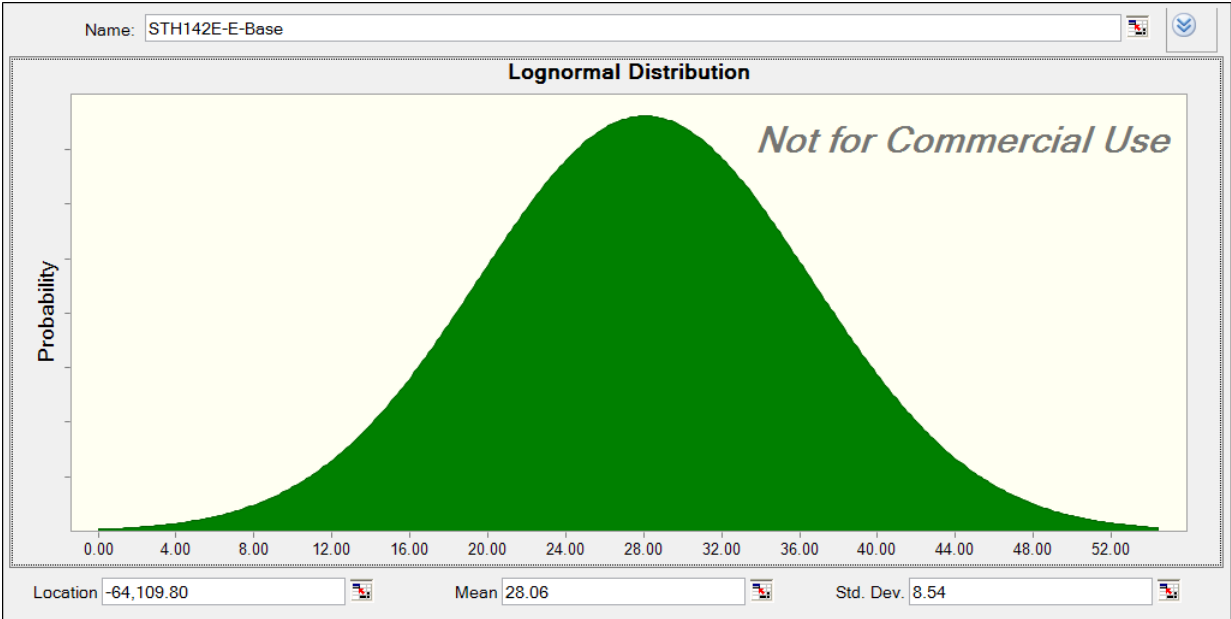
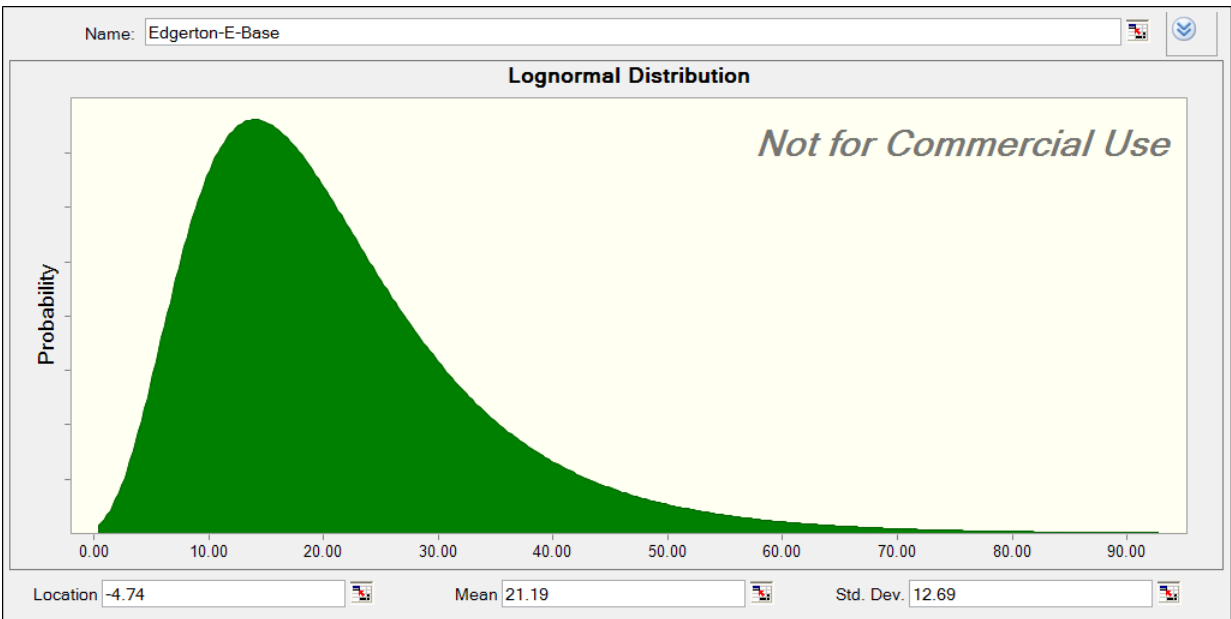


Figure 5.12: Box-whisker plot for E_{subgrade} of the investigated pavements.



Statistic Lognormal distribution: Mean: 28.06 ksi, Standard Deviation: 8.54 ksi, and Coefficient of Variation: 30.43%

(a) STH 142 E Base Modulus



Statistic Lognormal distribution: Mean: 21.19 ksi, Standard Deviation: 12.69 ksi, and Coefficient of Variation: 59.88%

(b) STH 142 E Base Modulus

Figure 5.13: Distribution of back-calculated layer moduli for aggregate base layers constructed with gravel/crushed gravel (STH 142 E and Edgerton Ave – weak bases).

5.4 Visual and Automated Distress Surveys

Figure 5.14 depicts the location of the test section, typical pavement surface distress, variation of ride quality, and PCI for USH 45 Pelican Lake pavement. Various pavement surface distresses were observed at USH 45 PL, including rutting and significant transverse and longitudinal cracking as depicted in Figure 5.14 b and c. In addition, measured pavement surface roughness reflected on the ride quality as indicated by the IRI shown in Figure 5.14 d. With such ride quality and pavement surface distresses, the PCI for this pavement indicated a rating that ranged between poor and very poor performance, as depicted in Figure 5.14 f. The results from other investigated pavement sections are presented in Figures 5.15-17 and in Appendix E.

Figure 5.18 depicts a summary of the results of the visual and automated distress surveys (in terms of calculated PCI). The classification of the pavement condition as either poor, fair, or good is also presented in the figure. The PCI values evaluated by the research team are, in general, lower than the PCI values obtained from WisDOT PIF files.



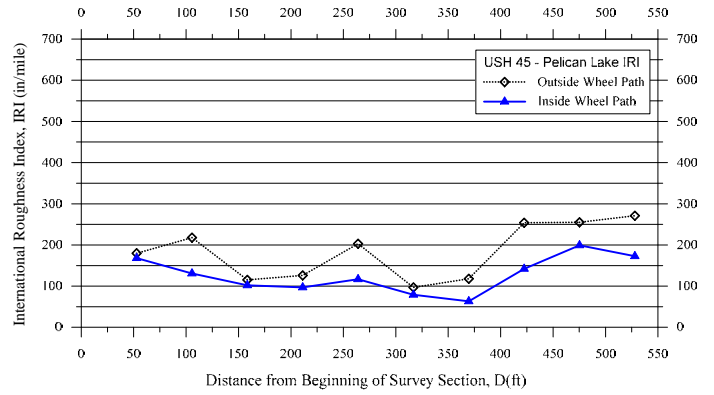
a) Pavement test section



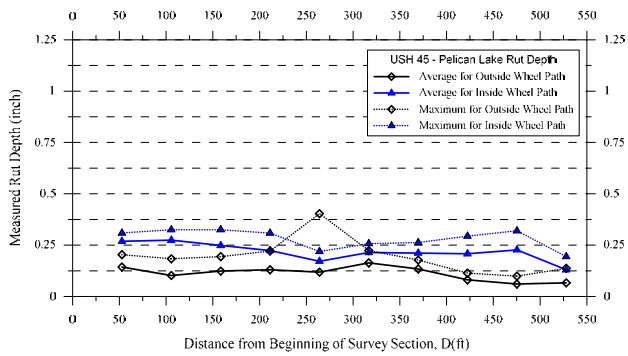
b) Pavement surface distresses



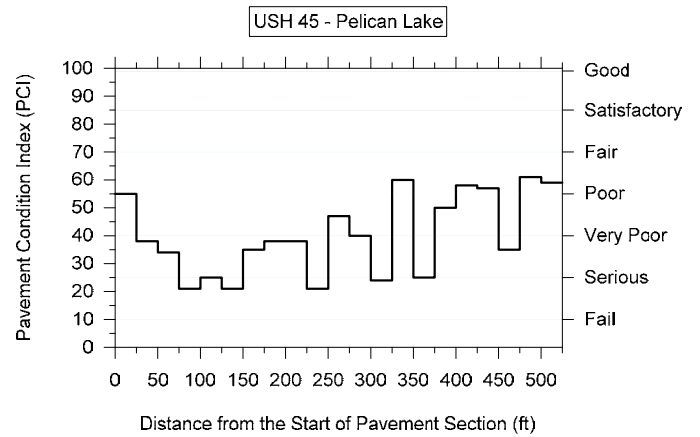
c) Pavement surface distresses



d) IRI calculated using WisDOT PIF database



e) Rut depth calculated using WisDOT PIF database



f) PCI calculated from the UWM visual distress survey

Figure 5.14: Results of visual and automated distress surveys at USH 45 – Pelican Lake.



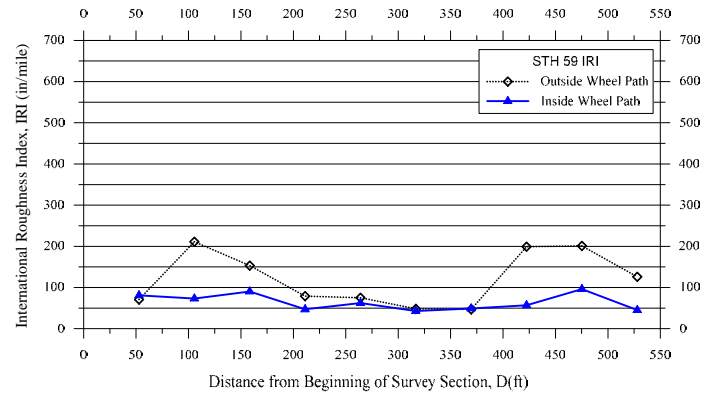
a) Pavement test section



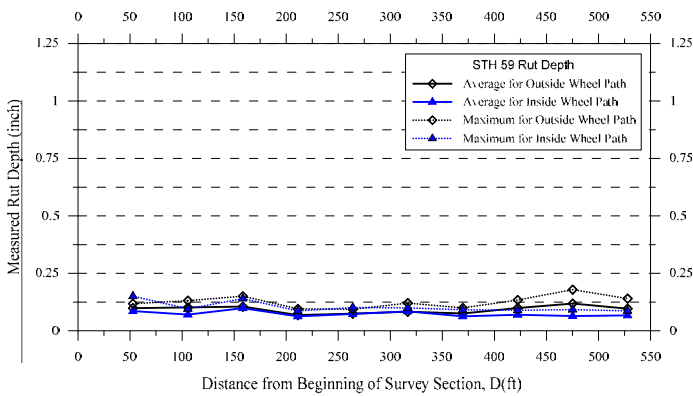
b) Pavement surface distresses



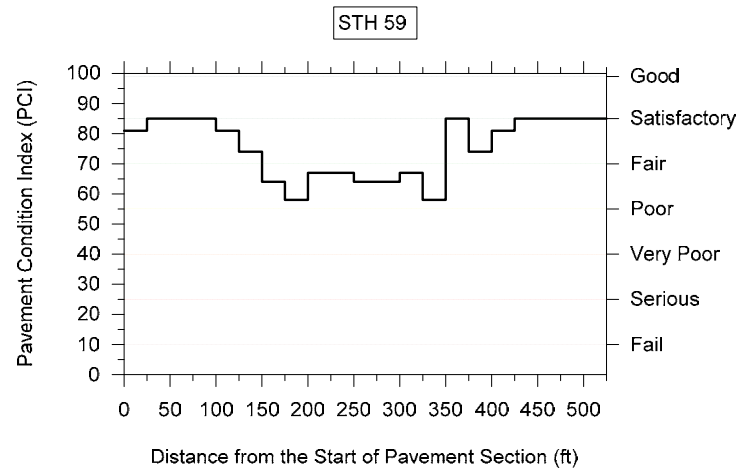
c) Pavement surface distresses



d) IRI calculated using WisDOT PIF database



e) Rut depth calculated using WisDOT PIF database



f) PCI calculated from the UWM visual distress survey

Figure 5.15: Results of visual and automated distress surveys at STH 59 – Edgerton.



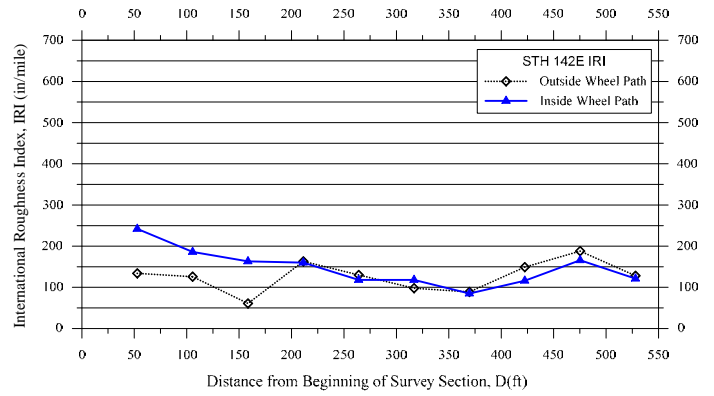
a) Pavement test section



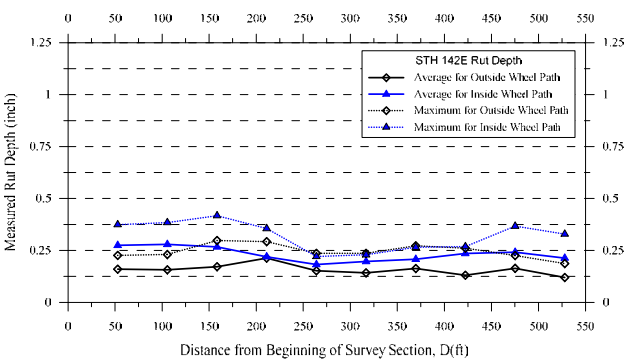
b) Pavement surface distresses



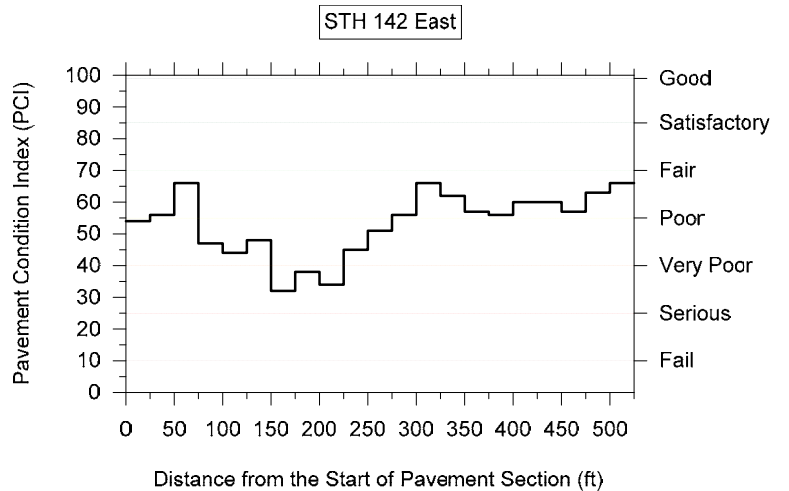
c) Pavement surface distresses



d) IRI calculated using WisDOT PIF database

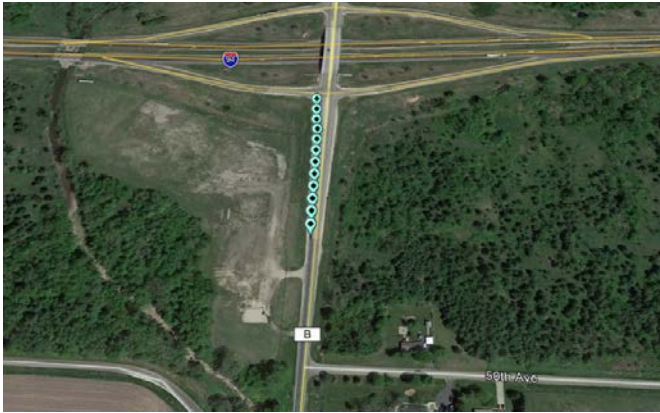


e) Rut depth calculated using WisDOT PIF database



f) PCI calculated from the UWM visual distress survey

Figure 5.16: Results of visual and automated distress surveys at STH 142 E – Burlington.



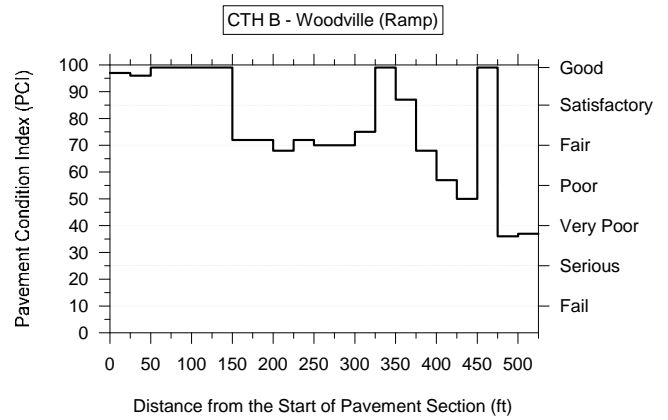
a) Pavement test section



b) Pavement surface distresses



c) Pavement surface distresses



d) PCI calculated from the UWM visual distress survey

Figure 5.17: Results of the visual distress survey at CTH B – Woodville (Ramp).

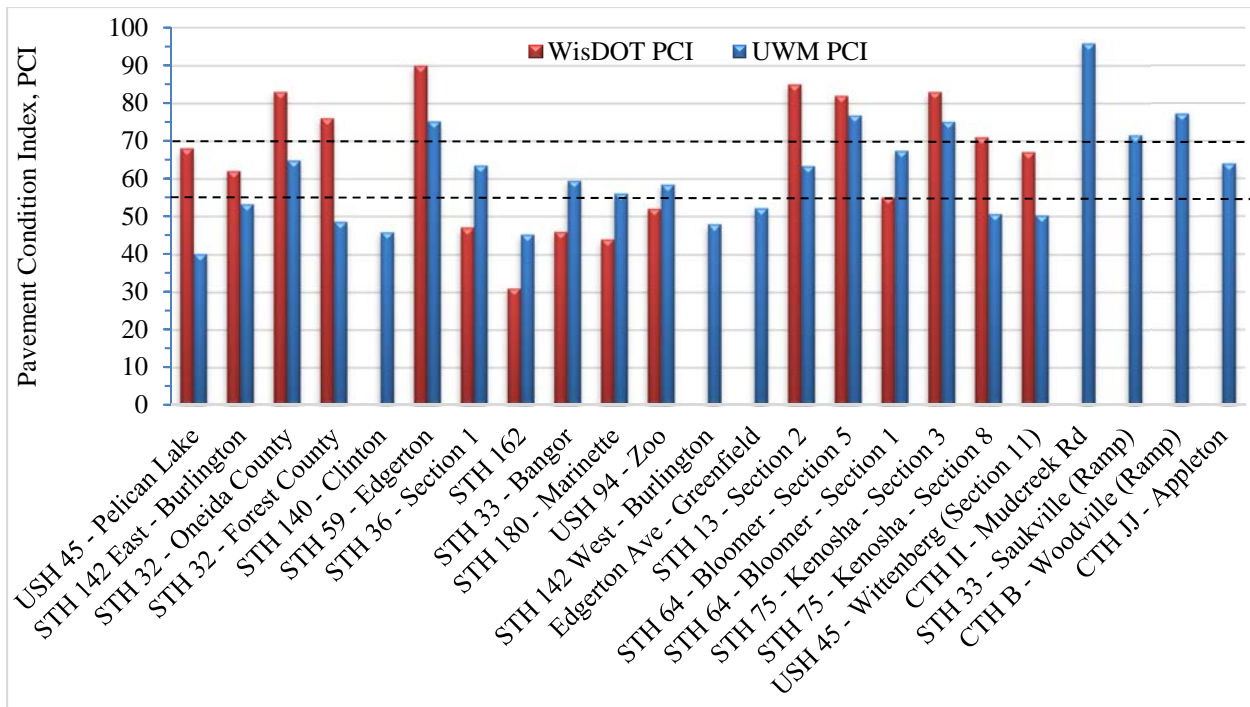


Figure 5.18: Comparison of PCI calculated from the visual and automated distress surveys (PCI < 55 is poor, 55 ≤ PCI < 70 is fair, PCI ≥ 70 is good).

Chapter 6

Evaluation of Investigated Base Layer Aggregates

This chapter presents a critical evaluation of the investigated base course layer aggregates in flexible pavements. Evaluation is presented in terms of statistical analysis of laboratory and field test results with respect to pavement performance.

6.1 Base Aggregate Properties – Correlations

Evaluation of laboratory test results from various studies conducted on Wisconsin virgin aggregates (including results from the WisDOT database and WHRP studies discussed in Chapter 4) showed mixed results with respect to correlations of individual aggregate properties. For example, coarse aggregate absorption values showed good correlation with Micro-Deval abrasion loss values but poor correlation with sodium sulfate soundness test values.

For the investigated base layer aggregates, statistical analyses were conducted to examine the correlations between the individual aggregate properties determined from laboratory and field tests in addition to other parameters. The analyses included multiple regression using the programs Statistica and Minitab, in an attempt to evaluate the performance of the investigated pavement sections (indicated by the PCI) using various base layer aggregate laboratory and field test results and parameters.

First, one to one correlations were attempted. Figure 6.1 depicts the plots and histograms of the individual properties/parameters of the investigated base layer aggregates. The aggregate test results and parameters evaluated were: coarse aggregate Micro-Deval abrasion loss (MDCA), fine aggregate Micro-Deval abrasion loss (MDFA), coarse aggregate sodium sulfate soundness loss (SSSCA), fine aggregate sodium sulfate soundness loss (SSSFA), coarse aggregate absorption (ABS), gravel content (G), sand content (S), fines content (F), FM, soaked CBR, IRI for both right (IRI_R) and left (IRI_L) wheel paths, and the FWD back-calculated E_{base} . Table 6.1 presents the correlation matrix for one of the various attempts (depicted in Figure 6.1) conducted during this research. Examination of the correlation matrix shows that the results of the tests and parameters for the investigated base layer aggregates are mixed and did not, in general, exhibit strong correlations between the various aggregate properties/parameters.

Multiple regression analysis was conducted to evaluate correlations between the PCI of the investigated pavement sections and the various base layer aggregate properties/parameters. The pavement condition index calculated from the visual distress survey, rather than the automated distress survey, was considered in the regression analysis. Various combinations of variables were considered in the analysis, including the square, square root, log, and cube root of each variable. The normality plots were obtained for each variable and used to make the decision to include it the multiple regression analysis or not. For example, normality plots for CBR,

CBR², \sqrt{CBR} , $\sqrt[3]{CBR}$, and log (CBR) were graphed and evaluated based on normality distribution. Equation 6.1 presents the results of the multiple regression analysis in which the PCI can be estimated from aggregate properties pertaining to abrasion/soundness and particle size distribution tests as follows:

$$PCI = 5.9 - 3.31MDCA - 1.26MDFA + 1.72SSSCA - 0.96SSSFA - 10.09ABS + 29.26FM + 1.23F \dots\dots\dots(6.1)$$

The predicted versus measured PCI values for the various pavement sections using Equations 6.1 are shown in Figure 6.2; the coefficient of determination for the relationship between them was 0.63. Another relationship between PCI, CBR, E_{base}, and IRI is described in Equation 6.2:

$$PCI = 65.1 + 0.12CBR + 0.07E_{base} - 0.106IRI_L - 0.017IRI_R \dots\dots\dots(6.2)$$

The predicted versus measured PCI values for Equation 6.2 are presented in Figure 6.2 and have a correlation with R² of 0.38. Relationships between PCI and various properties/parameters in linear and nonlinear combinations are also presented in Equations 6.3 and 6.4, respectively:

$$PCI = 30.2 - 1.109MDCA - 0.75MDFA + 0.76SSSCA + 0.70SSSFA - 6.71ABS + 12.26FM + 2.09F + 0.16CBR - 0.15IRI_L - 10.013IRI_R + 0.06E_{base} \dots\dots\dots(6.3)$$

$$PCI = 157.5 - 0.027MDCA^2 + 3.365\sqrt{MDFA} + 12.1 \log(SSSCA) + 0.706\sqrt[3]{SSSFA} - 14.93\sqrt[3]{ABS} + 18.82 \log(F) + 0.145FM^2 + 0.126CBR - 39.59 \log(IRI_L) - 17.18 \log(IRI_R) + 0.34\log(E_{base}) \dots\dots\dots(6.4)$$

The predicted versus measured PCI values for these two equations are also depicted in Figure 6.2 and they have correlations with coefficients of determination of 0.72 and 0.82, respectively. Based on the multiple regression analysis and availability of test results, Equations 6.1 to 6.4 (when satisfying the conditions of Equation 6.5) can be used to obtain a general evaluation of the performance of the base layer aggregate of pavements from the indicated test results and parameters.

$$PCI = \left\{ \begin{array}{l} \text{Equation 6.1 (6.2, 6.3, 6.4)} \\ \text{and} \\ \leq 100 \\ \text{or} \\ \geq 0 \end{array} \right\} \dots\dots\dots(6.5)$$

It should be noted that more analysis is required based on the FWD and resilient modulus test results to develop a better evaluation of base layer aggregates and their impact on pavement performance.

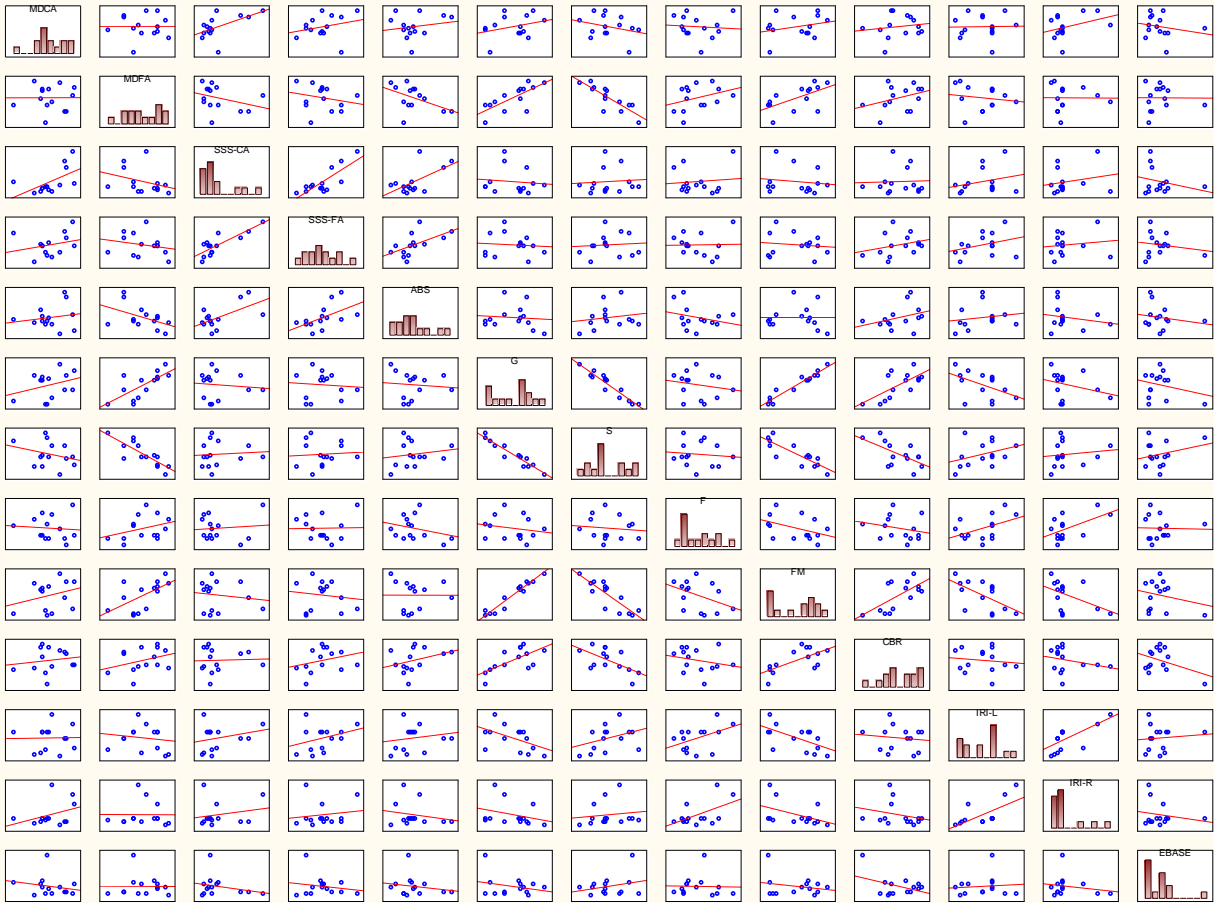


Figure 6.1: Plots and histograms of the individual properties and parameters of the investigated base layer aggregates.

Table 6.1: Correlation matrix for various test results of 14 investigated aggregates: marked correlations (red) are significant at $p < 0.05000$.

	Means														
MDCA	14.7494	2.84623	1.000000	0.001230	0.565345	0.259940	0.181443	0.310092	-0.289569	-0.082069	0.278964	0.155765	0.019345	0.363211	-0.209707
MDFA	20.2666	6.69172	0.001230	1.000000	-0.324012	-0.220010	-0.463854	0.720342	-0.830550	0.334268	0.593320	0.342048	-0.150878	-0.007988	-0.009061
SSSCA	6.3015	6.35151	0.565345	-0.324012	1.000000	0.818869	0.608173	-0.105453	0.077799	0.096645	-0.137397	0.038050	0.256693	0.208740	-0.254407
SSSFA	7.4111	3.01071	0.259940	-0.220010	0.818869	1.000000	0.555268	-0.081336	0.076029	0.021273	-0.125057	0.277995	0.321648	0.141488	-0.171188
ABS	2.2290	0.81816	0.181443	-0.463854	0.608173	0.555268	1.000000	-0.089576	0.173759	-0.275888	-0.001560	0.334085	0.169300	-0.198153	-0.184096
G	51.2786	11.25113	0.310092	0.720342	-0.105453	-0.081336	-0.089576	1.000000	-0.955454	-0.192724	0.964205	0.669035	-0.491163	-0.293347	-0.256122
S	39.6214	11.10213	-0.289569	-0.830550	0.077799	0.076029	0.173759	-0.955454	1.000000	-0.105467	-0.850477	-0.607138	0.361634	0.136446	0.267416
F	9.1000	3.33928	-0.082069	0.334268	0.096645	0.021273	-0.275888	-0.192724	-0.105467	1.000000	-0.421139	-0.235642	0.452564	0.534739	-0.026118
FM	4.7250	0.59042	0.278964	0.593320	-0.137397	-0.125057	-0.001560	0.964205	-0.850477	-0.421139	1.000000	0.650511	-0.579309	-0.450998	-0.222044
CBR	64.4429	18.78321	0.155765	0.342048	0.038050	0.277995	0.334085	0.669035	-0.607138	-0.235642	0.650511	1.000000	-0.119050	-0.252101	-0.399452
IRL	124.0825	50.82224	0.019345	-0.150878	0.256693	0.321648	0.169300	-0.491163	0.361634	0.452564	-0.579309	-0.119050	1.000000	0.657775	0.094029
IRLR	149.5733	91.35128	0.363211	-0.007988	0.208740	0.141488	-0.198153	-0.293347	0.136446	0.534739	-0.450998	-0.252101	0.657775	1.000000	-0.185482
EBASE	46.2857	30.69309	-0.209707	-0.009061	-0.254407	-0.171188	-0.184096	-0.256122	0.267416	-0.026118	-0.222044	-0.399452	0.094029	-0.185482	1.000000

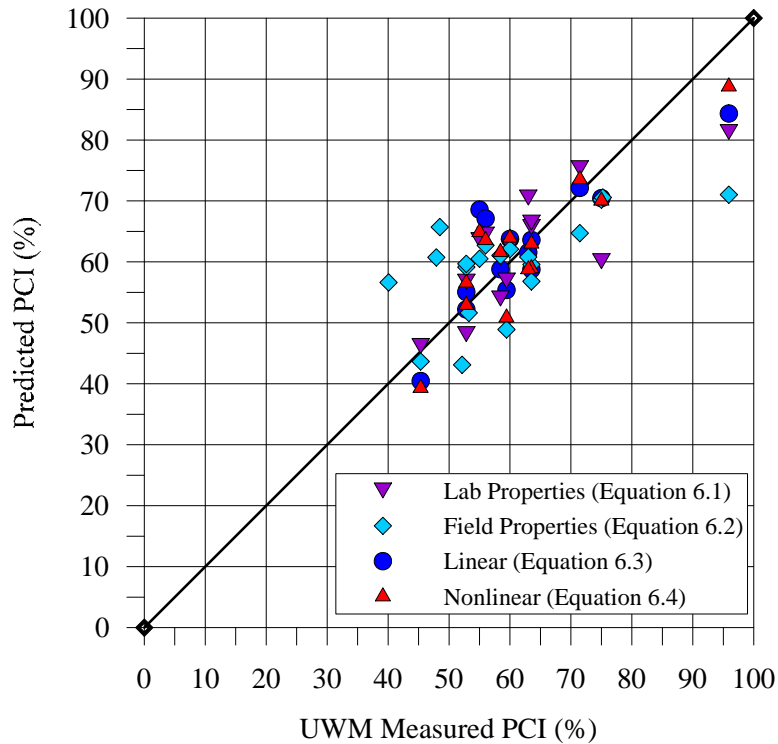


Figure 6.2: PCI predicted using various proposed relationships compared with PCI from visual distress surveys at different pavement test sections.

6.2 Strength and Modulus Based on Dynamic Cone Penetration Test

The DCP test results of the aggregate base layers were used to estimate the CBR variation with depth using the U.S. Army Corps of Engineers formula (Webster, 1992 and 1994) and to predict the changes in base layer modulus with depth using the Powell et al. (1984) formula presented in Chapter 2. The estimated CBR values were averaged over the aggregate base layer thickness and are summarized and compared with the soaked CBR values in Table 6.2 and depicted in Figure 6.3. In order to examine the variability of the base layer strength (and the base layer modulus), all DCP predicted CBR values were obtained from all tests and used to determine the lognormal distribution for the investigated pavement test sections. The results, depicted in Figure 6.4, show that variability in the CBR values for the presented pavement test sections was very high with COV ranging between 48% for CTH JJ and 103% for STH 180. An exception is USH 53 which had an average CBR of 20% and COV of 35%. Age was not a significant factor affecting the strength of the base layer (based on the CBR predicted from the DCP test results). For example, the STH 180 base aggregate with 79 years of service possessed an average CBR value of 87% compared with 20% for the USH 53 base aggregate with 18 years of service. The DCP test and the corresponding predicted base layer CBR and modulus values are significantly affected by the in-place density of the base layer aggregates and, therefore, by the quality of construction. Figure 6.5 presents the variability of the base layer modulus for CTH B as predicted by the DCP test.

Table 6.2: Summary of CBR from soaked laboratory test and CBR predicted by field DCP test for investigated aggregate base layers.

Project Site	Soaked CBR (%)	Average CBR (%)					
		DCP Test #1		DCP Test #2		DCP Test #3	
		Base	Subgrade	Base	Subgrade	Base	Subgrade
STH 33 – MR	58.0	70.6	21.2	73.1	11.5	32.7	13.1
STH 162 – MR	55.1	50.1	18.0	95.8	66.7	N/A	
STH 36 S1-B – Waterford	53.6	64.6	79.7	48.2	59.1	60.4	90.0
STH 36 S1-G – Waterford	87.0	32.9	64.6	32.8	48.2	33.7	60.4
STH 36 S2-G – Waterford	71.0	71.2	70.1	38.4	90.8	N/A	
STH 36 S3-G – Waterford	89.9	44.8	49.8	42.2	58.1	N/A	
STH 180 – Marinette	56.7	40.2	25.8	28.8	51.8	54.7	39.6
USH 53 – Minong	43.5	22.6	56.6	20.1	47.8	N/A	
I 94 S2 – Zoo	73.9	64.2	78.7	67.2	92.7	N/A	
STH 33 – Saukville	N/A	63.0	N/A	40.0	N/A	80.0	N/A
USH 45 – Larsen	N/A	37.0	N/A	29.0	N/A	40.0	N/A
CTH B – Woodville	N/A	29.0	N/A	43.0	N/A	40.0	N/A
CTH JJ – Appleton	N/A	62.0	N/A	82.0	N/A	55.0	N/A
STH 13 – Spencer	N/A	7.5	N/A	13.5	N/A	18.5	N/A

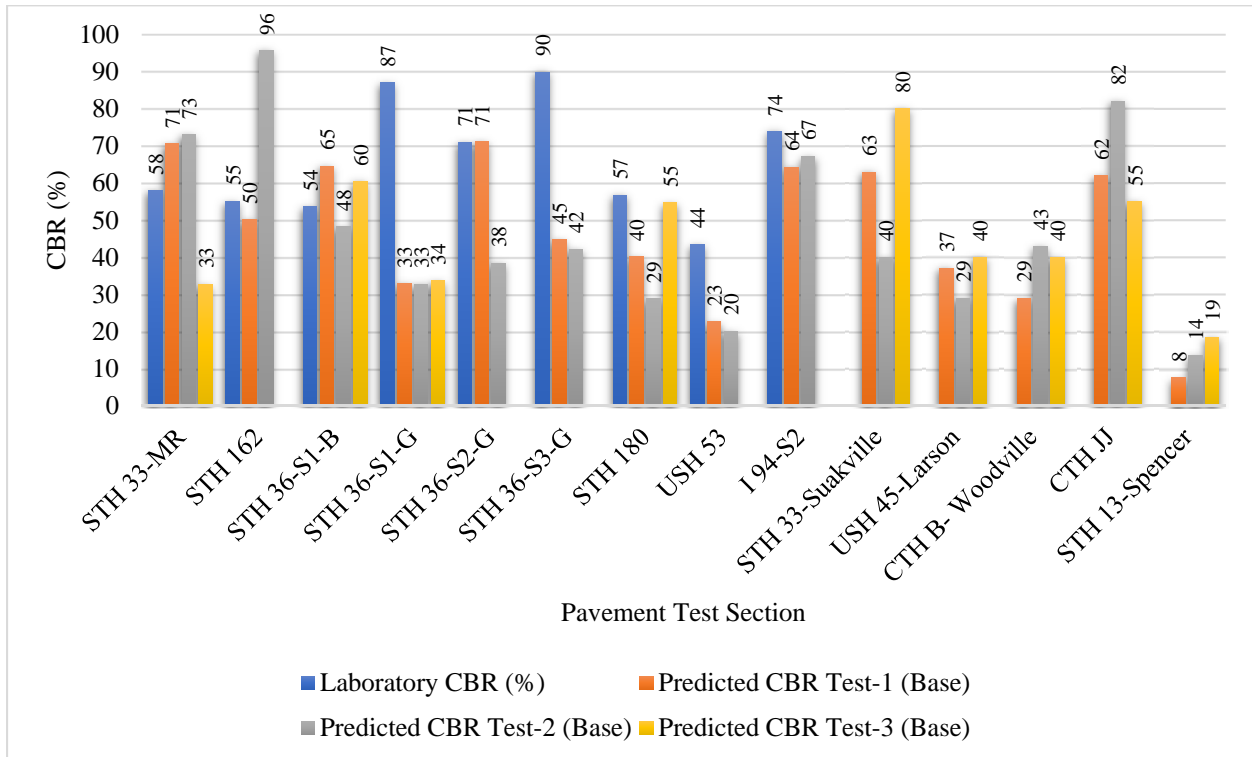


Figure 6.3: Comparison of CBR predicted by field DCP test and measured from soaked laboratory test.

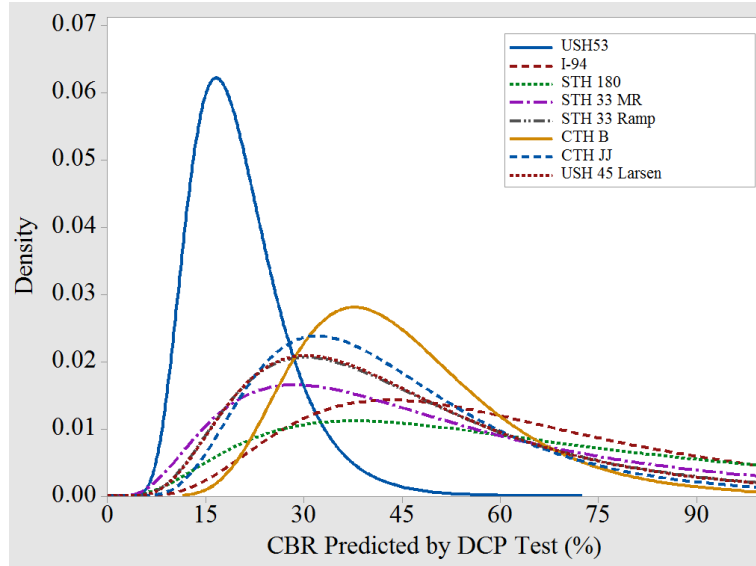


Figure 6.4: Lognormal distributions depicting the high variability of base layer strength of investigated pavement test sections.

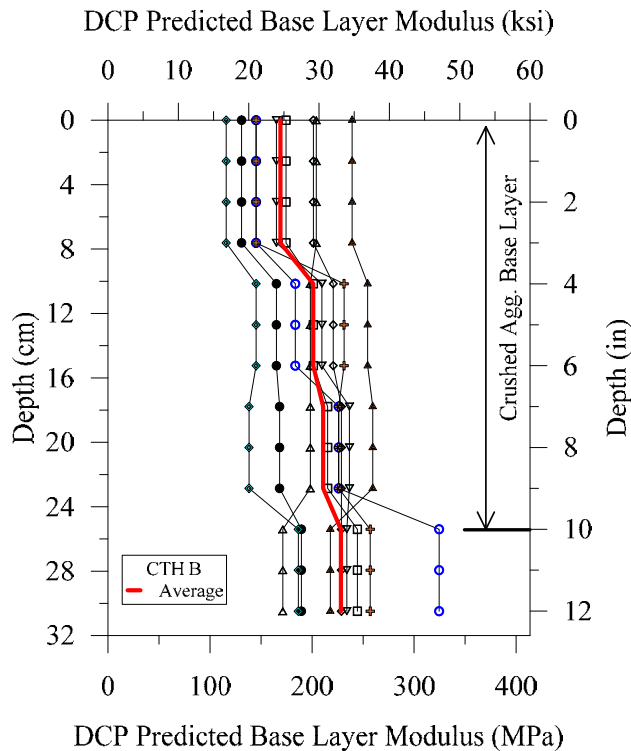


Figure 6.5: Variability with depth of base layer modulus of CTH B as predicted by the DCP test.

6.3 Resilient Modulus Based on Repeated Load Triaxial Test

The research team conducted a comprehensive analysis on resilient modulus tests conducted on virgin Wisconsin aggregates (Eggen and Brittnacher, 2004) obtained from quarries and pits around the state. The best fit statistical distribution of the resilient modulus of Wisconsin aggregates is presented in Figure 6.6 for all confining stress ranges and for confining stresses between 5 and 10 psi, which represents a typical stress range experienced by pavement base layers. Based on the test results, the lognormal distribution was selected with a mean of 23.79 ksi, standard deviation of 10.77 ksi, and COV of 45.3% for resilient modulus values when all confining stress levels are considered. However, for confining stresses between 5 and 10 psi, the lognormal distribution parameters had a mean of 20.33 ksi, standard deviation of 6.20 ksi, and COV of 30.5%, indicating a lower mean and less variability. It should be noted that these aggregates represent crushed stone from quarries and gravel/crushed gravel from pits. In order to compare aggregates of the same particle properties, another statistical analysis was performed on Wisconsin virgin aggregates by separating aggregates from quarries and pits. The results are depicted in Figure 6.7, which are similar to the results when all aggregates are analyzed together. Therefore, future comparisons will be conducted with respect to all Wisconsin virgin aggregates, regardless of the source.

The resilient modulus test results for crushed stone aggregate from CTH JJ, STH 33 Saukville, CTH B Woodville, and USH 45 Larsen are compared with the results of the typical Wisconsin virgin aggregates in Figure 6.8. Compared with the Wisconsin virgin aggregates, the aggregates at these highway sections exhibited a higher average resilient modulus and have been serving as base layers for about six years with very good performance, as indicated by visual distress surveys and ride quality. Therefore, these aggregates are considered to be a performance reference for comparisons with the resilient modulus values for all other base layer aggregates. Inspection of the box-whisker plot in Figure 6.8 demonstrated that the average resilient modulus values of the base layer aggregates are lower than the average Wisconsin virgin aggregate values for the gravel and crushed gravel and higher for the crushed stone base layer at STH 59. It should be noted that the ages of the base layer aggregates are greater than 15 years, which is the age of the aggregate from STH 59 (see Table 3.1 for age information).

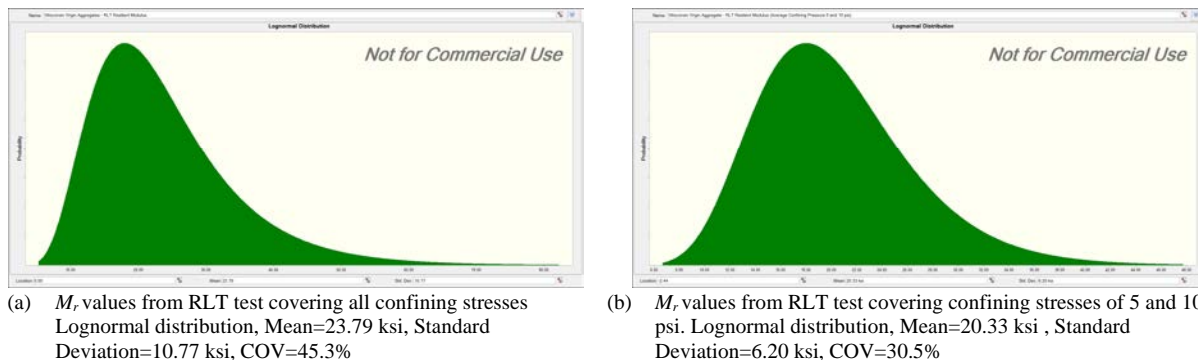
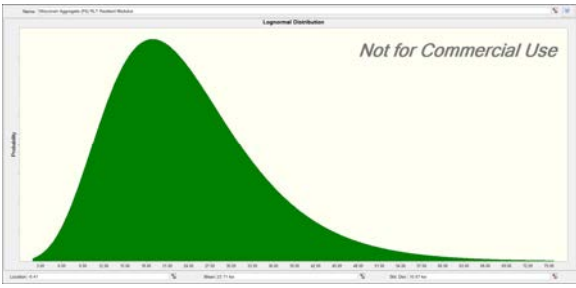
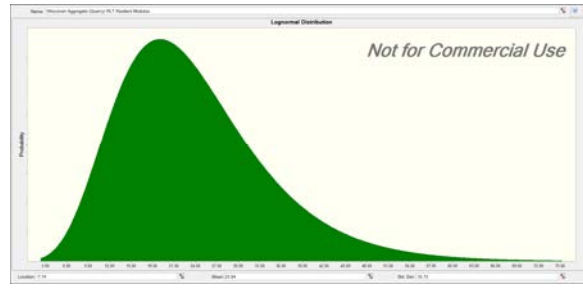


Figure 6.6: Statistical analysis of the resilient modulus data for Wisconsin virgin aggregates at different stress levels.



(a) M_r values from RLT test covering all aggregates from Pits

Lognormal distribution, Mean=23.71 ksi ,
Standard Deviation=10.87 ksi, COV=30.5%



(b) M_r values from RLT test covering all aggregates from Quarries

Lognormal distribution, Mean=23.84 ksi ,
Standard Deviation=10.73 ksi, COV=40.02%

Figure 6.7: Statistical analysis of the resilient modulus data for Wisconsin virgin aggregates from both quarries and pits.

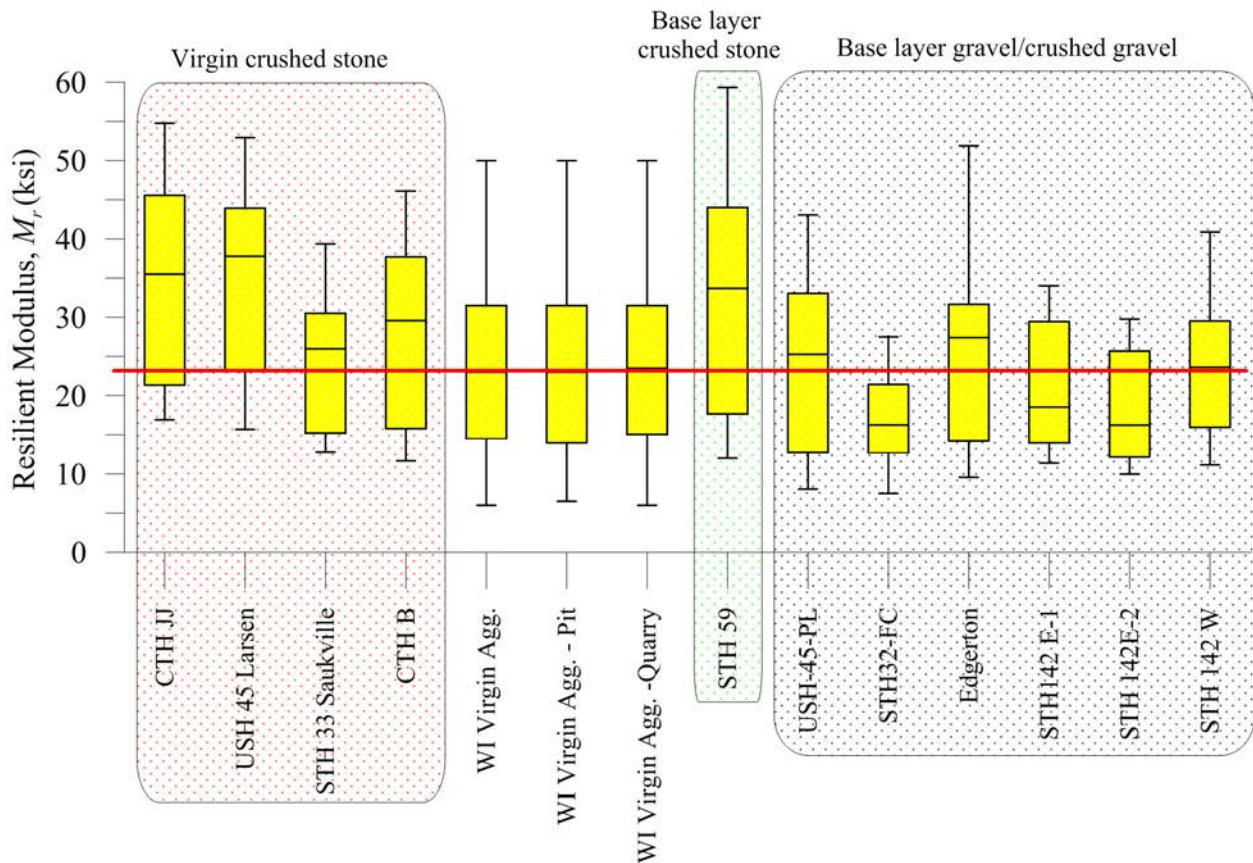
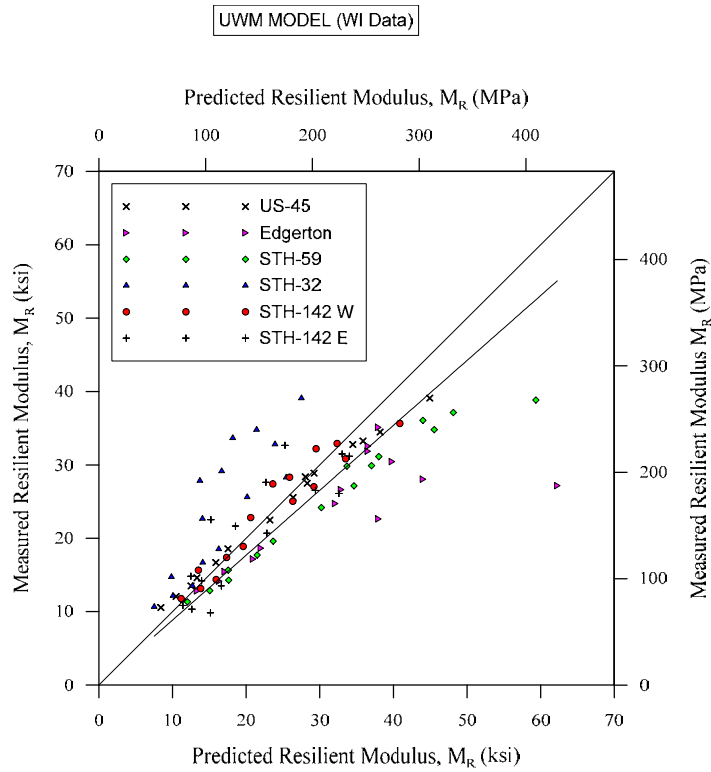


Figure 6.8: Comparison of resilient modulus test results for investigated base layer aggregates with Wisconsin virgin aggregates.

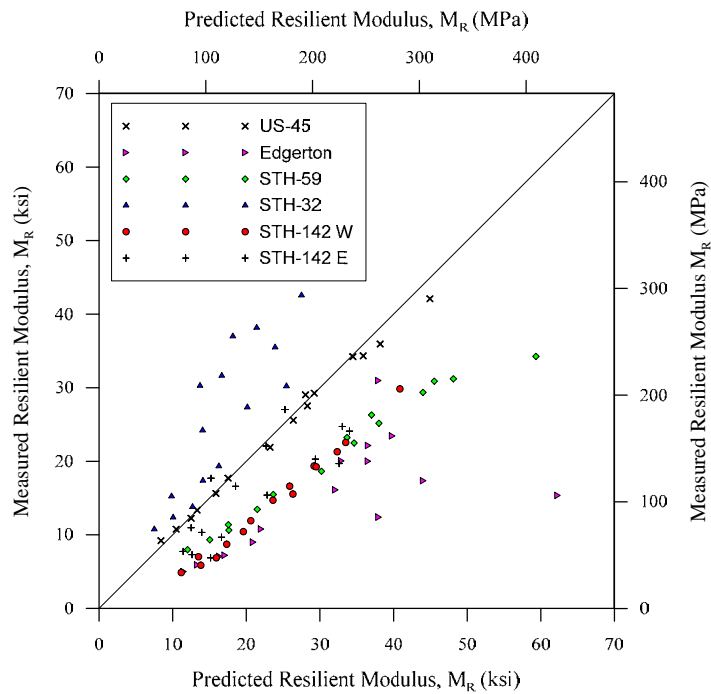
In order to provide an implementation tool that could be useful for WisDOT, the research team conducted a comprehensive analysis on resilient modulus of base aggregates using data

from Wisconsin (WisDOT, UW-Milwaukee), and Kentucky. The analysis included verification of existing LTPP models for crushed stone, gravel, and crushed gravel as well as models developed by Titi and Matar (2018) and presented in Chapter 2. These models are coded in a computer program that will be available for WisDOT use in which the resilient modulus of aggregates can be estimated from basic properties such as particle size distribution and compaction characteristics. For existing pavement design, a representative sample from base layer aggregates could be obtained by coring the surface and then performing particle size analysis and compaction tests. The test results can then be used in the software by selecting a model (e.g. LTPP and UW-Milwaukee models) to estimate the resilient modulus of the aggregates, which in turn can be input into the AASHTOWare Pavement ME Design to evaluate pavement performance for an overlay design. Such a method can also be coupled with the back-calculation module of the AASHTOWare Pavement ME Design using the FWD testing for pavement performance evaluations of overlay design (this is discussed in the next section). Using models to estimate the resilient modulus of the aggregate (via particle size distribution and other properties) accounts for the time (age) impact on the base layer aggregate degradation when the samples are taken from existing base layers, since finer sized particles have lower resilient modulus.

The computer program, using the various models, was used to estimate the resilient modulus of virgin and base layer aggregates used in this study as shown in Figures 6.9 and 6.10. The predictions of the resilient modulus of investigated base layer aggregates presented in Figure 6.9 and 6.10 demonstrate that these models can be used to estimate the resilient modulus of existing base layer aggregates in Wisconsin pavements with reasonable accuracy. To demonstrate the importance of the resilient modulus of base layer aggregates on pavement performance, a sensitivity analysis was conducted using data from USH 45 PL and STH 33, which represent pavements with poor and good performance, respectively, as indicated by the pavement condition surveys and ride quality. The results are presented in Figures 6.11 and 6.12 where comparison of pavement performance is presented for various levels of base layer aggregate modulus. The sensitivity analysis, conducted to assess the influence of aggregate base modulus on pavement performance, used base aggregate modulus values ranging from 10 to 50 ksi with increments of 5 ksi. Pavement performance, in terms of fatigue cracking, ride quality (IRI), and rutting, was investigated for a pavement life of 20 years. The influence of base layer modulus on fatigue cracking is more significant than its influence on ride quality and rutting at 90% reliability levels. For example, after 20 years of pavement life, bottom up cracking of the HMA surface layer propagated from 0.53% for a base layer modulus of 50 ksi and 4.59% for a base layer modulus of 10 ksi, as shown in Figure 6.11 b. On the other hand, the influence of the base layer modulus on ride quality (IRI) is insignificant at a reliability level of 90% for this particular pavement, as shown in Figure 6.11. The analysis also indicated that the

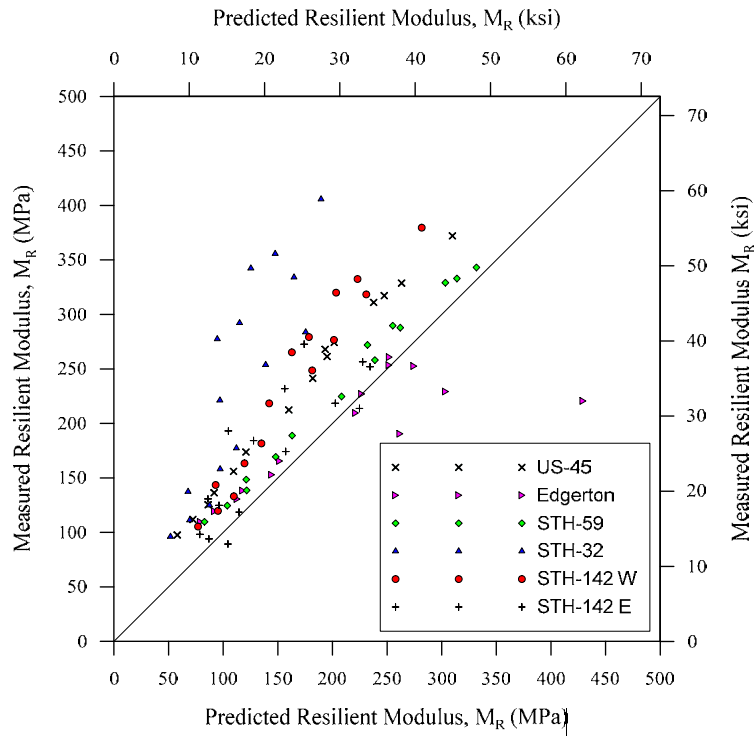


(a) UW-Milwaukee Model using Wisconsin data ($R^2 = 0.93$)

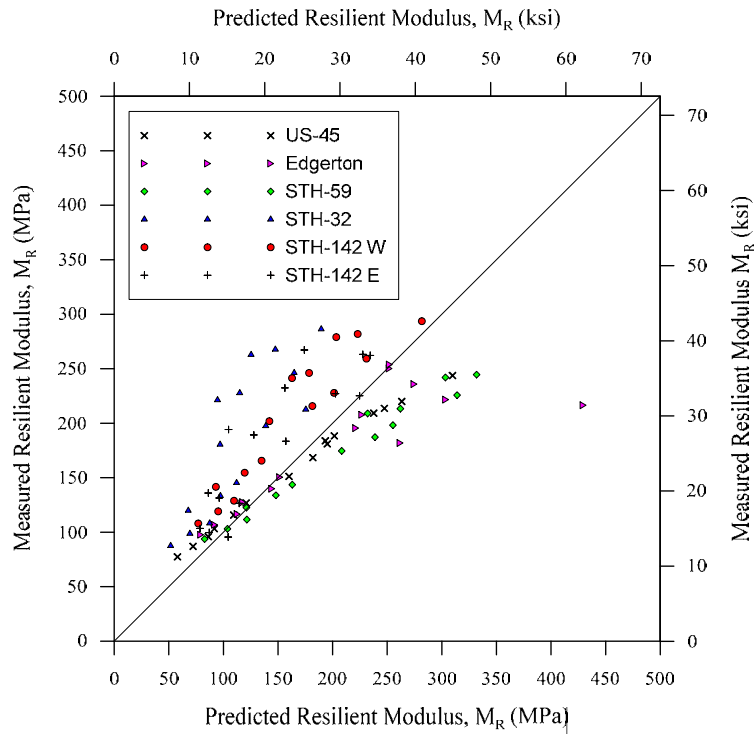


(b) UW-Milwaukee Model using Wisconsin and Kentucky data ($R^2 = 0.84$)

Figure 6.9: Comparison of measured and predicted resilient modulus of investigated base layer aggregates using UW-Milwaukee Model.



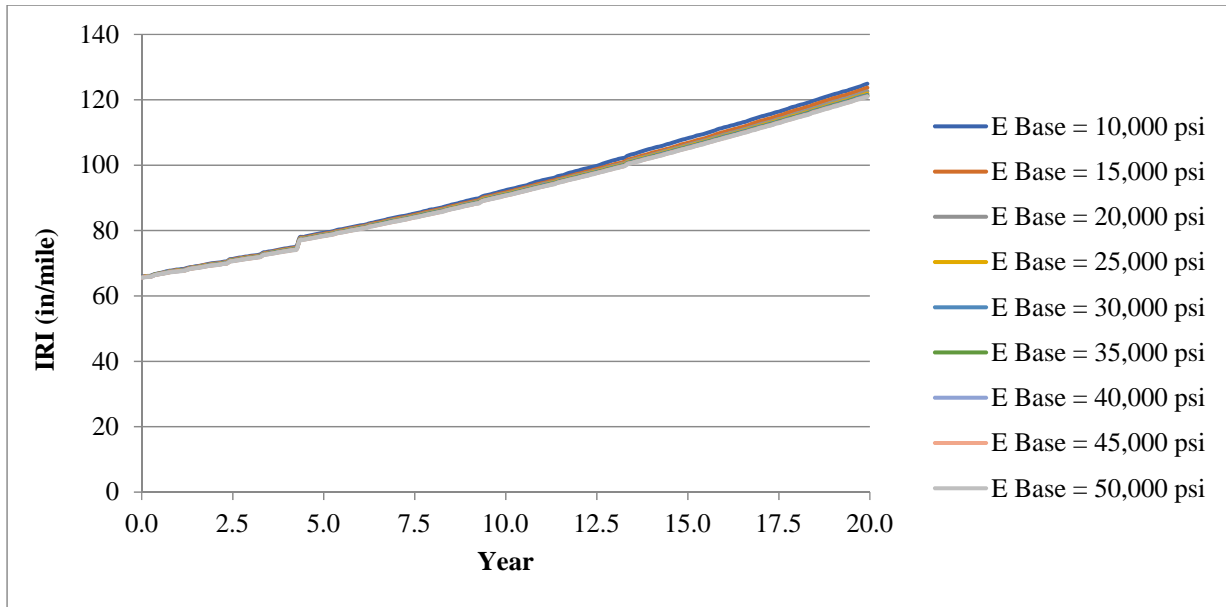
(a) LTPP 302 Model ($R^2=0.91$)



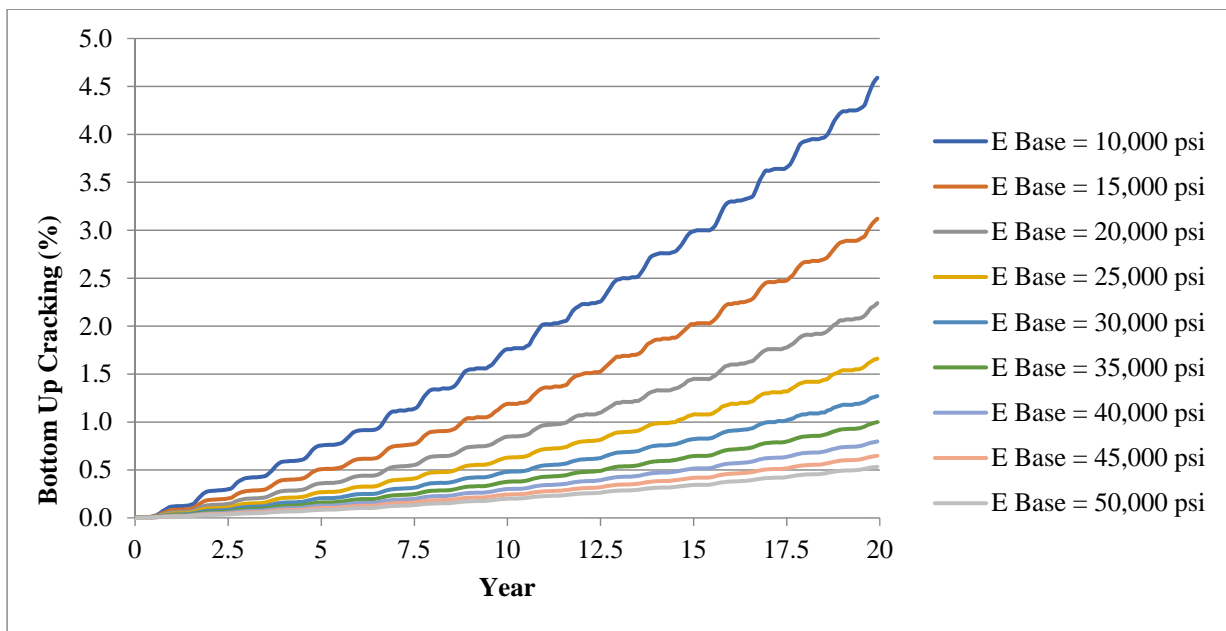
(b) LTPP 303 Model ($R^2 = 0.91$)

Figure 6.10: Comparison of measured and predicted resilient modulus of investigated base layer aggregates using LTPP Models.

base layer modulus has little influence on rutting for this particular pavement, as shown in Figure 6.11. For a base layer modulus of 10 ksi, a rut depth value of 0.38 in was reached in 20 years and for a base layer modulus of 50 ksi, the total rutting was 0.33 in over a 20 year performance period. For the USH 45 PL pavement, which had lower performance according to the distress survey and ride quality evaluation, the fatigue cracking increased from 0.57% for the pavement with a base layer aggregate modulus of 50 ksi to 8.37% for the same pavement with base aggregate modulus of 10 ksi, as shown in Figure 6.12. The difference in the performance of both pavements (STH 33 Saukville and USH 45 PL) is also highlighted in Figure 6.13 for comparison. It is important that the base layer aggregate is selected from good material and appropriate construction is achieved to have better performing pavements.

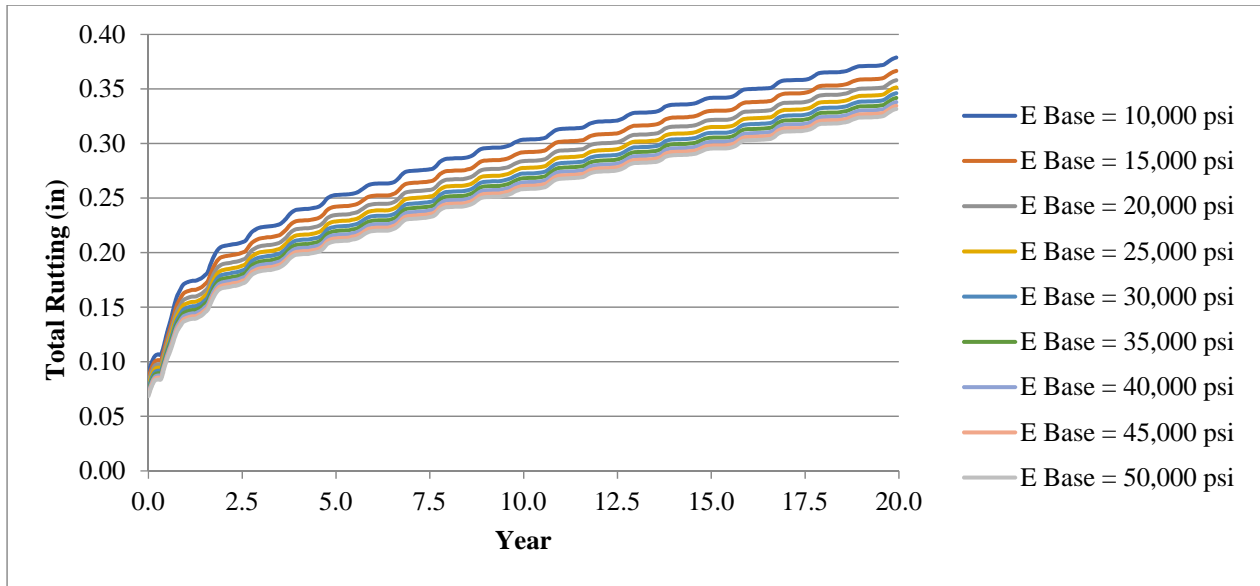


(a) Ride quality evaluation over time

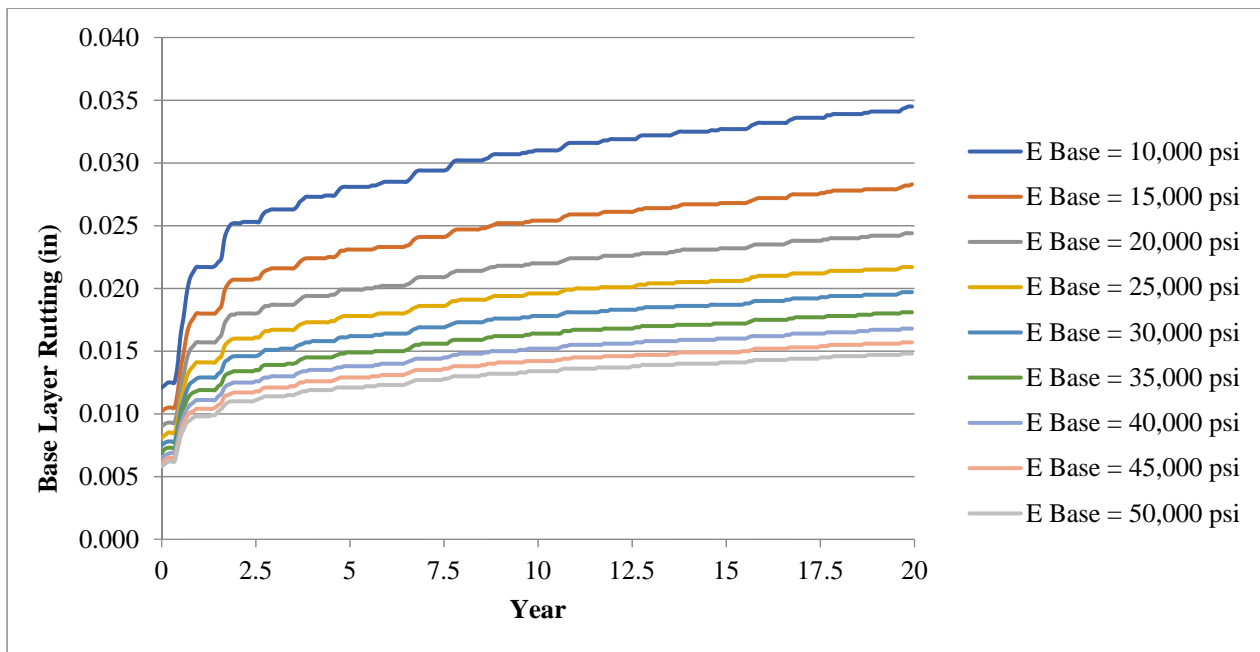


(b) Fatigue cracking over time

Figure 6.11: AASHTOWare Pavement ME Design evaluation of performance of STH 33 Saukville pavement for various base layer aggregate resilient moduli (input).

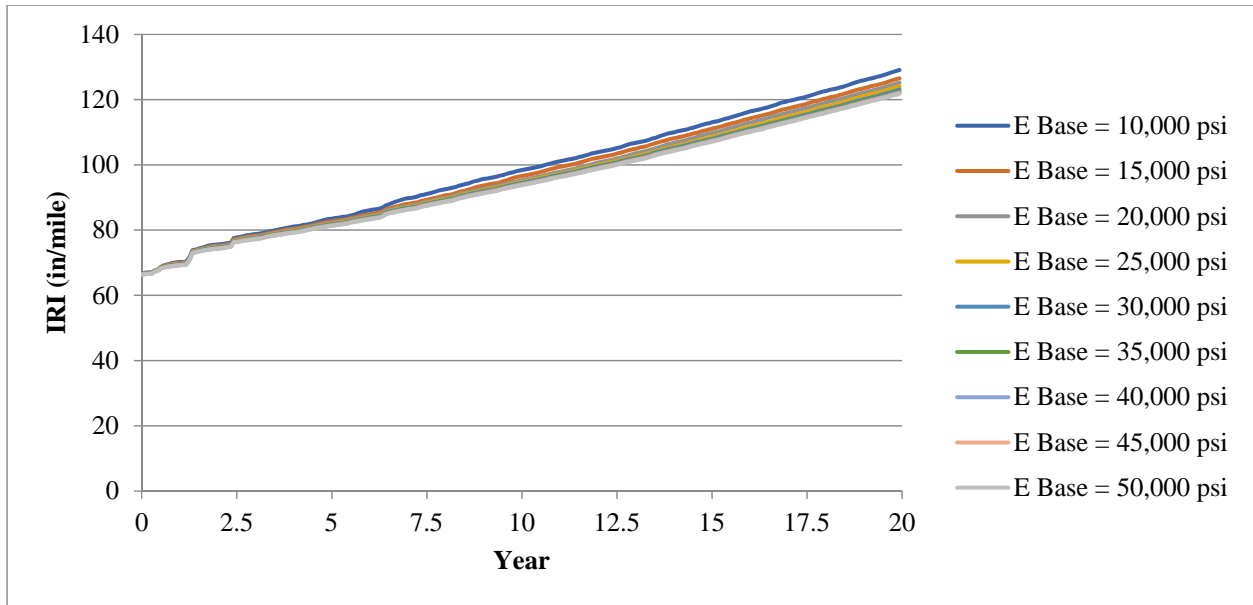


(c) Total rutting evaluation over time

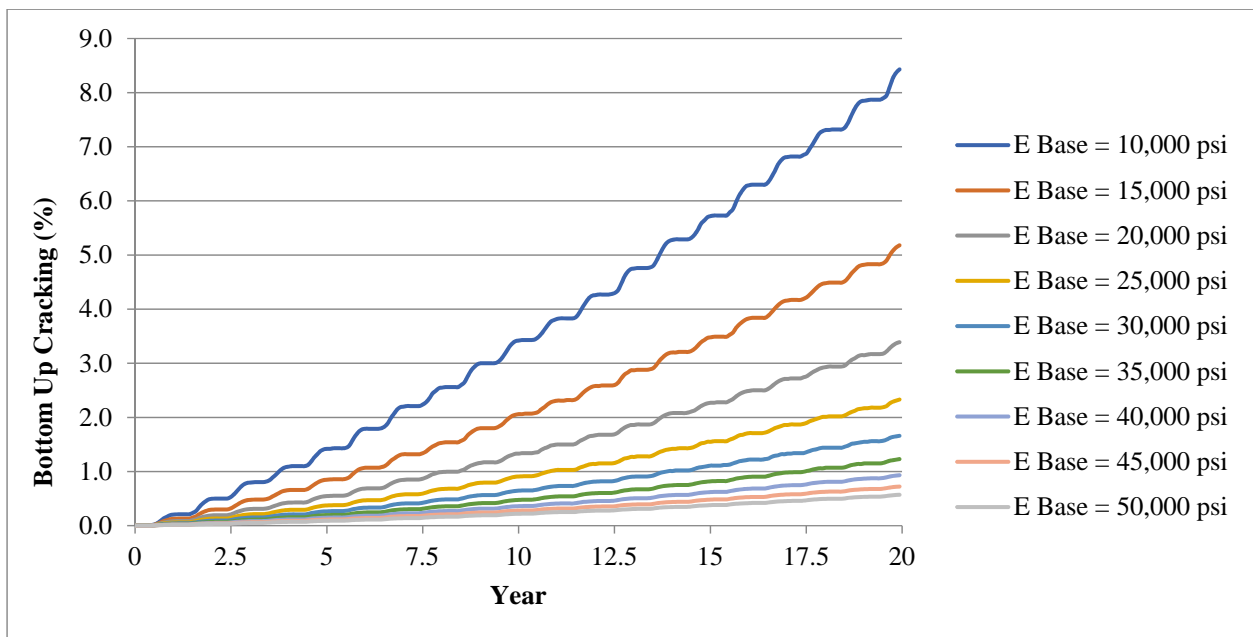


(d) Rutting of base layer over time

Figure 6.11 (Cont.): AASHTOWare Pavement ME Design evaluation of performance of STH 33 Saukville pavement for various base layer aggregate resilient moduli (input).

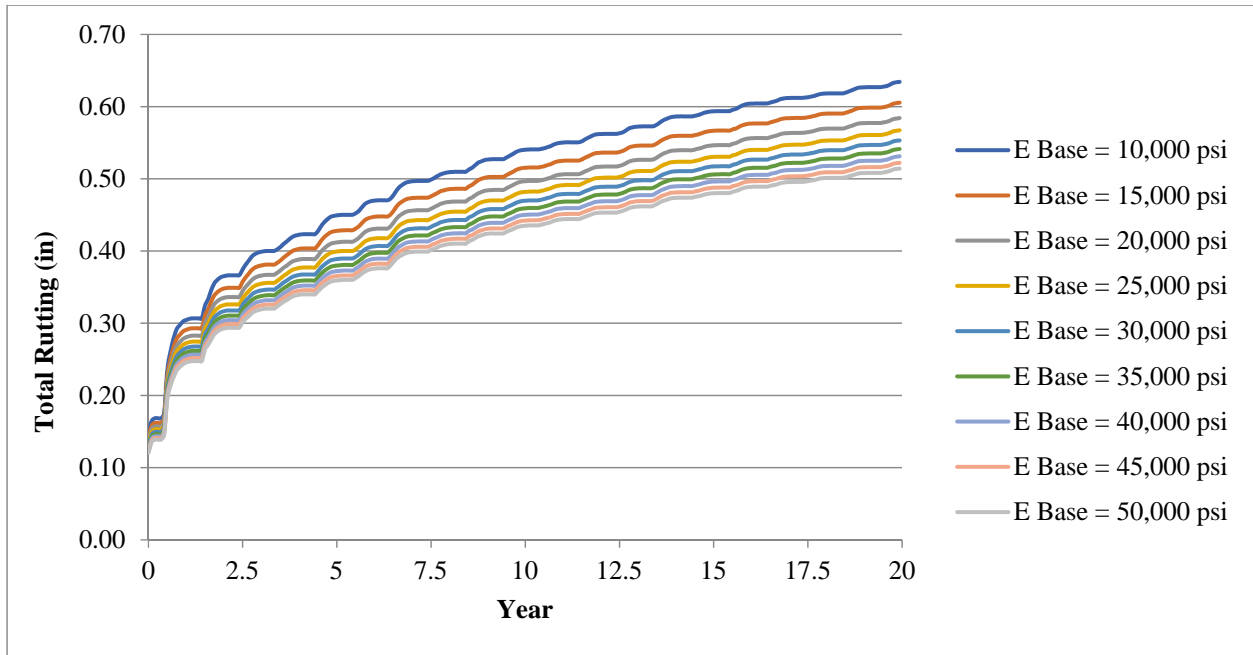


(a) Ride quality evaluation over time

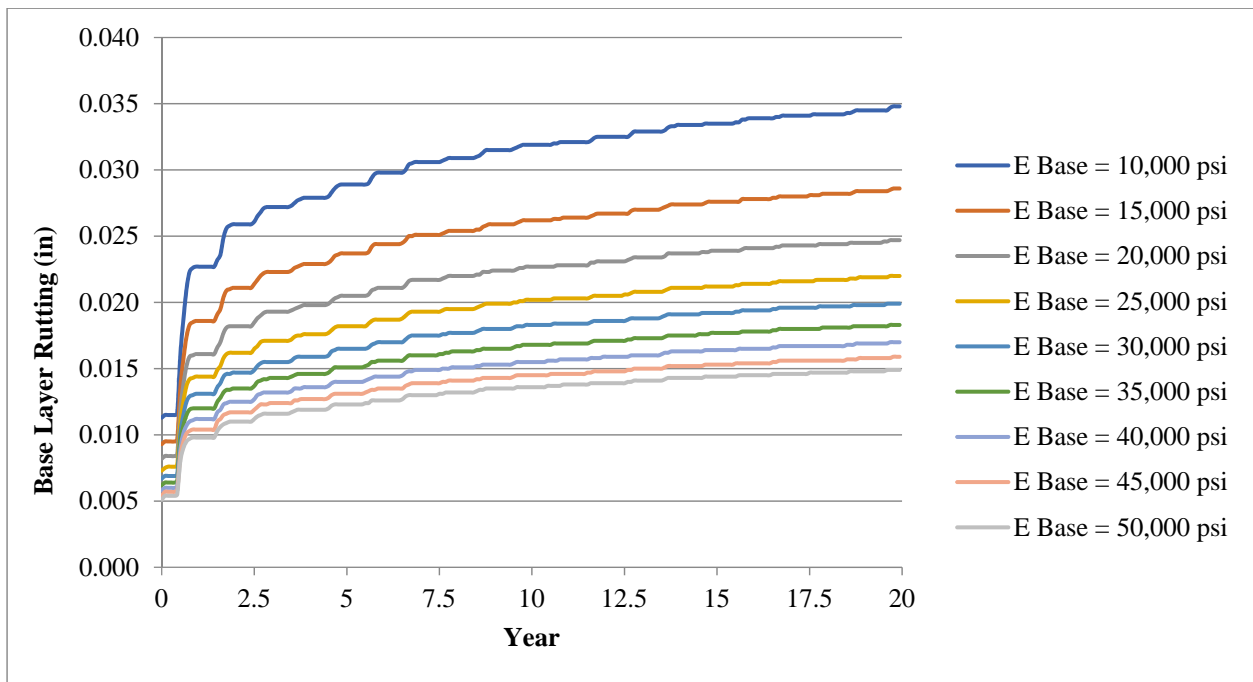


(b) Fatigue cracking over time

Figure 6.12: AASHTOWare Pavement ME Design evaluation of performance of USH 45 PL pavement for various base layer aggregate resilient moduli (input).

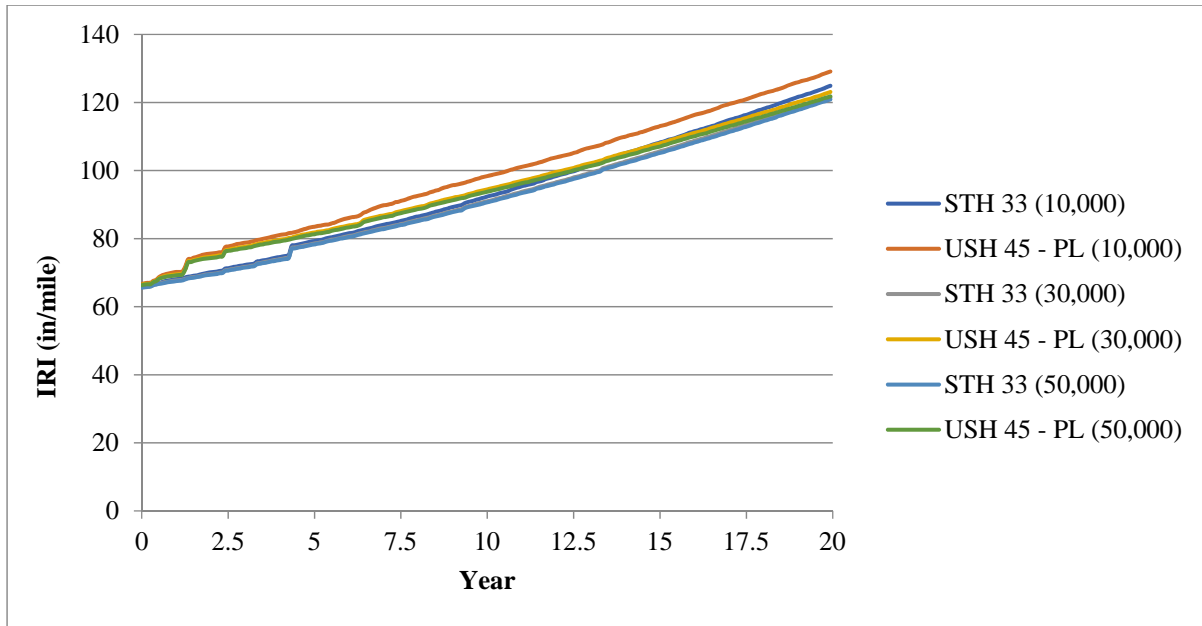


(c) Total rutting evaluation over time

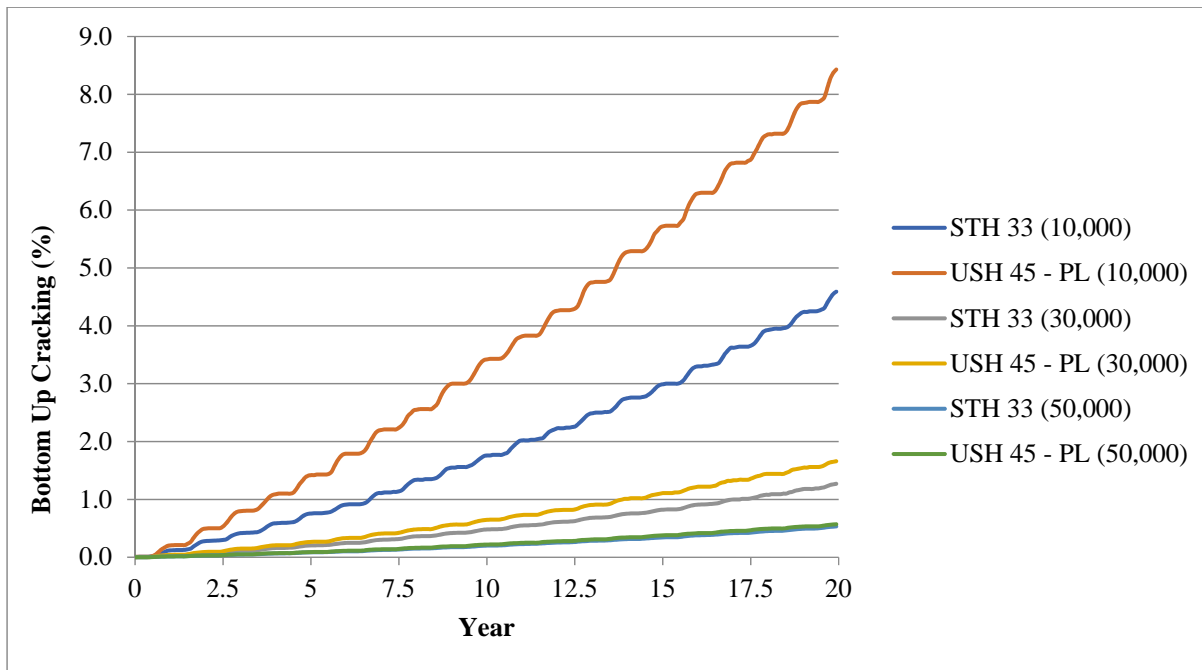


(d) Rutting of base layer over time

Figure 6.12 (Cont.): AASHTOWare Pavement ME Design evaluation of performance of USH 45 PL pavement for various base layer aggregate resilient moduli (input).

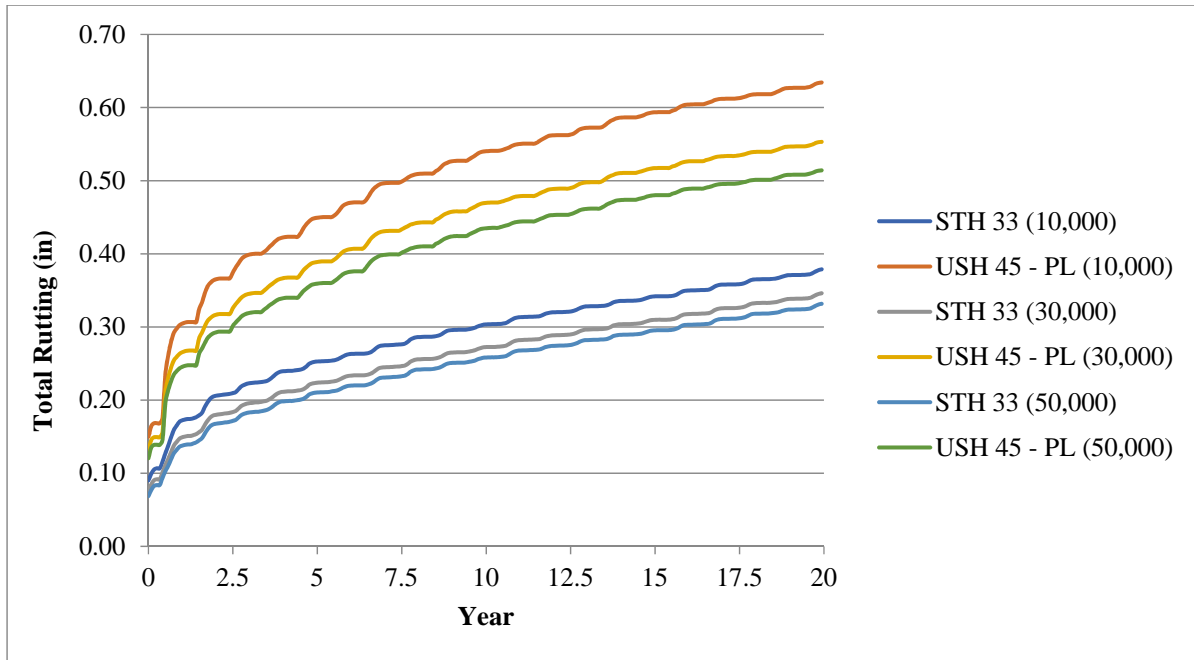


(a) Ride quality evaluation over time

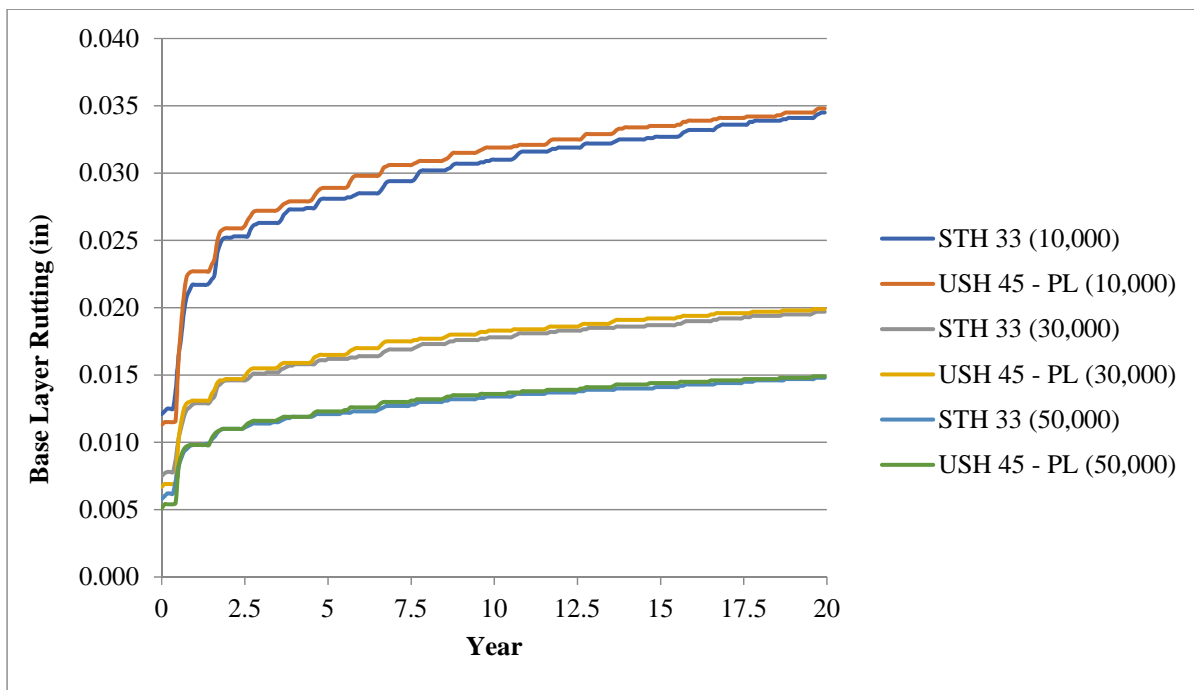


(b) Fatigue cracking over time

Figure 6.13: Comparison of pavements with good and poor performance due to base layer modulus.



(c) Total rutting evaluation over time

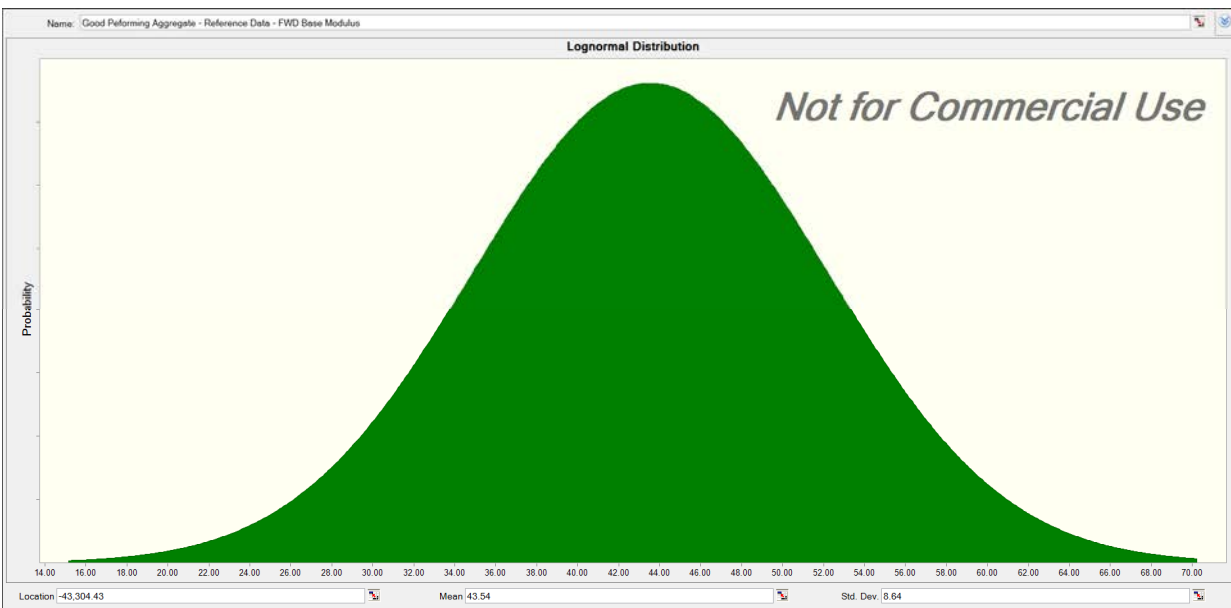


(d) Rutting of base layer over time

Figure 6.13 (Cont.): Comparison of pavements with good and poor performance due to variation in base layer modulus.

6.4 Back-calculated Layer Modulus Based on FWD

The research team established a reference of good performing pavements based on low pavement distress, good ride quality, and higher than average back-calculated base layer modulus. The pavements included as this reference are CTH T S1, CTH T S2, STH 33 S1, STH 33 S2, CTH B, CTH II, and STH 13. A statistical analysis was conducted on the FWD back-calculated base layer moduli for these pavements as depicted in Figure 6.14. The base layer back-calculated modulus is best represented by a lognormal distribution with a mean of 43.54 ksi, which is approximately twice the mean resilient modulus obtained from laboratory tests for base aggregates with good performance.



Lognormal distribution, Mean=43.54 ksi, Standard Deviation=8.64 ksi, and COV =19.84%

Figure 6.14: Distribution of back-calculated base layer modulus for pavements with good performance.

Figure 6.15 depicts a comparison of the back-calculated base layer moduli for the investigated pavements with poor performance with the values obtained for pavements with good performance (as determined by visual distress surveys and ride quality). It should be noted that the investigated base aggregates that exhibited poor performance had low resilient modulus values. Moreover, these base aggregates (with poor performance) were composed of gravel and crushed gravel, and have been in service as base layers for a range of 20 years to more than 70 years. The use of the FWD testing and the corresponding back-calculated layer modulus have accounted for the impact of time on the base aggregate degradation/disintegration as well as contamination and other effects. Inspection of Figure 6.15 demonstrates that the average back-calculated base layer modulus of investigated pavements is lower than that of the pavements with

good performance which were composed of crushed stone and had a younger age (between approximately 6 and 9 years). Among the investigated base layer aggregates, the back-calculated base layer modulus for STH 59 with crushed stone and about 15 years of service showed a higher average compared with other base layer aggregates (gravel and crushed gravel) in the same figure; however, this was still lower than the average for aggregates with good performance.

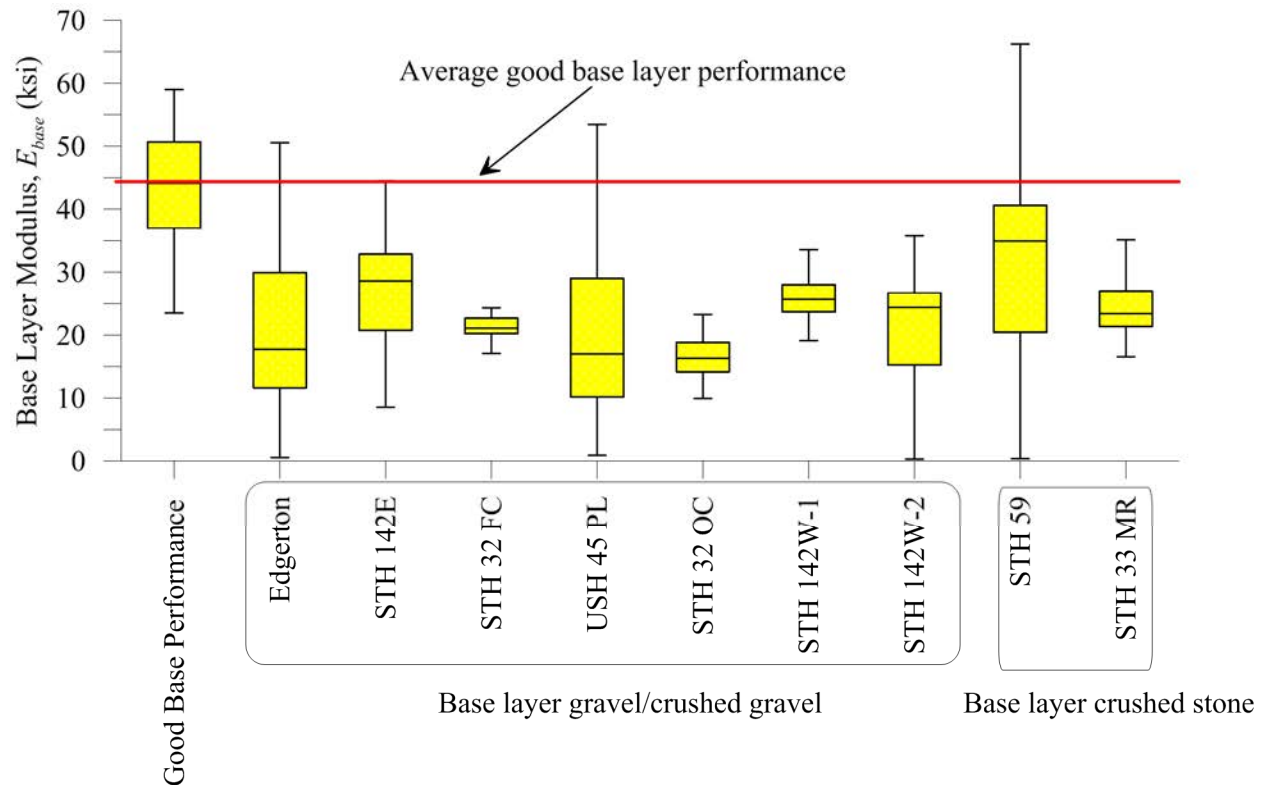
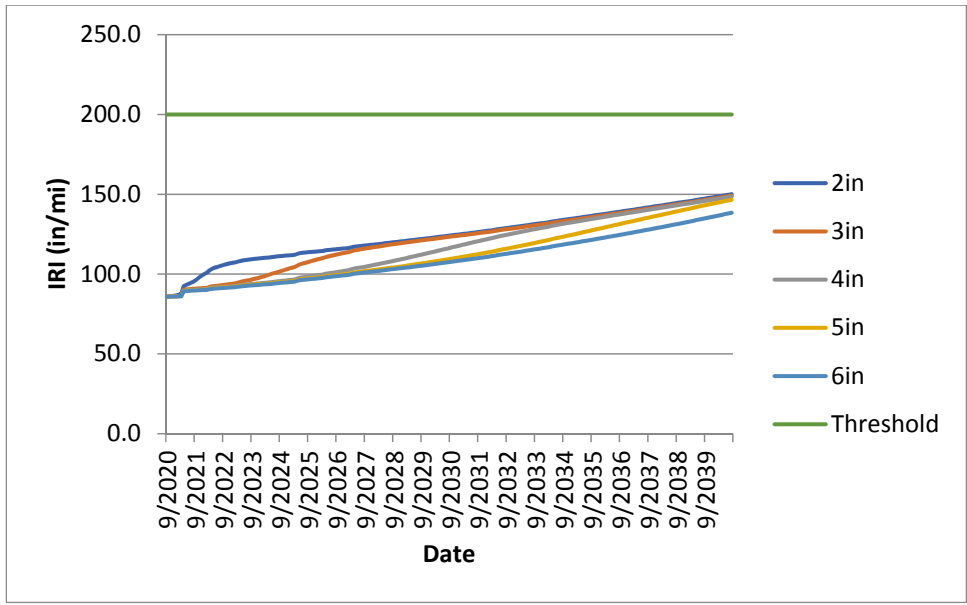
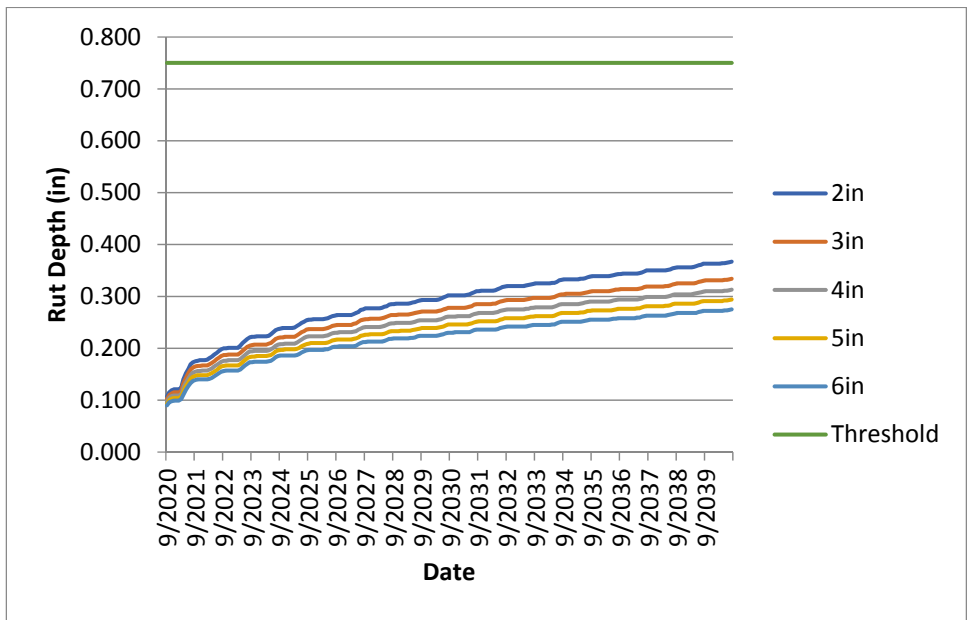


Figure 6.15: Comparison of back-calculated base layer modulus for all investigated pavements with the pavements with good performance.

In order to evaluate the impact of the back-calculated base layer modulus on pavement performance, the newly released AASHTOWare Pavement ME Design Back-calculation Module was used. It has been shown in this study (based on general observation and limited data) that the back-calculated layer modulus is, on average, about twice the resilient modulus calculated from the repeated load triaxial test. The AASHTO 1993 overlay design guide suggests a factor, C , of 0.33 to reduce the resilient modulus of subgrade soils when obtained from FWD analysis. In this study, the research team ran the AASHTOWare Pavement ME Design Back-calculation Module to evaluate overlay design pavement performance based on a “similar concept” with C of 1.0 and C of 0.33. The results are presented in Figures 6.16-6.18.

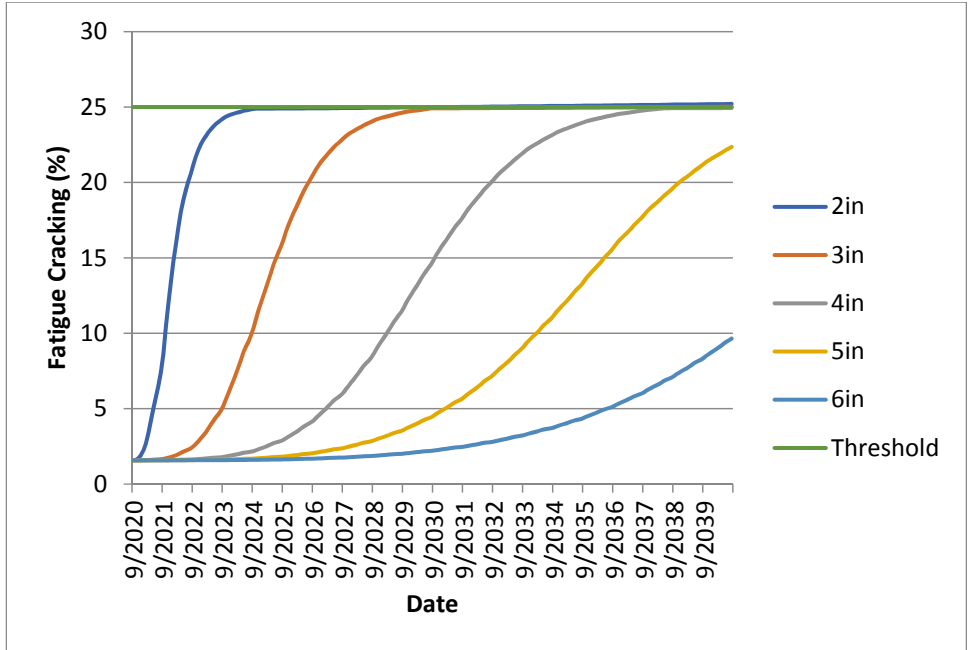


(a) IRI (C=0.33)

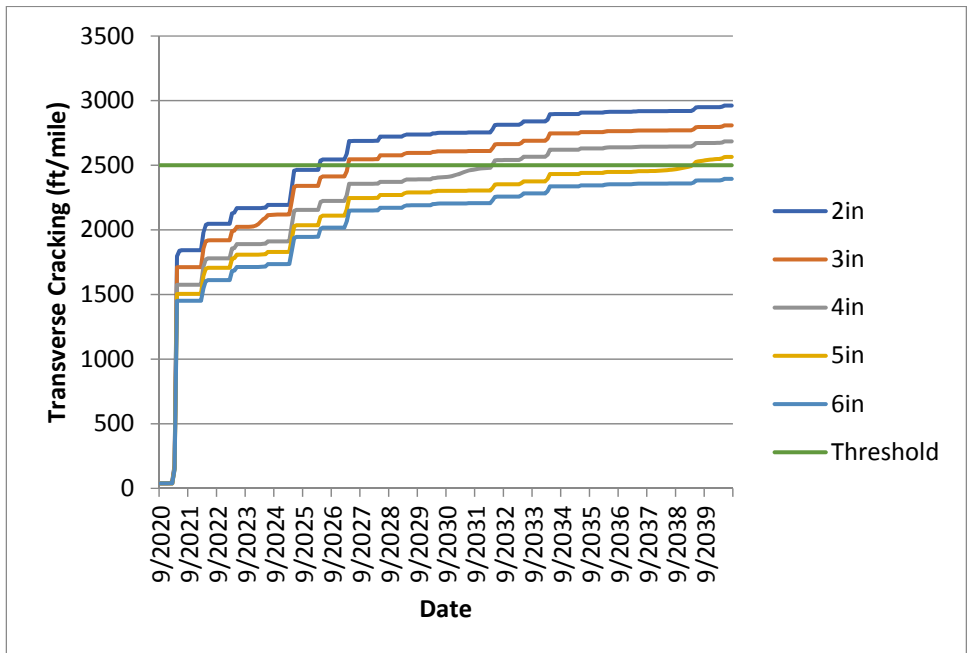


(b) Total Rut Depth (C=0.33)

Figure 6.16: Comparison of overlay performance based on thickness using AASHTOWare Pavement ME Design Back-calculation Module for USH 45 PL.

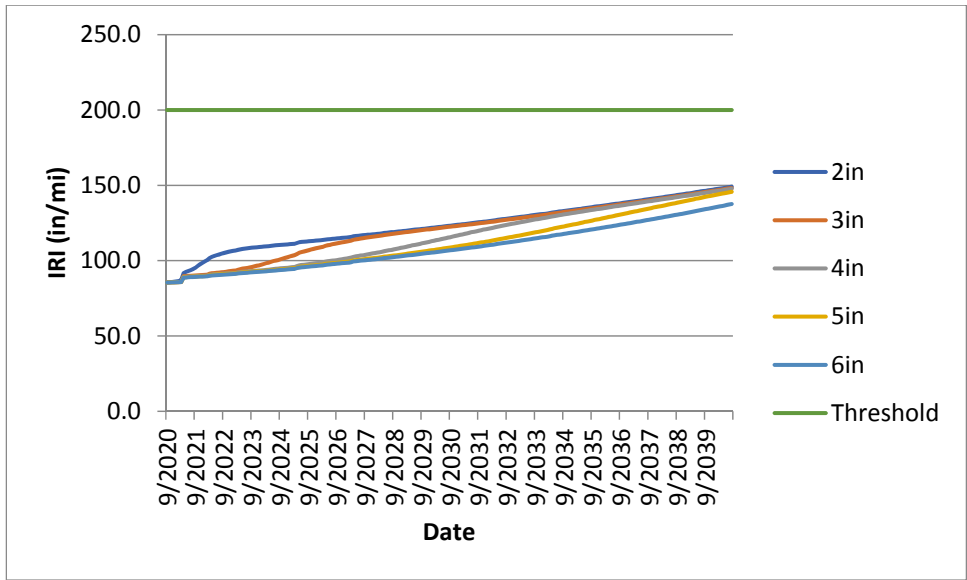


(c) AC Total Bottom Up + Reflective Cracking (C=0.33)

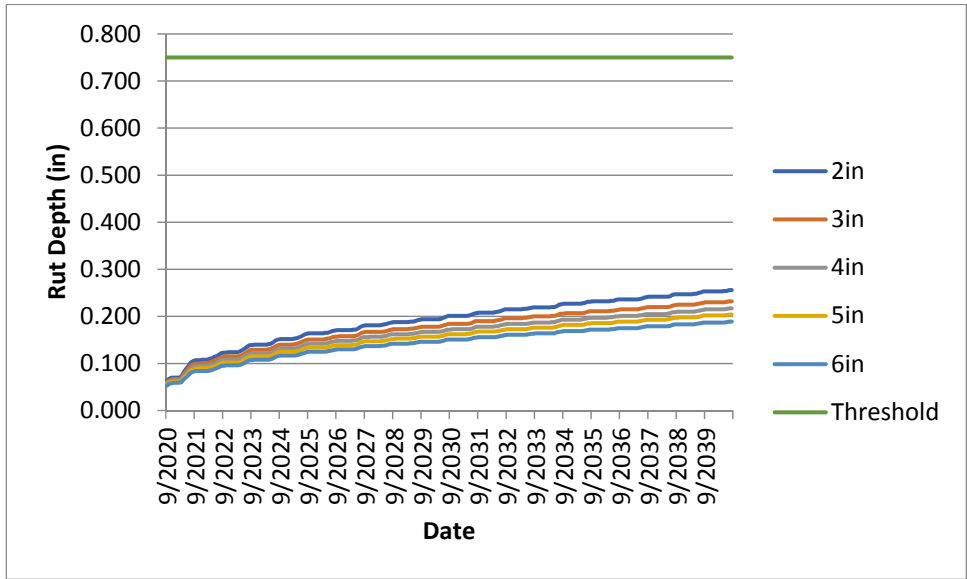


(d) AC Total Thermal + Reflective Cracking (C=0.33)

Figure 6.16 (Cont.): Comparison of overlay performance based on thickness using AASHTOWare Pavement ME Design Back-calculation Module for USH 45 PL.

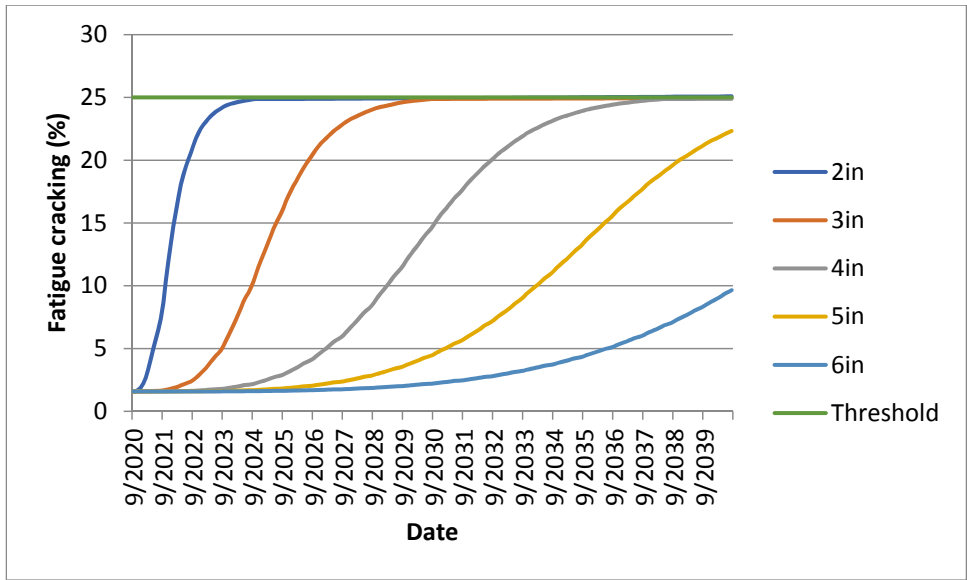


(a) IRI (C=1.0)

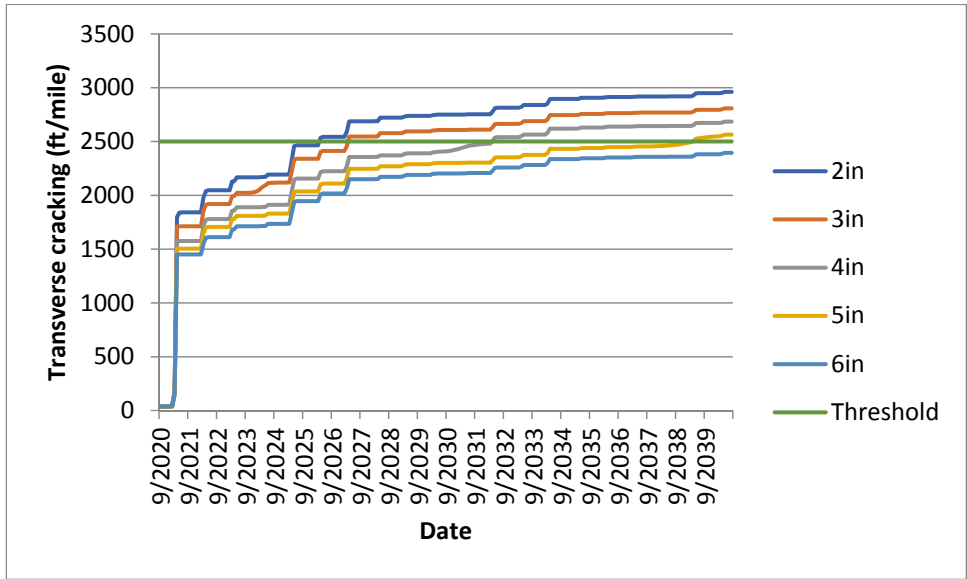


(b) Total Rut Depth (C=1.0)

Figure 6.17: Comparison of overlay performance based on thickness using AASHTOWare Pavement ME Design Back-calculation Module for USH 45 PL.

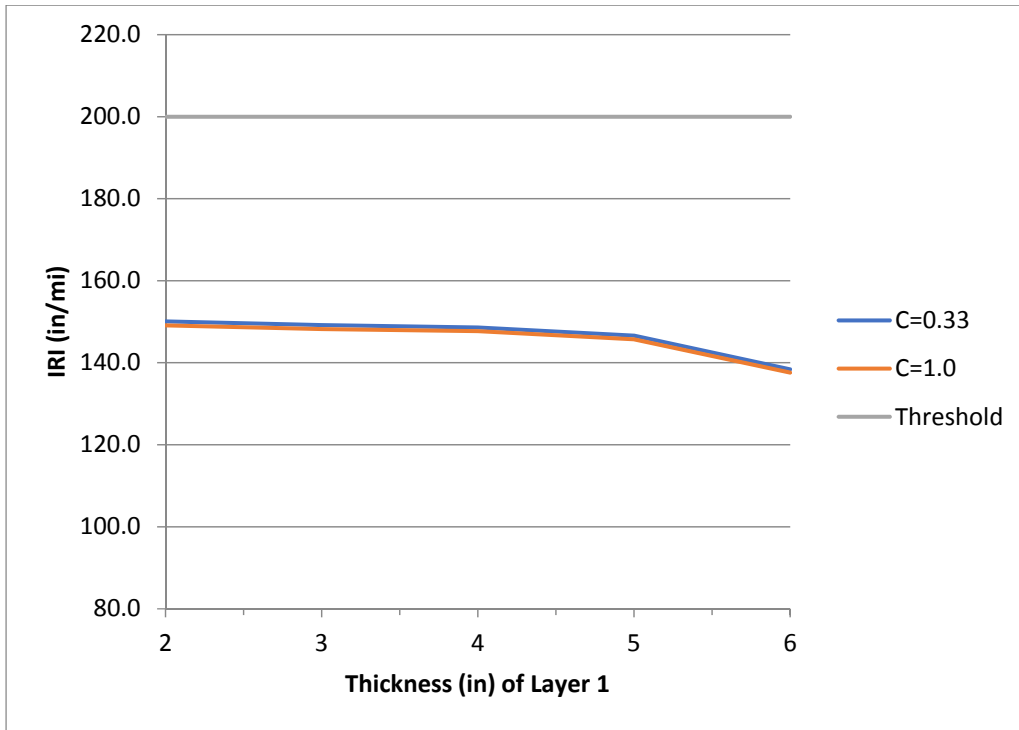


(c) AC Total Bottom Up + Reflective Cracking (C=1.0)

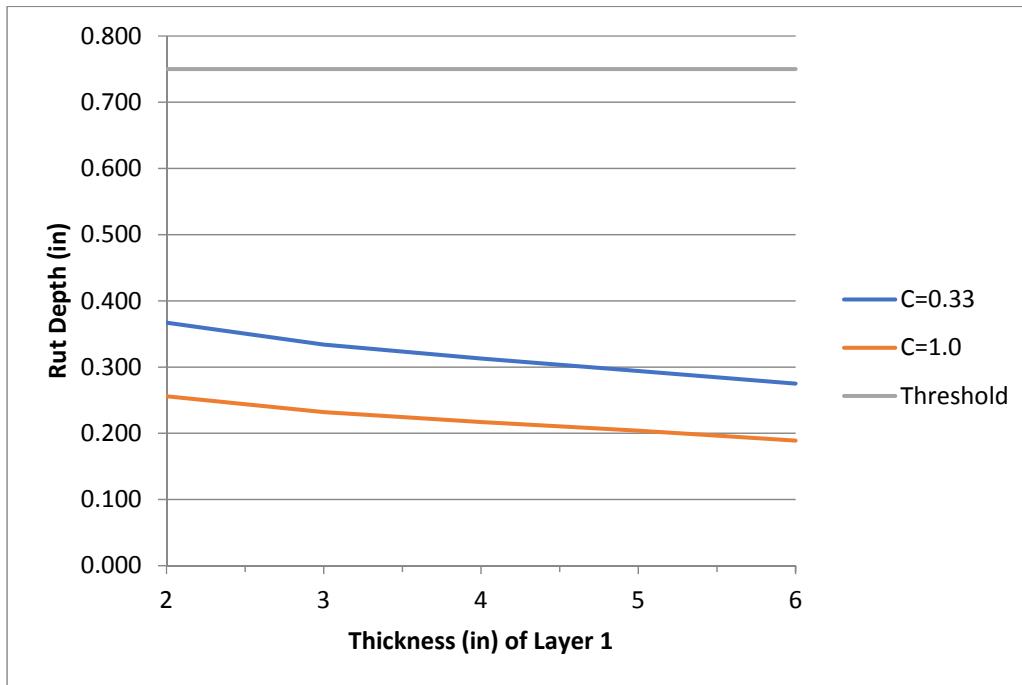


(d) AC Total Thermal + Reflective Cracking (C=1.0)

Figure 6.17 (Cont.): Comparison of overlay performance based on thickness using AASHTOWare Pavement ME Design Back-calculation Module for USH 45 PL.

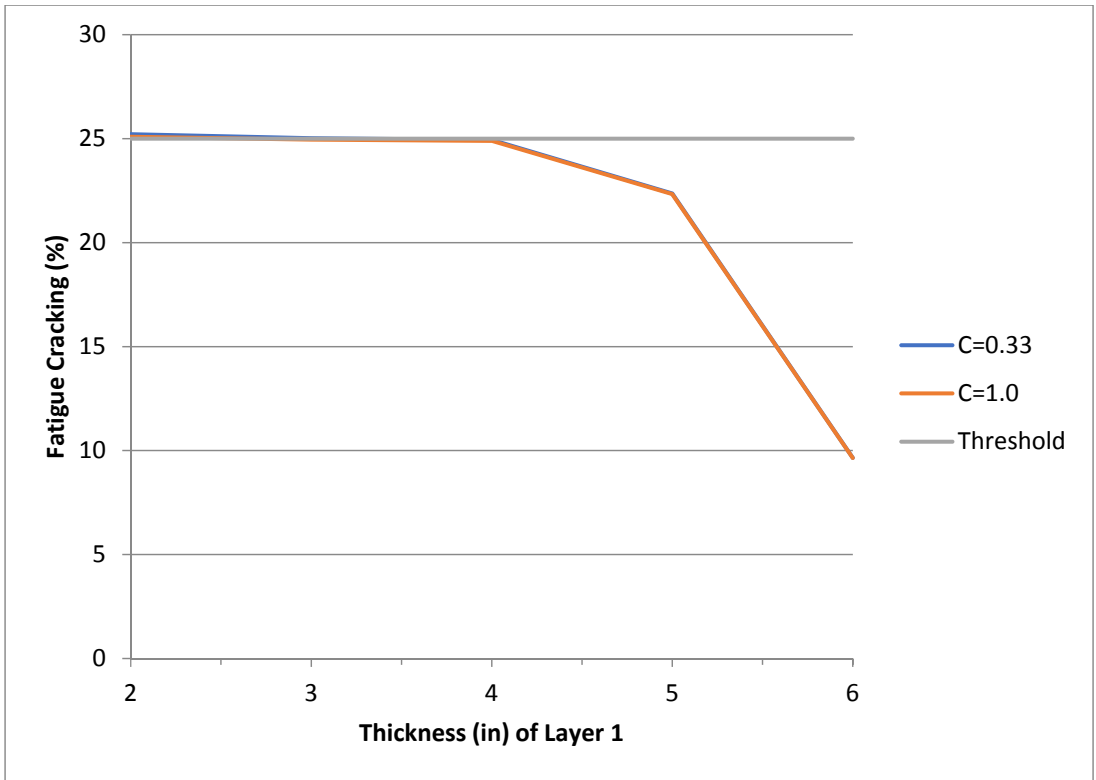


(a) IRI Comparison of C=0.33 and C=1.0

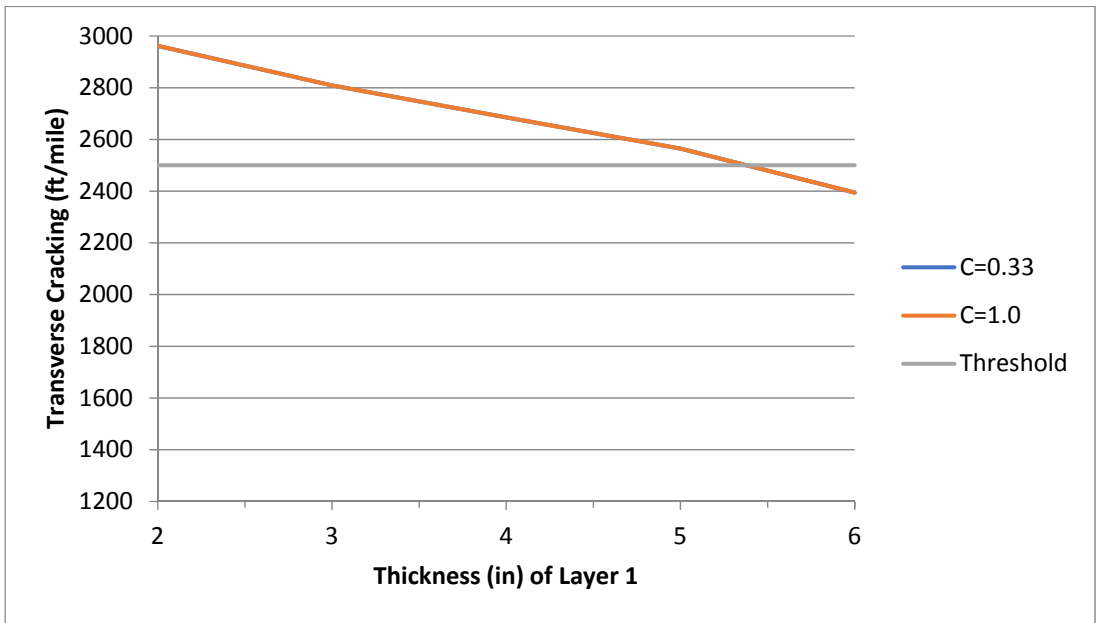


(b) Total Rut Depth (Permanent Deformation) Comparison of C=0.33 and C=1.0

Figure 6.18: Comparison of overlay performance based on thickness using AASHTOWare Pavement ME Design Back-calculation Module for USH 45 PL.



(c) AC Total Bottom Up + Reflective Cracking (% lane area) Comparison of C=0.33 and C=1.0



(d) AC Total Thermal + Reflective Cracking (ft/mile) Comparison of C=0.33 and C=1.0

Figure 6.18 (Cont.): Comparison of overlay performance based on thickness using AASHTOWare Pavement ME Design Back-calculation Module for USH 45 PL.

6.5 Proposed Methods of Modulus Estimation for In-service Aggregate Base Layers

Based on the results of the extensive field and laboratory testing programs and the corresponding statistical analyses and evaluations, the research team proposed the following methods to account for changes in base layer material performance over time as a result of degradation/disintegration and contamination:

(1) Using Aggregate Base Layer Age without Field or Laboratory Tests:

This method was developed based on statistical analysis of the back-calculated base layer modulus from FWD testing, the resilient modulus of base aggregates from repeated load triaxial tests, the PCI of investigated pavement sections, and the corresponding age of the in-service aggregate base layer. In this method no field (such as FWD or DCP tests) or laboratory (such as particle size distribution or repeated load triaxial tests) testing is required. The only required information is the aggregate base layer age and the PCI if available. The following equation was proposed based on the average back-calculated base layer modulus as depicted in Figure 6.19. It can be used to provide a *rough estimate* of the aggregate base layer modulus (E_{base} in ksi) or resilient modulus (M_r in ksi) for use as an input parameter for the AASHTOWare Pavement ME Design:

$$E_{base} = 68.35t^{-0.2718} \dots\dots\dots(6.6)$$

$$M_r = \frac{1}{2} E_{base} = 34.18t^{-0.2718} \dots\dots\dots(6.7)$$

where t is the aggregate base layer age in years. Based on the previously described statistical analysis, the ratio of the resilient modulus to the back-calculated base layer modulus was obtained as 0.5.

The pavement condition index is usually available and can be obtained from the WisDOT pavement data management unit via PIF files. In this case the following equations can be used to provide a *rough estimate* of the aggregate base layer modulus (E_{base} in ksi) or resilient modulus (M_r in ksi) for use as an input parameter for the AASHTOWare Pavement ME Design:

$$E_{base} = 12.85 + 0.351PCI - 0.1625t \dots\dots\dots(6.8)$$

$$M_r = 19.12 + 0.112PCI - 0.14t \dots\dots\dots(6.9)$$

These proposed equations were used to estimate the aggregate base layer modulus (E_{base}) and resilient modulus (M_r) as depicted in Figure 6.20. For Equations 6.8 and 6.9, the ratio of resilient modulus to back-calculated layer modulus is obtained as:

$$C = \frac{M_r}{E_{base}} = 0.659t^{0.0388} \dots\dots\dots(6.10)$$

This relationship is also depicted in Figure 6.21.

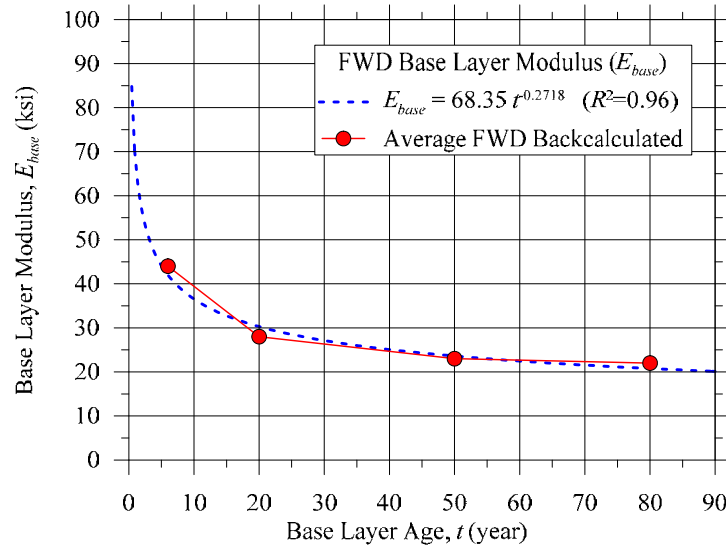


Figure 6.19: Comparison of predicted and measured base layer modulus (E_{base}) based on aggregate base layer age.

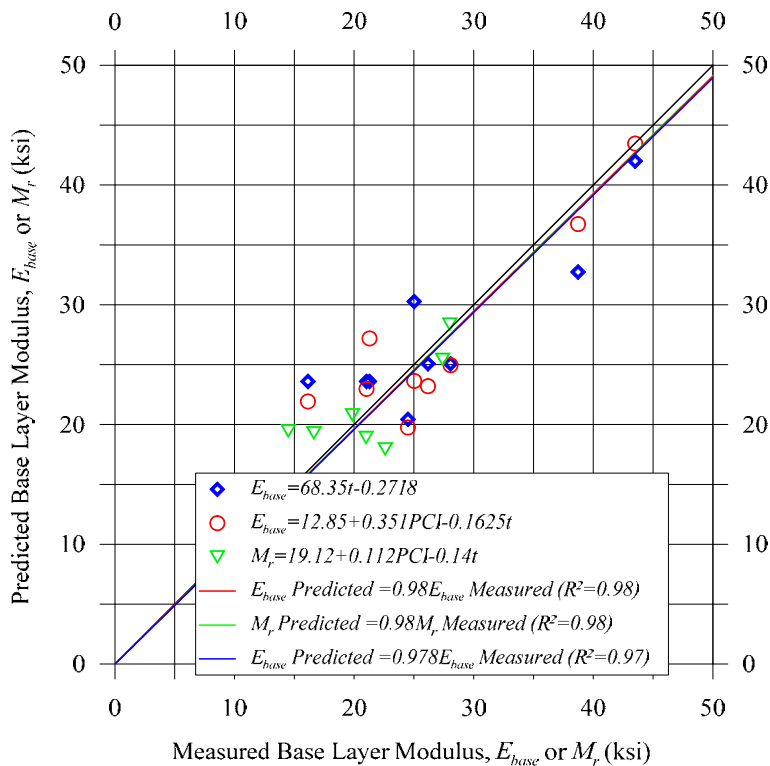


Figure 6.20: Comparison of predicted and measured base layer modulus (E_{base}) and resilient modulus (M_r) based on aggregate base layer age and PCI.

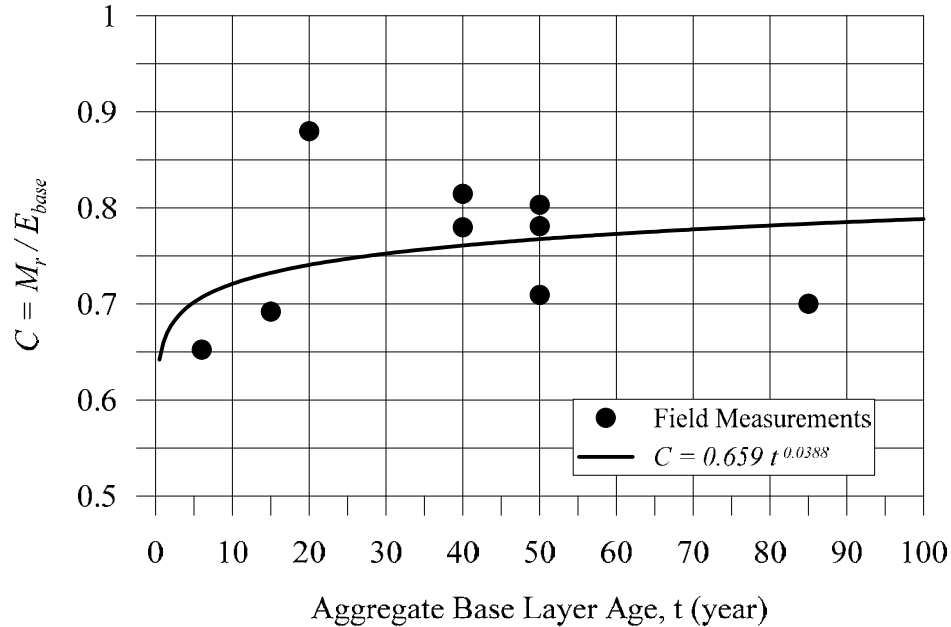


Figure 6.21: Variation of resilient modulus (M_r) to base layer modulus (E_{base}) ratio for aggregate base layers with age.

(2) Using Aggregate Base Layer Particle Size Distribution and Density (Basic Laboratory Tests):

This method can be used with minimal laboratory testing. Base aggregate samples must be obtained from existing pavements using pavement surface coring and base layer sampling. The retrieved aggregate specimens will then be subjected to sieve analysis and compaction tests to determine their basic properties, which are needed for the resilient modulus models presented in Tables 2.6 (LTPP models) and 2.8.

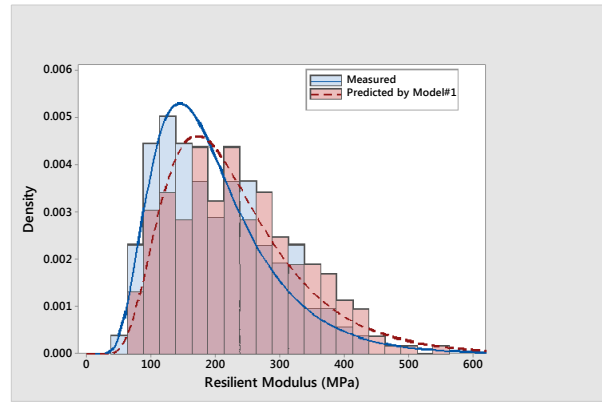
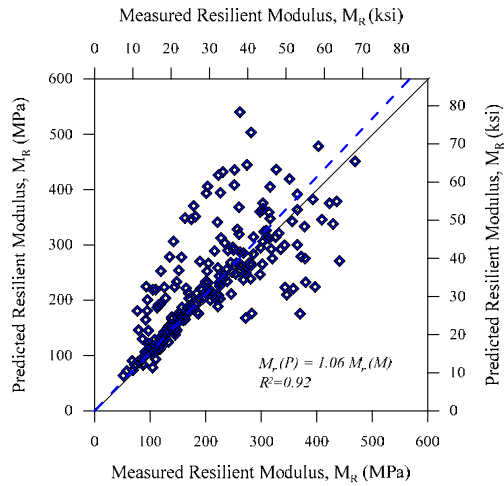
In order to demonstrate this method, base course layer aggregate samples collected from 15 different sources in Wisconsin were subjected to particle size analysis and standard compaction tests to find their corresponding properties. Then the test results were used in the material models to find k_1 , k_2 , and k_3 (Table 2.6 for LTPP models or Table 2.8 for UWM models) for each aggregate sample. Subsequently, k_1 , k_2 , and k_3 were employed in Equation 6.11 to predict the resilient modulus using the stress levels identified in the AASHTO T 307 load sequences. After resilient modulus predictions were made using the developed models, the repeated load triaxial test was conducted on the aggregate specimens and the resilient modulus values obtained were compared with the results predicted by these models. Figure 6.22 presents comparisons of the resilient modulus of the 15 aggregates predicted using Models #1, #2, and #3 and the results obtained from laboratory measurements. Inspection of Figure 6.22 shows that the performance of Models #1 and #3 was reasonable as indicated by the best fit line of the predicted versus measured values as well as the histograms and lognormal distribution parameters. It

should be noted that Model #1 was developed based on Wisconsin aggregates and has more material inputs compared with Model #2. Model #3 was developed based on both Wisconsin and Kentucky aggregates.

$$M_r = k_1 P_a \left(\frac{\sigma_b}{P_a} \right)^{k_2} \left(\frac{\tau_{oct}}{P_a} + 1 \right)^{k_3} \dots\dots\dots (6.11)$$

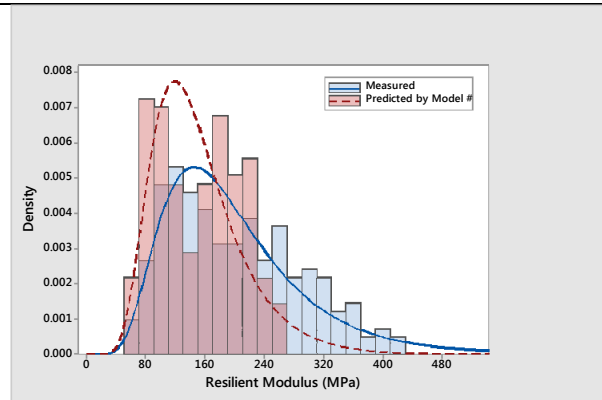
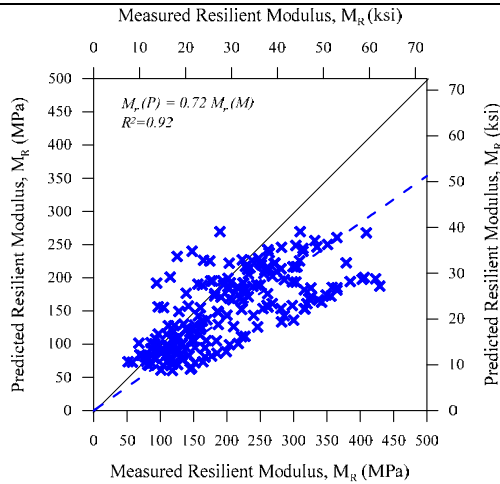
In order to assess the impact of the resilient modulus on pavement performance as determined by AASHTOWare Pavement ME Design software, the research team conducted a sensitivity analysis using STH 33, an urban principal arterial between Port Washington and Saukville in Wisconsin. The project was constructed during the summer of 2011 at which time the authors sampled the aggregates and conducted various tests for a research project. The pavement was constructed with a 6.5 in HMA surface layer and a 13.5 in dense graded crushed stone aggregate base layer over silty clay subgrade soil described as A-7-6 according to AASHTO soil classification. The traffic data for STH 33 was obtained from WisDOT in which the initial annual average daily truck traffic (AADTT) started at 1,500 and grew to 2.96 and 7.34 million after 10 and 20 years, respectively.

The results of STH 33 pavement performance over a 20 year period under various base layer resilient modulus input values were presented earlier in Figure 6.11. For the lowest base resilient modulus of 10 ksi, the pavement showed higher base and total rutting, more fatigue cracking, and higher IRI numbers compared with its performance with base layer resilient modulus of 50 ksi at any time over 20 years. The field performance data for the STH 33 pavement was obtained from the WisDOT PIF database, which is updated every two years. The resilient modulus of the STH 33 base layer at a bulk stress of 30 psi was obtained as 33 ksi from the repeated load triaxial test or by using the models presented in Table 2.8 and Equation 6.11. Comparison of field measurements and predicted performance values (as an example) for a base layer resilient modulus of 30 ksi showed that, at 5 years of service, the measured IRI was 103 in/mile and measured total rutting was 0.08 in while the AASHTOWare Pavement ME Design predicted an IRI of 78 in/mile and total rutting of 0.22 in.



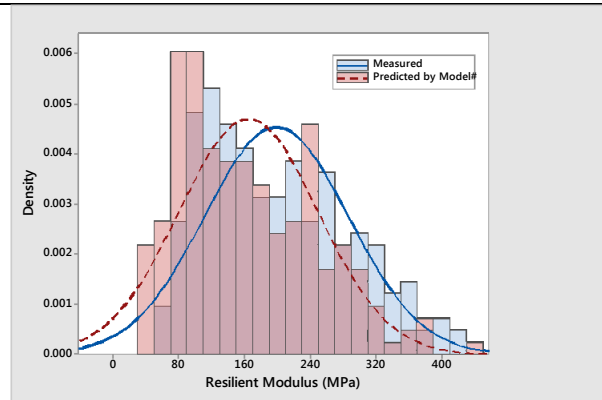
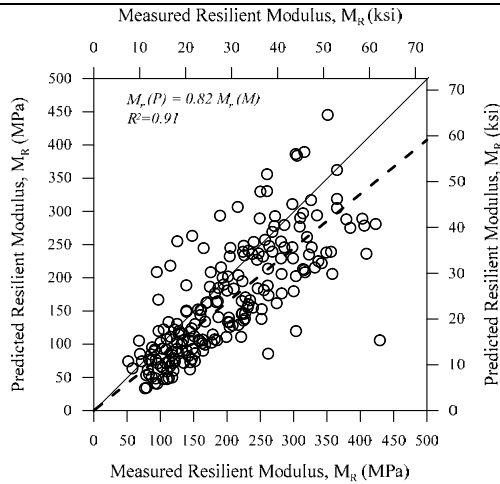
Predicted resilient modulus: Lognormal distribution
 $\mu=232.2$ MPa, $\sigma=101.9$ MPa

(a) Model #1



Predicted resilient modulus: Lognormal distribution
 $\mu=150.9$ MPa, $\sigma=57.4$ MPa

(b) Model #2



Predicted resilient modulus: Lognormal distribution
 $\mu=166.2$ MPa, $\sigma=92.5$ MPa

(c) Model #3

Figure 6.22: Performance of the developed models in predicting the resilient modulus of 15 base aggregates in HMA pavements in Wisconsin (measured values: lognormal distribution: $\mu=200.1$ MPa, $\sigma=94.4$ MPa)

(3) Using Base Layer Modulus from Back-calculation Module of AASHTOWare Pavement ME Design:

This method requires performing the FWD and GPR tests (due to the variability in pavement layers properties and thicknesses as well as variability in properties of subgrade soil) then using the Back-calculation Module of the AASHTOWare Pavement ME Design software to evaluate pavement design and performance over periods of time. It should be noted that the input for the aggregate base layer is the resilient modulus (sometimes denoted as M_R or M_r in the literature). In this case, the authors suggest using the following equation:

$$C = \frac{M_r}{E_{base}} = \left(\frac{0.5}{0.659t^{0.0388}} \right) \dots\dots\dots (6.12)$$

where t is the age in years of the aggregate base layer.

Chapter 7

Summary and Conclusions

This research project investigated the performance of base layer aggregates in HMA pavements using laboratory tests on collected base layer materials and field tests on corresponding pavement sections. The purpose of this research was to investigate potential degradation of base aggregates, to investigate strength/modulus reductions over time, and to evaluate the likely causes of both. Such information will be utilized for pavement design and performance evaluation using the AASHTOWare Pavement ME Design software.

Comprehensive field and laboratory testing programs were conducted to investigate base layer aggregates in which identified test sections at the selected pavement sites were subjected to testing using FWD, GPR and DCP. Visual distress surveys were also conducted at the selected pavement sections. Base layer aggregate samples were collected from these pavement sites and were subjected to a comprehensive laboratory testing program including: standard compaction, particle size analysis, Atterberg limits, sodium sulfate soundness test on both coarse and fine fractions, Micro-Deval abrasion test on both coarse and fine fractions, absorption, specific gravity, repeated load triaxial test (resilient modulus), and the CBR test. The base aggregates collected consisted of crushed stone composed of mainly carbonates and gravel/crushed gravel materials.

The results of the sieve analyses indicated that the particle size distribution for the majority of the investigated base aggregates fell partially outside the corresponding WisDOT base aggregate gradation specifications, with eight samples possessing a percent fines greater than the corresponding historical permitted percent fines range of 10 to 15% (currently 12%). In addition, fineness number values for approximately eight samples were lower than the specification limit (grading number values were higher). It should be noted that those eight samples have larger percent sand (or percent fines plus percent sand) > percent gravel. Since these samples exceeded the corresponding gradation specification limits at the time of construction, this could be due to degradation and disintegration of aggregate particles due to the impact of freeze-thaw cycles coupled with the repeated traffic loads. It should be mentioned that the historical gradation specifications were obtained for a number of these pavements and therefore the gradation of these materials was compared with the specifications at the time of construction.

The results of the Atterberg limits tests showed that fines found in 15 of the aggregate samples were non-plastic, with only three samples possessing plastic fines. Visual inspections and comparisons with subgrade soils did not show (in general) a widespread pumping and contamination of the base layers from subgrade soils. It should also be noted that in several of

the investigated pavement sections, large stone (breaker run or select materials) subbase layers were used, which could provide a barrier for minimizing/eliminating contamination effects.

The absorption values of the investigated base aggregates varied between 0.55% for gravel to 4.05% for base aggregate composed of a mixture of crushed stone and recycled concrete aggregate/recycled asphalt pavement. The crushed stone coarse aggregate samples possessed absorption values ranging from 1.09% to 2.78%, compared with 0.55% to 2.08% for gravel/crushed gravel samples. The average coarse aggregate absorption values obtained from earlier studies conducted on Wisconsin virgin aggregates (Tabatabai et al., 2013) were 1.99% and 1.35% for crushed stone and gravel/crushed gravel, respectively. Consequently, eight crushed stone samples exhibited absorption values greater than 1.99% and five gravel/crushed gravel samples possessed absorption values greater than 1.35%, leaving only seven samples with absorption values less than the corresponding averages.

Micro-Deval abrasion test results showed that fine aggregates exhibited more mass loss, in general, than coarse aggregates from the same aggregate source. The mass loss exhibited by the fine aggregate fraction varied between 6.9% (for gravel) and 29.7% (for crushed carbonates). On the other hand, the mass loss for coarse aggregates ranged from 7% (for gravel) to 20.3% (for crushed carbonates) compared with a mean mass loss of 15.05% for Wisconsin virgin coarse aggregates obtained by Tabatabai et al. (2013). Seven (all crushed stone) out of the twenty investigated existing base layer aggregate samples exhibited mass loss that exceeded this average (15.05%). Four out of these seven samples exhibited absorption that exceeded the mean value for Wisconsin virgin aggregates. Earlier WHRP studies (Tabatabai et al., 2013 and Weyers et al., 2005) indicated a correlation between aggregate absorption and Micro-Deval abrasion mass loss and to some degree the sodium sulfate soundness mass loss.

Sodium sulfate test results showed that fine aggregates exhibited more mass loss, in general, than coarse aggregates from the same aggregate source. For fine aggregates, the mass loss varied between 2.6% and 13.7% (for crushed carbonates). The mass loss for coarse aggregates ranged from 0.8% (for crushed carbonates) to 16.6% (for mixture of crushed carbonates and some recycled PCC/RAP) compared with a mean mass loss of 3.36% for Wisconsin virgin coarse aggregates reported by Tabatabai et al. (2013). Eight out of the fourteen investigated existing base layer aggregates exhibited mass loss that exceeded this average (3.36%), however, no base aggregate samples possessed mass loss values greater than the WisDOT threshold mass loss limit of 18%.

Mass loss from the sodium sulfate soundness test was compared with mass loss from the Micro-Deval abrasion test for both the virgin and base layer coarse aggregates. The comparison indicated a poor correlation between the mass loss percent from the two tests, which is consistent with the finding of Cooley (2000), Weyers et al. (2005), and Tabatabai et al. (2013).

Strength and modulus evaluations of the investigated base aggregates and pavement test sections were achieved via soaked CBR, repeated load triaxial (resilient modulus), DCP, and FWD tests. The soaked CBR values ranged from 20.2% (for gravel) to 91.9% (for crushed stone). For base layer aggregates composed of gravel/crushed gravel, the soaked CBR values varied between 20.2% and 75.2% and for base layer aggregates composed of crushed stone, the soaked CBR values ranged from 52.2% to 91.9%. The soaked CBR test results showed, in general, low CBR numbers, especially for aggregate samples with larger amounts of fines and for gravel/crushed gravel aggregate samples.

The repeated load triaxial test results showed an acceptable level of resilient modulus values compared with resilient modulus values in the database of Wisconsin virgin aggregates from both pits and quarries (gravel/crushed gravel and crushed stone). However, when the base aggregates are of gravel/crushed gravel origin, the resilient modulus values were lower compared with aggregates from crushed stone sources. For Wisconsin virgin aggregates, test results showed a mean of 23.79 ksi and a COV of 45.3% for a lognormal distribution of resilient modulus values. Resilient modulus test results of base aggregates from pavements with good performance (high PCI and low IRI) are higher compared with the Wisconsin virgin aggregates even though these materials were in-service as base layers for about six years.

The DCP test results provided information about the aggregate base quality of construction as well as the variability in such quality. Aggregate base layer performance is influenced by the aggregate material's characteristics and properties, however, the quality of base layer construction plays an important factor in pavement performance. DCP test results indicated variability in strength (as predicted by CBR), modulus (predicted resilient modulus), density, and thickness uniformity of the base materials at different test locations and depths. Variability in the predicted CBR values for the presented pavement test sections ranged between a COV of 48% and 103% for crushed stone base layers. The in-service age of base layer aggregates was not a significant factor in the strength of the base layer determined by CBR (predicted from the DCP test), however, percent fines and type/source of base aggregate (crushed stone versus gravel) were important.

GPR profiles and pavement surface coring showed variability in pavement layer thicknesses including both HMA surface and aggregate base course layers. GPR pavement profiles showed a 5.98 in average HMA pavement layer thickness with a COV of 16% compared with 5.0 in and 5.75 in cores extracted from one test section. In addition, GPR profiles showed the average thickness of the upper base layer was 2.06 in with a COV of 31% and the average thickness of the lower base layer was 2.83 in with a COV of 35%, indicating an average total base layer thickness of approximately 4.9 in compared with a thickness of 10 in measured by the research team. Consequently, the GPR test results demonstrate the existence of variability in the thickness of pavement layers, which is an important factor affecting pavement performance.

FWD test results showed significant variability in pavement surface deflections (D_0) within individual test sections and among the various pavement test sections. Within a test section, the highest variability showed D_0 ranging from 4.1 to 22.6 mils with an average of 7.9 mils and COV of 47.1%. Among all test sections, D_0 ranged from 3.3 mils to 36.3 mils with COV ranging from 13.7% to 47.1%.

The back-calculated base layer moduli (E_{Base}) for all investigated pavement test sections indicated significant variability, ranging from 4 to 400 ksi within individual pavement test sections and among pavements. The average back-calculated modulus for the investigated aggregate base layers was generally low, ranging from 16 to 139 ksi and with 14 out of 20 pavement test sections having E_{base} less than or equal to 45 ksi. It was noticed that variability in E_{base} was significant within the pavement test sections with lower PCI and higher IRI values. The average back-calculated layer moduli for the investigated base layers of more than 20 years of age were lower compared with base layers of younger age (about 6 to 9 years that had higher PCI and lower IRI values).

The results of the visual and automated distress surveys (in terms of calculated PCI and IRI) for investigated pavement test sections showed high variability with classified pavement conditions ranging from poor to good. The PCI values calculated by the research team are in general lower than the PCI values obtained from WisDOT PIF files.

Based on the results of the laboratory and field testing program (summarized in this chapter), the research team believes that the long-term performance of base layer aggregates impacted pavement performance. While base aggregate materials, in general, did not exhibit significant degradation or disintegration (as demonstrated by laboratory tests) or significant contamination from the subgrade, the performances of these aggregate base layers were lower compared with performance of “good pavements” established as a reference. In order to account for the reduction of in-service base layer aggregate condition over time (reduction in quality due to various factors including degradation, contamination, etc.), the research team proposed three methods to determine the aggregate base layer modulus to use as an input for the AASHTOWare Pavement ME Design software:

1. Using aggregate base layer age without field or laboratory tests. This method is detailed in Section 6.5 of Chapter 6. Equations 6.6 to 6.10 were developed to provide a rough estimate of aggregate base layer resilient modulus based on in-service aggregate base layer age or age and PCI.
2. Using existing base layer aggregate gradation and density. This method requires base aggregate material sampling using pavement surface coring and minimal laboratory testing (sieve analysis and compaction test). The retrieved aggregate specimens must be subjected to sieve analysis and a compaction test to determine their basic properties, which are needed for the resilient modulus material models

presented in Tables 2.6 (LTPP models) and 2.8 (UWM Models #1, #2, and #3). The performance of these models is presented in Chapters 2 and 6.

3. Using the Back-calculation Module of the AASHTOWare Pavement ME Design software. This method requires performing FWD and GPR tests (due to the variability in properties and thicknesses of pavement layers and the variability in properties of subgrade soils) then using the Back-calculation Module of the AASHTOWare Pavement ME Design software to estimate the base layer modulus. In order to obtain the resilient modulus as input for the AASHTOWare Pavement ME Design, the factor C can be calculated from Equation 6.12.

Pavement performance output from the AASHTOWare Pavement ME Design software depends to a large extent on the calibration factors used in the software. The research team conducted a comprehensive sensitivity analysis on the impact of variation of the resilient modulus on pavement performance for STH 33 and USH 45 Pelican Lake in Chapter 6, which demonstrated the influence of varying the resilient modulus on the thickness of overlay design. The analysis showed that pavements with lower base layer modulus values developed surface distress (cracking, rutting, roughness) at earlier age compared with pavements with higher base layer modulus values. Consequently, pavements with lower base layer modulus values require earlier rehabilitation (such as overlay) or thicker overlays at later times.

References

1. American Association of State Highway and Transportation Officials (1990). *Construction Manual for Highway Construction*, Washington, D.C.
2. American Association of State Highway and Transportation Officials (2018). AASHTOWare Pavement ME Design, <http://me-design.com/MEDesign/>.
3. American Association of State Highway and Transportation Officials, (2017). Standard Specifications for Transportation Materials and Methods of Sampling and Testing and Provisional Standards.
4. Annan, P., (2005). "Ground Penetrating Radar" in Near Surface Geophysics. SEG, Tulsa, OK. 357-438.
5. Barksdale, R. D., (1991). *The Aggregate Handbook*, National Stone Association, Washington, DC.
6. Barksdale, R. D., (2001). *The Aggregate Handbook*. National Stone, Sand and Gravel Association, 4th Ed.
7. Cooley, L. A., and James, R. S., (2003). "Micro-Deval Testing of Aggregates in the Southeast," In Transportation Research Record: Journal of the Transportation Research Board, No. 1837, TRB, National Research Council, Washington D.C., pp. 73-79.
8. Dai, S., and Kremer, C., (2006). Improvement and Validation of Mn/DOT DCP Specifications for Aggregate Base Materials and Select Granular (No. MN/RC-2005-32). Office of Materials Minnesota Department of Transportation.
9. Dong, Z., Ye, S., Gao, Y., Fang, G., Zhang, X., Xue, Z. and Zhang, T., (2016). 'Rapid Detection Methods for Asphalt Pavement Thicknesses and Defects by a Vehicle-Mounted Ground Penetrating Radar (GPR) System'. *Sensors*, 16; doi:10.3390/s16122067.
10. Eggen, P. R., and Brittnacher, D. J., (2004). Determination of Influences on Support Strength of Crushed Aggregate Base Course due to Gradational, Regional and Source Variations. OMNNI Associates, Wisconsin Department of Transportation.
11. Federal Highway Administration (FHWA, 2018). The Long-Term Pavement Performance (LTPP) Program.
12. Fowler, D. W., Allen, J. J., Lange, A., and Range, P., (2006). "The Prediction of Coarse Aggregate Performance by Micro-Deval and Other Aggregate Tests," Report ICAR 507-1F, International Center for Aggregate Research, University of Texas, Austin.
13. Harison, J. A., (1987). "Correlation between California Bearing Ratio and Dynamic Cone Penetrometer Strength Measurement of Soils." *Proc. Instn. Civ. Engrs*, Part 2, Technical Note 463. p. 833-844.
14. Heukelom, W., and Klomp, A. J. G., (1962). "Dynamic Testing as Means of Controlling Pavements during and After Construction," *Proc.*, 1st International Conference on Structural Design of Asphalt Pavement, University of Michigan.

15. Hoegh, K., Khazanovich, L., Dai, S., and Yu, T., (2015). "Evaluating asphalt concrete air void variation via GPR antenna array data". *Case Studies in Nondestructive Testing and Evaluation*, 3, 27-33.
16. Hopkins, T. C., Beckham, T.L., and Sun, C., (2007). *Resilient Modulus of Compacted Crushed Stone Aggregate Bases*. University of Kentucky, Lexington; Kentucky Transportation Cabinet; Federal Highway Administration, 112p
17. Hossain, Z., Zaman, M., and Doiron, C., (2012). *Evaluation of Resilient Response of Unbound Aggregates toward Implementation of the Mechanistic-Empirical Pavement Design in Oklahoma*. Transportation Research Board 91st Annual Meeting, Transportation Research Board, 19p
18. Kleyn, E. G., (1975). "The Use of the Dynamic Cone Penetrometer (DCP)." Report 2/74, Transvaal Roads Department, Pretoria, South Africa.
19. Li, L., Liu, J., and Zhang, X., (2010). *Resilient Modulus Characterization of Alaskan Granular Base Materials*. Alaska University Transportation Center; Alaska Department of Transportation and Public Facilities; Research and Innovative Technology Administration, 108p.
20. May, R.W., and Witczak, M. W., (1981). *Effective Granular Modulus to Model Pavement Responses*. Transportation Research Record, Issue 810, pp 1-9.
21. Ni, B., Hopkins, T.C., Sun, L., and Beckham, T. L., (2002). "Modeling the Resilient Modulus of Soils." *Proceedings of the 6th International Conference on the Bearing Capacity of Roads and Airfields*, Lisbon, Portugal, AA Balkema, Volume 2, p. 1131-42
22. Powell, W. D., Potter, J. F., Mayhew, H. C., and Nunn, M. E. (1984). "The Structural Design of Bituminous Roads." TRRL Report LR 1132, 62 pp.
23. Puppala, A. J., (2008). *Estimating Stiffness of Subgrade and Unbound Materials for Pavement Design*. NCHRP Synthesis of Highway Practice, Issue 382, 137p.
24. Rao, C., Titus-Glover, L., Bhattacharya, B., and Darter, M. I., (2012). *User's Guide: Estimation of Key PCC, Base, Subbase, and Pavement Engineering Properties from Routine Tests and Physical Characteristics*. Applied Research Associates, Incorporated; Federal Highway Administration, 90p.
25. Seed, H. B., Mitry, F. G., Monismith, C. L., and Chan, C.K., (1967). *Prediction of Flexible Pavement Deflections from Laboratory Repeated-Load Tests*. NCHRP Report, Issue 35.
26. Senior, S. A and Rogers, C. A., (1991). "Laboratory Tests for Predicting Coarse Aggregate Performance in Ontario," *Transportation Research Board 1301*, National Research Council, Washington DC, pp. 97-106.
27. Tabatabai, H., Titi, H. H., Lee, C. W., Qamhia, I., and Puerta Fella, G., (2013) "Investigation of Testing Methods to Determine Long-Term Durability of Wisconsin Aggregates," *Research Report*, Wisconsin Department of Transportation SPR # 0092-10-08, Wisconsin Highway Research Program, Madison, WI, 104 p.

28. Titi, H. H., and Matar, M. (2018). "Estimating Resilient Modulus of Base Aggregates for Mechanistic-Empirical Pavement Design and Performance Evaluation," Manuscript under review, Transportation Geotechnics, Elsevier.
29. Tutumluer, E., (2012). "Practice for Unbound Aggregate Pavement Layers," National Cooperative Highway Research Program (NCHRP) Synthesis Topic 43-03, Transportation Research Board, National Research Council, Washington, D.C.
30. Uzan, J., (1985). Characterization of Granular Material. Transportation Research Record, Issue 1022, pp 52-59.
31. Von Quintus, H. L., Rao, C., Minchin, R. E., Nazarian, S., Maser, K. R., and Prowell, B., (2009). "NDT Technology for Quality Assurance of HMA Pavement Construction," National Cooperative Highway Research Program (NCHRP) Report 626, Transportation Research Board (TRB), Washington, D.C.
32. Vose Software, (2018). "ModelRisk" software, <http://www.vosesoftware.com/>.
33. Weyers, R. E., Williamson, G. S., Mokarem, D. W., Lane, D.S., and Cady, P.D., (2005). "Testing Methods to Determine Long Term Durability of Wisconsin Aggregate Resources," Wisconsin Highway Research Program SPR# 0092-02-03, WHRP 06-07, 91 pages.
34. Witczak, M. W. Harmonized Test Methods for Laboratory Determination of Resilient Modulus for Flexible Pavement Design. Federal Highway Administration (FHWA). American Association of State Highway and Transportation Officials (AASHTO), National Cooperative Highway Research Program (NCHRP), NCHRP Project 1-28A. Results Digest 285.
35. Yau, A; Von Quintus, H. L., (2002). Study of LTPP Laboratory Resilient Modulus Test Data and Response Characteristics: Final Report. Federal Highway Administration (FHWA). Office of Infrastructure Research and Development, Issue FHWA-RD-02-051, 161p.

Appendix A

USDA Soil Survey

Table A-1: Soil data base acquired from the USDA website.

Project Site	Most Common Soil Type	Depth (in)	USDA Texture	Classification		Percent Passing Sieve Number 200	Plasticity Index
				Unified	AASHTO		
STH 180 – Marinette	Wainola	0-5	Loamy, fine sand	-	A-2-4	28	5
		5-18	Fine sand, loamy fine sand, very fine sand	-	A-2-4	35	5
		18-33	Fine sand, loamy fine sand, very fine sand	-	A-2-4	35	5
		33-60	Fine sand, loamy fine sand, very fine sand	-	A-2-4	35	4
Edgerton Ave – Greenfield	MtA – Mequon	0-8	Silt loam	CL-ML	A-4	90	7
		8-12	Silt loam, silty clay loam	CL	A-6	90	15
		12-19	Silty clay, clay	CH	A-7-6	85	34
		19-26	Silty clay loam, silty clay, clay	CH	A-7-6	85	28
		26-60	Silty clay loam	CL	A-6	85	15
CTH JJ – Appleton	HrB – Hortonville	0-8	Silt loam	CL	A-4	69	9
		8-14	Silt loam	CL	A-4	65	8
		14-27	Silty clay loam, loam, clay loam	CL	A-7-6	63	22
		27-79	Loam, fine sandy loam	CL	A-2, A-4, A-6	54	14
CTH B – Woodville	HaA – Halder	0-12	Silt loam	CL-ML	A-4	75	5
		12-25	Sandy clay loam, silt loam, loam	CL-ML	A-4	60	6
		25-28	Sandy loam, loamy sand	SM	A-2-4	26	4
		28-60	Sand, course sand	-	A-1-b	13	2
STH 33 – Saukville	WmA – Wasepi	0-8	Sandy loam	SC-SM, SM	A-2, A-4	38	4
		8-30	Sandy loam, sandy clay loam, fine sandy loam	SM, SC-SM, SC	A-2, A-4, A-6	33	9
		30-60	Sand	GP-GM, GP, SP, SP-SM	A-1, A-2, A-3	5	NP

Table A-1 (Cont.): Soil data base acquired from the USDA website.

USH 45 – Larsen	NeA – Nebago	0-9	Fine sand	SM	A-2-4	20	1	
		9-32	Fine sand, sand, loamy sand	SC-SM	A-2-4	20	4	
		32-34	Fine sandy loam, sandy loam	SC	A-6	40	14	
		34-60	Silty clay, clay	CH	A-7-6	85	44	
STH 13 – Spencer (Section 2)	MfA – Marshfield	0-9	Silt loam	CL, ML	A-6, A-4	77	8	
		9-14	Silt loam	CL, CL- ML, ML	A-4, A-6	79	7	
		14-30	Silt loam, silty clay loam	CL	A-7-6, A-4, A-6	76	13	
		30-36	Gravelly sandy clay loam, loam, clay loam	SC, CL	A-2, A-6, A- 7-6	52	18	
		36-79	Loam, gravelly sandy loam, sandy clay loam	CL, SC	A-2, A-4, A-6	46	10	
STH 32 – Forest County	Au – Au Gres	0-4	Loamy sand	SM	A-2-4	20	4	
		4-29	Sand, loamy sand	SP, SP- SM, SC- SM, SM	A-1-b, A-2-4, A-3	15	4	
		29-60	Sand	SM, SP, SP-SM	A-1-b, A-2-4, A-3	8	NP	
STH 32 – Oneida County	Cb – Carbondale, Lupton, Markey mucks	Carobondale	0-35	Muck	PT	A-8	100	NP
			35-60	Mucky peat	PT	A-8	100	NP
		Lupton	0-12	Muck	PT	A-8	100	NP
			12-60	Muck	PT	A-8	100	NP
		Markey muck	0-26	Muck	PT	A-8	100	NP
			26-60	Sand, fine sand, loamy sand	SM, SP, SP-SM	A-1, A-2, A-3, A-2-4	15	NP
STH 142 East – Burlington	HeB2 – Hebron Loam	0-11	Loam	CL	A-4	65	8	
		11-24	Clay loam, loam, sandy clay loam	CL	A-6	53	19	
		24-28	Silty clay loam, silty clay	CL	A-7-6	88	26	
		28-60	Silty clay loam, silty clay	CL	A-7-6	88	26	

Table A-1 (cont.): Soil data base acquired from the USDA website.

STH 142 West – Burlington	WeA – Warsaw	0-15	Loam	CL, ML	A-4, A-7-6, A-6	64	13
		15-31	Sandy clay loam, loam, clay loam	SC, CL	A-6	57	19
		31-79	Stratified very gravelly loamy sand to extremely gravelly coarse sand	GP, SP, GP-GM	A-1-b	7	2
STH 33 – Middle Ridge	132B2 –Brinkman	0-9	Silt loam	CL	A-6	90	12
		9-71	Silty clay loam, silt loam	CL	A-6	90	15
		71-80	Clay, silty clay, clay loam, silty clay loam, channery clay, flaggy clay loam	CH	A-7-6	60	40
STH 36 – Waterford	HtA – Houghton Muck	0-6	Muck	PT	A-8	100	-
		6-79	Muck	PT	A-8	100	-
USH 45 – Pelican Lake	PaB – Padus Loam	0-3	Loam	CL-ML	A-4	55	4
		3-7	Sandy loam, loam, gravelly fine sandy loam	CL-ML, SM, SC-SM, ML	A-1-b, A-2-4, A-4	48	4
		7-28	Sandy loam, loam, fine sandy loam	SC-SM	A-4	48	4
		28-33	Sandy loam, fine sandy loam, loam	SC-SM	A-4	48	5
		33-60	Sand, coarse sand	SM	A-1-b	13	0
STH 59 – Edgerton	SaB – St. Charles Silt Loam	0-9	Silt loam	CL	A-6	93	15
		9-48	Silt loam	CL	A-6	93	15
		48-54	Loam, sandy loam	SC	A-6	48	13
		54-79	Sandy loam, gravelly sandy loam, loam, gravelly loam	SC-SM	A-2-4	30	6
I-94 – Zoo S1 and S2 – Milwaukee	Cv – Clayey Land	0-10	Clay loam	-	-	-	-

Table A-1 (cont.): Soil data base acquired from the USDA website.

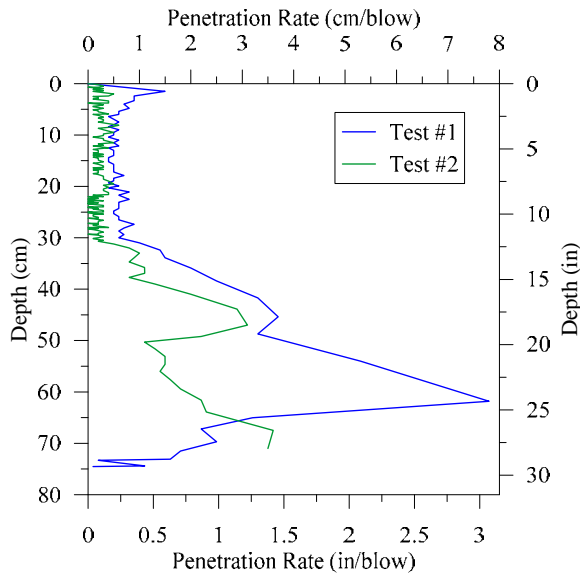
USH 53 – Minong	100C – Menahga Sand	0-1	Slightly decomposed plant material	PT	A-8	100	-
		1-2	Sand	SM, SP-SM	A-2, A-3	10	NP
		2-25	Loamy sand, sand	SM	A-2-4, A-3	15	NP
		25-80	Sand, coarse sand	SM, SP-SM	A-2, A-3	10	NP
STH 162 – Middle Ridge	1125F – Doreton	0-3	Loam, fine sandy loam, silt loam, sandy loam	CL-ML, ML	A-4	58	8
		3-10	Loam, sandy loam, fine sandy loam, silt loam	ML, CL-ML, CL	A-4	57	7
		10-15	Silty clay loam, loam, silt loam, clay loam	CL	A-6	64	18
		15-18	Clay loam, silty clay loam, silt loam, loam	CL	A-6	64	18
		18-30	Extremely flaggy loam, very channery loam, very flaggy loam, very flaggy clay loam, very channery clay loam	CL	A-6	51	19
		30-79	Extremely channery loam, very flaggy sand, very channery sandy loam, extremely flaggy loamy sand, very flaggy loamy sand, very gravelly loamy sand	SM, SC, SC-SM	A-2-4, A-1-b	15	10

Appendix B

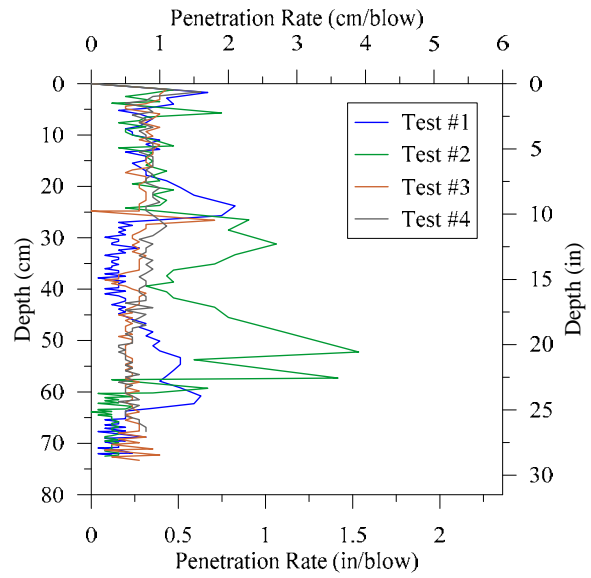
Dynamic Cone Penetration Test Results

And

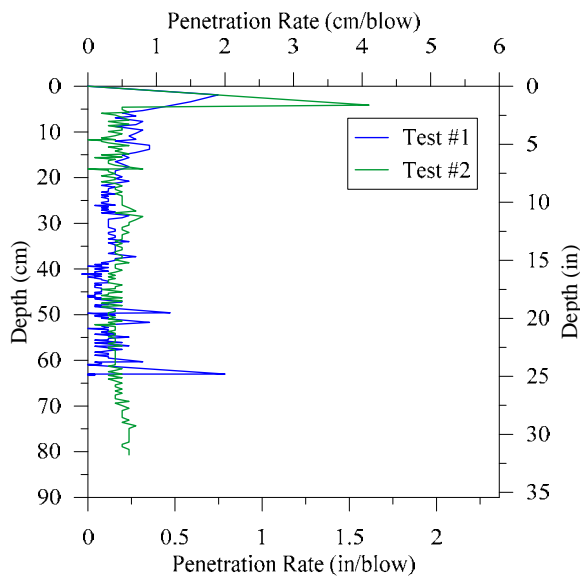
Corresponding Predicted CBR



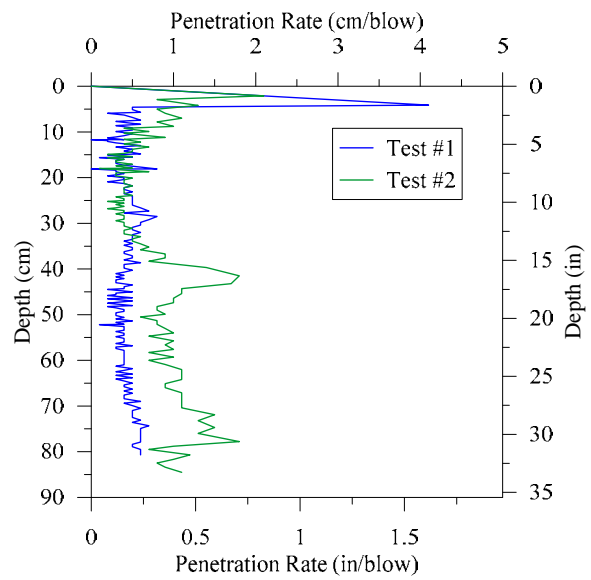
(a) STH 162



(b) STH 36-S2



(c) STH 36-S1



(d) STH 36-S3

Figure B-1: Dynamic cone penetration test results at aggregate base layers of investigated pavements.

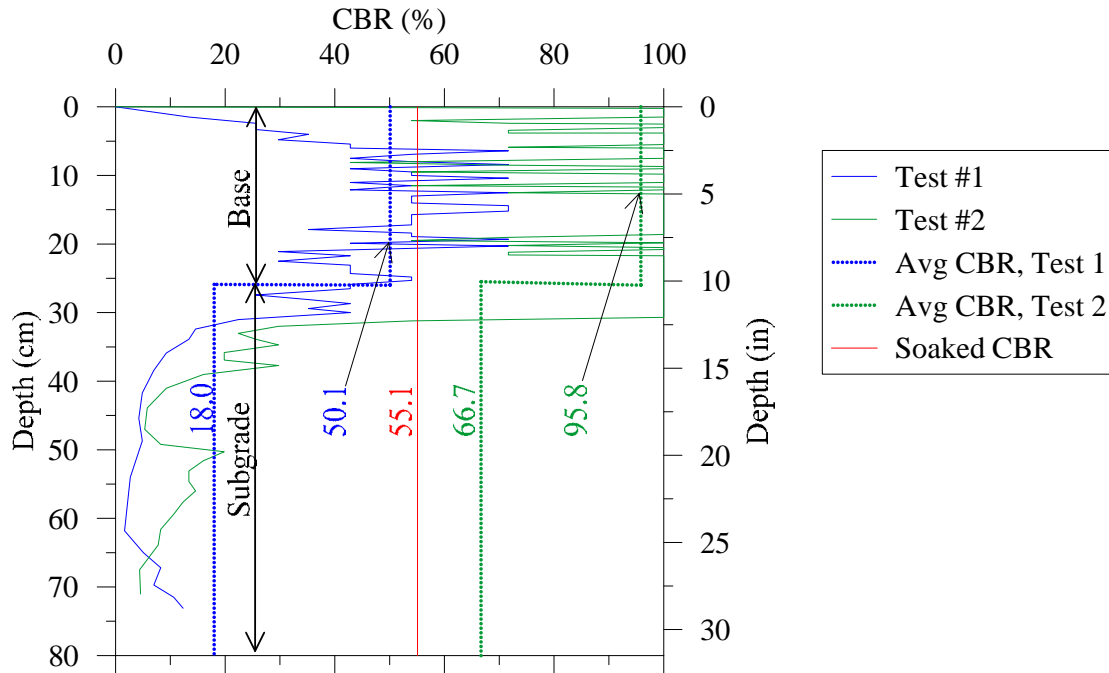


Figure B-2: Average CBR values estimated from Kleyn's equation compared to the soaked CBR value for STH 162.

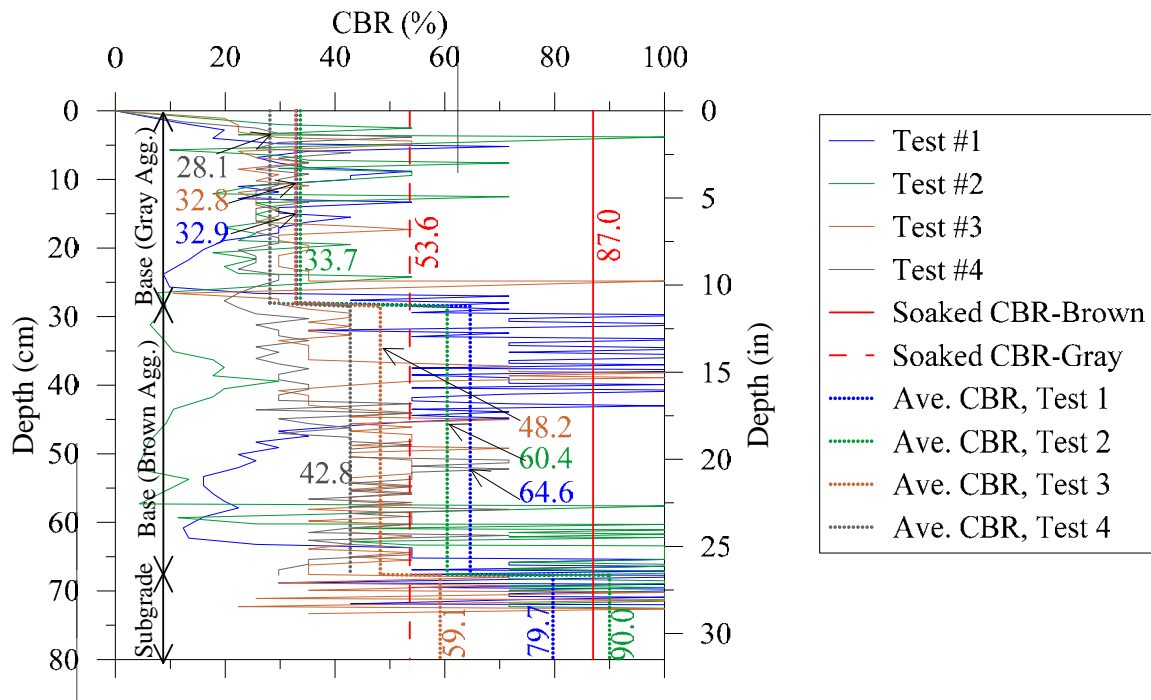


Figure B-3: Average CBR values estimated from Kleyn's equation compared to the soaked CBR value for STH 36-S1.

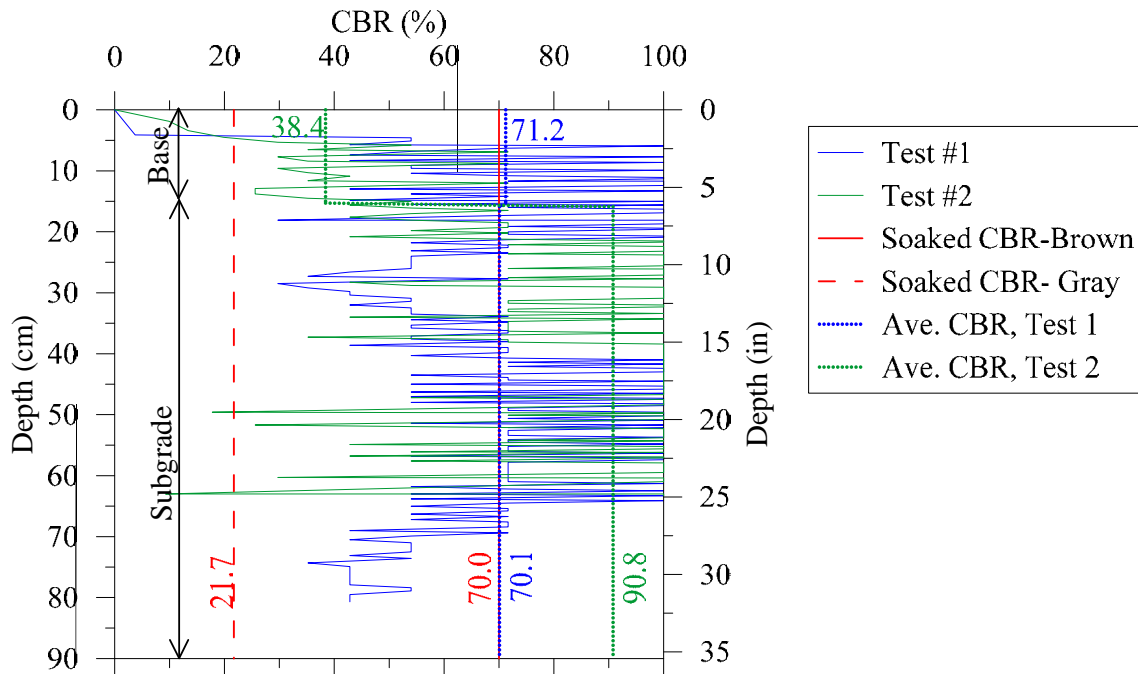


Figure B-4: Average CBR values estimated from Kleyn's equation compared to the soaked CBR value for STH 36-S2.

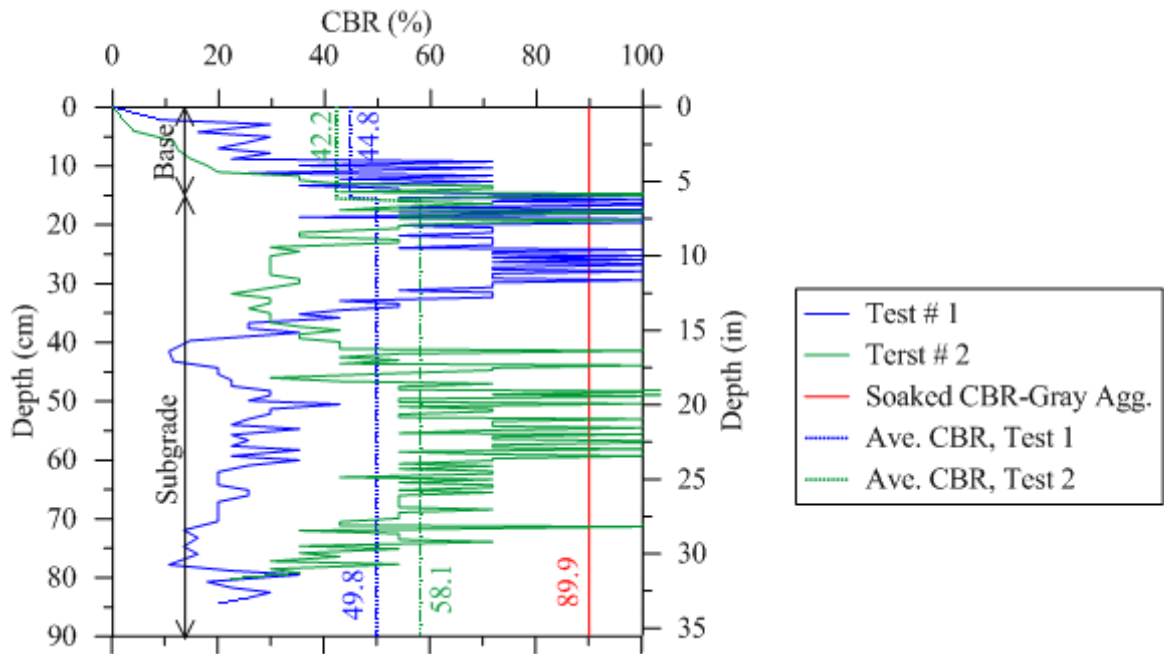


Figure B-5: Average CBR values estimated from Kleyn's equation compared to the soaked CBR value for STH 36-S3.

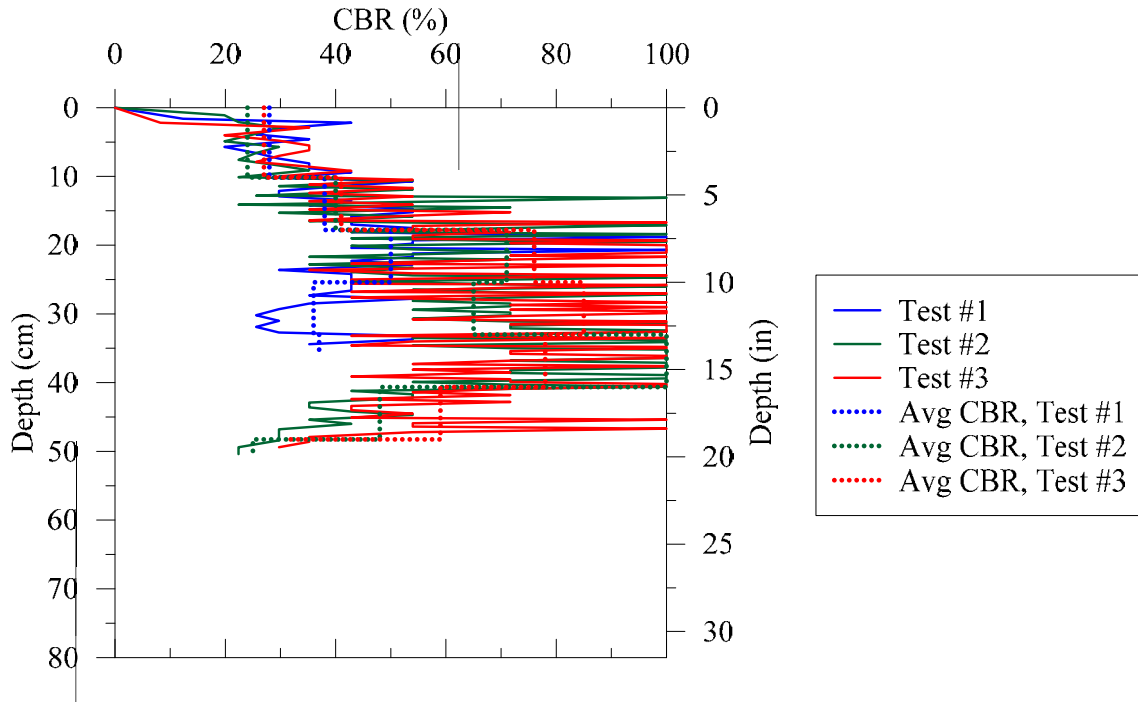


Figure B-6: Average CBR values estimated from Kleyn’s equation for STH 33-Saukville.

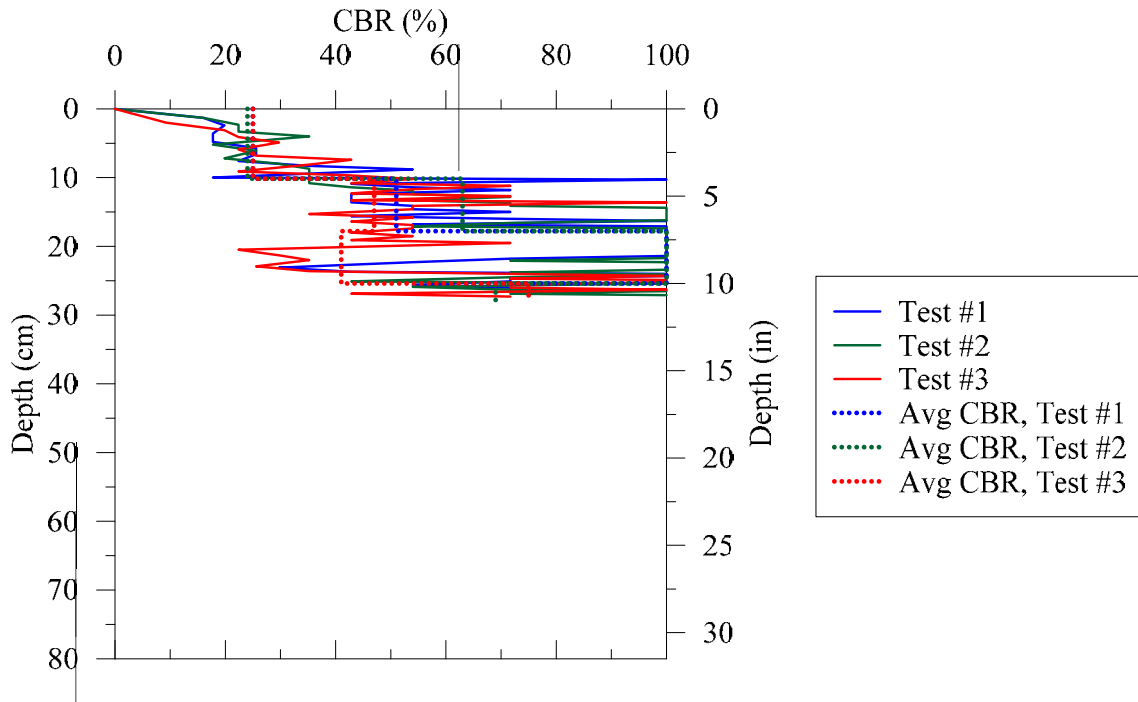


Figure B-7: Average CBR values estimated from Kleyn’s equation for USH 45-Larsen.

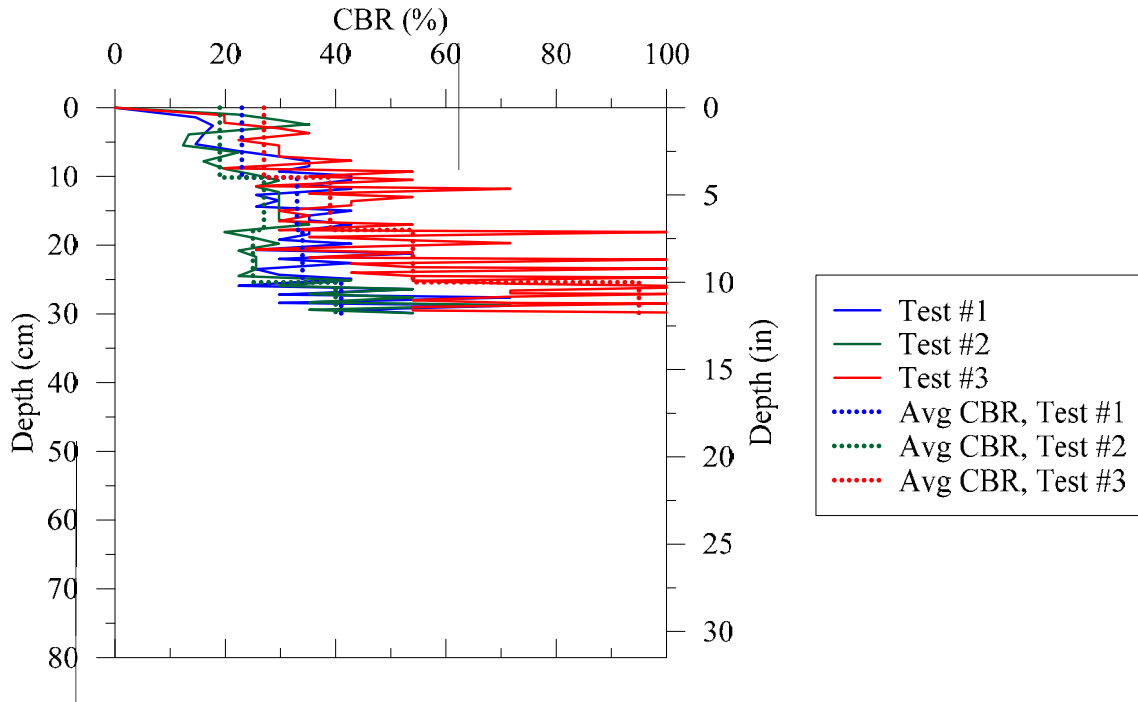


Figure B-8: Average CBR values estimated from Kleyn’s equation for CTH B.

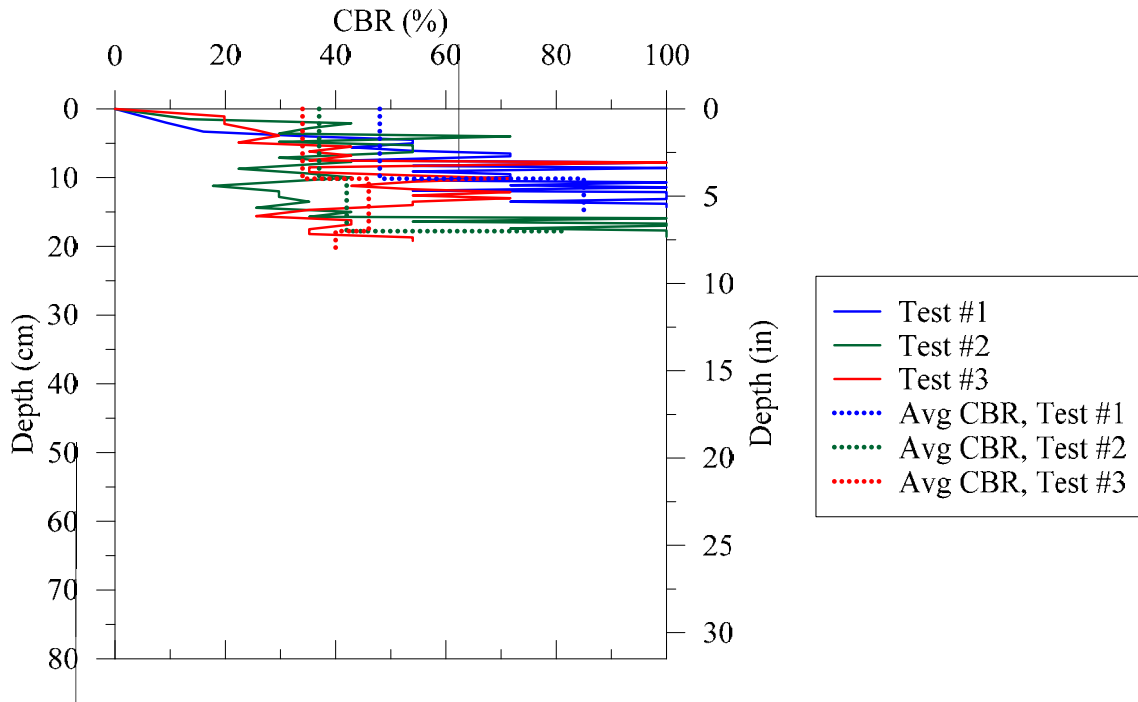


Figure B-9: Average CBR values estimated from Kleyn’s equation for CTH JJ.

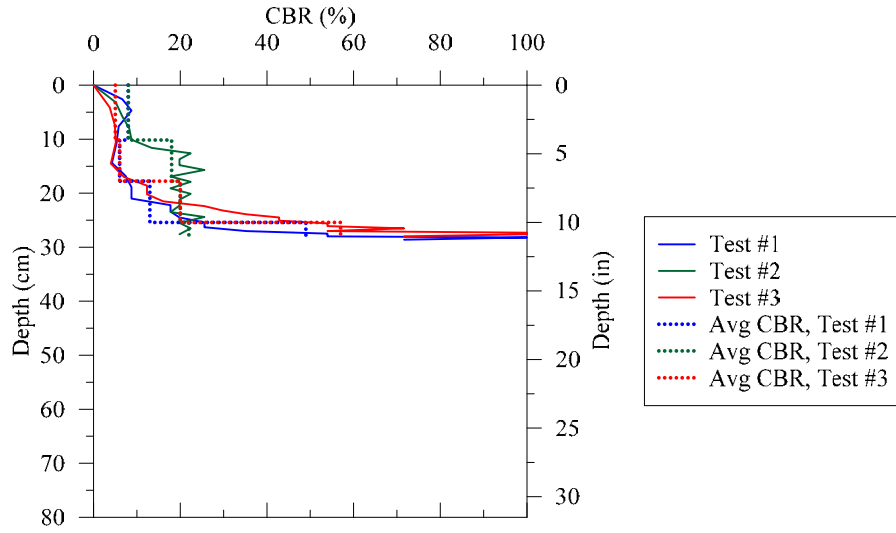


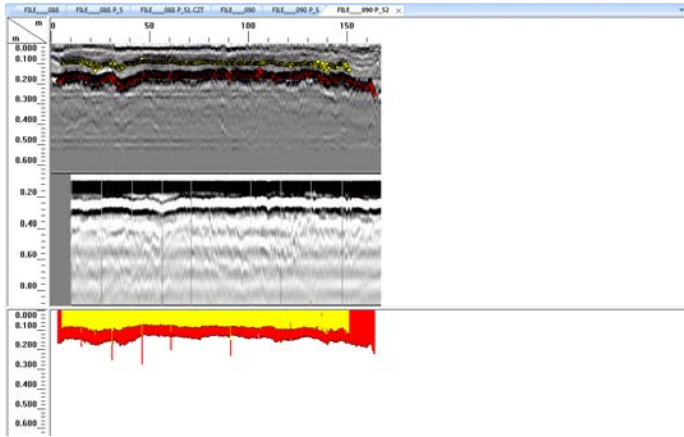
Figure B-10: Average CBR values estimated from Kleyn's equation for STH 13.

Appendix C

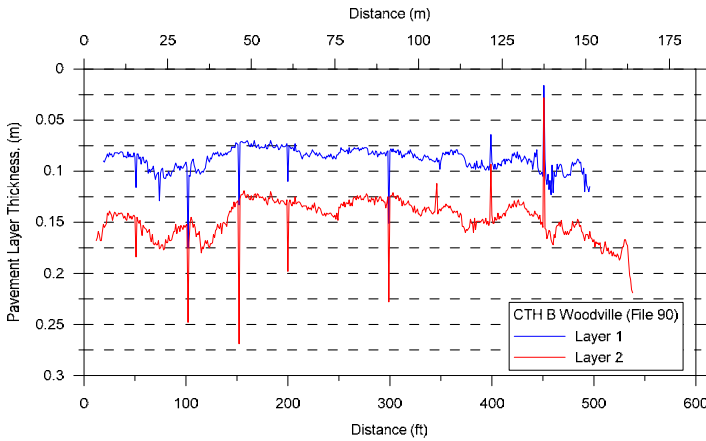
Ground Penetrating Radar Results



(a) Track of the GPR testing at CTH B, Woodville



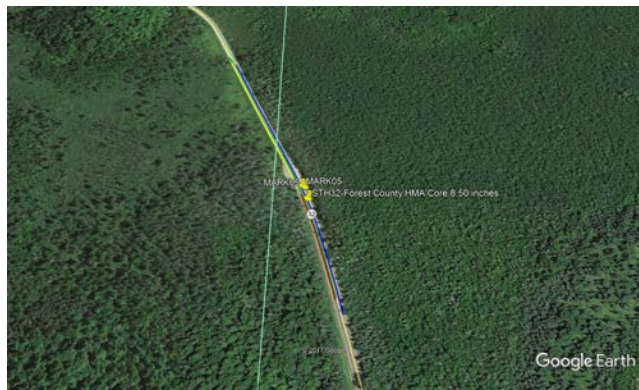
(b) Pavement layer profiles directly from RADAN



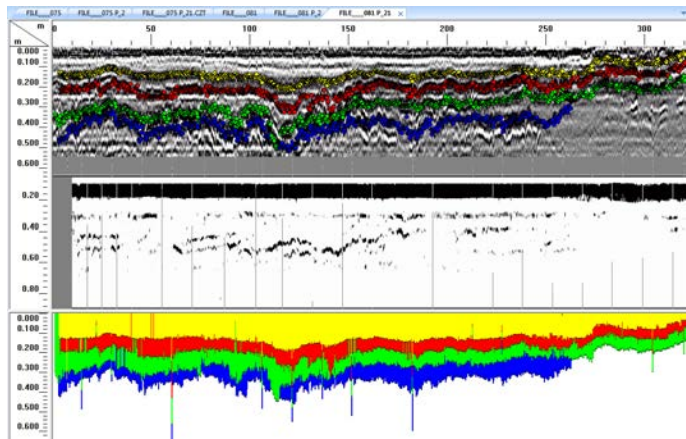
(c) Pavement layer profiles

Relative dielectric permittivity $k' = 4$, Observations: There is no HMA core for this survey so no ground-truthing may be performed. Two clear reflection layers are observed. The bottom of the second layer is assigned to the bottom of the HMA layer at about 0.2 m depth.

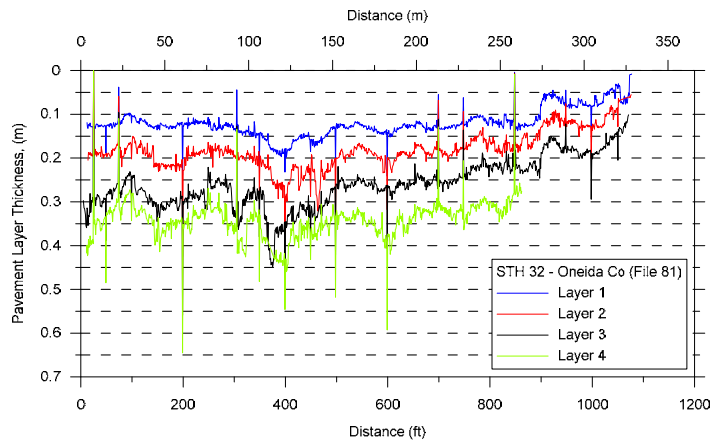
Figure C-1: Pavement layer profiles obtained from analysis of GPR data from CTH-B.



(a) Track of the GPR testing at STH 32 OC



(b) Pavement layer profiles directly from RADAN



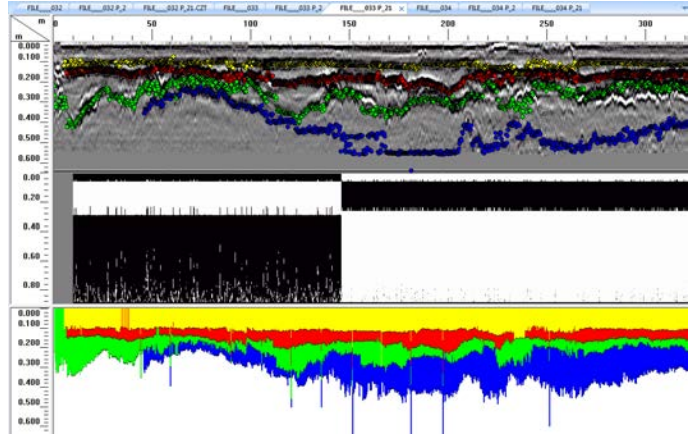
(c) Pavement layer profiles

Relative dielectric permittivity $k' = 4$. Observations: there are several layers and it appears that the third layer (green dots) corresponds to the bottom of the HMA layer. The intermediate layers correspond to HMA sublayers as shown in the core pictures (see above). The GPS file indicates that at the core location, the depth of the HMA layer is 0.22 m - 8.5 in. Please note that the core was collected just south of the end of the GPR survey.

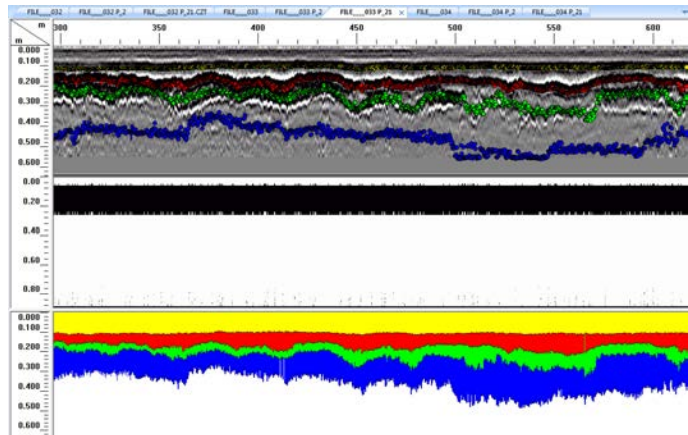
Figure C-2: Pavement layer profiles obtained from analysis of GPR data from STH 32 OC.



(a) Track of the GPR testing at STH 13 Spencer

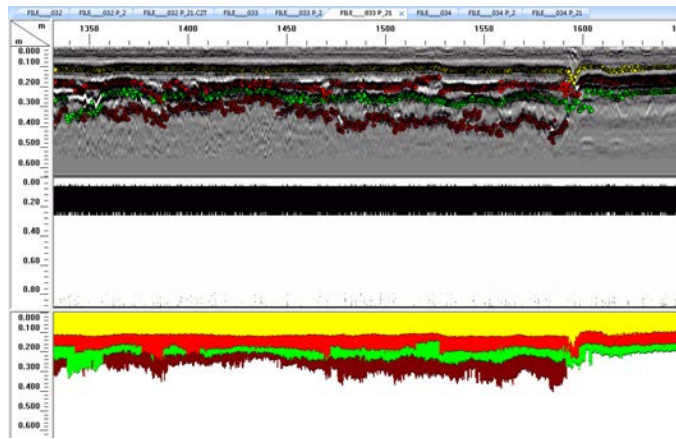


(b) Pavement layer profiles directly from RADAN

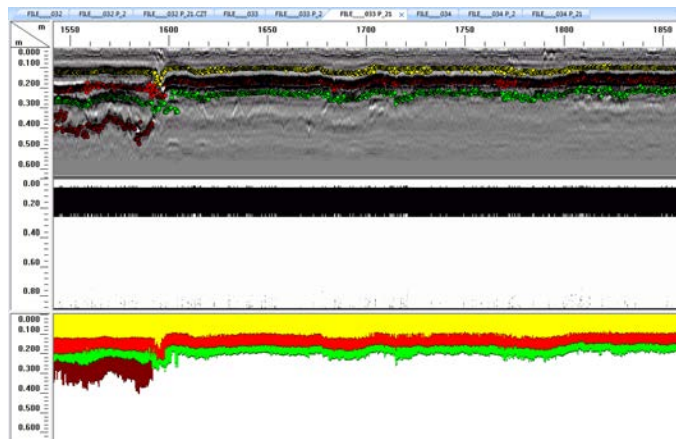


(c) Pavement layer profiles directly from RADAN

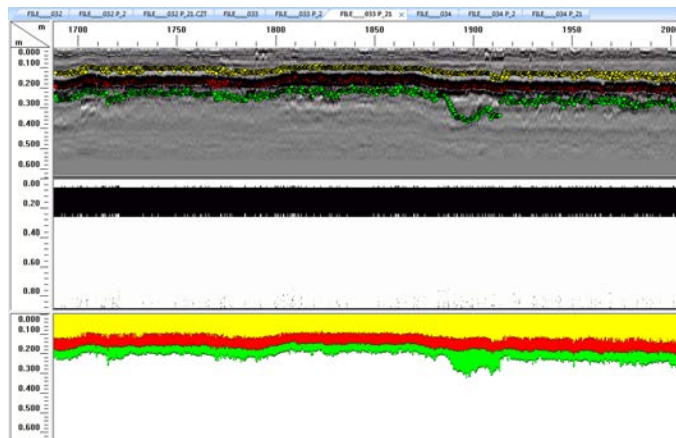
Figure C-3: Pavement layer profiles obtained from analysis of GPR data from STH 13 Spencer.



(d) Pavement layer profiles directly from RADAN

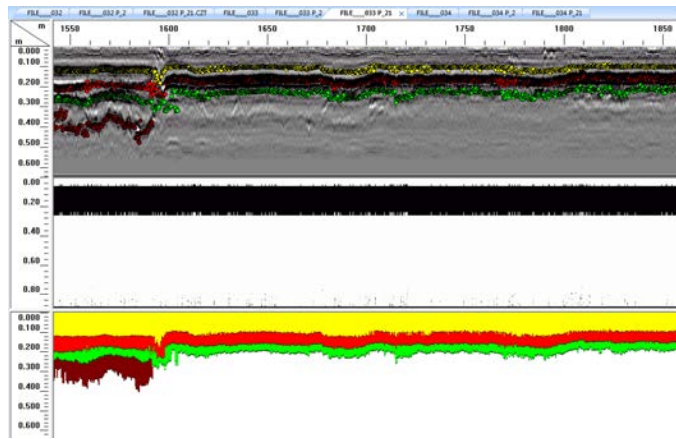


(e) Pavement layer profiles directly from RADAN

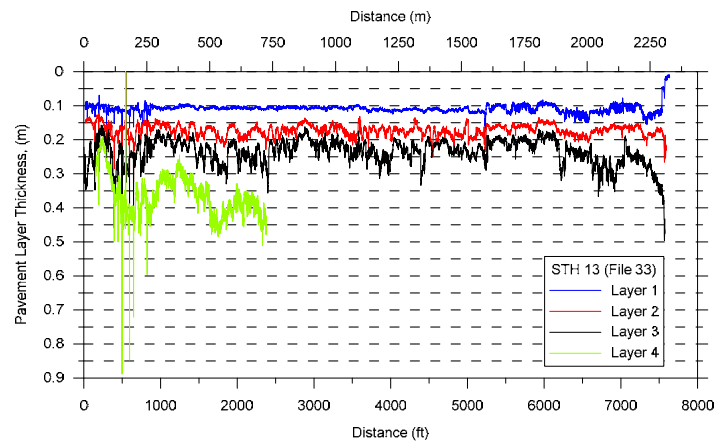


(f) Pavement layer profiles directly from RADAN

Figure C-3 (Cont.): Pavement layer profiles obtained from analysis of GPR data from STH 13 Spencer.



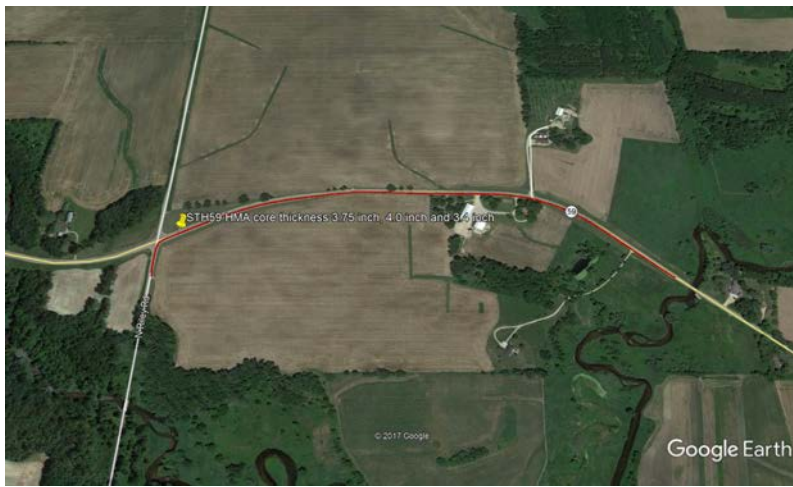
(g) Pavement layer profiles directly from RADAN



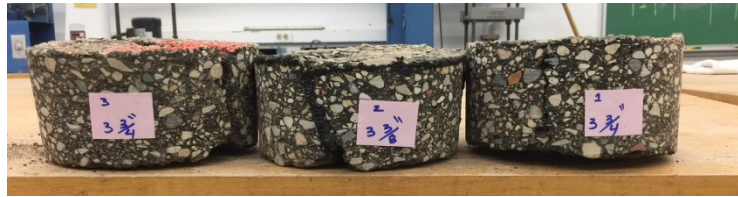
(h) Pavement layer profiles

–Relative dielectric permittivity $k' = 4$. Observations: There is no HMA core for this survey so no ground-truthing may be performed. Several clear reflection layers are observed. There is quite variation in the depth of the layers. As ground truth is not available, the variation cannot be assigned to changes in depth or to change in dielectric permittivity along the length of the road. The bottom of the first layer is assigned to the HMA layer at about 0.12 m depth but increases along the length of the survey. At position 1590 m, the mismatch property of the reflectors changes as the amplitude of the reflection suddenly changes.

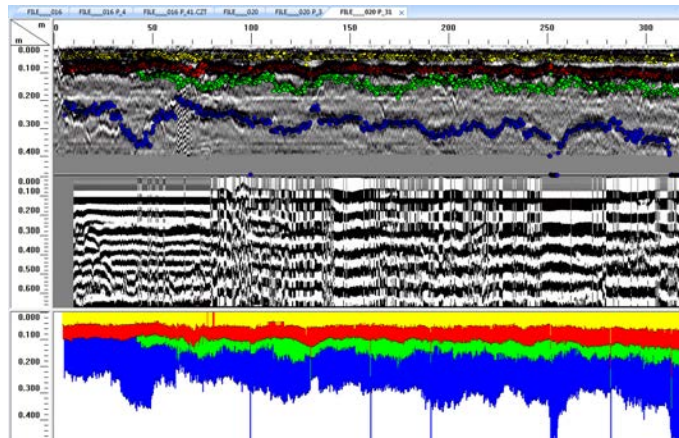
Figure C-3 (Cont.): Pavement layer profiles obtained from analysis of GPR data from STH 13 Spencer.



(a) Track of the GPR testing at STH 59, Edgerton

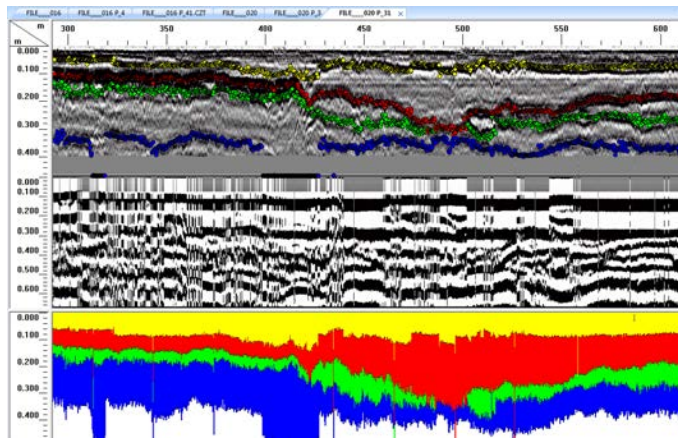


(b) Cores at STH 59

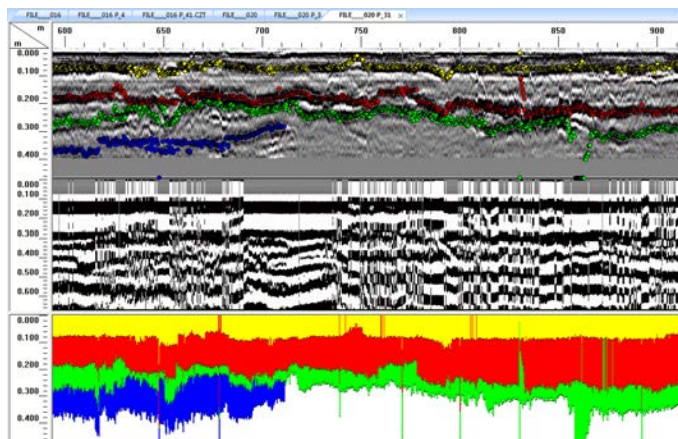


(c) Pavement layer profiles directly from RADAN

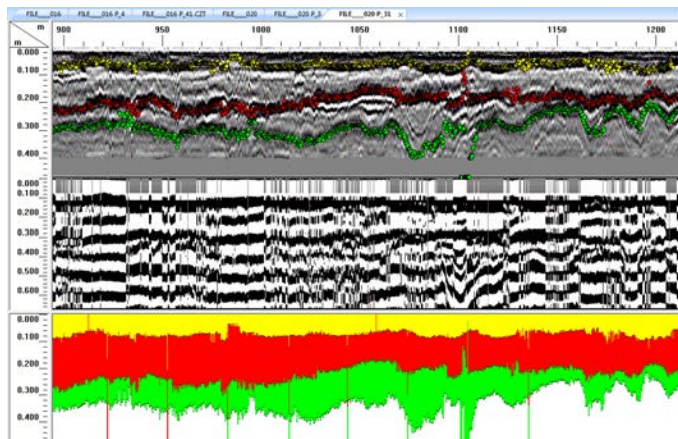
Figure C-4: Pavement layer profiles obtained from analysis of GPR data from STH 59, Edgerton.



(d) Pavement layer profiles directly from RADAN

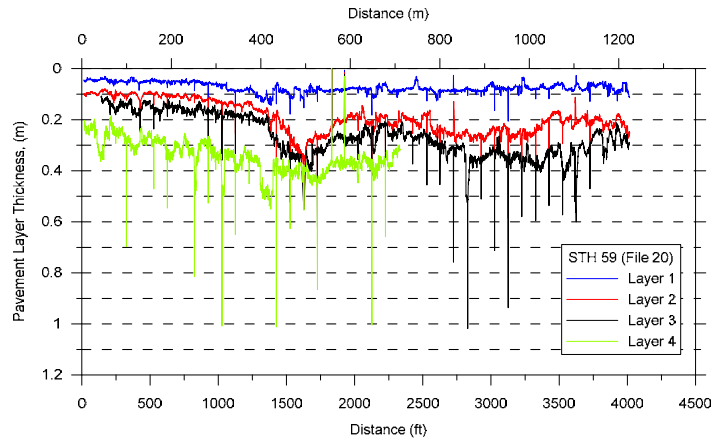


(e) Pavement layer profiles directly from RADAN



(f) Pavement layer profiles directly from RADAN

Figure C-4 (Cont.): Pavement layer profiles obtained from analysis of GPR data from STH 59, Edgerton.



(g) Pavement layer profiles

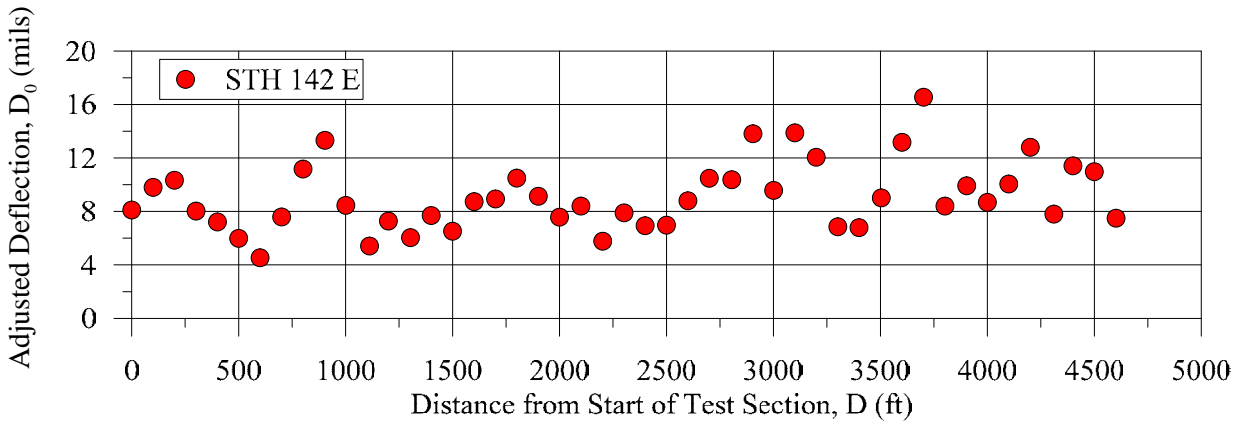
Relative dielectric permittivity $k' = 4$. Observations: There is an HMA core for this survey so ground-truthing may be performed. The bottom the second layer (red points in the figure) is the bottom of the HMA layer. Base layers may also be observed throughout the survey with deep as 0.4 m

Figure C-4 (Cont.): Pavement layer profiles obtained from analysis of GPR data from STH 59, Edgerton.

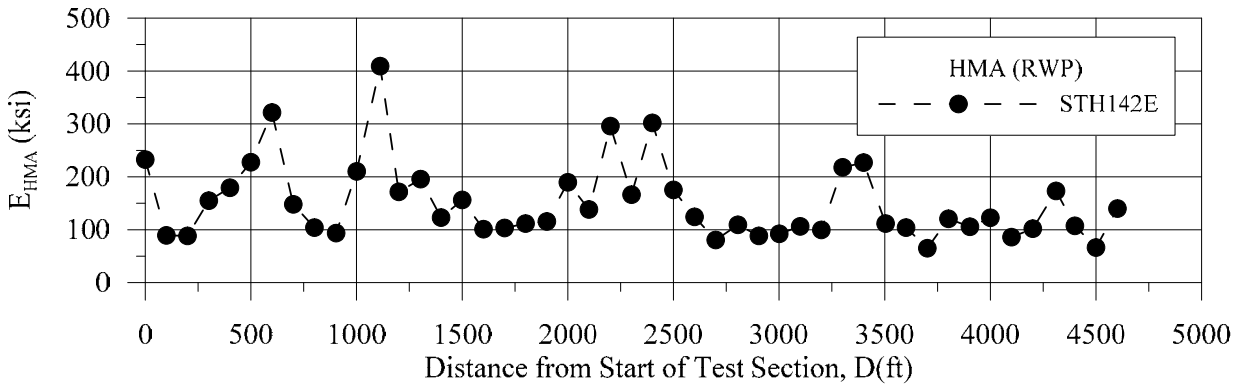
Appendix D

Falling Weight Deflectometer Test Results

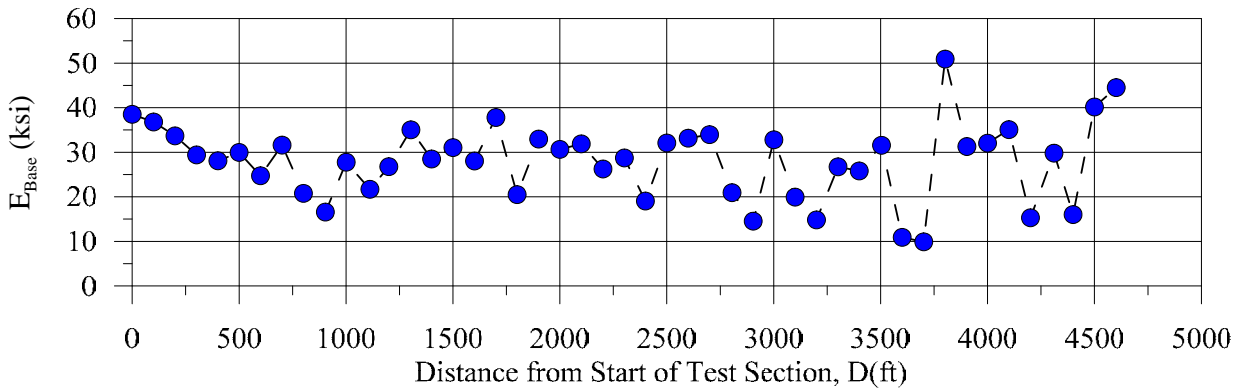
Plots of Deflection Under the Loading Plate (D_0) and the Corresponding Backcalculated Layer Moduli with Distance for Various Pavement Test Sections



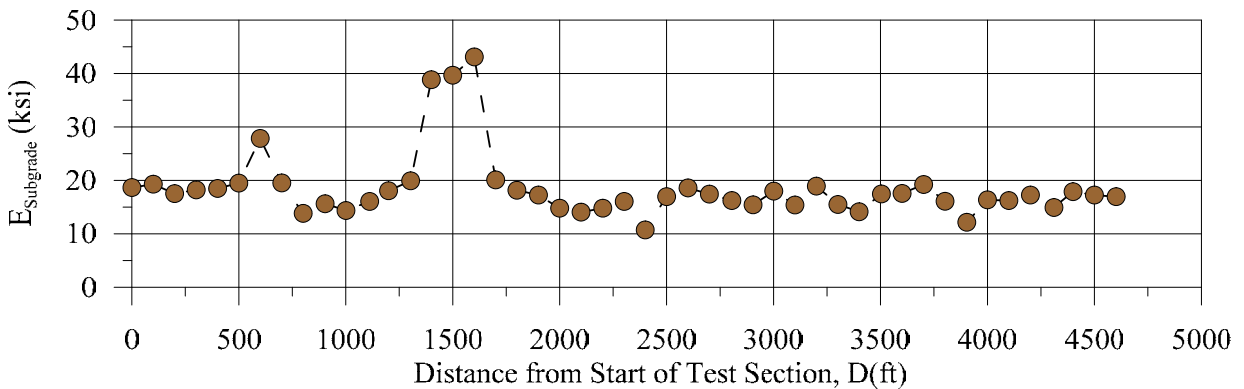
(a) Adjusted deflection under the loading plate (D_0) (corrected for a 9,000 lb drop and temperature)



(b) Backcalculated HMA layer modulus

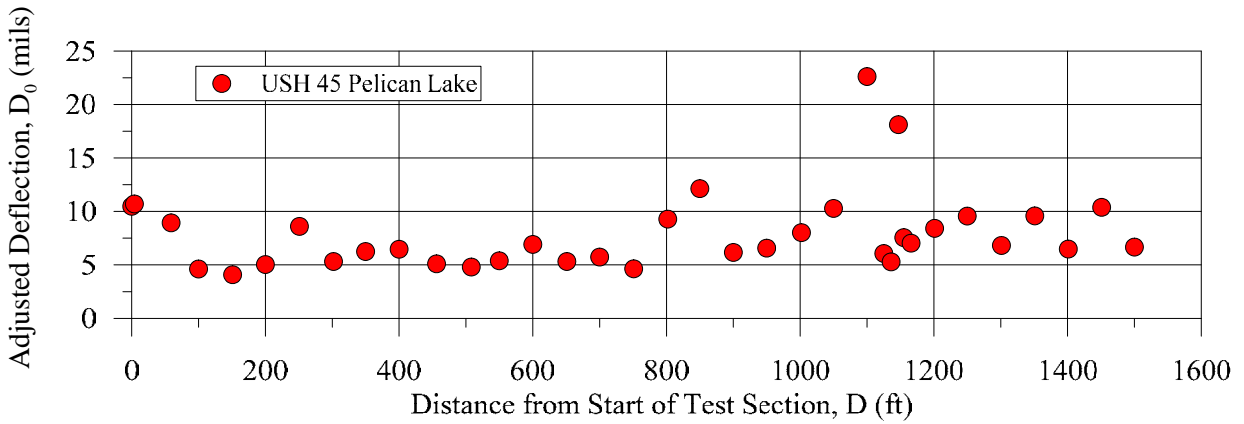


(c) Backcalculated base layer modulus

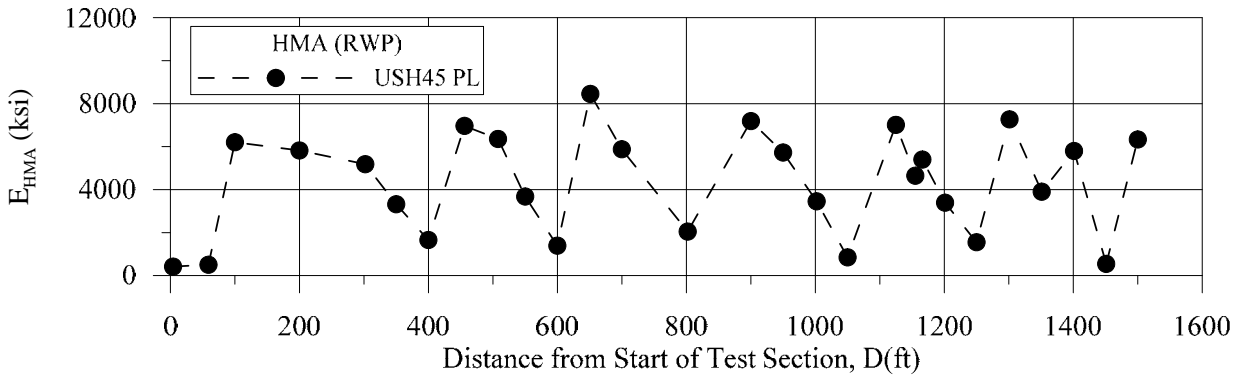


(d) Backcalculated subgrade modulus

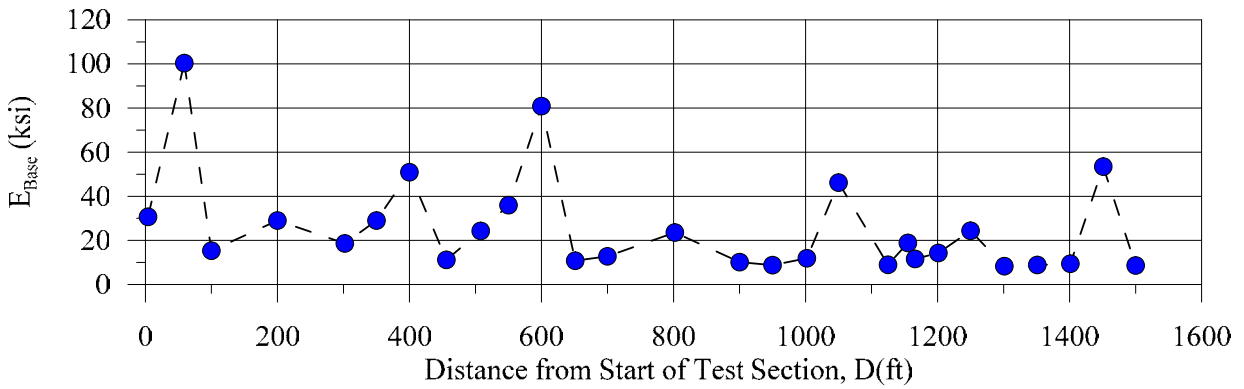
Figure D-1: Results of FWD tests on STH 142E pavement.



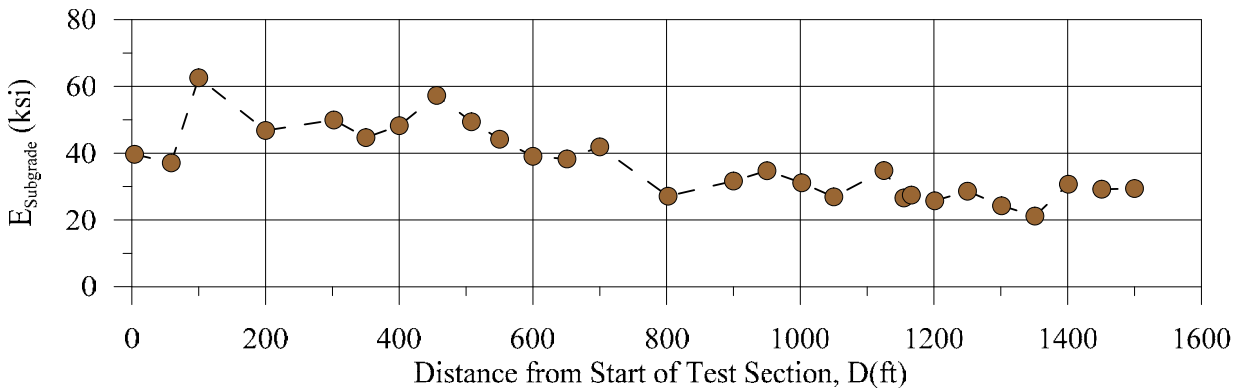
(a) Adjusted deflection under the loading plate (D_0) (corrected for a 9,000 lb drop and temperature)



(b) Backcalculated HMA layer modulus

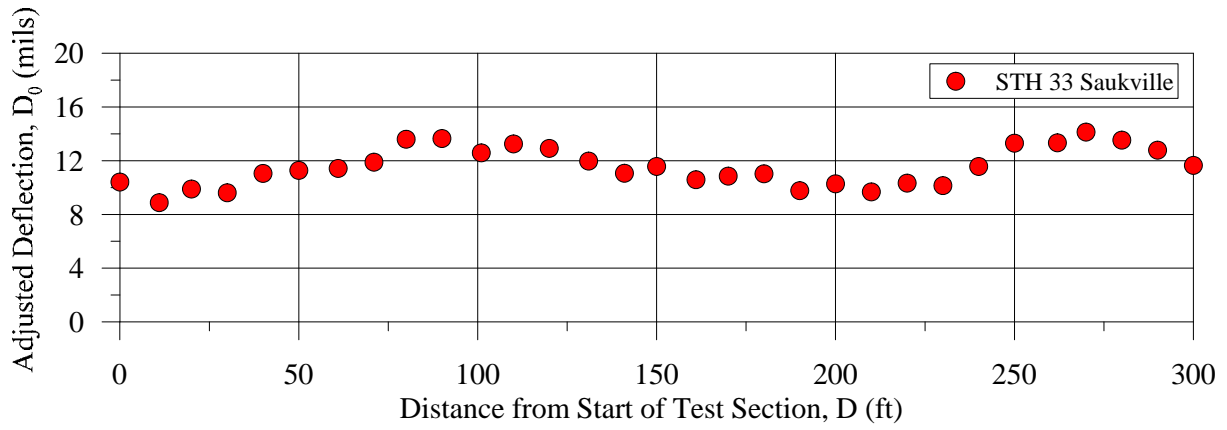


(c) Backcalculated base layer modulus

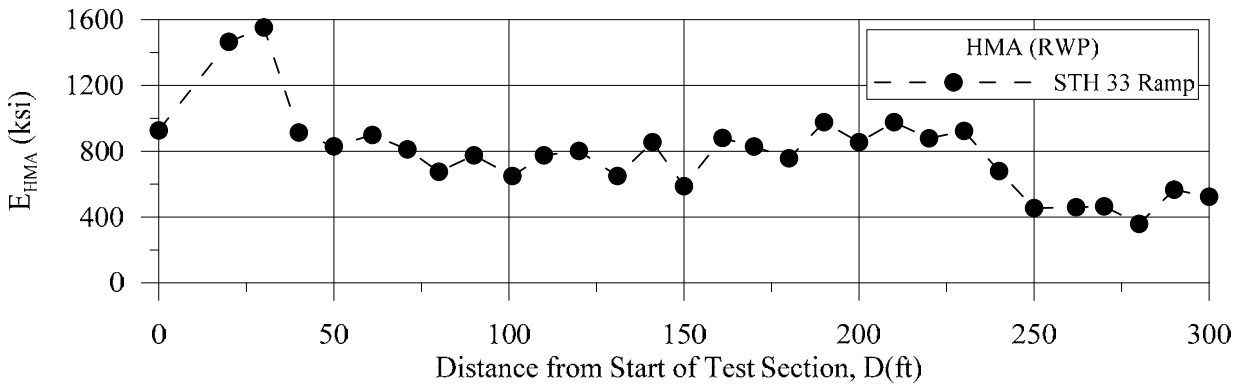


(d) Backcalculated subgrade modulus

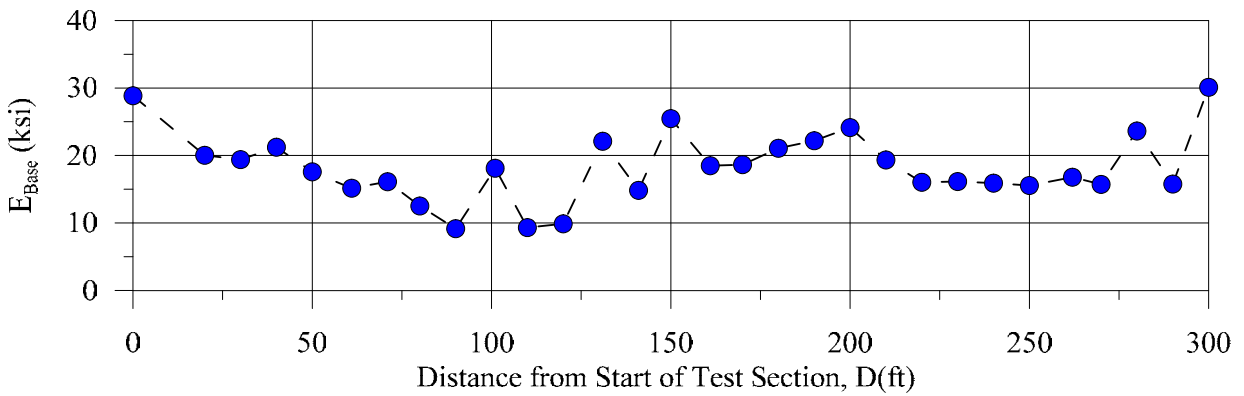
Figure D-2: Results of FWD tests on USH 45 pavement.



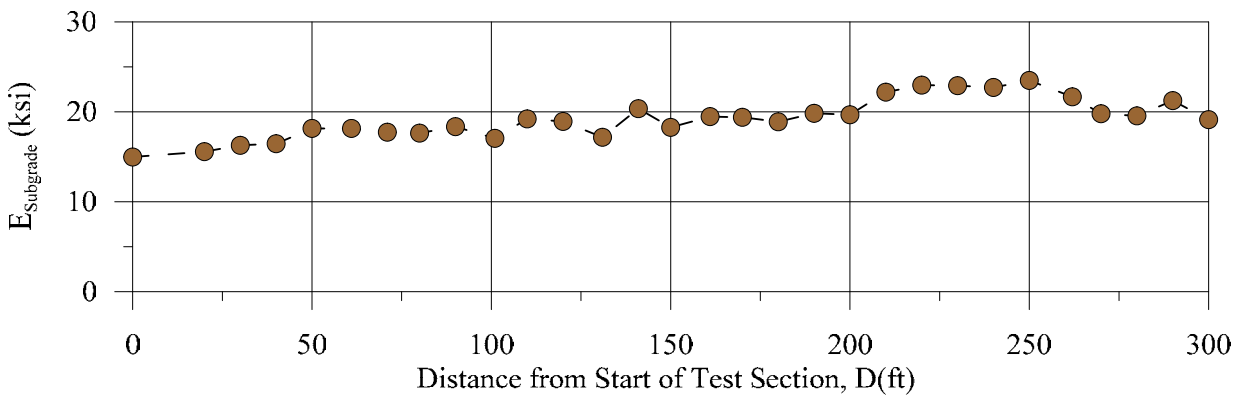
(a) Adjusted deflection under the loading plate (D_0) (corrected for a 9,000 lb drop and temperature)



(b) Backcalculated HMA layer modulus

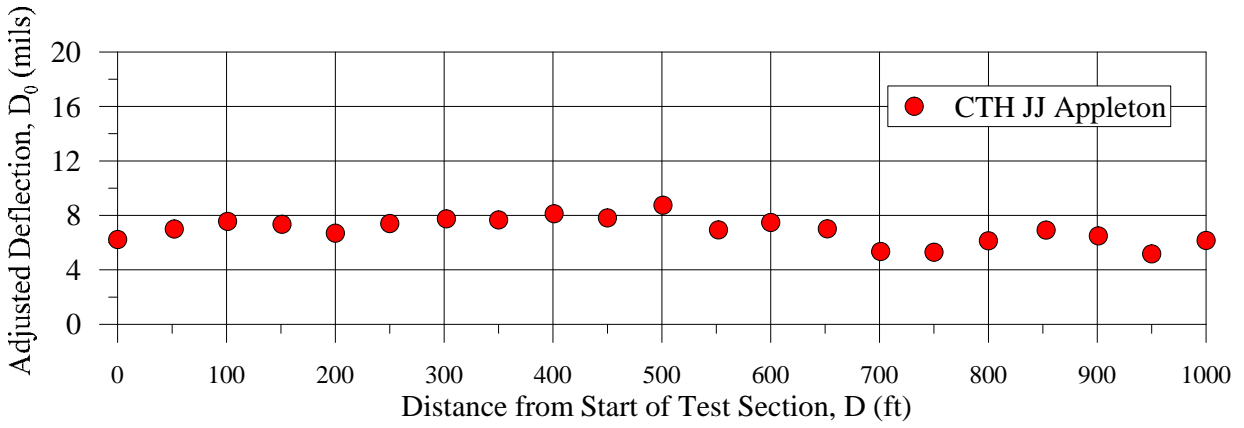


(c) Backcalculated base layer modulus

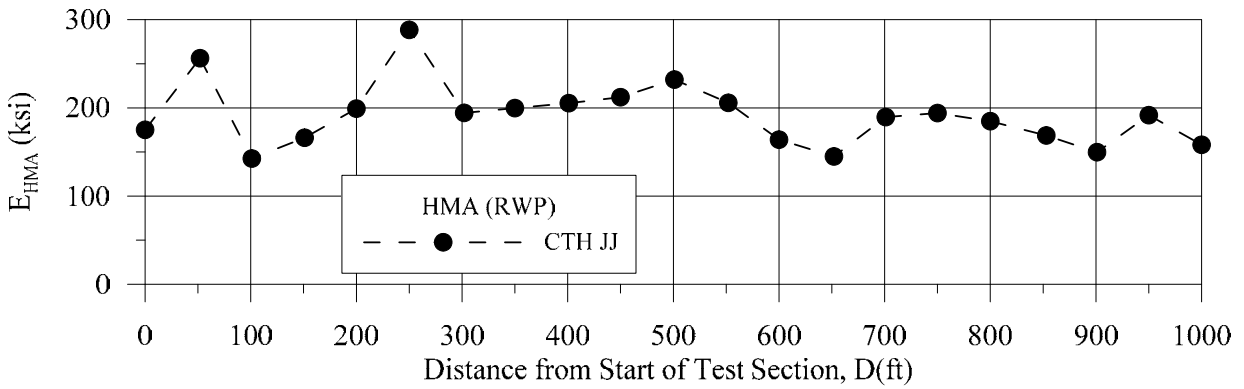


(d) Backcalculated subgrade modulus – (see gray aggregate in discussion)

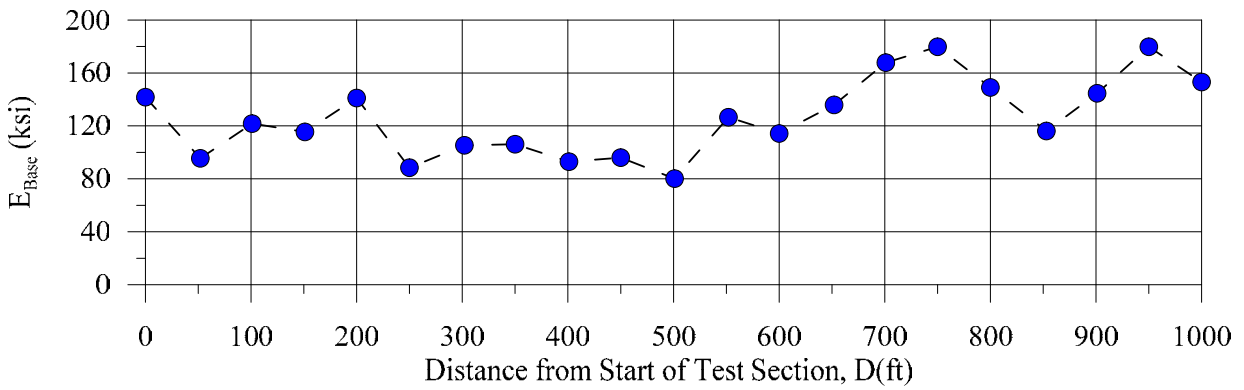
Figure D-3: Results of FWD tests on STH 33 Saukville (ramp) pavement.



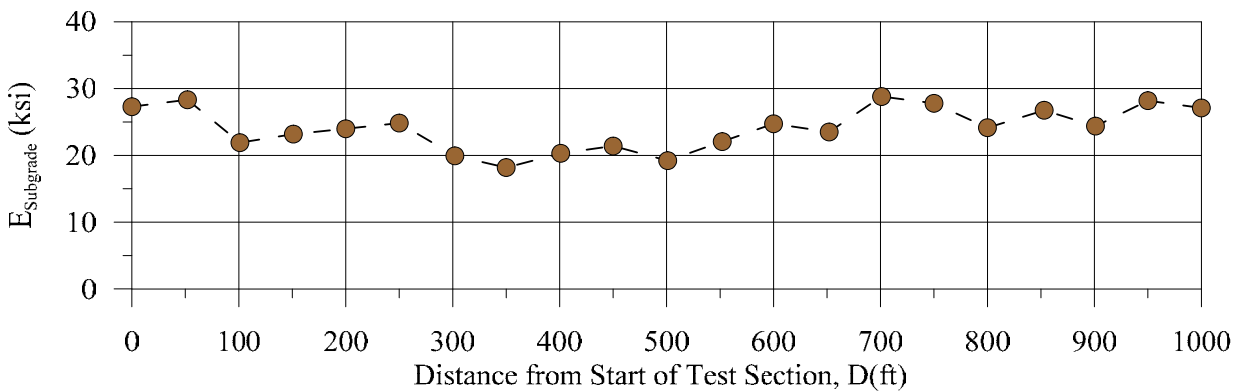
(a) Adjusted deflection under the loading plate (D_0) (corrected for a 9,000 lb drop and temperature)



(b) Backcalculated HMA layer modulus

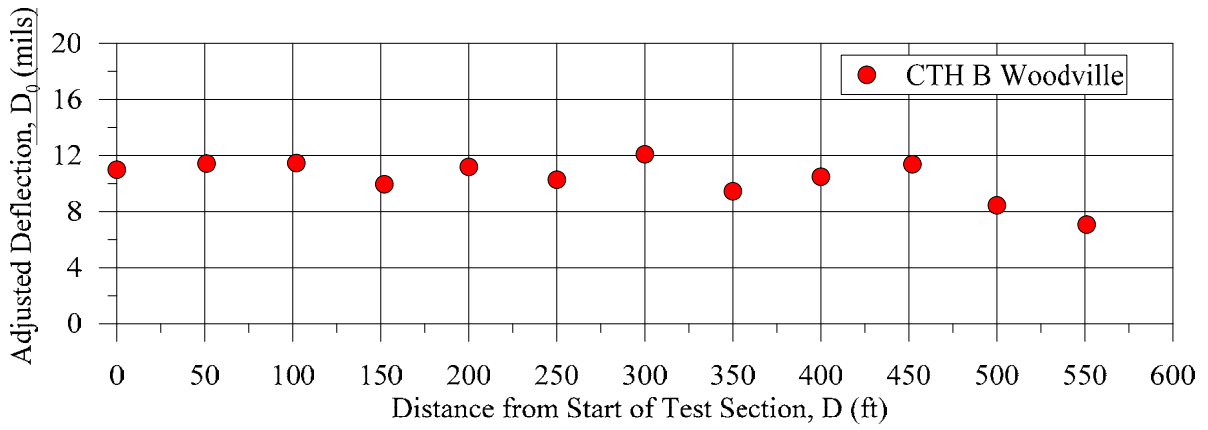


(c) Backcalculated base layer modulus

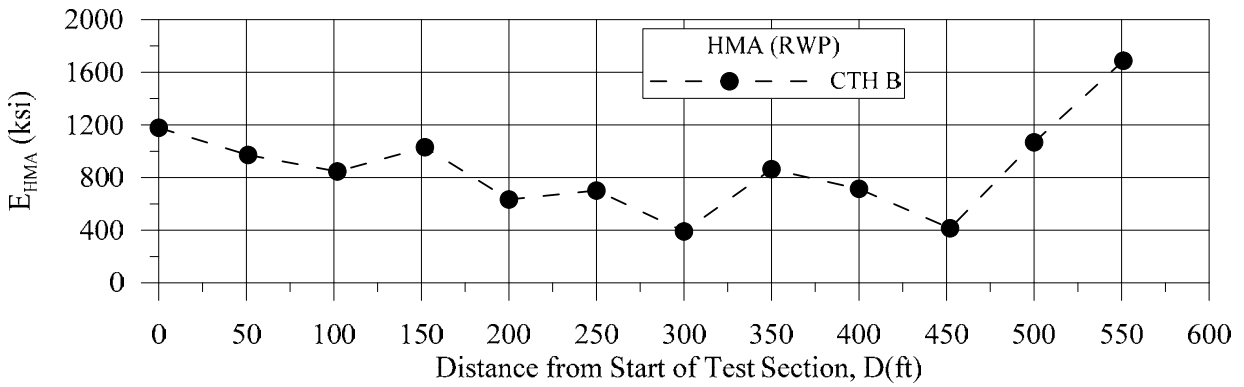


(d) Backcalculated subgrade modulus

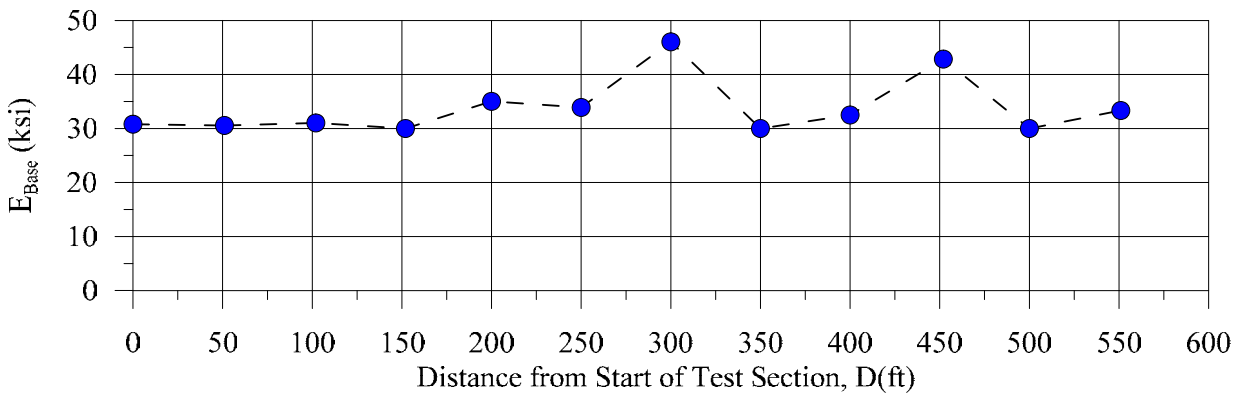
Figure D-4: Results of FWD tests on CTH JJ pavement.



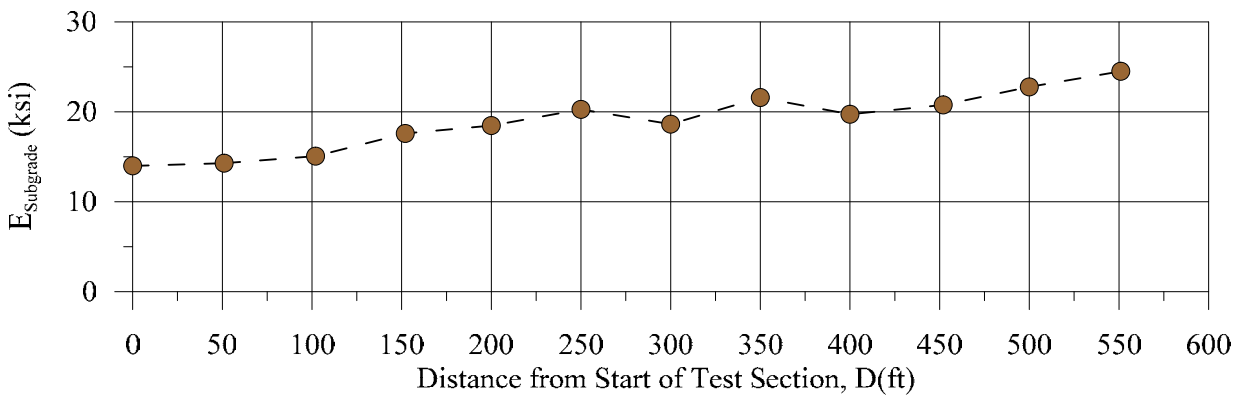
(a) Adjusted deflection under the loading plate (D_0) (corrected for a 9,000 lb drop and temperature)



(b) Backcalculated HMA layer modulus

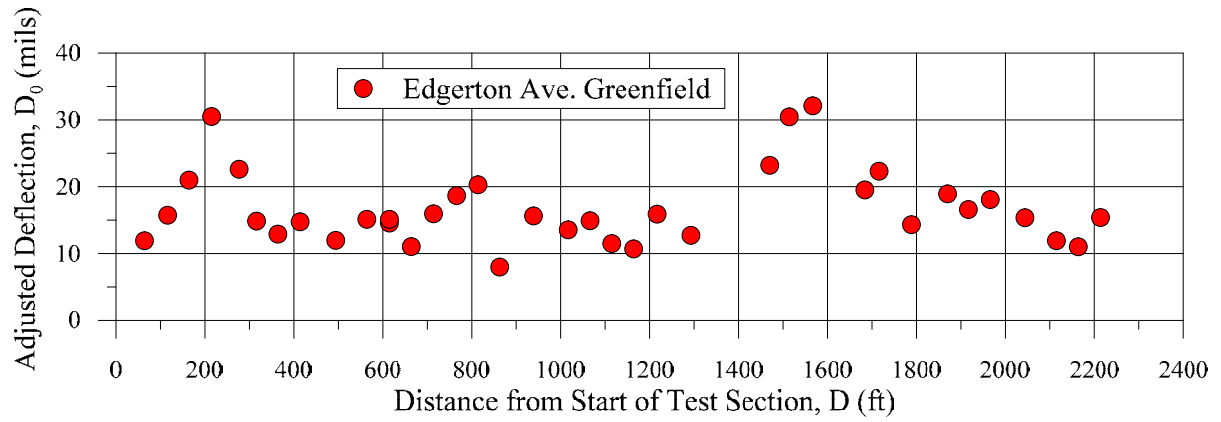


(c) Backcalculated base layer modulus

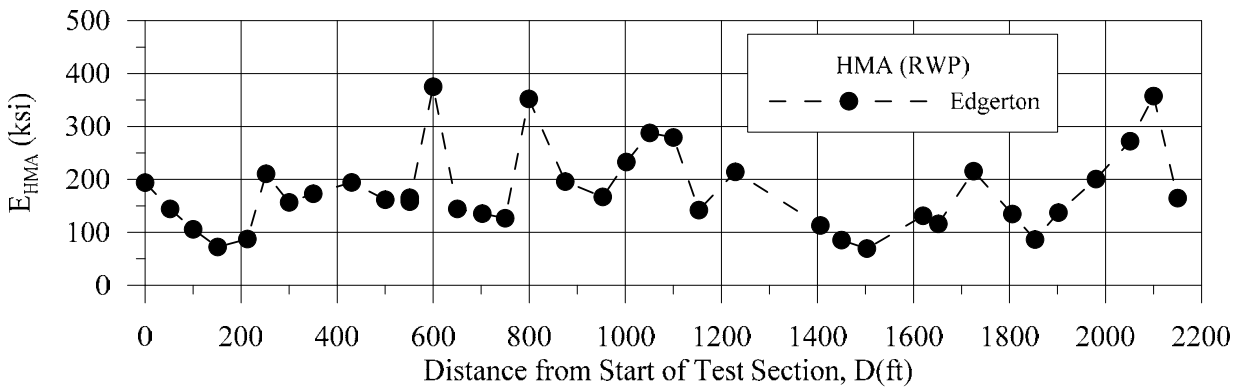


(d) Backcalculated subgrade modulus

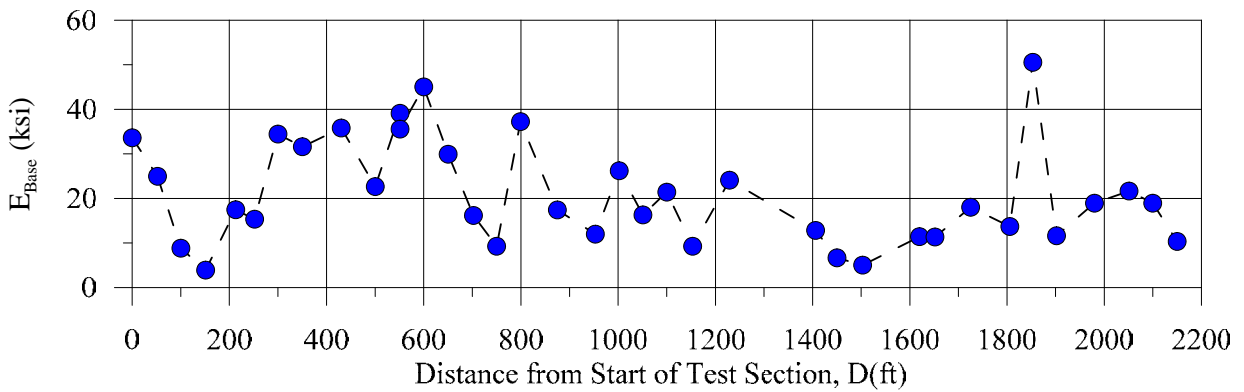
Figure D-5: Results of FWD tests on CTH B pavement.



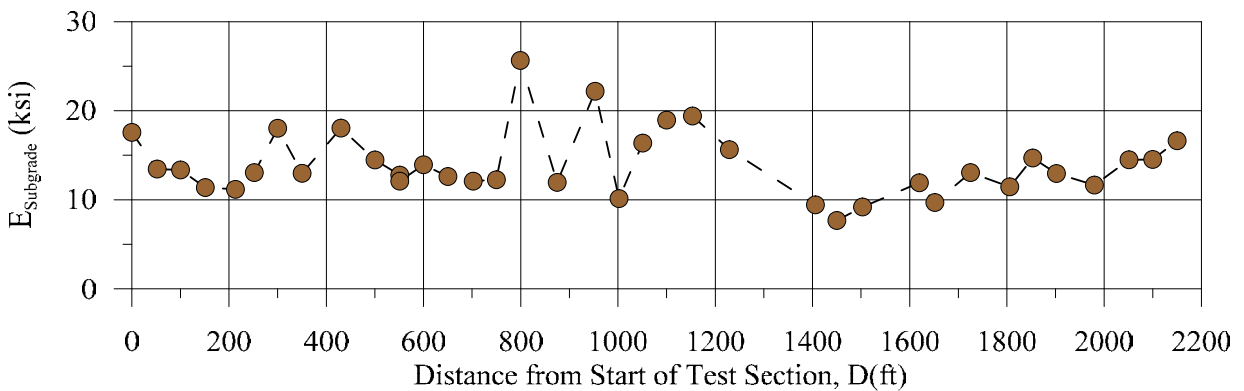
(a) Adjusted deflection under the loading plate (D_0) (corrected for a 9,000 lb drop and temperature)



(b) Backcalculated HMA layer modulus

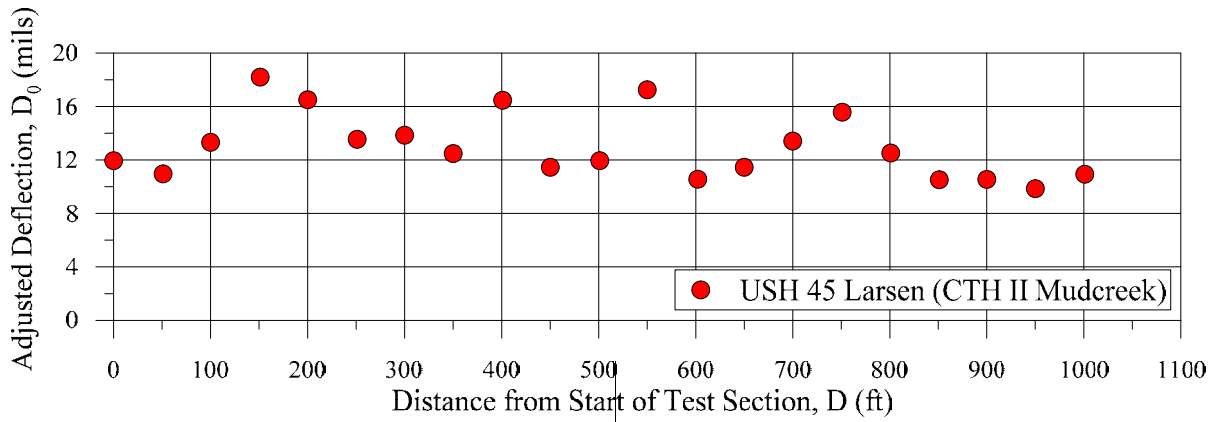


(c) Backcalculated base layer modulus

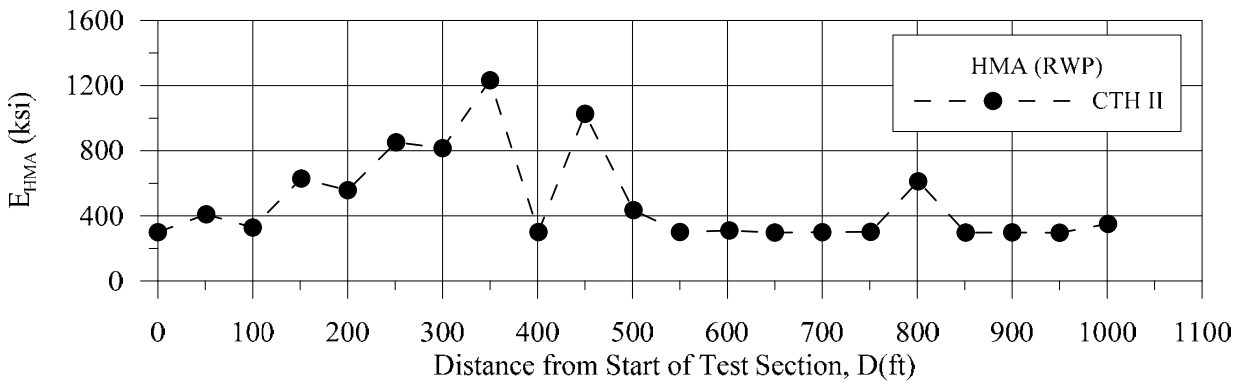


(d) Backcalculated subgrade modulus

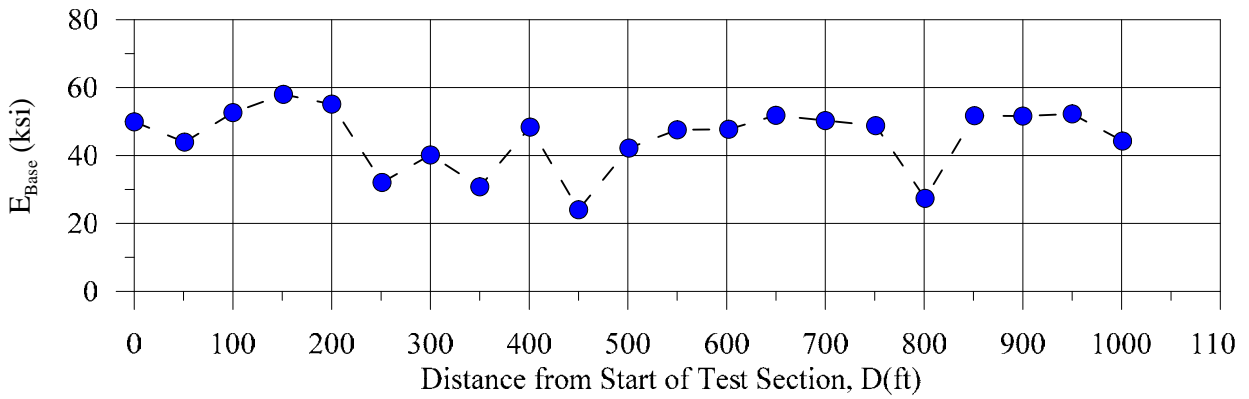
Figure D-6: Results of FWD tests on Edgerton Ave pavement.



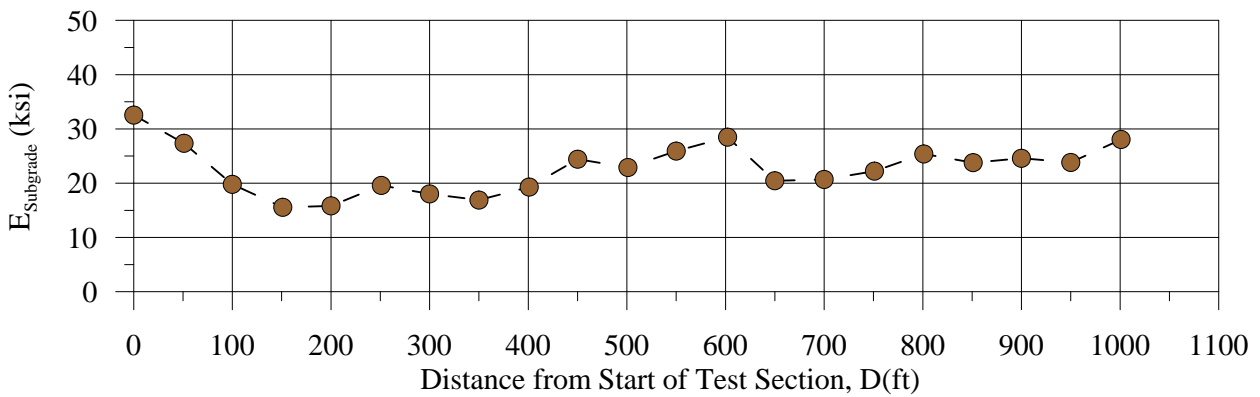
(a) Adjusted deflection under the loading plate (D_0) (corrected for a 9,000 lb drop and temperature)



(b) Backcalculated HMA layer modulus

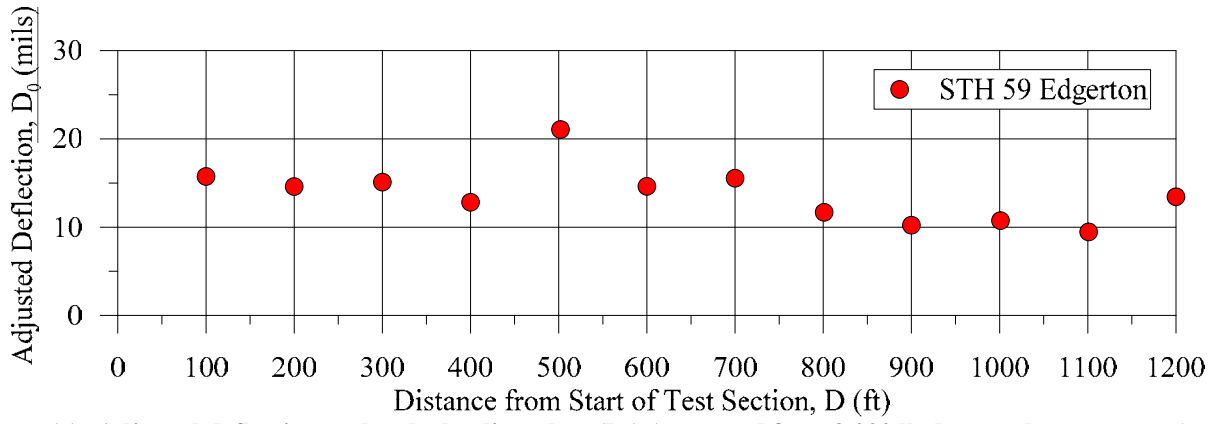


(c) Backcalculated base layer modulus

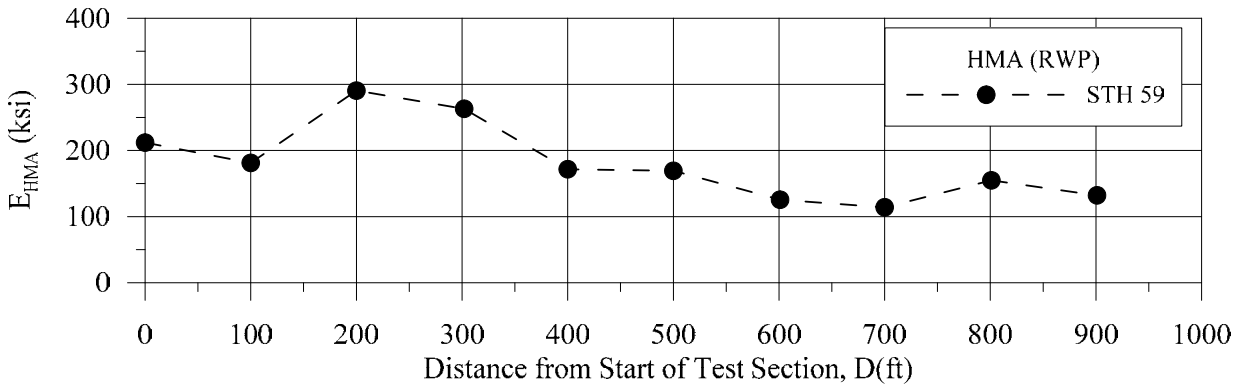


(d) Backcalculated subgrade modulus

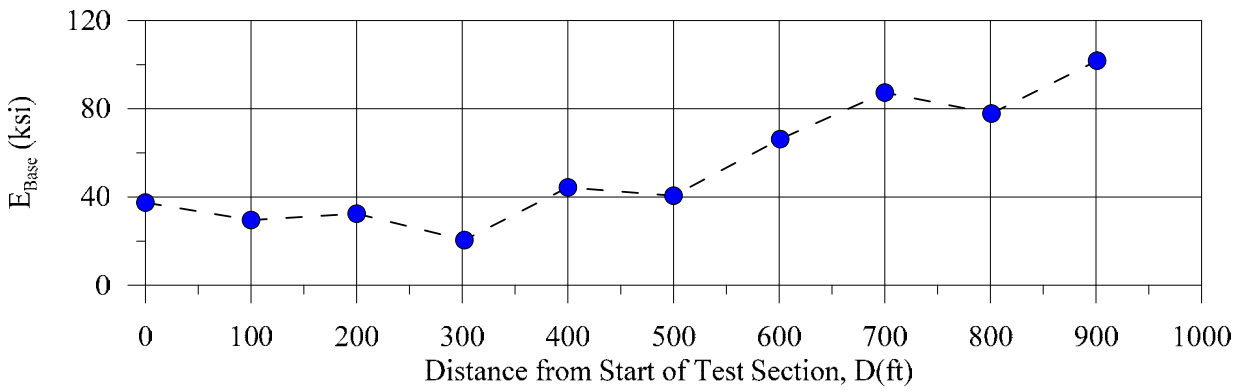
Figure D-7: Results of FWD tests on USH45 Larsen (CTH II Mudcreek) pavement.



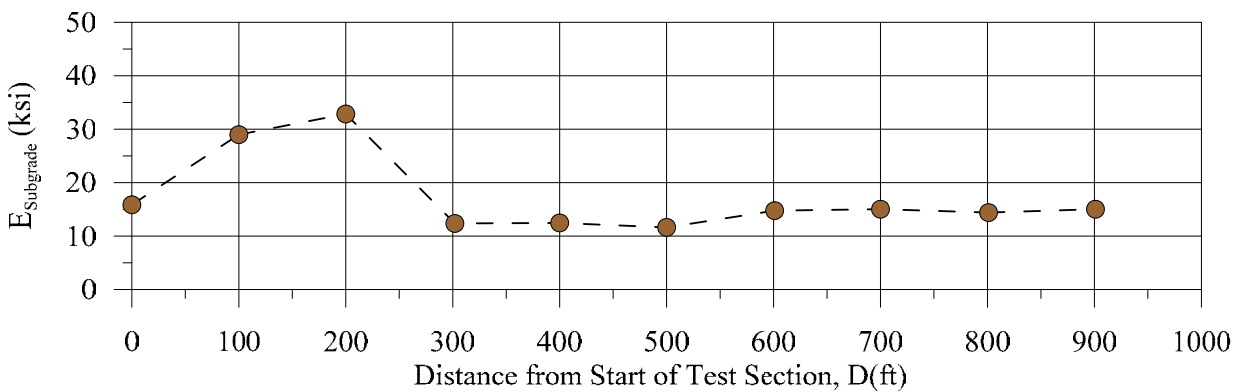
(a) Adjusted deflection under the loading plate (D_0) (corrected for a 9,000 lb drop and temperature)



(b) Backcalculated HMA layer modulus

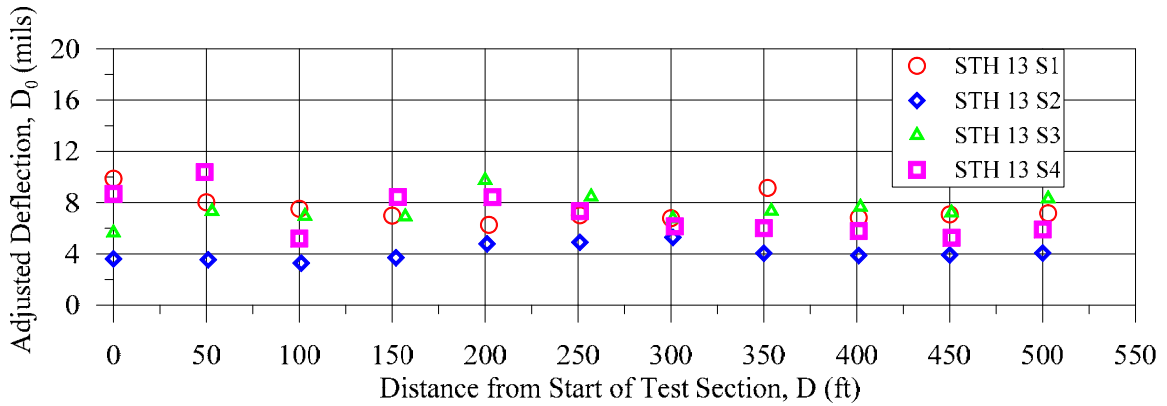


(c) Backcalculated base layer modulus

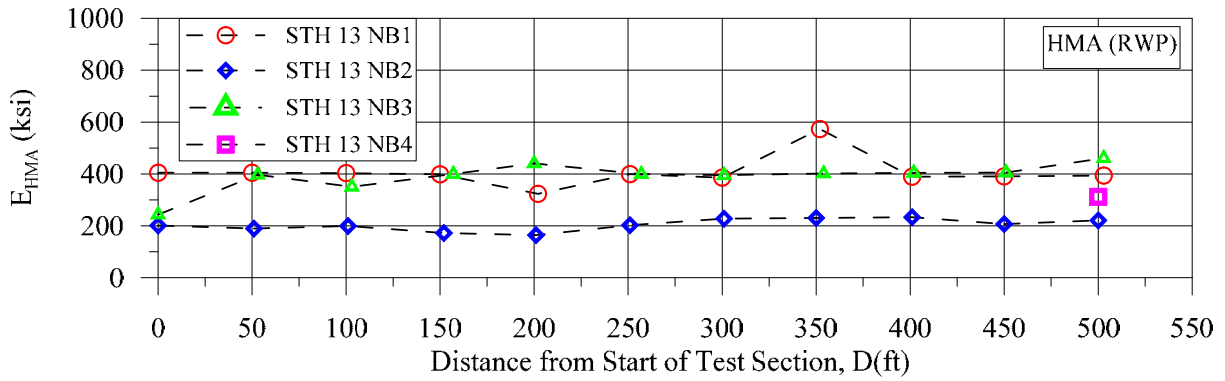


(d) Backcalculated subgrade modulus

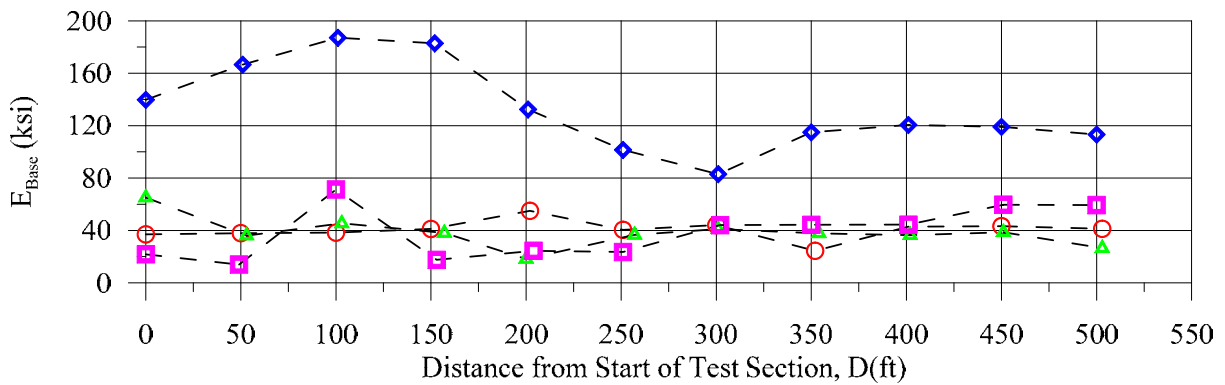
Figure D-8: Results of FWD tests on STH 59 pavement.



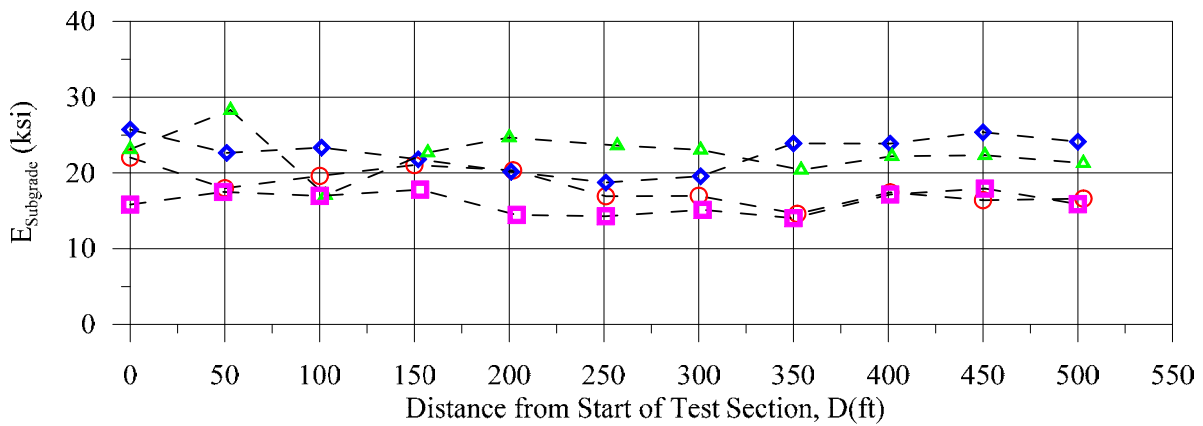
(a) Adjusted deflection under the loading plate (D_0) (corrected for a 9,000 lb drop and temperature)



(b) Backcalculated HMA layer modulus

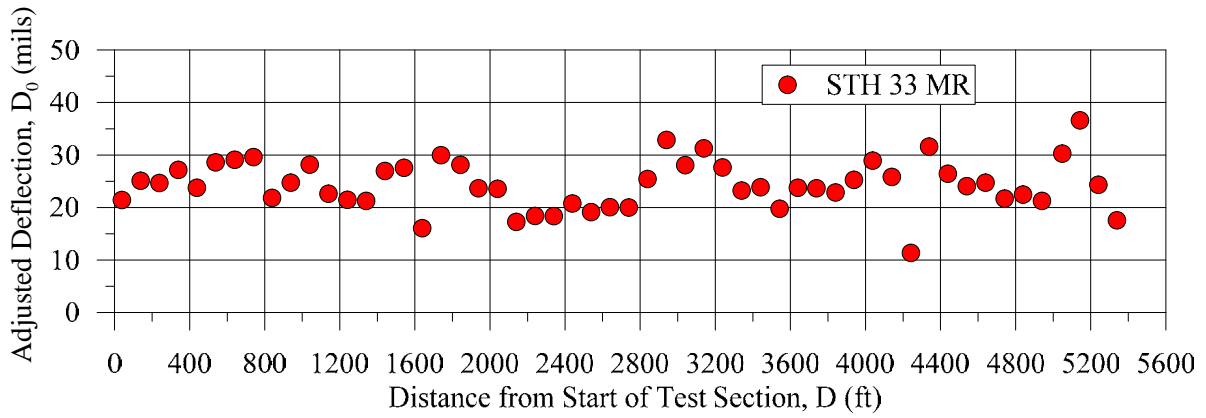


(c) Backcalculated base layer modulus

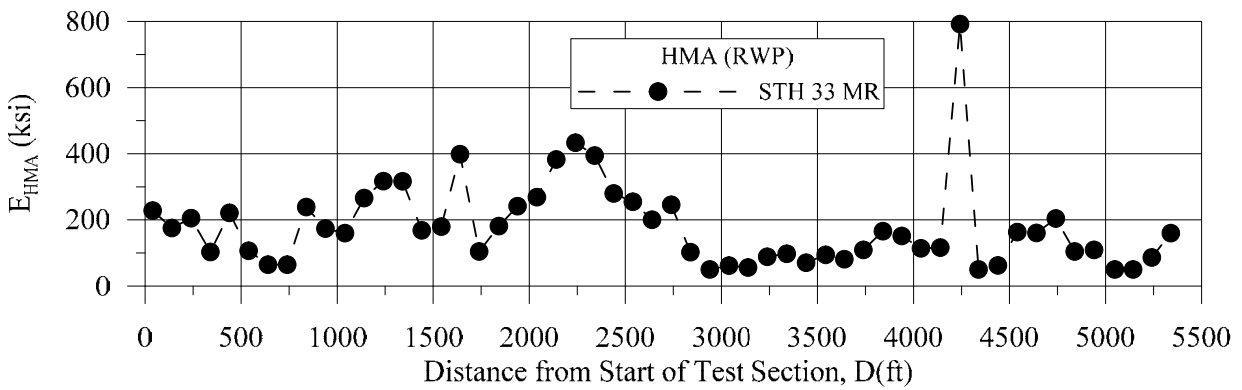


(d) Backcalculated subgrade modulus

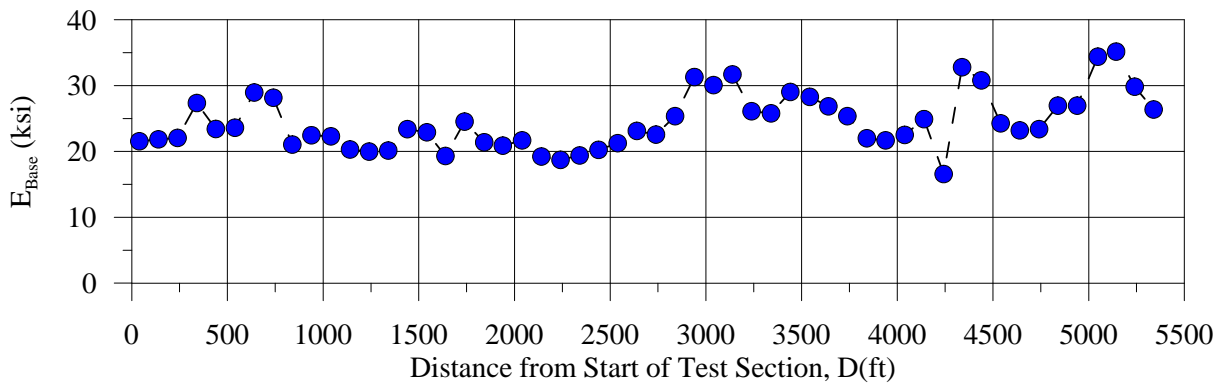
Figure D-9: Results of FWD tests on STH 13 pavement.



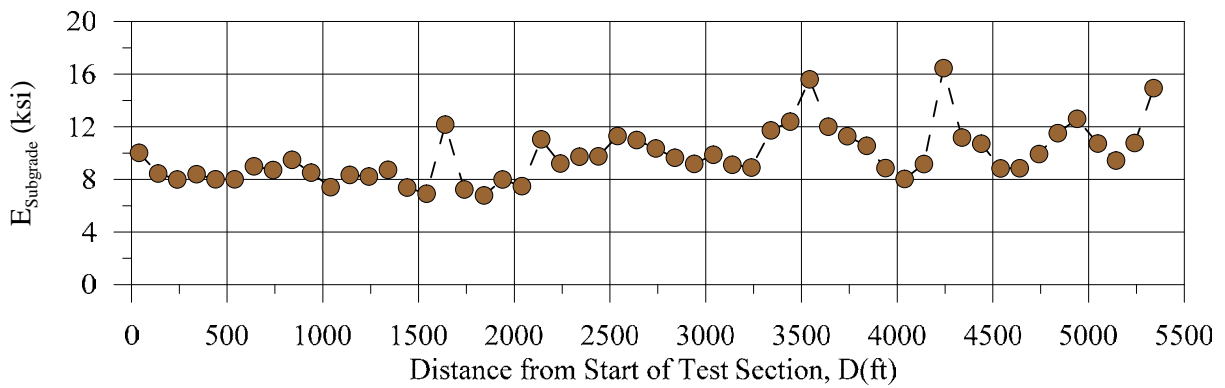
(a) Adjusted deflection under the loading plate (D_0) (corrected for a 9,000 lb drop and temperature)



(b) Backcalculated HMA layer modulus

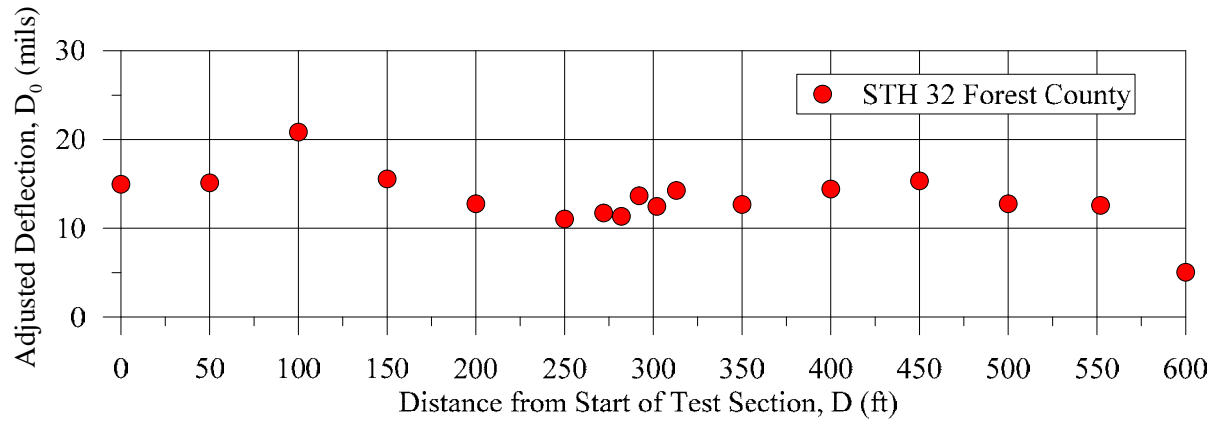


(c) Backcalculated base layer modulus

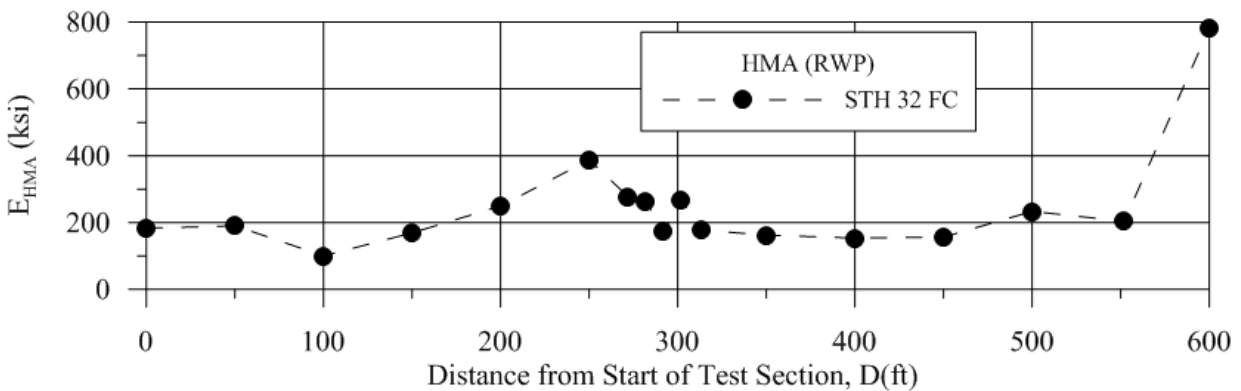


(d) Backcalculated subgrade modulus

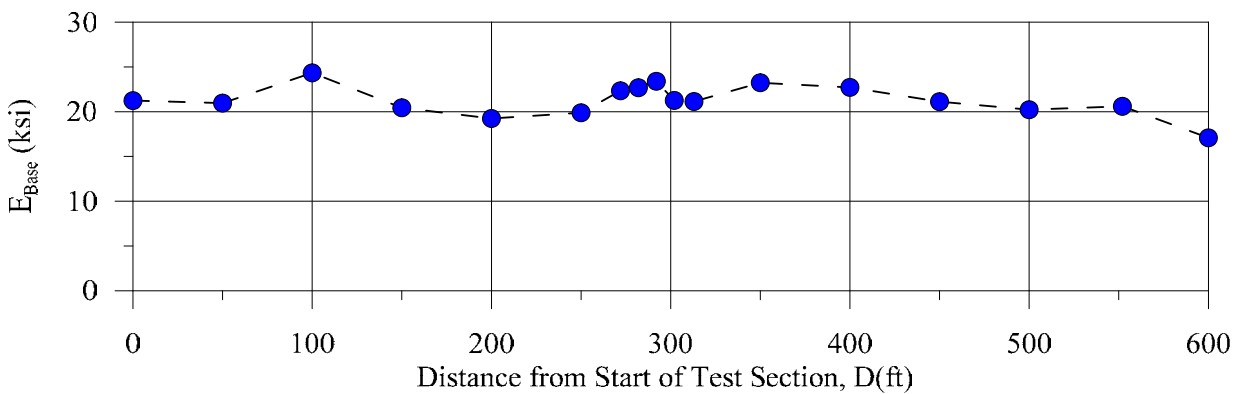
Figure D-10: Results of FWD tests on STH 33 MR pavement.



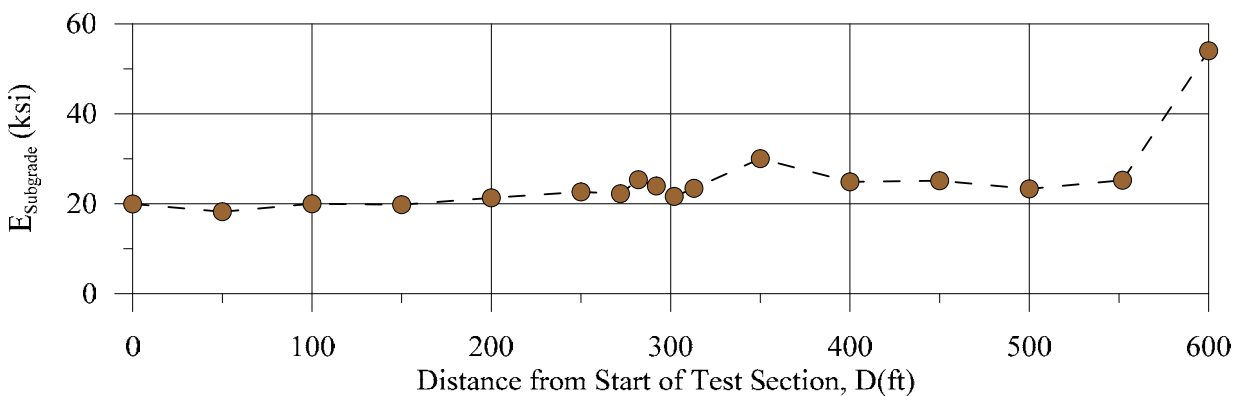
(a) Adjusted deflection under the loading plate (D_0) (corrected for a 9,000 lb drop and temperature)



(b) Backcalculated HMA layer modulus

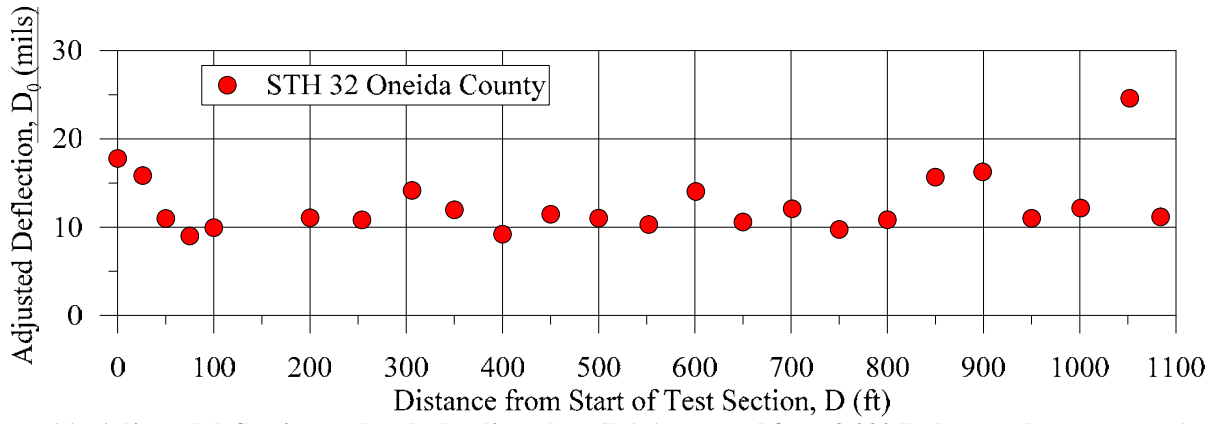


(c) Backcalculated base layer modulus

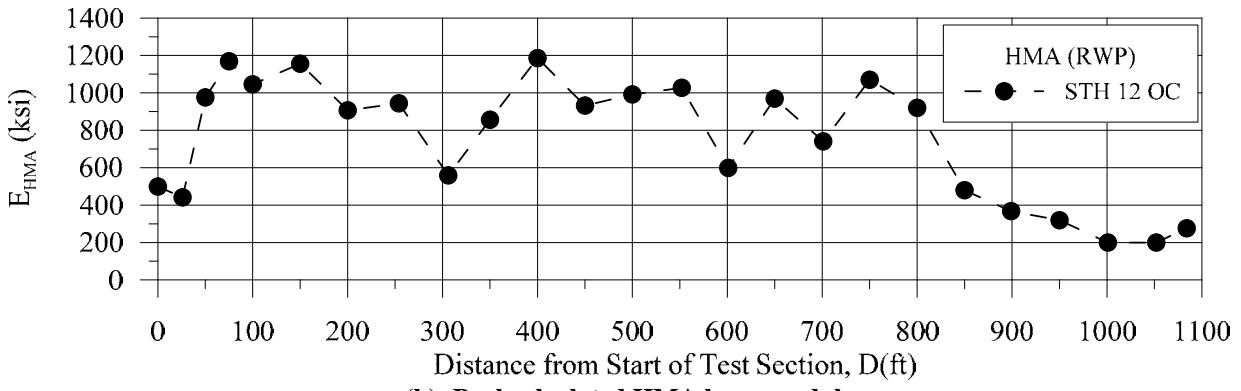


(d) Backcalculated subgrade modulus

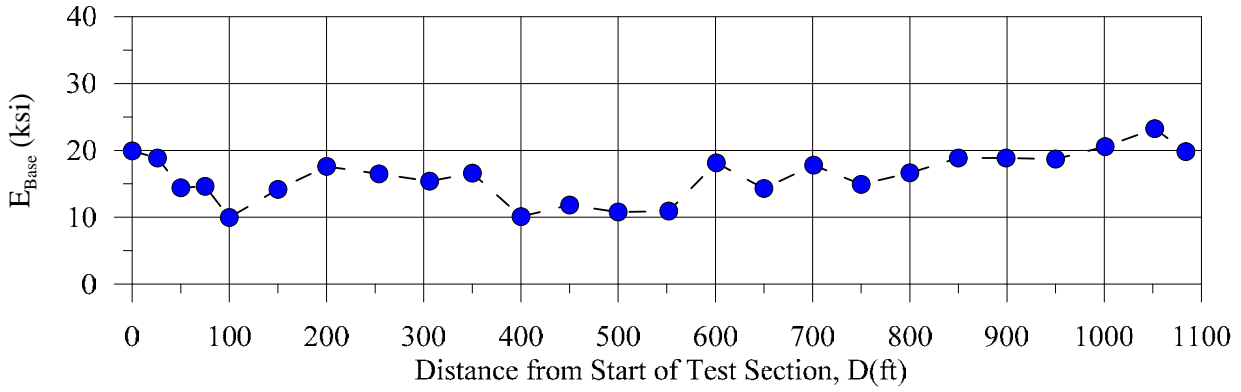
Figure D-11: Results of FWD tests on STH 32 FC pavement.



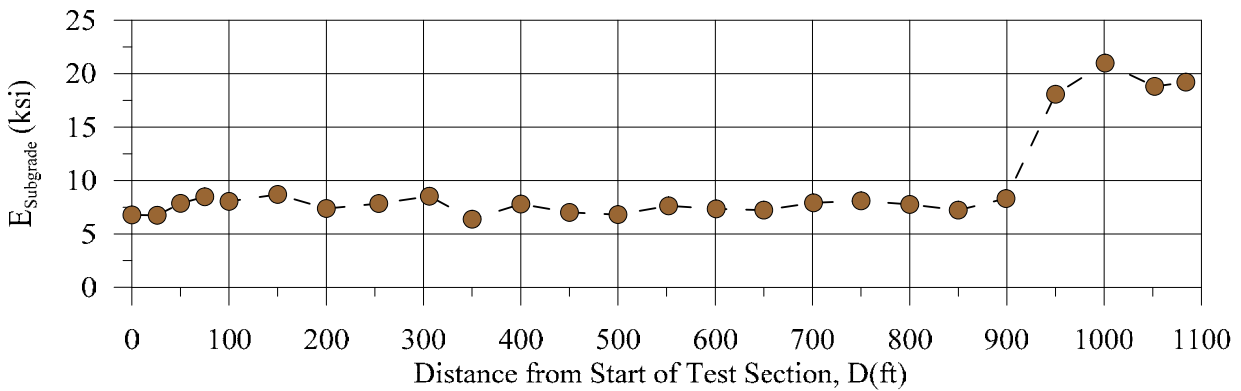
(a) Adjusted deflection under the loading plate (D_0) (corrected for a 9,000 lb drop and temperature)



(b) Backcalculated HMA layer modulus

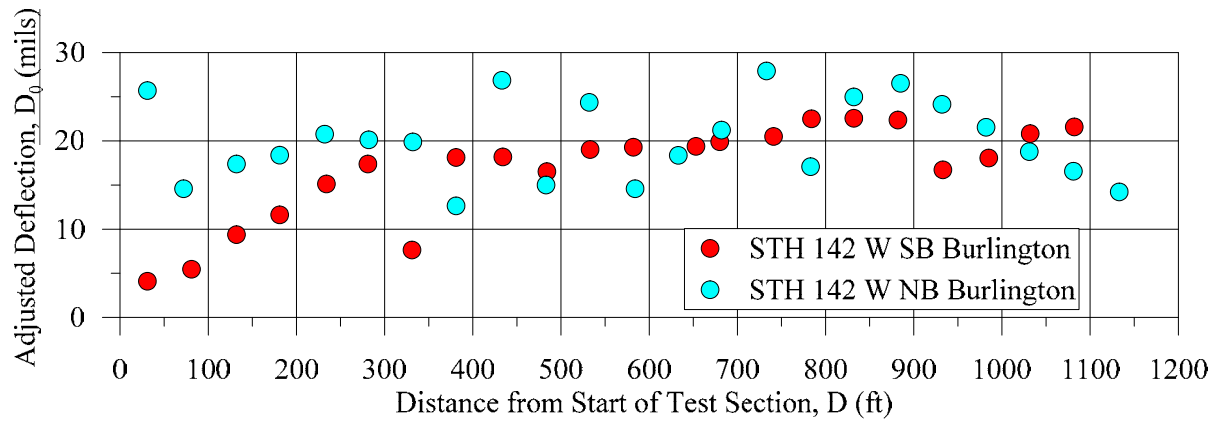


(c) Backcalculated base layer modulus

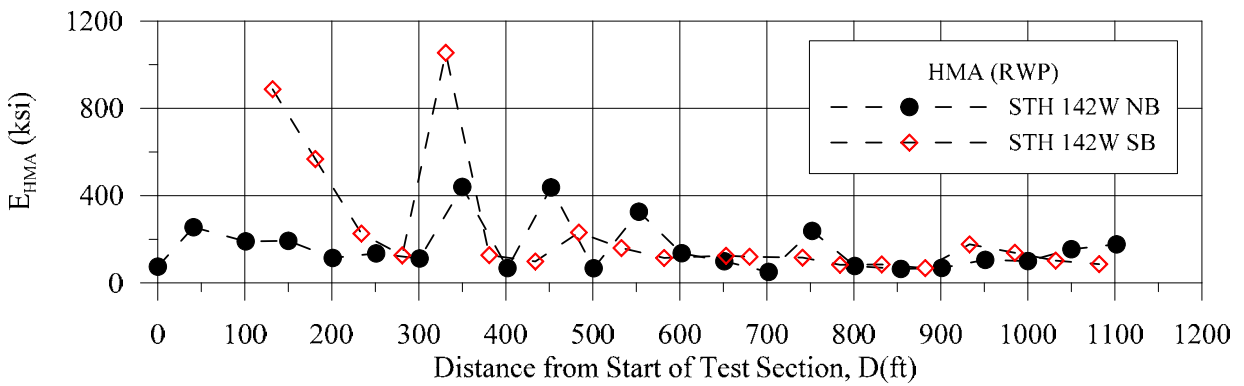


(d) Backcalculated subgrade modulus

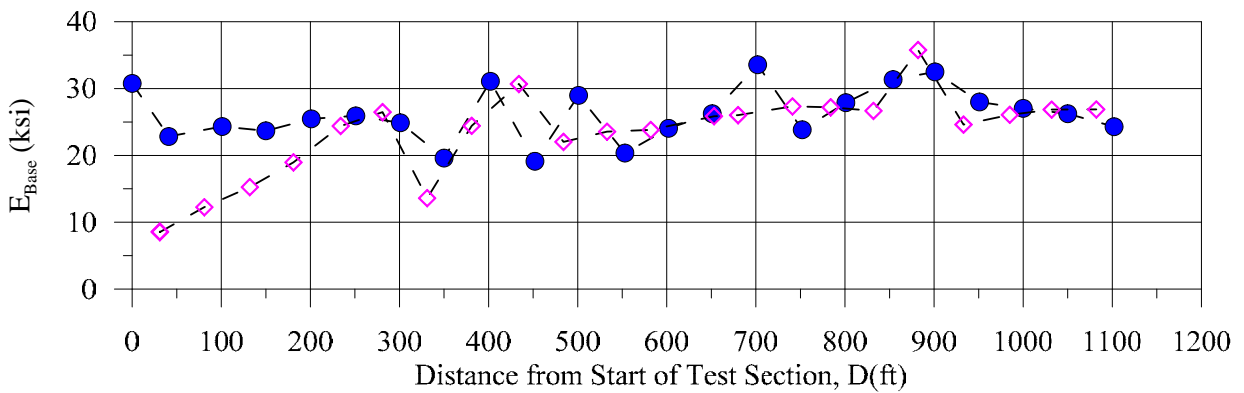
Figure D-12: Results of FWD tests on STH 32OC pavement.



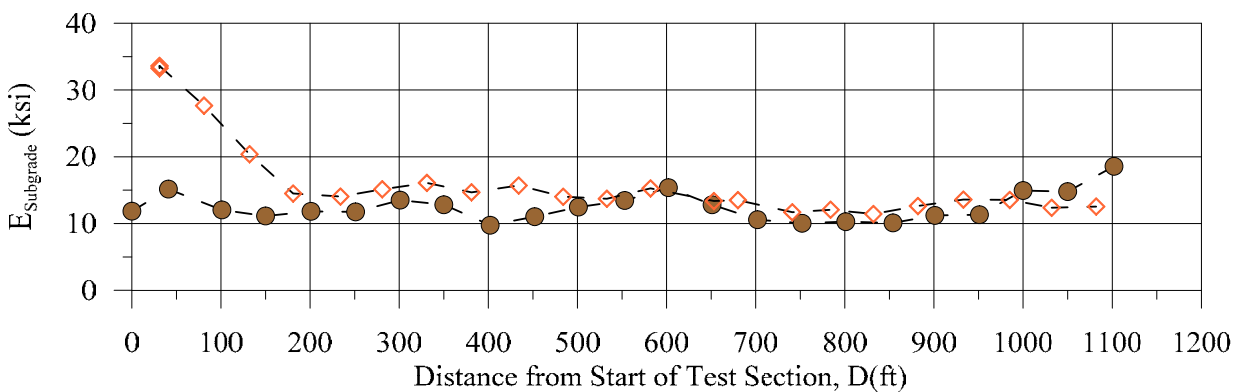
(a) Adjusted deflection under the loading plate (D_0) (corrected for a 9,000 lb drop and temperature)



(b) Backcalculated HMA layer modulus

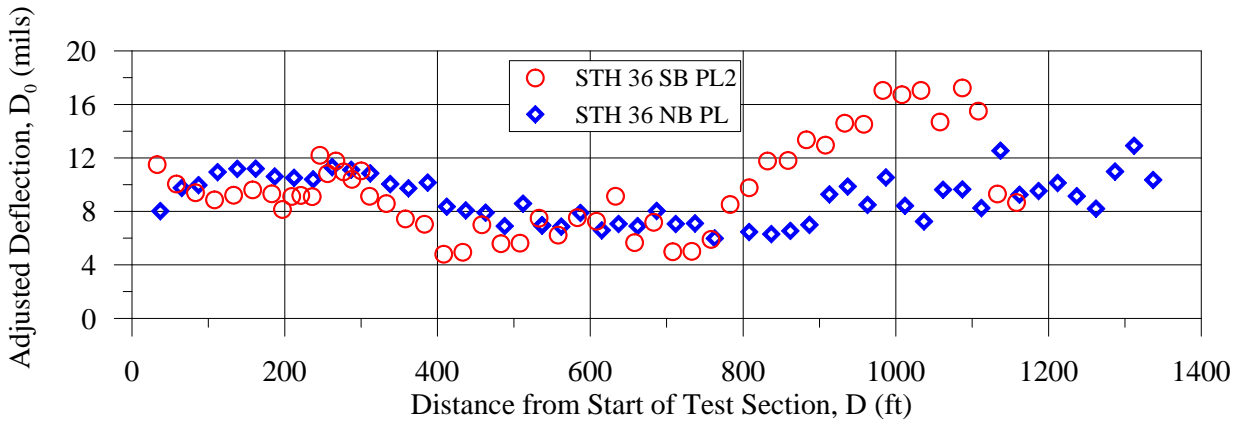


(c) Backcalculated base layer modulus

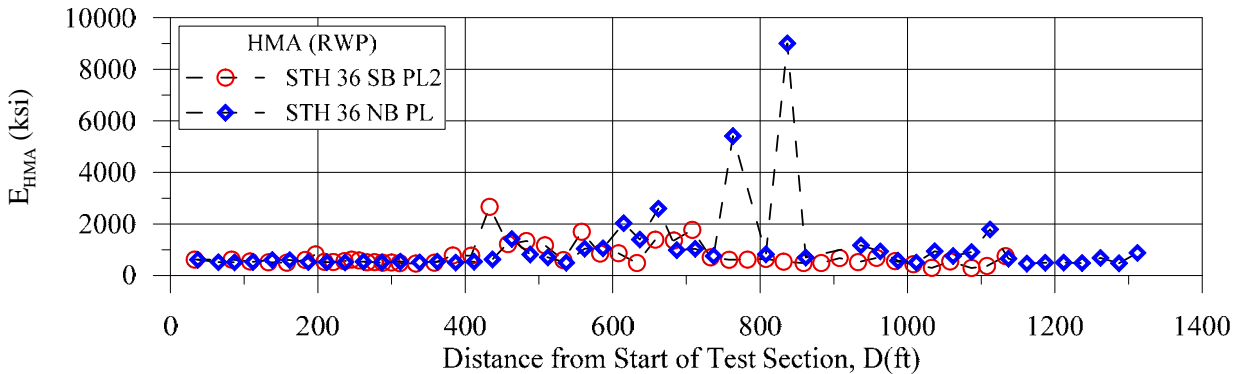


(d) Backcalculated subgrade modulus

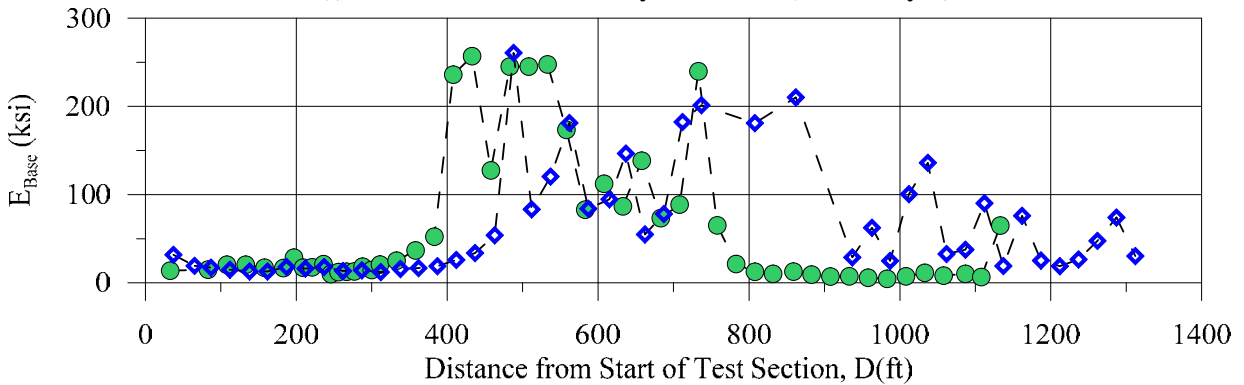
Figure D-13: Results of FWD tests on STH 142 W pavement.



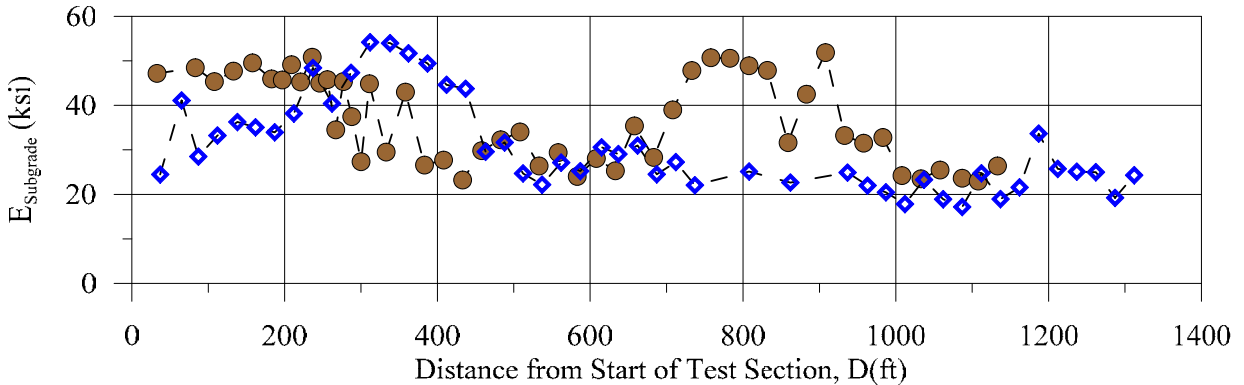
(e) Adjusted deflection under the loading plate (D_0) (corrected for a 9,000 lb drop and temperature)



(f) Backcalculated HMA layer modulus (surface layer)



(g) Backcalculated base layer modulus (upper base layer – brown aggregate)



(h) Backcalculated subgrade modulus (see gray aggregate in discussion)

Figure D-14: Results of FWD tests on STH 36 pavement.

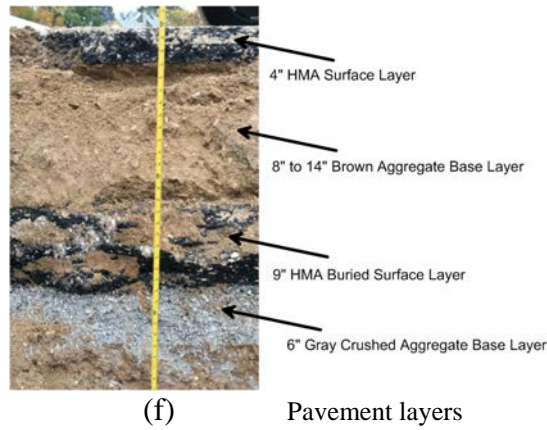
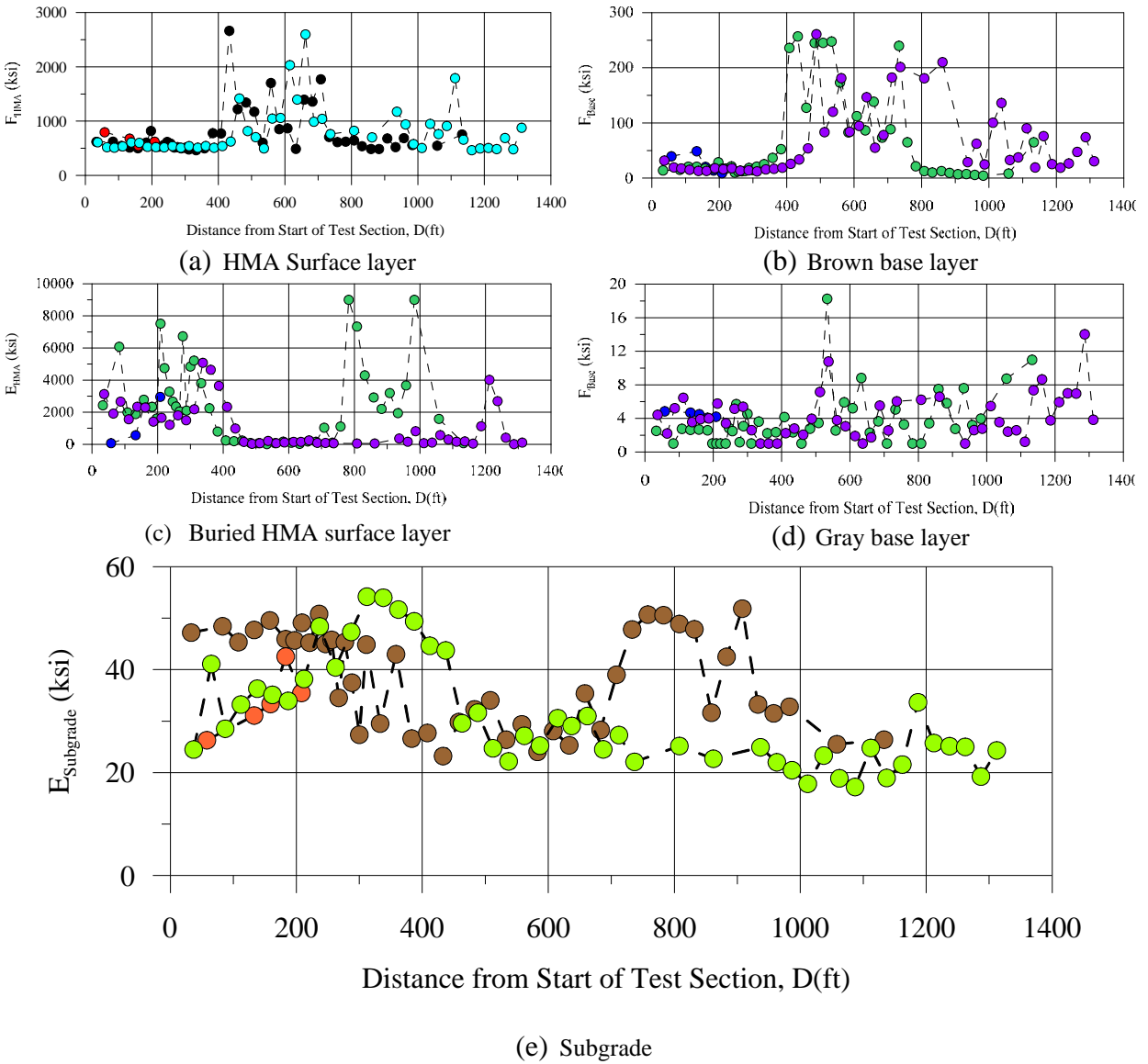


Figure D-15: Results of FWD tests on STH 36 pavement.